Reynolds Stress Modelling for Turbomachinery Flow Applications

Vom Fachbereich Maschinenbau
an der Technischen Universität Darmstadt
zur
Erlangung des Grades eines
Doktors der Naturwissenschaften (Dr. rer. nat.)
genehmigte

Dissertation

vorgelegt von

Dipl.-Phys. Christian Morsbach

aus Wuppertal

Berichterstatter:	Prof. Dr.-Ing. habil. Cameron Tropea
Mitberichterstatter:	Prof. Dr.-Ing. Reinhard Mönig
	apl. Prof. Dr.-Ing. habil. Suad Jakirlic
Tag der Einreichung:	02.08.2016
Tag der mündlichen Prüfung:	19.12.2016

Darmstadt 2016
D17

Abstract

Most industrially relevant flows in turbomachinery components are of a turbulent or at least transitional nature. Hence, the success of the numerical simulation of such flows depends significantly on the correct representation of turbulent effects. In the framework of continuum mechanics, these are described by the Navier-Stokes equations. A direct solution of these equations (Direct Numerical Simulation, DNS) is, however, not feasible at industrially relevant Reynolds numbers due to the enormous computational requirements. For this reason, the Reynolds-averaged Navier-Stokes equations are used to describe the flow and turbulent effects are considered by appropriate statistical models.

The present thesis addresses the analysis of differential Reynolds stress models (DRSM). The models are implemented in the DLR solver TRACE and qualified for the application to turbomachinery flows. After a rigorous literature review, with the SSG/LRR-ω and the JH-ω^h model, two models of different complexity and robustness were chosen. Since the latter is a crucial factor for the successful application of these models, the numerical properties of the DRSMs with special focus on the pressure-strain correlation term are investigated by means of a model problem. In this respect, both a dynamical systems analysis and a numerical phase space analysis are conducted exemplarily. For the robust numerical solution of the model equations, the linearisation of the sophisticated source terms is derived in the context of the implicit solution procedure. Since the transport equations of the turbulence variables are not solved in a coupled manner, a correction to the convective fluxes is developed, which ensures a conservative, second order accurate formulation. Numerous requirements for the application in turbomachinery flows, such as the solution in a rotating frame of reference, rotationally periodic boundary conditions or mixing planes are considered.

The implementation of the models is verified and validated by computing a substantial number of building block flows relevant to turbomachinery applications. In the framework of this activity the respective models' strengths and weaknesses compared to linear eddy viscosity models and explicit algebraic Reynolds stress models as well as each other are highlighted. The applicability of the DRSMs to industrially relevant configurations and their limits are demonstrated and discussed by a detailed evaluation of flows through a compressor cascade, a Ranque-Hilsch vortex tube and a 1.5 stage cold air turbine. The present critical evaluation is supposed to expose the different models' strengths and weaknesses and to recommend a suitable choice for respective applications.

Zusammenfassung

Die meisten Strömungen in industrierelevanten Turbomaschinenkomponenten sind turbulenter oder zumindest transitioneller Natur. Der Erfolg einer numerischen Simulation dieser Strömungen hängt daher in großem Maße von der korrekten Darstellung turbulenter Effekte ab. Diese werden im Rahmen der Kontinuumsmechanik durch die Navier-Stokes-Gleichungen beschrieben. Eine direkte Lösung der Gleichungen (Direct Numerical Simulation, DNS) ist allerdings aufgrund der Anforderungen an die Rechenleistung bei industrierelevanten Reynoldszahlen nicht durchführbar. Aus diesem Grund werden die Reynolds-gemittelten Navier-Stokes-Gleichungen zur Beschreibung der Strömung herangezogen und turbulente Effekte durch geeignete statistische Modelle berücksichtigt.

Die vorliegende Arbeit beschäftigt sich mit der Untersuchung von differentiellen Reynoldsspannungsmodellen (DRSM). Die Modelle wurden in den DLR Strömungslöser TRACE implementiert und für die Anwendung in Turbomaschinenströmungen qualifiziert. Für die Untersuchung wurden nach ausführlicher Literaturstudie mit dem SSG/LRR-ω- und dem JH-ω^h-Modell zwei Modelle sehr unterschiedlicher Komplexität und Robustheit ausgewählt. Da letzteres ein entscheidender Faktor für den erfolgreichen Einsatz dieser Modelle ist, werden die numerischen Eigenschaften der DRSMs mit besonderem Fokus auf den Druck-Scher-Korrelationsterm anhand eines Modellproblems auf ihre Stabilitätseigenschaften untersucht. Dabei wird das Verhalten der Modelle als dynamisches System analytisch und numerisch im Phasenraum untersucht. Zur robusten numerischen Lösung der Modellgleichungen wird im Rahmen des impliziten Lösungsverfahrens die Linearisierung der Quellterme hergeleitet. Da die Transportgleichungen der Turbulenzvariablen nicht gekoppelt gelöst werden, wird eine Korrektur der konvektiven Flüsse entwickelt, die eine konservative Formulierung mit Genauigkeit zweiter Ordnung gewährleistet. Für die Anwendung in Turbomaschinenströmungen werden eine Vielzahl von Anforderungen wie zum Beispiel rotierende Bezugssysteme, in Umfangsrichtung periodische Randbedingungen oder Mischungsebenen berücksichtigt.

Die Implementierung der Modelle wird an verschiedensten grundlegenden Strömungen mit Bezug zu Turbomaschinenströmungen verifiziert und validiert. Dabei werden die Stärken und Schwächen der verwendeten Modelle im Vergleich zu Wirbelzähigkeitsmodellen und expliziten algebraischen Reynoldsspannungsmodellen sowie untereinander herausgearbeitet. Die Anwendbarkeit der DRSMs auf industrierelevante Konfigurationen und deren Grenzen werden anhand der detaillierten Untersuchung von Strömungen durch ein Verdichtergitter, ein Ranque-Hilsch-Wirbelrohr sowie eine anderthalbstufige Kaltluftturbine demonstriert und diskutiert. Die vorliegende kritische Analyse soll die Stärken und Schwächen der verschiedenen Modelle darlegen und Empfehlungen für eine geeignete Modellauswahl für die entsprechenden Anwendungen geben.

Danksagung

Diese Arbeit ist während meiner Zeit als wissenschaftlicher Mitarbeiter am Institut für Antriebstechnik des Deutschen Zentrums für Luft- und Raumfahrt e.V. in der Abteilung Numerische Methoden entstanden. Zuallererst gilt mein besonderer Dank Prof. Suad Jakirlić für die Betreuung der Arbeit und die zahlreichen Diskussionen über Reynoldsspannungsmodelle. Weiterhin bedanke ich mich bei Prof. Reinhard Mönig für die Übernahme des Koreferates, bei Prof. Cameron Tropea für die Übernahme des Referates und bei Prof. Heinz-Peter Schiffer für die Übernahme des Vorsitzes der Prüfungskommission.

Meinem Abteilungsleiter Dr. Edmund Kügeler danke ich für sehr viel Freiraum bei der Arbeit an diesem Thema. Ganz besonders hervorzuheben ist die Betreuung durch Dr. Martin Franke, der mich von Grund auf mit dem Thema Turbulenzmodellierung vertraut gemacht hat und meine Arbeit fachlich durch viele Diskussionen, Anregungen und Kritik begleitet hat. Meinen Kollegen gilt mein Dank für eine tolle Atmosphäre, die vielen offenen Ohren, das Wissen über Strömungssimulation und Turbomaschinen sowie ihre einzigartige Hilfsbereitschaft. Hervorheben möchte ich außerdem den überaus offenen und hilfreichen Austausch mit Dr. Bernhard Eisfeld und Dr. Axel Probst über Institutsgrenzen hinweg.

Für die inspirierende Zusammenarbeit im Projekt TurboVaLd danke ich meinen Kollegen von der Abteilung Triebwerksmesstechnik sowie meinem damaligen Studenten Daniel Schlüß. Stephan Behre vom Institut für Strahlantriebe und Turboarbeitsmaschinen bin ich für die Messdaten zur Kaltluftturbine und die Unterstützung bei deren Interpretation überaus dankbar.

Nicht zuletzt gilt mein Dank meiner Familie, die mir meine Ausbildung ermöglicht hat, mich in jeglicher Hinsicht unterstützt und mir großartigen Rückhalt bietet. Meiner Freundin Anne danke ich dafür, dass sie immer an mich glaubt und mir im richtigen Moment entscheidende Impulse in die richtige Richtung gegeben hat.

Köln, im Dezember 2016 Christian Morsbach

Contents

1 Introduction and motivation **1**

1.1 Computational Fluid Dynamics - CFD 1

1.2 Reynolds-Averaged Navier-Stokes approach - RANS 2

1.3 Differential Reynolds stress modelling - DRSM 3

1.4 Outline of the thesis 4

2 State of the art **7**

2.1 Statistical turbulence modelling 7

2.2 Differential Reynolds stress modelling 8

3 Turbulence modelling **13**

3.1 Statistical turbulence modelling 13

3.2 Differential Reynolds stress modelling 16

3.2.1 Reynolds stress transport equations 16

3.2.2 Reynolds stress anisotropy and its visualisation 17

3.2.3 Pressure-strain correlation 20

3.2.4 Dissipation correlation 21

3.2.5 Diffusion of Reynolds stresses 21

3.3 Studied DRSMs 22

3.3.1 SSG/LRR-ω model 22

3.3.2 Jakirlić, Hanjalić and Maduta's $\overline{u_i u_j}$-ω^h model 23

3.4 Numerical properties of pressure-strain models 30

3.4.1 Model problem 31

3.4.2 Dynamical systems analysis 33

3.4.3 Numerical phase space analysis 35

4 Numerical method **43**

4.1 Flow solver 43

4.2 Discretisation of transport equations 46

4.3 Linearisation of the residual 48

4.4 Boundary conditions for turbulent flows 51

4.4.1 Solid walls 51

4.4.2 Rotationally periodic boundaries 51
4.4.3 Mixing planes 52
4.4.4 Inflow 53
4.4.5 Symmetry plane 54
4.5 Numerical performance 54

5 Model validation in generic flows **57**
5.1 Channel flow 57
5.2 Boundary layer 70
5.3 Curved boundary layer 74
5.4 Separated boundary layer 78
5.5 Shock wave/boundary layer interaction 83

6 Model application to turbomachinery flows **87**
6.1 Compressor cascade 87
6.1.1 Description 87
6.1.2 Numerical setup 87
6.1.3 Discussion 89
6.2 Ranque-Hilsch vortex tube 96
6.2.1 Description 96
6.2.2 Numerical setup 98
6.2.3 Discussion 98
6.3 One and a half stage cold air turbine 107
6.3.1 Description 107
6.3.2 Numerical setup 109
6.3.3 Post-processing 110
6.3.4 Discussion 111

7 Summary and Outlook **125**

Nomenclature **129**

Bibliography **134**

List of figures **145**

List of tables **151**

A Model specifications **153**
A.1 Menter SST k-ω 153
A.2 Hellsten EARSM k-ω 154
A.3 DRSM: common terms 157

A.4 SSG/LRR-ω model 158
A.5 Jakirlić, Hanjalić and Maduta's $\overline{u_i u_j}$-ω^h model 159

B Vortex detection methods **163**
B.1 The λ_2-criterion 163
B.2 Streamwise vorticity 163

1 Introduction and motivation

1.1 Computational Fluid Dynamics - CFD

Turbomachinery is heavily employed in various industrial sectors. Types of turbomachines used in the energy sector are wind turbines, water turbines in hydroelectric plants, steam turbines in coal or nuclear power plants or gas turbines in gas power plants. Most importantly, gas turbines also play a major role in aircraft propulsion systems both in turbofan and turboprop engines. For the aviation industry, the Advisory Council for Aviation Research and Innovation in Europe (ACARE) has developed ambitious goals to reduce the environmental impact of the whole air transport system (European Commission *et al.*, 2011). The improvement of engines plays a crucial role in achieving these goals. In order to devise designs both quieter and more efficient, it is essential to understand the fluid dynamic processes within these machines.

Traditionally, most of the development was supported by rig testing. Obviously, this method is rather expensive and the number of different designs that can be evaluated is limited. Furthermore, turbomachinery components provide limited access to the flow for measurement equipment. Probes introduced into the machines disturb flow field and laser measurements require visual access. Above all, measurements in the rotating parts of the machine are a significant challenge. Engineers, therefore, have to build all their designs based on a very limited knowledge of the actual flow field.

On the other hand, the governing equations of continuum fluid flow, the Navier-Stokes equations, were derived over a century ago. So far, neither a general analytical solution has been found, nor exists a proof that a smooth solution always exists. The latter is one of the Millennium Problems in mathematics. Yet, with the advent of the digital computer, methods have been devised and employed which can numerically find solutions that satisfy the equations. This is done on a discrete grid where the state variables such as density, velocity and pressure are computed at every point in space. Such a grid has to be generated for every geometry. The overall process is called Computational Fluid Dynamics (CFD).

The availability of such a method enables several new approaches. First, the flow field can be investigated in great detail anywhere where it is of interest because the solution is computed for the complete domain. This can result in a better understanding of the flow physics. Second, it becomes possible to investigate great numbers of different geometries at relatively low cost. In this process, the geometry is parameterised and grid generation, simulation, extraction and evaluation of results are automated. Optimising algorithms can then find the optimal geometry with respect to defined target functions such as efficiency or noise level. Because of that, CFD has found its way into the design process of modern fluid dynamic devices.

Highly accurate CFD simulations are part of DLR's aviation research strategy and are represented in the research portfolio around the virtual product. The goal is to be able to numerically represent a complete aircraft system with all relevant physical processes. If such a highly accurate tool were available, the vision would be to completely design a product using CFD without the need for rig tests. To achieve this goal, numerical methods as well as physical models have to be developed and validated. DLR's flow solver TRACE represents one part of this strategy. It has been developed with special focus on turbomachinery flows and has been employed in the industrial design process for over a decade.

1.2 Reynolds-Averaged Navier-Stokes approach - RANS

A flow problem can be characterised by its Reynolds number Re describing the ratio of inertial to viscous forces. As long as the Reynolds number is low, the flow remains laminar and a numerical simulation is possible with reasonable effort. However, if the Reynolds number becomes sufficiently large, the flow enters the turbulent regime, which is described by Bradshaw (1971) as follows:

> "Turbulence is a three dimensional time dependent motion in which vortex stretching causes velocity fluctuations to spread to all wavelengths between a minimum determined by viscous forces and a maximum determined by the boundary conditions. It is the usual state of fluid motion except at low Reynolds numbers."

Such turbulent flows can, in principle, be described completely by the Navier-Stokes equations. However, the range of length and time scales that are found in a turbulent flow scales with its Reynolds number. All these scales have to be accounted for by sufficient grid and time resolution in the computational domain. Hence, the cost for the direct solution of the Navier-Stokes equations (Direct Numerical Simulation, DNS) would also scale with the Reynolds number. Based on current development of computational power and cost, industry readiness of DNS is not expected before 2080 (Spalart, 2010).

There are two options to reduce the computational cost. One is to filter the equations and resolve only the largest structures, which leads to the concept of Large Eddy Simulation (LES). Then, only the effect of the smallest structures below the grid resolution remains to be modelled. Still, as the simulations require a high temporal and spatial resolution, especially for wall-bounded flows at practical Reynolds numbers, the computational effort remains high and industry readiness is not expected before 2045 (Spalart, 2010). However, from a point of view of a designer of machines, the intricate and detailed structures in turbulent flow are of less interest than the average or mean flow. Therefore, the idea is to solve equations directly for the averaged flow solution concerning the turbulent flow motion. To achieve this, a statistical approach is chosen and the flow quantities are split into an average and a fluctuating part. This approach is called Reynolds averaging for incompressible flows or Favre averaging for compressible flows and leads to the Reynolds-averaged Navier-Stokes (RANS) equations. Due to the non-linearity of the convection term, the correlations of fluctuating velocity components appear in momentum and energy equations. These are called Reynolds stresses $\overline{\rho u_i'' u_j''}$.

The problem of this statistical approach is that it cannot provide a solution for the Reynolds stresses. It is possible to devise governing equations for Reynolds stresses

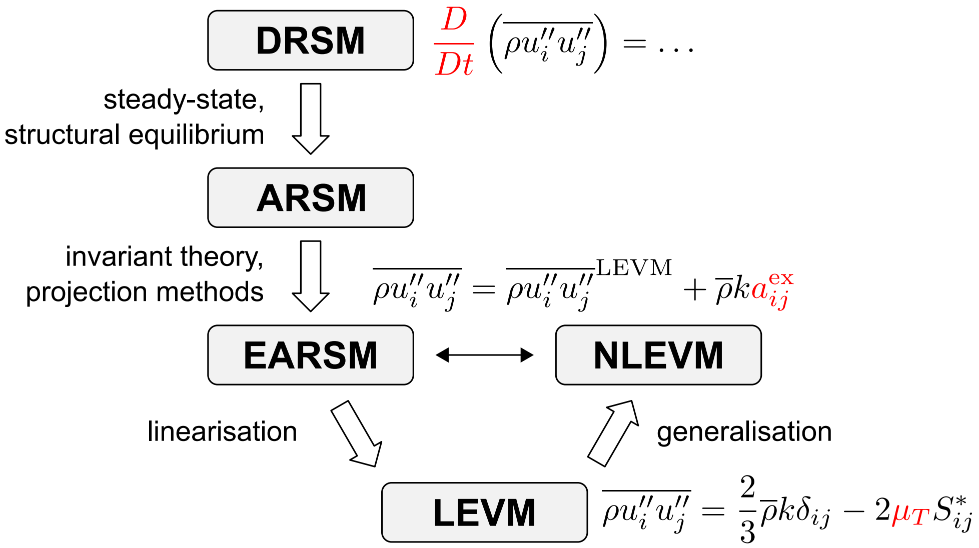
DRSM
$\frac{D}{Dt}\left(\overline{\rho u_i'' u_j''}\right) = \dots$
steady-state, structural equilibrium
ARSM
invariant theory, projection methods
$\overline{\rho u_i'' u_j''} = \overline{\rho u_i'' u_j''}^{\mathrm{LEVM}} + \overline{\rho} k a_{ij}^{\mathrm{ex}}$
EARSM
NLEVM
linearisation
generalisation
LEVM
$\overline{\rho u_i'' u_j''} = \frac{2}{3}\overline{\rho} k \delta_{ij} - 2\mu_T S_{ij}^*$

Figure 1.1: Hierarchy of RANS turbulence models. Reproduced after Gatski & Jongen (2000).

but in these, higher order correlations of fluctuating quantities occur. This is called closure problem and dictates that the statistical approach will always require some sort of physical model for unknown correlations. The community has tried to address this problem for over a century now. What basically distinguishes different approaches is the level at which the equations are closed with models.

1.3 Differential Reynolds stress modelling - DRSM

It is instructive to categorise turbulence models based on the level at which closure is obtained as shown in Figure 1.1. There are several ways to close the RANS equations. Historically, mixing length models form the simplest approach to model the Reynolds stresses. They are based on the idea that, on average, the convective processes governed by turbulent eddies can be viewed as a diffusive process. An algebraic relation is used to define a turbulent viscosity requiring *a priori* knowledge about the flow, i.e. the dominant mixing length scale. As a generalisation of this, many turbulence models in use nowadays are based on the Boussinesq assumption which relates the Reynolds stress tensor directly to the rate of strain tensor S_{ij} of the flow (Wilcox, 2006). This relation is linear or isotropic, which is why linear eddy viscosity models (LEVM), placed at the bottom of the figure, are often called isotropic turbulence models. It has to be mentioned, however, that only the relation between strain rate and Reynolds stress is linear. Hence, the Reynolds stress tensor inherits all anisotropy from the strain rate tensor. This closes the RANS equations but shifts the modelling task to the determination of the apparent viscosity or eddy viscosity μ_T. It can be achieved by different means ranging from algebraic models to two equation models solving transport equations for the turbulent kinetic energy and a turbulent length or time scale. The critical issue in this approach is that the effect of turbulence is reduced to an increased effective viscosity of the fluid although turbulence is a property of the flow and not a property of the fluid.

Connected with this conceptual problem there are a series of phenomena which cannot be properly described by turbulence models based on the Boussinesq assumption (Hanjalić & Jakirlić, 2002). First, there are stagnating flows, for which an unphysically large amount of turbulent kinetic energy is produced. In flows with streamline curvature or system rotation and in turbulence driven secondary flows LEVMs fail due to the incorrect prediction of turbulence anisotropy. Furthermore, three dimensional boundary layers, or flows with more than one relevant shear stress, can only be properly described by models which resolve all components of the Reynolds stress tensor. Recently, the validity of the Boussinesq approximation in a turbomachinery flow was investigated by means of DNS (Michelassi *et al.*, 2014). The authors showed that the linear stress-strain coupling is violated in large parts of the flow field, especially in the boundary layer.

For the above reasons, an extension was suggested in the form of non-linear eddy viscosity models (NLEVM). Such models employ the Boussinesq approximation as a linear base but add an extra anisotropy a_{ij} generalising the constitutive relation. The extra anisotropy is determined by algebraic relations as a function of gradients of mean flow variables and their invariants. A different derivation starts from the governing equations for the Reynolds stress tensor. The assumption that the transport of individual Reynolds stress tensor components is proportional to the transport of turbulent kinetic energy leads to algebraic Reynolds stress models. These are computationally inconvenient owing to implicit relations for the Reynolds stresses. Projection methods and invariant theory can be used to obtain explicit algebraic relations. This class is called explicit algebraic Reynolds stress model (EARSM) and is formally equivalent to a NLEVM. These models promise to be a compromise between the numerical robustness of LEVMs and the ability to predict flows involving turbulence anisotropy inherited from DRSMs. However, it has been argued that they are often used in flows which do not fulfil the basic assumptions made in their derivation (Spalart, 2015).

The models described above close the RANS equations by an algebraic model for the Reynolds stresses. In contrast, differential Reynolds stress models (DRSM) or second moment closures (SMC) model each component of the Reynolds stress tensor $\overline{\rho u_i'' u_j''}$ directly by means of transport equations whose exact formulation is derived from the Navier-Stokes equations. As will be shown later on, these transport equations contain a number of higher correlations. Here, the modelling task is shifted to these higher correlations. The hope is that these are easier to grasp physically but there is considerable doubt about that (Spalart, 2015). Nevertheless, the exact production term of Reynolds stresses in this type of model is a clear advantage over eddy viscosity models. Furthermore, redistribution of energy between individual components, individual history and transport effects can be considered. So even the most basic DRSMs can, at least qualitatively, capture effects such as streamline curvature or system rotation and are, in theory, superior to LEVMs and EARSMs.

1.4 Outline of the thesis

In Chapter 2 the relevant literature review is given, aiming at providing the state of the art of simulation of turbulent flows in turbomachinery components. The strengths and weaknesses of the commonly applied approaches are highlighted, illustrating consequently the motivation for development and application of differential Reynolds stress models (DRSM) to turbomachinery flows. Chapter 3 presents the theoretical background in detail and introduces the two specific DRSMs studied in this thesis. One of the major challenges in establishing DRSMs in an industrial environment is their numerical robustness relative to simpler models, mostly based on the eddy-viscosity concept. For this reason, the numerical properties of the adopted sophisticated Reynolds stress models, with particular emphasis on the corresponding pressure-strain terms concerning their solution stability is evaluated by means of a model problem procedure. With respect to the latter both a dynamical systems analysis and a numerical phase space analysis are conducted exemplarily. The implementation of the two considered DRSMs into an existing Reynolds-averaged Navier-Stokes (RANS) solver represents the prime objective of the present work. Apart from the stable and robust numerical formulation of the models, an industrial CFD code for multi-stage turbomachinery applications on hybrid grids requires the treatment of rotating frames of reference, interfaces between rotating and non-rotating parts as well as between structured and unstructured grids. Therefore, the model implementation has to be correspondingly adjusted to this high fidelity numerical method and solution algorithm. The code features which differ from previously implemented methods are described in Chapter 4.

The turbulence model implementation is interactively verified and validated by computing a substantial number of building block flows relevant to turbomachinery applications (Chapter 5); in the framework of this activity the respective models' strengths and weaknesses are highlighted. To demonstrate their feasibility in computing industrially relevant configurations, the models are subsequently applied to a compressor cascade, a Ranque-Hilsch vortex tube and a cold air turbine flow (Chapter 6). The thesis ends with the concluding Chapter 7 summarising the modelling activities and achieved results and giving recommendations for future work.

Résumé: the present thesis introduces two differential Reynolds stress models of different complexity; the verification of their implementation and consequent validation is performed by means of representative flow configurations relevant to turbomachinery applications. The models have been devised following different strategies. Hence, they differ largely in their complexity and stability. The present critical evaluation is supposed to expose their strengths and weaknesses and to recommend a suitable choice for respective applications.

2 State of the art

2.1 Statistical turbulence modelling

Even though the extreme computational effort of DNS makes the application in industrial environments unattractive, a large scientific effort has gone into these simulations. DNS has proven to be useful for "numerical experiments" to investigate turbulent flows in representative configurations (e.g. turbulent plane channel flow (Kim *et al.*, 1987) or turbulent flat plate boundary layer (Spalart, 1988)) in great detail. They also supply detailed validation data for turbulence models and aid their development. Nevertheless, DNS of turbomachinery components have been reported recently. One such example is the work of Sandberg *et al.* (2015) and Michelassi *et al.* (2014). They describe the development of a highly efficient DNS solver, capable of computing the flow through turbine cascades. This solver does not involve any turbulence modelling and is hence even capable of predicting laminar to turbulent transition. It employs compact finite difference schemes for the spatial discretisation in axial and pitchwise directions while a Fourier method is used in the spanwise direction. They showed the flow through a turbine cascade at a Reynolds numbers up to 10^5.

In view of industrial applications and/or flows at higher Reynolds numbers significant effort has gone into the development of LES methods. LES is especially helpful in free shear flows in the absence of solid walls because significant grid requirements arise if wall bounded flows are computed. A massively separated flows is a combination of a wall bounded flow and a free shear flow. RANS models typically fail in this situation since they have been developed for attached or mildly separated flows (Spalart, 2009). Therefore, an approach that has been followed with enthusiasm is the combination of RANS and LES to a hybrid RANS-LES method because this promises the earliest integration of scale-resolving simulations in industrially relevant computational tools. It employs RANS in attached boundary layers and LES in separated flows. Various approaches exist such as detached eddy simulation (DES) (Spalart & Shur, 1997) and its refinements, scale adaptive simulations (SAS) (Menter & Egorov, 2005) or partially averaged Navier-Stokes (PANS) methods (Girimaji, 2006). In an extensive review of LES and hybrid RANS-LES application to turbomachinery flows, Tucker states that these methods show great potential for capturing the highly unsteady flow effects. Yet their application still requires a significant degree of expertise and many results are obtained with under-resolved simulations (Tucker, 2011).

Turbomachinery flows present quite a few challenges for RANS turbulence models. Due to the geometrical configuration of blades and end walls, a broad range of secondary flows is induced (Langston, 2001). These include interacting vortices such as horse shoe, passage and tip leakage vortex as well as corner separation from the blade surface. The flow is highly three dimensional and anisotropic. For rotor blade rows, the flow is influenced by centrifugal and Coriolis forces due to the rotating frame of reference. Finally, unsteady phenomena have to be considered owing to the relative motion of the adjacent blade rows.

For industrial turbomachinery applications, RANS turbulence models developed in the 80's and 90's of the last century still form the basis in day-to-day business. These are mostly two equation LEVMs based on the turbulent kinetic energy k and its specific dissipation rate ω such as the Wilcox k-ω model (Wilcox, 1988) or the Menter SST k-ω model (Menter, 1994). As pointed out in the introduction, LEVMs have inherent modelling weaknesses which affect the predictive accuracy for flows in turbomachinery components. They have to be overcome by introduction of ad hoc modifications or "turbomachinery specific extensions" (Franke *et al.*, 2010), most commonly applied to the scale-determining equation.

A more general approach to deal with these deficiencies is this application of refined modelling techniques. NLEVMs or EARSMs present an attractive compromise between predictive accuracy and numerical robustness (Franke, 2010). EARSMs such as the one suggested by Hellsten (2005) are currently being evaluated as a viable alternative to highly tuned LEVMs. It is expected that a more general modelling approach yields a broader range of applicability, which motivates the investigation of applying DRSMs for turbomachinery flows.

2.2 Differential Reynolds stress modelling

More than fifty years after Reynolds laid the ground for RANS turbulence models (Reynolds, 1895), Chou derived the governing equations for the individual Reynolds stress components (Chou, 1945). Rotta then analysed the pressure-strain redistribution term in great detail and suggested a simple return-to-isotropy model for the slow term which still forms the basis for most closures today (Rotta, 1951). Also, he took up considerations by Kolmogorov about local isotropy of turbulence at high Reynolds numbers which lead to isotropic dissipation models for the Reynolds stresses.

An early solution to the transport equations for the Reynolds stresses and the dissipation rate of turbulent kinetic energy was presented by Daly and Harlow. They computed the set of equations simplified for the case of flow between two parallel flat plates (Daly & Harlow, 1970). One of the first full differential Reynolds stress closures was presented by Hanjalić & Launder (1972). Their strategy was a term-by-term modelling of the Reynolds stress and dissipation equations. The pressure-strain correlation was an early version of one of the most cited pressure-strain models, published three years later by Launder *et al.* (1975) (LRR). The blocking effect of a solid wall had to be considered explicitly in the model by modifications of the redistribution term. The model, which is linear in the velocity gradient and Reynolds stress tensors, formed the basis of many more sophisticated closures developed later on. Investigations of decaying anisotropic turbulence, however, showed that the return-to-isotropy process cannot be described accurately by a linear model. Hence, Speziale *et al.* (1991) (SSG) suggested a quadratic pressure-strain model which has prevailed in some form in many modern closures.

Even in the late 1990s and early 2000s, thirty years after the first full DRSMs were suggested, they were still not sufficiently used to assess their advantages over LEVMs with respect to turbomachinery applications (Bradshaw, 1996). Especially low-Reynolds closures had not yet been widely adopted (Leschziner *et al.*, 2000). However, there are more recent developments which show encouraging results for the application of those models to industrially relevant configurations.

One area of research towards the application in complex geometries is the removal of wall geometry related parameters. Craft & Launder (1996) formulated a model independent of the wall geometry by replacing the wall-normal vector, which is usually found in wall modifications, by the gradient of a turbulence anisotropy parameter. A modified version of this model was applied to compressible flows involving shock-wave/boundary-layer interaction. The complex flow around a blunt-fin/flat-plate junction could be simulated successfully and showed superior results compared to the Menter SST k-ω model as well as the DRSM of Hanjalić and Jakirlić (Batten *et al.*, 1999). The approach of Craft and Launder was also adopted by Gerolymos and his co-workers who published a series of papers about DRSMs applied to turbomachinery-related flows. They extended their model (Gerolymos & Vallet, 1997) in a similar fashion, to obtain a "wall-normal free" model (Gerolymos *et al.*, 2002; Gerolymos & Vallet, 2002). Based on this model, they were able to obtain a superior predictive accuracy compared to eddy viscosity models (Gerolymos & Vallet, 2007; Gerolymos *et al.*, 2010).

Hanjalić and Jakirlić developed their model by detailed assessment of the model's behaviour when it is supplied with DNS data. It is based on the low-Reynolds closure developed by Hanjalić & Launder (1976). Their efforts began with the improvement of the dissipation model (Hanjalić & Jakirlić, 1993). Furthermore, they employ linear formulations of pressure-strain redistribution models, but, similar to Gerolymos, they obtain model coefficients that are now functions of turbulence anisotropy invariants (Hanjalić & Jakirlić, 1998). More recently, the authors tested the formulation of several closure models for the pressure-strain term (Jakirlić & Hanjalić, 2013). They found that its general tensorial formulation is justified since the coefficient values obtained for different components of the tensor collapsed reasonably. Away from solid walls, the coefficients showed nearly uniform values, agreeing closely with the SSG model. But even in simple boundary layer flows, such as a plane turbulent channel flow (Kim *et al.*, 1987), the model coefficients cannot be properly described by constant values close to solid walls. The presence of solid walls is modelled by terms including the wall-normal vector and the turbulent Reynolds number. The performance of the model is investigated in separating flows such as a backward facing step flow. They conclude that low-Reynolds-number and wall effects need to be considered, if wall phenomena such as friction or heat transfer are of interest.

Jakirlić has since continued to develop and refine the model. An important step was the introduction of the homogeneous dissipation rate ϵ^h, derived from the two-point velocity correlation equation, as the scale-determining variable (Jakirlić & Hanjalić, 2002). This approach satisfies the dissipation wall limits without any wall topography parameters. To remove wall topography dependence in the pressure-strain terms, the author followed a strategy similar to that of Gerolymos and computed the wall-normal vector as a gradient of a turbulence anisotropy parameter (Jakirlić *et al.*, 2007). The application of the model to a 3D wing showed superior results compared to a simpler DRSM closure and a LEVM. Since the mesh requirements cannot be always properly met, especially when industrial configurations are computed, work was spent on the robustness of low-Reynolds boundary conditions. In the current version of the model, the boundary condition for the scale-determining equation is formulated based on the Taylor microscale λ (Jakirlić & Jovanović, 2010). It was shown that this approach tolerates y^+-values of up to 3 without loss in predictive accuracy (Jakirlić *et al.*, 2013). More recently, the model was developed towards the application as the RANS part in a scale-resolving simulation based on the SAS approach and called an "instability-sensitive"

RSM (Maduta, 2013). In this context, the scale-determining equation was changed from ϵ^h to ω^h. In view of application to turbomachinery flows, it can be said that the model was intensively tested in rotating and swirling flows (Jakirlić *et al.*, 2002). At very low Reynolds numbers, the model, similar to many other DRSM closures, erroneously predict premature relaminarisation at high rotation rates which could be cured by introduction of an additional source term in the dissipation equation. It is expected that this will not be necessary at Reynolds numbers usually encountered in turbomachinery.

Other authors choose a different approach and focus primarily on the prediction of mean flow quantities. Wilcox (2006) developed a high Reynolds, compressible DRSM based on the most recent version of his k-ω LEVM. It was calibrated for boundary-layer flows and a range of homogeneous turbulence flows. No wall-reflection terms are employed in the pressure-strain model because, according to the author, they are not required to obtain the boundary layer profile if the ω-equation is used in contrast to ϵ-equation in original LRR-model. The model was intensively tested and compared to other DRSMs by Sciberras & Coleman (2007). In plane turbulent channel flow, it was found that the model has serious deficits in normal-stresses prediction, but, due to cancellation of errors, the mean velocity profile and skin friction coefficient are predicted successfully. However, the authors state that correct normal stress prediction is essential especially for flows with separation.

Eisfeld (2006) developed his model for the application in industrially relevant external aerodynamic flows. He followed the approach of Menter and combined the SSG model for free shear flows with the Stress-ω model for wall bounded flows using the blending function developed by Menter for his SST k-ω model. Hence, close to solid walls, the model inherits the deficiencies of the Stress-ω model concerning the prediction of normal-stresses (Morsbach *et al.*, 2012). Mean flow features of complex 3D flows, however, are captured more accurately than with standard LEVM approaches as shown for the ONERA M6 wing (Cécora *et al.*, 2012). Furthermore, Eisfeld (2010*a*) studied the influence of the scale-determining equation on the prediction of the shock-position for the RAE 2822 aerofoil. It was found that it can have a larger influence than the choice of pressure-strain model. Nguyen *et al.* (2011) developed near-wall extensions for the model to overcome the deficiencies in normal-stress prediction.

Reports on the application of DRSMs to industrially relevant turbomachinery configurations are rather limited. One of the first to apply a near-wall DRSM to such configurations were Gerolymos *et al.* (2002). They studied subsonic stator row, a transonic compressor rotor and a 1.5 stage turbine. The DRSM performed significantly better than a reference LEVM when the flows featured separation or shock-wave/boundary-layer interaction. In a later paper, Gerolymos & Vallet (2007) demonstrated the simulation of a 3.5 stage compressor using DRSMs.

Rautaheimo *et al.* (2003) published computational results of a centrifugal compressor obtained with a DRSM. The two LEVMs performed better in predicting total values such as efficiency and total pressure ratio. This was attributed to shortcomings in the near-wall modelling of the employed DRSM which resulted in an overprediction of skin friction. Secondary flow effects, however, were qualitatively better reproduced by the DRSM.

The complex 3D structure of the flow through a linear compressor cascade with tip clearance was investigated using the DRSM of Hanjalić & Jakirlić (1998) by Borello *et al.* (2007). As expected, simulations using the DRSM resulted in improved predictive accuracy of the mean velocity profiles at most measured stations. The most significant improvements could be seen in the representation of the interacting vortices where the flow is 3D and the turbulence is anisotropic. Thus, according to the authors, DRSMs are the most adequate form of RANS turbulence modelling.

The model in its later forms has also been applied to transonic aerodynamic flows (Jakirlić *et al.*, 2007). It was found that it gave superior predictions of the shock structure in a 3D wing computation over Eisfeld's SSG/LRR-ω DRSM. On the other hand, the authors were able to obtain satisfactory results for a generic transport aircraft configuration with the latter. This was not possible using Jakirlić's model due to stability problems. It becomes clear at this point that there has to be a compromise between complexity, accuracy and stability of the models. Probst implemented the model into a general purpose CFD solver which is employed in industrial environments (Probst & Radespiel, 2008). He applied it to simulate complex flows such as nacelle stall (Probst, 2013). Although the model was not built to predict laminar to turbulent transition, he reported sensitivity to free-stream turbulence intensity for a zero-pressure-gradient flat plate. At very low turbulence intensities, the predicted skin friction coefficient was that of a laminar flow. In an eddy-viscosity model context, this laminarisation tendency could be traced back to low Reynolds number modifications in the model (Rumsey *et al.*, 2006). Probst suggested a transition treatment which introduces source terms based on linear stability theory to the Reynolds stress equations.

In his stimulating paper on "Philosophies and fallacies in turbulence modeling", Spalart (2015) raises several concerns about the development of DRSMs. First, there is the motivation. The general line of argument is that modelling on the second moment level is the "natural" level of closure. Higher correlations of fluctuating quantities, such as the dissipation or pressure-strain tensors should be easier to model and modelling errors should be less severe due to less direct influence on the mean flow. However, no clear evidence exists that the higher correlations recede in importance or magnitude. Models for them involve empiricism as much as models on the eddy viscosity level do. The remaining motivation for DRSM is, hence, the natural incorporation of rotation and curvature - although exactly only in the production term - and secondary flows of the second kind such as corner vortices. Second, he questions the way turbulence models are calibrated to purely generic flows that are special cases never encountered in realistic flows. Models should be calibrated to flows representative of the area of application of the model. Finally, there is no "best current offer" of a DRSM by the community. This is indicative of the current lack of theoretical understanding of DRSMs. It motivates a broad validation of these models implemented in different and independent codes using a large number of test cases. Such an effort, however, with emphasis on LEVMs, is currently under way by the Turbulence Model Benchmarking Working Group (TMBWG) (Rumsey *et al.*, 2010).

3 Turbulence modelling

In this chapter, the theoretical background is given for the understanding of differential Reynolds stress turbulence models. The models are based on the Favre-averaged Navier-Stokes equations (termed RANS even though they are not Reynolds averaged) in which the need for a model for the Reynolds stress tensor emerges. For this tensor, transport equations can be derived, which require the modelling of higher correlations of velocity fluctuations. This represents the closure problem encountered in statistical turbulence modelling. The physical meaning of and relevant modelling approaches for these higher correlations are presented. Finally, the models used for the computations in this thesis are presented.

3.1 Statistical turbulence modelling

The Navier-Stokes equations form the basis for the description of laminar as well as turbulent flows. They can be derived from mass, momentum and energy conservation principles under the assumption of continuum mechanics. In differential conservation form, the continuity, momentum and energy equations read (cf. Wilcox, 2006):

$$\frac{\partial \rho}{\partial t} + \frac{\partial}{\partial x_i}(\rho u_i) = 0 \tag{3.1}$$

$$\frac{\partial}{\partial t}(\rho u_i) + \frac{\partial}{\partial x_j}(\rho u_j u_i) = -\frac{\partial p}{\partial x_i} + \frac{\partial \sigma_{ij}}{\partial x_j} \tag{3.2}$$

$$\frac{\partial}{\partial t}\left[\rho\left(e + \frac{u_i u_i}{2}\right)\right] + \frac{\partial}{\partial x_j}\left[u_j \rho\left(h + \frac{u_i u_i}{2}\right)\right] = \frac{\partial}{\partial x_j}\left[-q_j + u_i \sigma_{ij}\right] \tag{3.3}$$

Wherever the same index occurs twice in a product, summation over all three spatial directions is implied following Einstein's convention (Einstein, 1916). The viscous stresses

$$\sigma_{ij} = 2\mu\left(s_{ij} - \frac{1}{3}s_{kk}\delta_{ij}\right), \quad s_{ij} = \frac{1}{2}\left(\frac{\partial u_i}{\partial x_j} + \frac{\partial u_j}{\partial x_i}\right) \tag{3.4}$$

are based on the Stokes hypothesis which ensures a vanishing trace of the stress tensor. Equation (3.3) describes the conservation of total energy in the fluid. It contains the molecular heat flux vector

$$q_j = -\lambda\frac{\partial T}{\partial x_j} \tag{3.5}$$

which is modelled by a diffusion law with a constant Prandtl number relating molecular viscosity to conductivity via

$$Pr = \frac{c_p \mu}{\lambda} = 0.72 \tag{3.6}$$

with the specific heat at constant pressure c_p. The specific internal energy is given by e and the corresponding enthalpy is given by h. The thermodynamic state of the system described by the ideal caloric and thermal state equations

$$p = (\gamma - 1)\rho e, \quad e = c_v T \tag{3.7}$$

closes the set of equations, where γ denotes the adiabatic index and c_v the specific heat at constant volume.

In principle, all flows of Newtonian fluids can be described with the above set of equations. The Reynolds number

$$Re = \frac{\rho_0 U_0 L_0}{\mu_0} \tag{3.8}$$

based on a reference density ρ_0, velocity U_0, length L_0 and viscosity μ_0 describes the ratio of inertial and viscous forces. For small Reynolds numbers the flow is dominated by viscous forces and called laminar. In this case, the above equations can be used to compute the time resolved flow field with a reasonable effort. If, however, the Reynolds number is sufficiently large, the flow enters the turbulent regime.

As described in Section 1.2, knowledge about the mean flow is often sufficient from an aerodynamic design point of view. To obtain a set of equations describing the mean flow, all instantaneous flow quantities are split into a mean and a fluctuating part

$$\phi = \overline{\phi} + \phi'. \tag{3.9}$$

The averaging operation can be a time, space or ensemble average. This approach is called Reynolds averaging and was developed for the incompressible Navier-Stokes equations (Reynolds, 1895). For the compressible equations, however, it is advisable to define a density weighted average

$$\widetilde{\phi} = \frac{1}{\overline{\rho}}\overline{\rho\phi} \tag{3.10}$$

called the Favre average (Wilcox, 2006) for all quantities but density and pressure. In this notation, the instantaneous quantities are split up as

$$\phi = \widetilde{\phi} + \phi''. \tag{3.11}$$

The relations

$$\rho = \overline{\rho} + \rho' \tag{3.12}$$
$$u_i = \widetilde{u}_i + u_i'' \tag{3.13}$$
$$e = \widetilde{e} + e'' \tag{3.14}$$
$$h = \widetilde{h} + h'' \tag{3.15}$$
$$p = \overline{p} + p' \tag{3.16}$$

are inserted into equations (3.1)-(3.3). Averaging leads to the Favre-averaged Navier-Stokes equations:

$$\frac{\partial \overline{\rho}}{\partial t} + \frac{\partial}{\partial x_i}(\overline{\rho}\widetilde{u}_i) = 0 \tag{3.17}$$

$$\frac{\partial}{\partial t}(\overline{\rho}\widetilde{u}_i) + \frac{\partial}{\partial x_j}(\overline{\rho}\widetilde{u}_j\widetilde{u}_i) = -\frac{\partial \overline{p}}{\partial x_i} + \frac{\partial}{\partial x_j}\left[\overline{\sigma}_{ij} - \overline{\rho u_i'' u_j''}\right] \tag{3.18}$$

$$
\begin{aligned}
&\frac{\partial}{\partial t}\left[\overline{\rho}\left(\widetilde{e}+\frac{\widetilde{u}_i\widetilde{u}_i}{2}+\frac{\widetilde{u_i''u_i''}}{2}\right)\right]+\frac{\partial}{\partial x_j}\left[\widetilde{u}_j\overline{\rho}\left(\widetilde{h}+\frac{\widetilde{u}_i\widetilde{u}_i}{2}+\frac{\widetilde{u_i''u_i''}}{2}\right)\right]\\
&=\frac{\partial}{\partial x_j}\left[-\overline{q}_j-\overline{\rho}\widetilde{u_j''h''}+\overline{\sigma_{ij}u_i''}-\frac{1}{2}\overline{\rho}\widetilde{u_j''u_i''u_i''}\right]\\
&+\frac{\partial}{\partial x_j}\left[\widetilde{u}_i\left(\overline{\sigma}_{ij}-\overline{\rho u_i''u_j''}\right)\right]
\end{aligned}
\tag{3.19}
$$

To shorten the notation we introduce the following conventions:

- Mean velocities and strain rate components are denoted by a capital letter $\widetilde{u}_i \to U_i$ and $\widetilde{s}_{ij} \to S_{ij}$.
- The trace free strain rate is denoted by $s^*_{ij} = s_{ij} - \frac{1}{3}s_{kk}\delta_{ij}$.
- The turbulent kinetic energy is denoted by $k = \frac{1}{2}\widetilde{u_i''u_i''}$.

$$
\frac{\partial\overline{\rho}}{\partial t}+\frac{\partial}{\partial x_i}\left(\overline{\rho}U_i\right)=0 \tag{3.20}
$$

$$
\frac{\partial}{\partial t}\left(\overline{\rho}U_i\right)+\frac{\partial}{\partial x_j}\left(\overline{\rho}U_jU_i\right)=-\frac{\partial\overline{p}}{\partial x_i}+\frac{\partial}{\partial x_j}\left[\overline{\sigma}_{ij}-\overline{\rho u_i''u_j''}\right] \tag{3.21}
$$

$$
\begin{aligned}
&\frac{\partial}{\partial t}\left[\overline{\rho}\left(\widetilde{e}+\frac{U_iU_i}{2}+k\right)\right]+\frac{\partial}{\partial x_j}\left[U_j\overline{\rho}\left(\widetilde{h}+\frac{U_iU_i}{2}+k\right)\right]\\
&=\frac{\partial}{\partial x_j}\left[-\overline{q}_j-\overline{\rho u_j''h''}+\overline{\sigma_{ij}u_i''}-\overline{\rho u_j''\tfrac{1}{2}u_i''u_i''}+U_i\left(\overline{\sigma}_{ij}-\overline{\rho u_i''u_j''}\right)\right]
\end{aligned}
\tag{3.22}
$$

We have now arrived at a set of equations for the mean flow quantities. However, new unknown correlations of fluctuating quantities have emerged. This is called the turbulence closure problem. Equations for higher correlations always lead to new unknowns due to the non-linearity of the problem. A turbulence model has to be devised to close the equations at a certain point. The Reynolds stress tensor $\overline{\rho u_i''u_j''}$ describes the mean transport of momentum due to turbulence. Several other correlations occur in the Favre-averaged energy equation (3.22). The turbulent transport of heat is denoted by

$$
q_j^T=\overline{\rho u_j''h''}. \tag{3.23}
$$

The terms

$$
\overline{\sigma_{ij}u_i''}-\overline{\rho u_j''\tfrac{1}{2}u_i''u_i''} \tag{3.24}
$$

represent the molecular diffusion and turbulent transport of turbulent kinetic energy (Wilcox, 2006). All these terms describe enhanced transport of energy due to turbulent motions.

3.2 Differential Reynolds stress modelling

3.2.1 Reynolds stress transport equations

The system of transport equations for the Reynolds stress tensor can be derived directly from the RANS equations and includes a number of higher order correlations that need to be closed in this context. The form derived by Wilcox (2006) can be rewritten into the following formulation using relations for Reynolds and Favre averaged quantities (Barre *et al.*, 2002)

$$\frac{D\overline{\rho u_i'' u_j''}}{Dt} = \overline{\rho} P_{ij} + \frac{1}{2}\overline{\rho} R_{ij} - \overline{\rho}\epsilon_{ij} + \overline{\rho}\Pi_{ij} + \overline{\rho} M_{ij} + \frac{\partial}{\partial x_k}\left[D^{\mu}_{ij,k} + D^{T}_{ij,k}\right] \tag{3.25}$$

with

$$\begin{aligned}
\overline{\rho} P_{ij} &= -\left(\overline{\rho u_i'' u_k''}\frac{\partial U_j}{\partial x_k} + \overline{\rho u_j'' u_k''}\frac{\partial U_i}{\partial x_k}\right) && (3.26)\\
\frac{1}{2}\overline{\rho} R_{ij} &= -\left(\overline{\rho u_i'' u_q''}\Omega_{qj} + \overline{\rho u_j'' u_q''}\Omega_{qi}\right), \quad \Omega_{ij} = \Omega_p \epsilon_{ijp} && (3.27)\\
\overline{\rho}\epsilon_{ij} &= \overline{\sigma_{kj}\frac{\partial u_i''}{\partial x_k} + \sigma_{ki}\frac{\partial u_j''}{\partial x_k}} && (3.28)\\
\overline{\rho}\Pi_{ij} &= \overline{p'\left(\frac{\partial u_i''}{\partial x_j} + \frac{\partial u_j''}{\partial x_i}\right)} && (3.29)\\
\overline{\rho} M_{ij} &= \overline{u_i''}\left(\frac{\partial \overline{\sigma}_{kj}}{\partial x_k} - \frac{\partial \overline{p}}{\partial x_j}\right) + \overline{u_j''}\left(\frac{\partial \overline{\sigma}_{ki}}{\partial x_k} - \frac{\partial \overline{p}}{\partial x_i}\right) && (3.30)\\
D^{\mu}_{ij,k} &= \overline{\sigma_{kj} u_i'' + \sigma_{ki} u_j''} && (3.31)\\
D^{T}_{ij,k} &= -\overline{\rho u_i'' u_j'' u_k''} - \overline{p' u_i''}\delta_{jk} - \overline{p' u_j''}\delta_{ik}. && (3.32)
\end{aligned}$$

For symmetry reasons only six independent components of the Reynolds stress tensor have to be determined. The terms on the right hand side are the production P_{ij}, redistribution due to system rotation R_{ij}, dissipation ϵ_{ij}, pressure-strain redistribution Π_{ij}, contribution of turbulent mass flux due to density fluctuations M_{ij}, molecular diffusion $D^{\mu}_{ij,k}$ and turbulent diffusion $D^{T}_{ij,k}$.

One of the big advantages of DRSMs is the fact that the production term $\overline{\rho} P_{ij}$ (3.26) is exact in the Reynolds-averaged framework, i.e. no modelling is needed. Through the exact production term, the model can respond properly to the normal straining in stagnating flows and to extra strain rates present in case of streamline curvature (Hanjalić & Jakirlić, 2002). DRSMs solve one of the problems associated with the Boussinesq assumption. While the former correctly use the linear relationship between production of turbulent kinetic energy and strain rate, the latter yield proportionality to the square of the strain norm. This poses a problem in regions of great strain, such as stagnation points, where it leads to an overproduction of turbulent kinetic energy if the flow is computed with an LEVM.

System rotation with the rotation vector Ω_i enters the equations in two ways. Half of the contribution originates from the transformation of the basis vectors and is found explicitly in the equations as $1/2\overline{\rho} R_{ij}$ in (3.27). The other half is incorporated by using the absolute velocity in all velocity derivatives and is hence found implicitly in the production term (Durbin & Pettersson Reif, 2000) but also in all other modelled terms containing velocity derivatives. As the trace of this term vanishes, rotation purely accounts for redistribution of energy between the individual Reynolds stress components.

In line with Morkovin's hypothesis, the effect of density fluctuations $\overline{\rho} M_{ij}$ (3.30) is considered to be negligible up to Mach numbers of about 5 (Wilcox, 2006). Hence, this term will not be investigated in more detail for the application in view. The remaining terms include other higher order correlations. They are characterised in the following sections and modelling strategies are presented. Most models are based on the incompressible Navier-Stokes equations and simply transferred from the RANS to the Favre-averaged context.

3.2.2 Reynolds stress anisotropy and its visualisation

As most of the following models are formulated in terms of the Reynolds stress anisotropy tensor and its invariants, it will be introduced here and its physical interpretation will be discussed. It serves as a measure to describe turbulence anisotropy and is defined as

$$a_{ij} = \frac{\widetilde{u_i'' u_j''}}{k} - \frac{2}{3}\delta_{ij}. \tag{3.33}$$

This quantity describes the deviation of the Reynolds stress tensor from the isotropic state $\widetilde{u_i'' u_j''} = 2/3 k \delta_{ij}$ and can be interpreted as its non-dimensional deviatoric part. However, it depends on the chosen coordinate system. Therefore, invariants of the anisotropy tensor, which are independent of the coordinate system, are an appropriate measure to model turbulence in a frame-invariant way. By design, the first invariant, the trace of a_{ij}, is zero. The second and third invariants can be defined as

$$\begin{aligned} A_2 &= a_{ij} a_{ji} && (3.34)\\ A_3 &= a_{ij} a_{jk} a_{ki}. && (3.35) \end{aligned}$$

Directional information, however, is lost as rotation of the anisotropy tensor will lead to the same invariants.

Physical constraints on the Reynolds stress tensor are positive diagonal elements and that its trace must equal the turbulent kinetic energy:

$$0 \leq \widetilde{u_\alpha'' u_\alpha''} \leq 2k. \tag{3.36}$$

Furthermore, the Schwarz inequality

$$\widetilde{u_\alpha'' u_\beta''}^2 \leq \widetilde{u_\alpha'' u_\alpha''} \cdot \widetilde{u_\beta'' u_\beta''} \tag{3.37}$$

must be fulfilled. No summation is implied over Greek indices. From these restrictions, an area of physically realisable states in the (A_3, A_2) plane can be derived leading to the invariant map introduced by Lumley (1979). All physically realisable turbulence must lie within the triangular area shown in Figure 3.1.

The borders of the invariant map are limiting states of turbulence. Both invariants are zero in case of isotropic turbulence which is the natural state turbulence returns to in the absence of strain. Opposed to that, there is the two-component limit towards which turbulence tends close to a solid wall because fluctuations normal to the wall

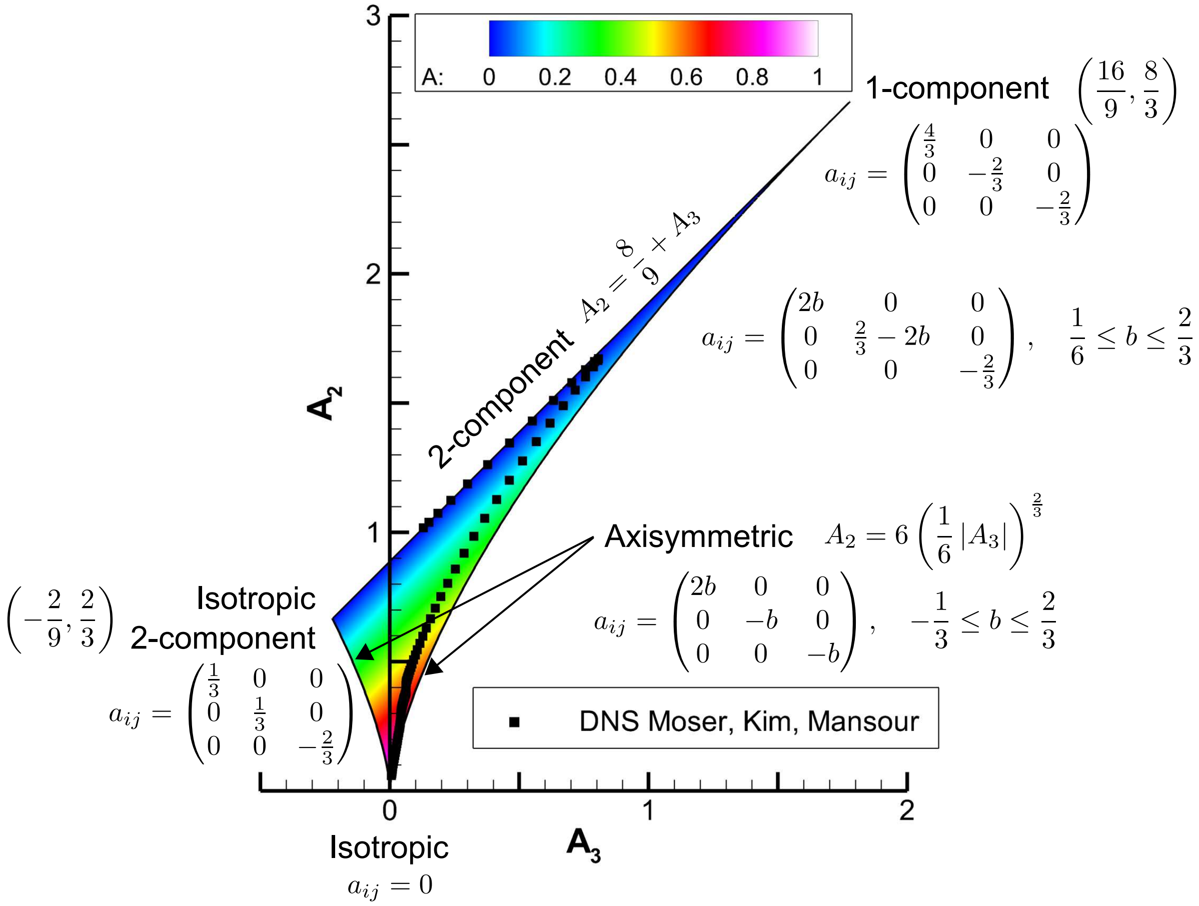

Figure 3.1: Invariant map of realisable turbulence states (Lumley, 1979). For orientation, DNS results of channel flow (Moser *et al.*, 1999) are plotted with nearly isotropic turbulence in the centre of the channel and two-component limit at the wall.

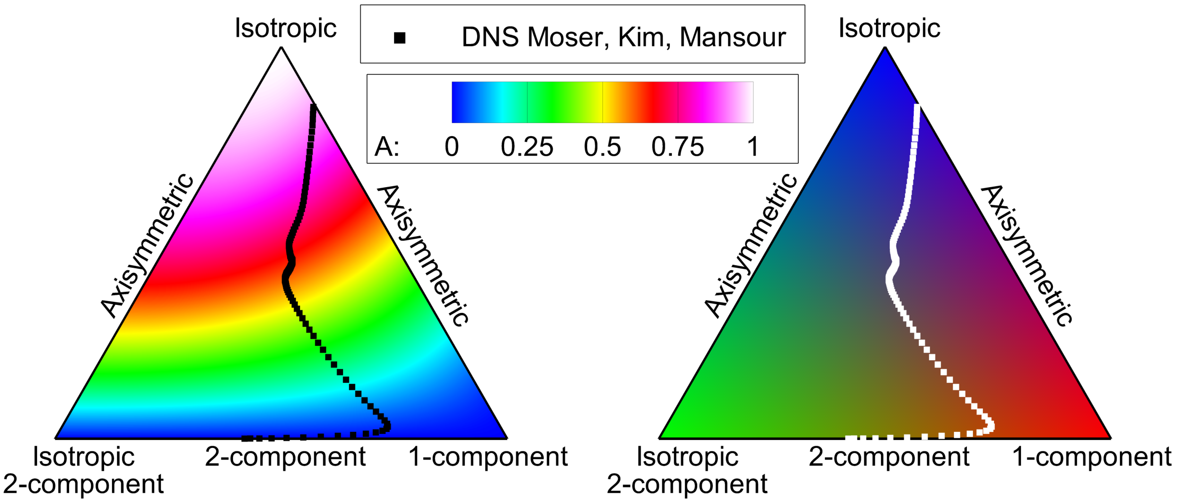

Figure 3.2: Barycentric map describing turbulence anisotropy tensor (Banerjee *et al.*, 2007). For orientation DNS of channel flow (Moser *et al.*, 1999) is plotted with nearly isotropic turbulence in the centre of the channel and two-component limit at the wall. It is filled with contours of two-component parameter A for comparison with the anisotropy invariant map (*left*) and with RGB colouring to allow for a contour plot field visualisation of turbulence anisotropy states (Emory & Iaccarino, 2014) (*right*).

are damped. Hence, a practical measure to describe wall effects is the two-component factor

$$A = 1 - \frac{9}{8}\left(A_2 - A_3\right) \tag{3.38}$$

which is 1 for isotropic turbulence and 0 in the two-component limit. The contours in Figure 3.1 show A. The remaining two borders are different types of axisymmetric turbulence. Extreme states are reached at the corners of the triangle. On the left at $(-2/9,\, 2/3)$ there is isotropic two-component turbulence while on the right at $(16/9,\, 8/3)$ there is one-component turbulence. Possible forms of the anisotropy tensor are given at the respective edges and corners, which can be transformed to an arbitrary base by rotation. To attach some physical context to the rather abstract invariant map, the DNS results of turbulent plane channel flow at $Re_\tau = 590$ (Moser *et al.*, 1999) are plotted as black squares. In the centre of the channel turbulence is almost isotropic whereas it approaches the two-component towards the solid wall. A more detailed description of the invariant map can be found in (Lumley, 1979; Simonsen & Krogstad, 2005).

Instead of Lumley's invariant map, a barycentric map can be constructed using the eigenvalues of a_{ij} (Banerjee *et al.*, 2007). In principal coordinates, the spectral theorem states that the anisotropy tensor can be constructed as a linear combination

$$\hat{a}_{ij} = C_{1C}\hat{a}_{ij}^{1C} + C_{2C}\hat{a}_{ij}^{2C} + C_{3C}\hat{a}_{ij}^{3C} \tag{3.39}$$

of its limiting states one-component (1C), isotropic two-component (2C) and isotropic (3C) turbulence with the weights

$$\begin{aligned} C_{1C} &= \lambda_1 - \lambda_2 && (3.40)\\ C_{2C} &= 2(\lambda_2 - \lambda_3) && (3.41)\\ C_{3C} &= 3\lambda_3 + 1 && (3.42) \end{aligned}$$

given by the ordered eigenvalues of the anisotropy tensor

$$\lambda_1 > \lambda_2 \quad \text{and} \quad \lambda_3 = -(\lambda_1 + \lambda_2). \tag{3.43}$$

The map is constructed by introducing the barycentric coordinates which can be chosen as

$$x_B = C_{1C} + \frac{1}{2}C_{3C} \quad \text{and} \quad y_B = \frac{\sqrt{3}}{2}C_{3C}. \tag{3.44}$$

It can be shown that there is bijection between the anisotropy invariant map and the barycentric map. An advantage of the latter is that it is linear in eigenvalues and limiting states are weighted equally. Figure 3.2 (*left*) shows the barycentric map with the same channel flow DNS data and the two-component parameter A for comparison with the invariant map in Figure 3.1.

The concept introduced above has been taken a step further with the idea to use the weights as RGB colour channels to assign a unique colour to each state in the barycentric map (Emory & Iaccarino, 2014). The direct mapping of weight to channel is shown in Figure 3.2 (*right*) with the one-component weight C_{1C} assigned to red, the isotropic two-component weight C_{2C} assigned to green and the isotropic weight C_{3D} assigned to blue. This method allows showing colour-coded field data making it possible to identify areas of the flow field with certain turbulence anisotropy properties. Another quantity that could be used in this fashion is the two-component parameter. In contrast to the method described above, the latter only has a unique value for isotropic turbulence while it can assume the same value for different anisotropy states.

3.2.3 Pressure-strain correlation

The pressure-strain correlation Π_{ij} (3.29) has probably received the most attention by turbulence modellers. It is usually divided into several parts motivated by an expression that can be obtained for incompressible flows by integrating the Poisson equation for the fluctuating pressure and applying Green's theorem.

$$\Pi_{ij} = \Pi_{ij,1} + \Pi_{ij,2} + \Pi^w_{ij,1} + \Pi^w_{ij,2} \tag{3.45}$$

The slow part $\Pi_{ij,1}$ depends only on fluctuating velocity gradients and will drive turbulence towards isotropy whereas the rapid part $\Pi_{ij,2}$ is proportional to the mean velocity gradient and can be seen as an isotropisation-of-production (IP) process. The latter reacts more rapidly to sudden changes in the mean velocity field. For this reason, separate models are usually developed for each part of the pressure-strain correlation. $\Pi^w_{ij,1}$ and $\Pi^w_{ij,2}$ are due to blockage by and pressure reflection at solid walls. (Hanjalić & Jakirlić, 2002)

As the slow part of the pressure-strain correlation describes the return to isotropy of turbulence, it is convenient to formulate the model using the Reynolds stress anisotropy tensor a_{ij} (3.33). According to the Caley-Hamilton theorem, the most general isotropic tensorial formulation of $\Pi_{ij,1}$ depending on the anisotropy tensor a_{ij} only is the quadratic expression (Lumley, 1979)

$$\Pi_{ij,1} = -\epsilon \left[C_1 a_{ij} + C_1' \left(a_{ik} a_{jk} - \frac{1}{3}\delta_{ij} A_2 \right) \right]. \tag{3.46}$$

For $C_1' = 0$, it reduces to the classical linear model suggested by Rotta (1951). Most differential Reynolds stress closures rely on (3.46). They are distinguished by the values of the coefficients C_1 and C_1'. More modern models employ functions of anisotropy invariants instead of constants (Jakirlić, 2004). The most cited models are the linear LRR model with $C_1 = 1.5$, $C_1' = 0$ (Launder *et al.*, 1975) and the quadratic SSG model with $C_1 = 1.7$, $C_1' = -1.05$ (Speziale *et al.*, 1991).

The most general formulation of the rapid part $\Pi_{ij,2}$ is

$$\Pi_{ij,2} = \frac{\partial U_l}{\partial x_m} \left(b^{mi}_{lj} + b^{mj}_{li} \right) \tag{3.47}$$

where b^{mi}_{lj} is a function of up to fourth order in a_{ij} (Jakirlić, 2004). In this work, we restrain ourselves to the quasi-linear form

$$\begin{aligned} \Pi_{ij,2} = \Bigg[& \left(C_3 - C_3' \sqrt{A_2} \right) k S^*_{ij} \\ & + C_4 k \left(a_{ip} S_{pj} + a_{jp} S_{pi} - \frac{2}{3} a_{pq} S_{pq} \delta_{ij} \right) \\ & + C_5 k \left(a_{ip} W_{pj} + a_{jp} W_{pi} \right) - \frac{1}{2} C_2' a_{ij} P_{qq} \Bigg] \end{aligned} \tag{3.48}$$

which can be used to describe all employed models where

$$W_{ij} = \frac{1}{2} \left(\frac{\partial U_i}{\partial x_j} - \frac{\partial U_j}{\partial x_i} \right) \tag{3.49}$$

is the vorticity tensor. The LRR IP model (Launder *et al.*, 1975)

$$\Pi_{ij,2} = -C_2 \left(P_{ij} - \frac{1}{3} P_{qq} \delta_{ij} \right) \tag{3.50}$$

can be written in the above form with $C_3 = \frac{4}{3}C_2$ and $C_4 = -C_5 = C_2$ and all other constants set to 0. All constants have finite values in the SSG model (Speziale *et al.*, 1991). Again, more advanced models use functions of anisotropy invariants for the coefficients.

The presence of a solid wall significantly influences the Reynolds stress anisotropy. The wall-normal velocity fluctuation component is damped more than the parallel components. This effect has to be incorporated in models for the redistribution terms to guarantee a proper description of Reynolds stresses close to the wall. It is achieved using the above mentioned explicit wall terms or by proper modification of coefficients approaching the wall.

3.2.4 Dissipation correlation

For high Reynolds numbers, the dissipation ϵ_{ij} (3.28) is considered to be isotropic because it is associated with the smallest scales. Therefore, the simplest model reads

$$\epsilon_{ij} = \frac{2}{3}\epsilon\delta_{ij} \tag{3.51}$$

and reduces the problem to the determination of the isotropic dissipation rate ϵ (Rotta, 1951). At low Reynolds numbers, dissipation anisotropy is usually equated with Reynolds stress anisotropy (Hanjalić & Launder, 1976)

$$\epsilon_{ij} = \epsilon\left[\frac{2}{3}\delta_{ij} + f_s a_{ij}\right]. \tag{3.52}$$

This is not strictly physically justified but has provided satisfying results if the function f_s is chosen adequately (Jakirlić, 2004).

For the isotropic dissipation rate, most DRSMs employ either a transport equation for ϵ or the specific dissipation rate ω. This is analogous to LEVMs. However, the production term of turbulence kinetic energy in the respective equation can be formulated in an exact manner. Apart from that, the dissipation rate equation remains highly empirical and is one of the big weaknesses of DRSMs, as, in fact, of basically any RANS model.

3.2.5 Diffusion of Reynolds stresses

The diffusion of Reynolds stresses can be split into molecular and turbulent diffusion. Molecular diffusion

$$D^{\mu}_{ij,k} = \overline{\sigma'_{kj}u'_i + \sigma'_{ki}u'_j} \tag{3.53}$$

is modelled with a gradient diffusion approach

$$D^{\mu}_{ij,k} = \mu\frac{\partial\widetilde{u''_i u''_j}}{\partial x_k} \tag{3.54}$$

which is exact for incompressible RANS. More variations exist for the turbulent diffusion

$$D^{T}_{ij,k} = -\overline{\rho u''_i u''_j u''_k} - \overline{p'u'_i}\delta_{jk} - \overline{p'u'_j}\delta_{ik}. \tag{3.55}$$

The simplest model is the simple gradient diffusion (SGD) approach which assumes an eddy viscosity (Shir, 1973). This is analogous to molecular diffusion and given by

$$D_{ij,k}^{T} = \frac{C_S^{\mathrm{SGD}}}{C_\mu} \mu_T \frac{\partial \widetilde{u_i'' u_j''}}{\partial x_k}. \tag{3.56}$$

The generalised gradient diffusion (GGD) approach uses a tensorial viscosity. It is found in literature in coordinate-frame invariant formulations (Hanjalić & Launder, 1972) such as

$$D_{ij,k}^{T} = C_S^{\mathrm{HL}} \frac{\overline{\rho} k}{\epsilon} \left[\widetilde{u_k'' u_l''} \frac{\partial \widetilde{u_i'' u_j''}}{\partial x_l} + \widetilde{u_i'' u_l''} \frac{\partial \widetilde{u_k'' u_j''}}{\partial x_l} + \widetilde{u_j'' u_l''} \frac{\partial \widetilde{u_k'' u_i''}}{\partial x_l} \right] \tag{3.57}$$

or a simplified version (Daly & Harlow, 1970)

$$D_{ij,k}^{T} = C_S^{\mathrm{GGD}} \frac{\overline{\rho} k}{\epsilon} \widetilde{u_k'' u_l''} \frac{\partial \widetilde{u_i'' u_j''}}{\partial x_l}. \tag{3.58}$$

Jakirlić (2004) states that due to the dominance of production terms, simpler diffusion models usually suffice in complex flows. Eisfeld (2014) studied the influence of the three diffusion treatments in combination with his SSG/LRR-ω DRSM. He concluded that, while the choice of gradient diffusion model has a negligible effect on the pressure distribution in two transonic aerofoil test cases, the onset and shape of separation regions showed slight differences between the SGD and the more complex formulations.

3.3 Studied DRSMs

In this section, the turbulence models employed in this thesis are introduced. The description of the reference models Menter SST k-ω and Hellsten EARSM k-ω can be found in the appendix. The focus is on the DRSMs, which will be described in detail. While the conceptual differences between the models will be pointed out, their implications on the results will be presented in Chapter 5.

3.3.1 SSG/LRR-ω model

The SSG/LRR-ω model is a combination of the SSG model (Speziale *et al.*, 1991) for regions of free shear flow and the LRR (Launder *et al.*, 1975) model within the turbulent boundary layer. Eisfeld followed the same rationale as Menter (1994) did when he developed the BSL model. The blending function F_1 is used to switch between both model formulations by blending the constants as

$$\phi = F_1 \phi^{\mathrm{LRR},\omega} + (1 - F_1) \phi^{\mathrm{SSG},\epsilon}. \tag{3.59}$$

Since the blending of the Reynolds stress equations and the scale-determining equation is performed with the same blending function, the SSG model is used in conjunction with the ϵ-version of the BSL-ω-equation. Eisfeld (2010*a*) motivates this choice because the SSG model was developed in conjunction with the ϵ-equation. This choice, however, is debatable because this way, the simpler, linear model is used close to solid walls without any corrections. The performance of the model close to the wall will be discussed later on. Nevertheless, in a range of transonic flows and configurations relevant to aircraft aerodynamics the model was shown to be numerically robust and to produce results comparable to those obtained with the model of Jakirlić and Hanjalić (Jakirlić *et al.*, 2007; Cécora *et al.*, 2014).

The model equations for the Reynolds stresses have been introduced in the previous sections. For the pressure strain term, the constants in equations (3.46) and (3.48) are selected to represent the LRR or SSG model, respectively. The coefficients corresponding to the latest version of the model (Cécora *et al.*, 2014) are listed in Table 3.1. C_4 and C_5 for the LRR part are obtained from the equation for the LRR model

$$C_4 = \frac{9C_2 + 6}{11} \quad \text{and} \quad C_5 = \frac{7C_2 - 10}{11} \tag{3.60}$$

with $C_2 = 0.52$. Both SGD (3.56) and GGD (3.58) can be selected as diffusion models. The dissipation is assumed to be isotropic as described by equation (3.51). Menter's BSL equation

$$\frac{D\overline{\rho}\omega}{Dt} = \alpha\frac{\overline{\rho}\omega}{k}P_k - \beta\overline{\rho}\omega^2 + \sigma_d\frac{\overline{\rho}}{\omega}\frac{\partial k}{\partial x_j}\frac{\partial \omega}{\partial x_j} + \frac{\partial}{\partial x_k}\left[(\mu + \sigma_\omega \mu_T)\frac{\partial \omega}{\partial x_k}\right] \tag{3.61}$$

serves as transport equation for the scale-determining variable ω which is used to compute the turbulent dissipation

$$\epsilon = C_\mu k\omega \tag{3.62}$$

with the standard value of $C_\mu = 0.09$. For turbulent diffusion, the eddy viscosity is determined by

$$\mu_T = \frac{\overline{\rho}k}{\omega}. \tag{3.63}$$

All model equations in a compact form can be found in the appendix A.4.

3.3.2 Jakirlić, Hanjalić and Maduta's $\overline{u_i u_j}$-ω^h model

Motivated by the conceptual deficiency of Eisfeld's model close to solid walls, the model of Jakirlić and Hanjalić was chosen for further investigations. The model of Hanjalić & Launder (1972) forms the basis of the closure which has been continuously developed by Jakirlić and his group over the past decades. His approach is the analysis of the model terms on the basis of existing DNS data. The idea is to take a modelled term such as the pressure-strain term and solve for the model coefficient. In this manner, the model coefficients can be determined for a range of building block flows. It can be concluded that, even for simple turbulent plane channel flow, the coefficients cannot be properly described by constant values (Jakirlić, 2004). However, large variations are mostly limited to areas close to solid walls. Hence, in the present model, the coefficients are functions of turbulence anisotropy invariants.

Pressure-strain term

The coefficients are formulated as suggested by Hanjalić & Jakirlić (1998) for the slow and rapid parts of the pressure-strain term Π_{ij} using the same formulation as in the SSG/LRR-ω model, given by (3.46) and (3.48). All non-zero coefficients are given in

Table 3.1: Coefficients of Reynolds stress and dissipation rate equations for SSG/LRR-ω model (Cécora *et al.*, 2014).

Coefficient	SSG,ϵ	LRR,ω
C_1	1.7	1.8
C_1'	-1.05	0
C_3	0.8	
C_3'	0.65	0
C_4	0.625	0.9709
C_5	-0.2	-0.5782
C_2'	0.9	0
C_S^{GGD}	0.22	0.75 C_μ
C_S^{SGD}	$2C_S^{\mathrm{GGD}}/3$	
α	0.44	0.5556
β	0.0828	0.075
σ_ω	0.856	0.5
σ_d	1.712	0

Table 3.2; all primed coefficients C_1', C_2' and C_3' are set to zero. Wall effects are modelled, on the one hand, through the functional dependency of coefficients on the anisotropy invariants. Low Reynolds number effects are explicitly taken into account in the slow pressure-strain term $\Pi_{ij,1}$ by a reduction of C_1 depending on the turbulent Reynolds number Re_T. In contrast to the SSG/LRR-ω model, explicit wall terms, on the other hand, are employed to account for the blocking effect of the solid wall. They are formulated in terms of the wall-normal vector $\mathbf{n}$

$$\begin{aligned}\Pi_{ij}^w \;=\;& C_1^w f_w \frac{\epsilon^h}{k}\left(\widetilde{u_k''u_m''}n_k n_m \delta_{ij} - \frac{3}{2}\widetilde{u_i''u_k''}n_k n_j - \frac{3}{2}\widetilde{u_k''u_j''}n_k n_i\right) \\ &+ C_2^w f_w \left(\Pi_{km,2} n_k n_m \delta_{ij} - \frac{3}{2}\Pi_{ik,2} n_k n_j - \frac{3}{2}\Pi_{kj,2} n_k n_i\right)\end{aligned} \tag{3.64}$$

with

$$f_w = \min\left[\frac{k^{\frac{3}{2}}}{2.5\epsilon^h y_n}, 1.4\right] \tag{3.65}$$

which depends on the ratio of the turbulence length scale to the distance to the wall.

This introduces a strong dependency on the wall geometry which can become a problem in complex geometries where turbulence is affected by multiple walls. To alleviate this problem, $\mathbf{n}$ can interpreted as a direction of change in turbulence anisotropy. It is then defined as the normalised gradient

$$\mathbf{n} = \frac{\nabla\left(Ak^{\frac{3}{2}}/\epsilon^h\right)}{\left|\nabla\left(Ak^{\frac{3}{2}}/\epsilon^h\right)\right|} \tag{3.66}$$

in line with the approach of Craft & Launder (1996). In some cases, however, it has appeared to be numerically more stable to simply use the gradient of the distance to

Table 3.2: Coefficients of Reynolds stress and dissipation rate equations for the JH-ω^h model (Morsbach *et al.*, 2015*a*).

Model	Coefficient	Model	Coefficient
$\Pi_{ij,1}$	$C_1 = C + \sqrt{A}E^2$	Π_{ij}^w	$C_1^w = \max\left[1.0 - 0.7C, 0.3\right]$
	$C = 2.5AF^{\frac{1}{4}}f$		$C_2^w = \min\left[A, 0.3\right]$
	$F = \min\left[0.6, A_2\right]$	Diffusion	$C_S^{\mathrm{SGD}} = \sigma_\omega C_\mu$
	$f = \min\left[\left(\frac{\mathrm{Re}_T}{150}\right)^{\frac{3}{2}}, 1\right]$	ω^h	$\alpha = 0.44$
	$Re_T = \frac{\overline{\rho}k^2}{\mu\epsilon^h}$		$\beta = 0.072$
	$C_1' = 0$		$\sigma_\omega = 0.9091$
$\Pi_{ij,2}$	$C_2 = 0.8\sqrt{A}$		$\sigma_d = 0.25$
	$C_2' = 0$		$C_{\mathrm{cr}} = 0.55$
	$C_3 = \frac{4}{3}C_2$		$C_{\epsilon 3}^1 = 0.3$
	$C_3' = 0$		$C_{\epsilon 3}^2 = 0.64$
	$C_4 = C_2$		$C_{\epsilon 3}^2 = 2.0$
	$C_5 = -C_2$		

the wall y_n

$$\mathbf{n} = \frac{\nabla y_n}{|\nabla y_n|}. \tag{3.67}$$

This approach has been chosen for the present version of the model.

The model of Hanjalić and Jakirlić differs from approaches by other groups. It employs rather simple, linear formulations of the pressure-strain term in contrast to formulations up to third order in a_{ij}, used e.g. by Craft & Launder (1996). The entire model's complexity is found in the coefficient functions dependent only on invariants. To illustrate this, the variation of the coefficient functions for the slow part (*left*) and the rapid part (*right*) is plotted in Figure 3.3 using results obtained with the SSG/LRR-ω and JH-ω^h models for turbulent plane channel flow. While the coefficients are practically constant throughout the boundary layer and only blended by Menter's F_1 function at the boundary layer edge for the SSG/LRR-ω model, stress redistribution is significantly reduced towards the wall for the JH-ω^h model. This holds true for both slow and rapid pressure strain parts.

Turbulent diffusion term

Originally, turbulent diffusion was modelled using a GGD approach (3.58) for both the Reynolds stresses and the ϵ-equation (Hanjalić & Jakirlić, 1998). In the ω^h-version of the model, diffusion is modelled by a SGD approach (3.56). Again, the diffusion approach is the same in all seven equations in contrast to an earlier formulation suggested by Maduta (2013) who used GGD for the Reynolds stresses and SGD for the specific turbulent dissipation rate ω^h. In his latest version, he has switched to SGD in all seven equations (Jakirlić & Maduta, 2015). This enhances the stability of the solution method especially in complex 3D cases. The diffusion constant C_S^{SGD} for the Reynolds stresses is chosen in a way to match the diffusion constant σ_ω for the dissipation rate by

$$C_S^{\mathrm{SGD}} = \sigma_\omega C_\mu. \tag{3.68}$$

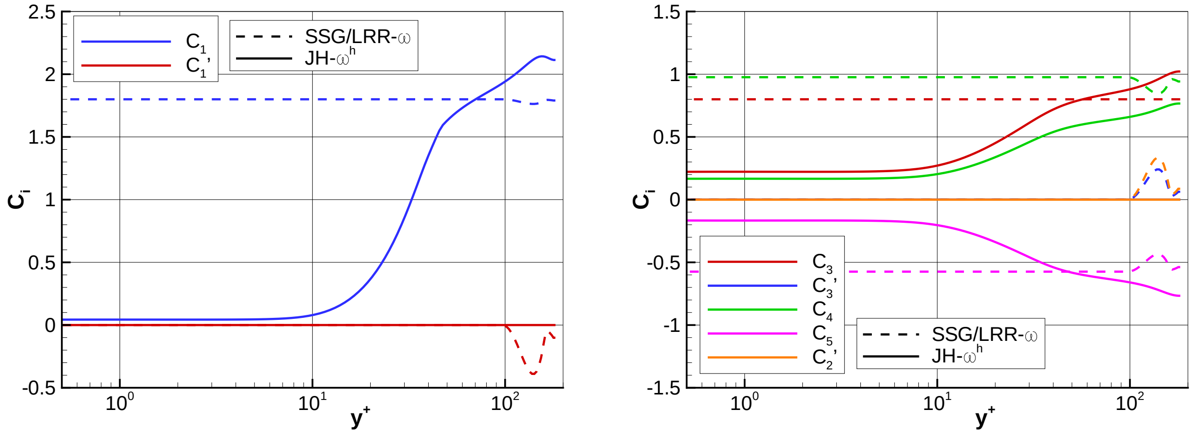

Figure 3.3: Coefficient functions for the slow (*left*) and rapid (*right*) pressure-strain terms of the JH-ω^h model compared to the SSG/LRR-ω model in turbulent plane channel flow.

The formulation of the turbulent viscosity μ_T was optimised to match DNS data resulting in

$$\mu_T = 0.144 A\overline{\rho} k^{\frac{1}{2}} \max\left[10\eta_K, L\right] \tag{3.69}$$

with the Kolmogorov length scale

$$\eta_K = \left(\frac{\nu^3}{C_\mu k \omega^h}\right)^{\frac{1}{4}} \tag{3.70}$$

and the RANS length scale

$$L = \frac{k^{\frac{1}{2}}}{C_\mu \omega^h} \tag{3.71}$$

respectively (Jakirlić, 2004).

Turbulent dissipation rate

The appropriate modelling of the turbulent dissipation rate ϵ has received much attention from Jakirlić & Hanjalić (2002). Based on the transport equation for the two-point correlation (Jovanović *et al.*, 1995), they showed that the dissipation tensor ϵ_{ij} can be divided into a homogeneous part ϵ_{ij}^h and contributions due to inhomogeneity of the flow, which is to equal the viscous diffusion of Reynolds stresses D_{ij}^{ν}:

$$\epsilon_{ij} = \epsilon_{ij}^h + \frac{1}{2} D_{ij}^{\nu}. \tag{3.72}$$

The expression (3.52) is used for the homogeneous part of the dissipation rate tensor

$$\epsilon_{ij}^h = \epsilon^h \left[\frac{2}{3}\delta_{ij} + f_s a_{ij}\right] \tag{3.73}$$

to model anisotropic dissipation effects. The blending function f_s is chosen as

$$f_s = 1 - \sqrt{A} E^2 \tag{3.74}$$

with the dissipation two-component parameter given by

$$E = 1 - \frac{9}{8}(E_2 - E_3), \quad E_2 = e_{ij}e_{ji}, \quad E_3 = e_{ij}e_{jk}e_{ki}, \quad e_{ij} = \frac{\epsilon^h_{ij}}{\epsilon^h} - \frac{2}{3}\delta_{ij}. \tag{3.75}$$

The inhomogeneous part enters the Reynolds stress transport equations by introduction of a factor of $\frac{1}{2}$ in the viscous diffusion term. An advantage of this approach is the satisfaction of wall limits for the normalised dissipation components.

Dissipation rate equation based on ω^h

As argued above, the scale-determining equation represents one of the major uncertainties in RANS modelling. Therefore, to improve comparability between the employed DRSMs and the reference models, the ω^h-version of the Jakirlić & Hanjalić model is introduced. Its derivation is explained below, to illustrate the assumptions and simplifications made in changing from ϵ^h to ω^h.

The starting point is the model transport equation for the homogeneous dissipation rate ϵ^h (Jakirlić & Hanjalić, 2002):

$$\frac{D\left(\overline{\rho}\epsilon^h\right)}{Dt} = \frac{\partial}{\partial x_p}\left[\left(\frac{1}{2}\mu\delta_{pq} + C_\epsilon \frac{\overline{\rho}k}{\epsilon^h}\widetilde{u''_p u''_q}\right)\frac{\partial \epsilon^h}{\partial x_q}\right] \underbrace{-\overline{\rho}\epsilon^h_{ij}\frac{\partial U_i}{\partial x_j} + \overline{\rho}P_k\frac{\epsilon^h}{k}}_{\text{mixed production}} - C_{\epsilon 2}\overline{\rho}f_\epsilon\tilde{\epsilon}^h\frac{\epsilon^h}{k} + P_{\epsilon 3} \tag{3.76}$$

with

$$\tilde{\epsilon}^h = \epsilon^h - \nu\frac{\partial\sqrt{k}}{\partial x_j}\frac{\partial\sqrt{k}}{\partial x_j} \tag{3.77}$$

and

$$f_\epsilon = 1 - \frac{C_{\epsilon 2} - 1.4}{C_{\epsilon 2}}e^{-(Re_T/6)^2}. \tag{3.78}$$

The viscous diffusion of the homogeneous dissipation rate can be approximated as half the viscous diffusion of the total dissipation rate. The gradient production term $P_{\epsilon 3}$ will be discussed below. A first simplification for complex flows is to replace the mixed production term by the standard model (Jakirlić & Maduta, 2015) (see also Jakirlić *et al.*, 2007) resulting in

$$\frac{D\left(\overline{\rho}\epsilon^h\right)}{Dt} = \frac{\partial}{\partial x_p}\left[\left(\frac{1}{2}\mu\delta_{pq} + C_\epsilon \frac{\overline{\rho}k}{\epsilon^h}\widetilde{u''_p u''_q}\right)\frac{\partial \epsilon^h}{\partial x_q}\right] + \overline{\rho}\left(C_{\epsilon 1}P_k - C_{\epsilon 2}f_\epsilon\tilde{\epsilon}^h\right)\frac{\epsilon^h}{k} + P_{\epsilon 3}. \tag{3.79}$$

Maduta (2013) chose the specific homogeneous dissipation rate defined by $\epsilon^h = k\omega^h$ as scale-determining variable. To obtain a variable consistent with the remaining turbulence models in TRACE, ω^h is chosen as

$$\epsilon^h = C_\mu k\omega^h. \tag{3.80}$$

This transformation of variables leads to the transport equation for ω^h

$$\frac{D\left(\overline{\rho}\omega^h\right)}{Dt} = \frac{1}{C_\mu k}\frac{D\left(\overline{\rho}\epsilon^h\right)}{Dt} - \frac{\omega^h}{k}\frac{D\left(\overline{\rho}k\right)}{Dt}. \tag{3.81}$$

The transport equation for the turbulent kinetic energy k is derived from the original transport equation of Reynolds stresses (Jakirlić & Hanjalić, 2002) by taking half the trace

$$\frac{D\left(\overline{\rho}k\right)}{Dt} = \frac{\partial}{\partial x_p}\left[\left(\frac{1}{2}\mu\delta_{pq} + C_S\frac{\overline{\rho}k}{\epsilon^h}\widetilde{u_p''u_q''}\right)\frac{\partial k}{\partial x_q}\right] + \overline{\rho}P_k - \overline{\rho}\epsilon^h. \tag{3.82}$$

All redistribution terms then vanish by design. Both the ϵ^h-equation (3.79) and the k-equation (3.82) are further simplified by assuming that the dissipation rate and Reynolds stresses follow the same diffusion mechanism chosen to be modelled by SGD with the same diffusion constant $C_S = C_\epsilon$. Furthermore, the destruction term of the ϵ^h-equation is simplified by setting $\tilde{\epsilon}^h \approx \epsilon^h$ (Jakirlić & Maduta, 2015) and neglecting the low-Reynolds function f_ϵ. Then, the following form of the transport equation for the specific homogeneous turbulent dissipation rate

$$\begin{aligned}\frac{D\left(\overline{\rho}\omega^h\right)}{Dt} &= \frac{\partial}{\partial x_i}\left[\left(\frac{1}{2}\mu + \sigma_\omega\mu_T\right)\frac{\partial\omega^h}{\partial x_i}\right] \\ &\quad + \left(C_{\epsilon1} - 1\right)\frac{\overline{\rho}\omega^h}{k}P_k - C_\mu\left(C_{\epsilon2} - 1\right)\overline{\rho}\left(\omega^h\right)^2 \\ &\quad + \frac{2}{k}\left(\frac{1}{2}\mu + \sigma_\omega\mu_T\right)\frac{\partial\omega^h}{\partial x_i}\frac{\partial k}{\partial x_i} + \frac{1}{C_\mu k}P_{\epsilon3}\end{aligned} \tag{3.83}$$

can be obtained. The diffusion constant is renamed to σ_ω in line with most ω-based models. Different model variants based on different formulations of the cross diffusion term and the gradient production term $P_{\epsilon3}$, respectively, will be discussed below.

Gradient production term $P_{\epsilon3}$

The general tensor invariant form of the gradient production term $P_{\epsilon3}$ involves gradients of Reynolds stresses (Jakirlić & Hanjalić, 2002). Several simplified versions of this term are employed in conjunction with the Jakirlić & Hanjalić model. These are

$$P^1_{\epsilon3} = C^1_{\epsilon3}\mu\frac{k}{\epsilon^h}\widetilde{u_j''u_k''}\frac{\partial^2 U_i}{\partial x_j\partial x_l}\frac{\partial^2 U_i}{\partial x_k\partial x_l}, \qquad C^1_{\epsilon3} = 0.3$$

Jakirlić *et al.* (2007); Jakirlić & Jester-Zürker (2010) (3.84)

$$P^2_{\epsilon3} = C^2_{\epsilon3}\frac{\mu\mu_T}{\overline{\rho}}\frac{\partial^2 U_i}{\partial x_p\partial x_q}\frac{\partial^2 U_i}{\partial x_p\partial x_q}, \qquad C^2_{\epsilon3} = 2.0$$

Jakirlić & Maduta (2014); Jakirlić & Maduta (2015) (3.85)

$$P^3_{\epsilon3} = C^3_{\epsilon3}\frac{C_\mu\mu k^2}{\epsilon^h}\frac{\partial^2 U_i}{\partial x_p\partial x_q}\frac{\partial^2 U_i}{\partial x_p\partial x_q}, \qquad C^3_{\epsilon3} = 0.64 \tag{3.86}$$

with different values for the constant $C^i_{\epsilon3}$. Assuming that $\widetilde{u_j''u_k''} \approx \frac{2}{3}k\delta_{jk}$ and $\mu_T = C_\mu\overline{\rho}k^2/\epsilon^h$, the first two constants can be related to each other by

$$C^2_{\epsilon3} \approx \frac{2}{3}\frac{C^1_{\epsilon3}}{C_\mu}. \tag{3.87}$$

Nevertheless, its definite value has been used for calibration as the model is rather sensitive to its choice. The third version (3.86) was calibrated to be used in cases where

$P^2_{\epsilon 3}$ fails. The three models will be combined with different formulations of the cross diffusion term below.

Cross diffusion term

Jakirlić & Maduta (2015) adjusted the cross diffusion term for better reproduction of the dissipation rate near the wall. His asymptotic analysis led to the introduction of two new model constants $C_{\text{cr}} = 0.55$ and $\sigma_d = 0.25$. His version of the term reads

$$CD^{\text{Maduta}}_{k\omega} = \frac{2}{k}\left(\frac{1}{2}C_{\text{cr}}\mu + \sigma_d \mu_T\right)\frac{\partial \omega^h}{\partial x_i}\frac{\partial k}{\partial x_i}. \tag{3.88}$$

In contrast to that, the cross diffusion term can be limited to positive values

$$CD^{\text{limited}}_{k\omega} = \frac{2}{k}\left(\frac{1}{2}C_{\text{cr}}\mu + \sigma_d \mu_T\right)\max\left[\frac{\partial \omega^h}{\partial x_i}\frac{\partial k}{\partial x_i}, 0\right] \tag{3.89}$$

as e.g. in Wilcox's models (Wilcox, 2006). Also in the Menter's BSL-ω only positive values effectively influence the budget although no explicit limit is enforced. This is due to the fact that negative values of cross diffusion are mainly reached very close to the wall where the blending function F_1 is zero. Limiting cross diffusion to positive values enhances the solution stability at the expense of slightly deteriorating the model's performance in the viscous sublayer.

Another issue concerning the stability of the solution method is the formulation of the eddy viscosity μ_T (3.69) at low turbulent kinetic energies, which scales with $\sqrt{k}$ instead of k. Hence, it cannot balance the inverse k in the cross diffusion term in this case and small values of k can lead to excessive values of the source term and consequently to divergence. When the limited version of cross diffusion is used, it is clipped to zero in the viscous sublayer, where the molecular viscosity would dominate. Since $\mu \ll \mu_T$ in most of the turbulent flow field, the cross diffusion term can be approximated by

$$CD^{\text{highRe}}_{k\omega} = \frac{2\sigma_d \overline{\rho}}{\omega^h}\max\left[\frac{\partial \omega^h}{\partial x_i}\frac{\partial k}{\partial x_i}, 0\right]. \tag{3.90}$$

Applying this measure shows no deviations from solutions obtained with the original term $CD^{\text{limited}}_{k\omega}$ in the cases used for validation but greatly enhances the stability of the solution method. The simplification is consistent with most ω-equations from LEVM (Menter *et al.*, 2003) over EARSM (Hellsten, 2005) to DRSM (Wilcox, 2006; Eisfeld, 2010*b*).

Model versions based on ω^h

The formulations of cross diffusion $CD_{k\omega}$ and gradient production terms $P_{\epsilon 3}$ are combined to yield the following two versions of the ω^h-equation:

JH-ω^h

$$\begin{aligned}\frac{D\left(\overline{\rho}\omega^h\right)}{Dt} &= \frac{\partial}{\partial x_i}\left[\left(\frac{1}{2}\mu + \sigma_\omega \mu_T\right)\frac{\partial \omega^h}{\partial x_i}\right] + \alpha\frac{\overline{\rho}\omega^h}{k}P_k - \beta\overline{\rho}\left(\omega^h\right)^2 \\ &\quad + CD^{\text{highRe}}_{k\omega} + \frac{1}{C_\mu k}P^1_{\epsilon 3}\end{aligned} \tag{3.91}$$

JH-ω^h (Maduta)

$$\begin{aligned}\frac{D\left(\overline{\rho}\omega^h\right)}{Dt} &= \frac{\partial}{\partial x_i}\left[\left(\frac{1}{2}\mu+\sigma_\omega\mu_T\right)\frac{\partial\omega^h}{\partial x_i}\right]+\alpha\frac{\overline{\rho}\omega^h}{k}P_k-\beta\overline{\rho}\left(\omega^h\right)^2\\ &\quad +CD_{k\omega}^{\text{Maduta}}+\frac{1}{C_\mu k}P_{\epsilon3}^2 \qquad (3.92)\end{aligned}$$

with

$$\begin{aligned}\alpha &= (C_{\epsilon1}-1) &(3.93)\\ \beta &= C_\mu\left(C_{\epsilon2}-1\right). &(3.94)\end{aligned}$$

The implementation of JH-ω^h (Maduta) in TRACE was checked against results obtained for turbulent plane channel flow (Maduta, 2013). The new JH-ω^h model will be validated in the Chapter 5 where results obtained with JH-ω^h (Maduta) will be shown for reference.

Dissipation rate equation based on ϵ^h

For reference purposes, the original formulation of the model based on the homogeneous dissipation rate ϵ^h has been implemented as well. Its transport equation is given by (3.79). The values of the production and dissipation term model coefficients are $C_{\epsilon1} = 1.44$ and $C_{\epsilon2} = 1.8$ respectively and are consistent with the values used in the ω^h-equation. Turbulent diffusion is treated using the GGD approach (3.58) for stresses with $C_S = 0.22$ and for the dissipation rate with $C_\epsilon = 0.18$. The turbulent viscosity μ_T is used only for the turbulent transport of heat in the energy equation (3.22) and is obtained simply by

$$\mu_T = C_\mu\frac{\overline{\rho}k^2}{\epsilon^h}. \qquad (3.95)$$

The gradient production term is used in its version $P_{\epsilon3}^1$. All remaining coefficients used in the models of the Reynolds stress equations take the values listed in Table 3.2. This model version will be called JH-ϵ^h and is equivalent to the one termed JHh-v1 by Probst (2013) without the S_l-term but with active non-linear slow pressure-strain term controlled by

$$C_1' = -\max\left(0.7A_2, 0.5\right)C_1. \qquad (3.96)$$

Consistence was checked against TAU results of turbulent plane channel flow.

3.4 Numerical properties of pressure-strain models

Using the full JH-ω^h model, a tendency towards pseudo-laminar solutions could be observed in the channel flow depending on the formulation of coefficient functions for the pressure-strain models. A turbulent solution could only be obtained with an appropriate turbulent initialisation of both the flow and turbulence fields. While this issue was solved by choosing a greater factor for the C_2 coefficient, problems still occurred when aerofoil test cases were considered. Figure 3.4 shows the skin friction coefficient c_f over x/c of the RAE2822 supercritical aerofoil as computed by the different

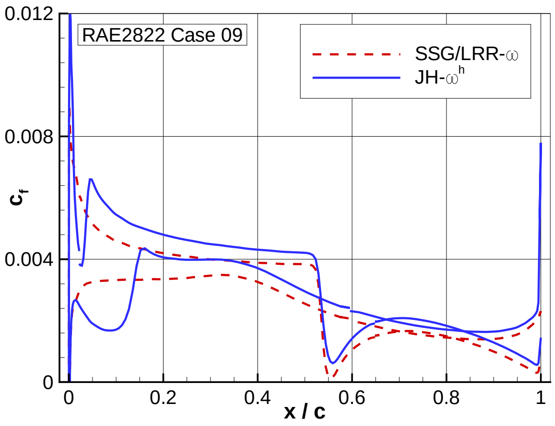

Figure 3.4: Motivation for the investigation of homogeneous shear model problem: Skin friction coefficient c_f of RAE2822 aerofoil.

DRSMs. While the solution with SSG/LRR-ω model develops a turbulent boundary layer within fractions of the chord length, the JH-ω^h model shows a laminar like or transitional c_f-distribution over 10-20%.

Probst (2013) reported similar results for the boundary layer over a flat plate. The JH-ϵ^h model shows a strong susceptibility to the ambient turbulence intensity. At $Tu = 0.1\%$, no turbulent solution could be obtained at all. Since the turbulence model was developed and calibrated as a pure turbulence model, this behaviour is not desirable from a point of view of appropriate transition modelling or being able to trip transition.

Rumsey *et al.* (2006) reported arbitrary steady-state solutions that produced degenerate pseudo-laminar regions in the flow depending on initial conditions and solution method for k-ϵ models. Low-Reynolds modifications of the models were identified as trigger for this behaviour. They introduced a dynamical systems analysis of the model properties in homogeneous shear flow which was extended to k-ω models and EARSMs by Pettersson-Reif *et al.* (2006). Speziale & Mhuiris (1989) presented such an analysis for, amongst others, the LRR DRSM. Rumsey (2007) also showed that both the Spalart-Allmaras and the Menter SST k-ω models exhibited grid-dependent laminar regions of flow in fully turbulent aerofoil computations. Lardeau & Manceau (2014) presented a work-around for this problem by appropriate initialisation of the flow field to aid convergence. The following analysis is inspired by the above studies and parts of this section have been published earlier by the author (Morsbach, 2015).

3.4.1 Model problem

Although the described problem manifests in inhomogeneous flows such as the turbulent boundary layer, it is instructive to study the case of homogeneous turbulence. This simplification is justified by the assumption that in the logarithmic part of the boundary the flow can be approximated as "locally homogeneous" (Rumsey *et al.*, 2006). The model problem is specified by the constant velocity gradient tensor

$$\frac{\partial U_i}{\partial x_j} = \begin{cases} S & i = 1, j = 2 \\ 0 & \text{otherwise} \end{cases} \tag{3.97}$$

with the only finite component given by the shear rate S. Convection, diffusion and any explicitly wall-related model terms vanish in the governing Reynolds stress equations and the partial differential equations reduce to a non-linear system of ordinary differential equations

$$\frac{d\widetilde{u_i''u_j''}}{dt} = P_{ij} - \epsilon_{ij} + \Pi_{ij}. \tag{3.98}$$

Since the absolute value of the Reynolds stresses is unbounded in this problem, the evolution of the Reynolds stress anisotropy tensor a_{ij} is studied. Starting from the evolution equations for the Reynolds stresses, an evolution equation for the Reynolds stress anisotropy tensor a_{ij} is derived as

$$\frac{da_{ij}}{dt} = \frac{1}{k}\left[\left(P_{ij} - \frac{2}{3}P_k\delta_{ij}\right) - \left(\epsilon_{ij} - \frac{2}{3}\epsilon\delta_{ij}\right) + \Pi_{ij} - a_{ij}\left(P_k - \epsilon\right)\right]. \tag{3.99}$$

The pressure-strain and dissipation models of the JH-ω^h model can be written as

$$\begin{aligned}\Pi_{ij} = \Pi_{ij,1} + \Pi_{ij,2} &= -C_1\epsilon a_{ij} - C_2\left(P_{ij} - \frac{2}{3}P_k\delta_{ij}\right) && (3.100)\\ \epsilon_{ij} &= \epsilon\left(\frac{2}{3}\delta_{ij} + f_s a_{ij}\right) && (3.101)\end{aligned}$$

with the rapid part formulated as an isotropisation-of-production (IP) model. For reasons of simplicity, the specific turbulent dissipation rate is defined as $\epsilon = k\omega$ without the constant factor C_μ. Its evolution equation

$$\frac{d\omega}{dt} = (C_{\epsilon 1} - 1)\frac{\omega}{k}P_k - (C_{\epsilon 2} - 1)\omega^2. \tag{3.102}$$

is equivalent to (3.83) with all inhomogeneous terms set to zero and constant density. Substituting the pressure-strain and dissipation models yields

$$\frac{da_{ij}}{dt} = (1 - C_2)\frac{P_{ij} - \frac{2}{3}P_k\delta_{ij}}{k} - \omega a_{ij}(f_s + C_1 - 1) - a_{ij}\frac{P_k}{k}. \tag{3.103}$$

Because only one component of the velocity gradient tensor is different from zero, the only finite components of the production tensor P_{ij} are

$$P_{11} = -2a_{12}kS \quad \text{and} \quad P_{12} = -\left(a_{22} + \frac{2}{3}\right)kS. \tag{3.104}$$

We introduce the following non-dimensional variables

$$\begin{aligned}dt^* &= Sdt && (3.105)\\ \omega^* &= \frac{\omega}{S} && (3.106)\end{aligned}$$

for the time and the specific turbulent dissipation rate. Since the problem is two-dimensional, a_{13} and a_{23} are always zero. Therefore and because of the vanishing trace of a_{ij}, the problem can effectively described by a system of four ordinary differential equations (cf. Speziale & Mhuiris, 1989)

$$\begin{aligned}\frac{da_{11}}{dt^*} &= \frac{4}{3}B_1a_{12} - a_{11}\omega^*B_2 + a_{11}a_{12} && (3.107)\\ \frac{da_{12}}{dt^*} &= B_1\left(a_{22} + \frac{2}{3}\right) - a_{12}\omega^*B_2 + a_{12}^2 && (3.108)\\ \frac{da_{22}}{dt^*} &= -\frac{2}{3}B_1a_{12} - a_{22}\omega^*B_2 + a_{22}a_{12} && (3.109)\\ \frac{d\omega^*}{dt^*} &= -B_3\omega^*a_{12} - B_4(\omega^*)^2 && (3.110)\end{aligned}$$

Table 3.3: Turbulence model coefficient functions simplified for homogeneous shear problem.

Coefficient	LRR-ω	JH-ω^h
C_1	1.8	$2.5A\min(A_2, 0.6)^{0.25}\min((Re_T/150)^{1.5}, 1) + \sqrt{A}E^2$
C_2	0.6	$0.8\sqrt{A}$
f_s	0	$1 - \sqrt{A}E^2$
$C_{\epsilon 1}$	1.5556	1.44
$C_{\epsilon 2}$	1.833	1.8

for the solution vector $\mathbf{q} = (a_{11}, a_{12}, a_{22}, \omega^*)$ with the coefficients

$$B_1 = C_2 - 1 \tag{3.111}$$

$$B_2 = f_s + C_1 - 1 \tag{3.112}$$

$$B_3 = C_{\epsilon 1} - 1 \tag{3.113}$$

$$B_4 = C_{\epsilon 2} - 1. \tag{3.114}$$

The turbulence models are completely specified by the form of their coefficient functions as given in Table 3.3, which is consistent with the formulation of the JH-ω^h model in Table 3.2. Due to the dependence of the dissipation anisotropy two-component parameter E on f_s, the latter is given as an implicit formulation. However, this does not pose a problem because the terms involving E in C_1 and f_s cancel each other in B_2. As a reference model with constant coefficients, the near-wall part of the SSG/LRR-ω model is used and termed LRR-ω. The focus is on understanding the influence of the functional dependence of coefficients on the two-component parameter A and the turbulent Reynolds number Re_T on the solution stability. The analysis is divided into two steps. First, the stability of steady-state solutions of the system of equations will be investigated by linearisation about these solutions. Second, phase space trajectories for different sets of initial conditions will be studied to identify factors promoting degenerate solutions.

3.4.2 Dynamical systems analysis

A steady-state solution to the system of ODEs (3.107)-(3.110) can be obtained by setting the time derivative to zero. For the LRR-ω model with constant coefficients, the solution can be obtained algebraically as

$$a_{11} = -\frac{4}{3}\frac{B_1 B_4}{B_2 B_3 + B_4} \tag{3.115}$$

$$a_{22} = \frac{2}{3}\frac{B_1 B_4}{B_2 B_3 + B_4} \tag{3.116}$$

$$a_{12} = -\frac{\sqrt{-\frac{2}{3}B_1 B_4 (B_1 B_4 + B_2 B_3 + B_4)}}{B_2 B_3 + B_4} \tag{3.117}$$

$$\omega^* = \frac{B_3\sqrt{-\frac{2}{3}B_1 B_4 (B_1 B_4 + B_2 B_3 + B_4)}}{B_4 (B_2 B_3 + B_4)} \tag{3.118}$$

Table 3.4: Steady-state solutions of homogeneous shear flow.

Model	a_{11}	a_{12}	a_{22}	ω^*	Comment
LRR-ω	0.3478	-0.3585	-0.1739	0.2391	stable
	$-2/3 < a_{11} < 4/3$	0	$-2/3$	0	unstable
JH-ω^h	0.2437	-0.3156	-0.1219	0.1736	stable, $Re_T \geq 150$
	$-2/3 < a_{11} < 4/3$	0	$-2/3$	0	further analysis required

taking the physically realisable solution of positive dissipation rate. Due to the functional dependency of B_1 and B_2 on the invariants of a_{ij}, the steady-state solution for the JH-ω^h model is computed numerically. Both the LRR-ω and the JH-ω^h model have an additional steady-state solution for the homogeneous shear flow as shown in Table 3.4. It is a range of solutions characterised by vanishing A, which labels the solution as two-component turbulence, and vanishing specific dissipation rate ω^*, which indicates a laminarisation (Rumsey *et al.*, 2006). The stability properties of such degenerate solutions can indicate if a numerical scheme will converge towards them.

To study the stability of the fixed points, the behaviour of the system of ODEs under small disturbances is evaluated. To this end, a Taylor series expansion about the fixed points $\mathbf{q}_0$

$$\frac{d\mathbf{q}}{dt^*} = \mathbf{f}(\mathbf{q}) = \mathbf{f}(\mathbf{q}_0) + \left.\frac{\partial \mathbf{f}}{\partial \mathbf{q}}\right|_{\mathbf{q}=\mathbf{q}_0} (\mathbf{q} - \mathbf{q}_0) + \ldots \tag{3.119}$$

is performed. The eigenvalues of the Jacobian matrix

$$\frac{\partial \mathbf{f}}{\partial \mathbf{q}} = \begin{pmatrix} -\omega^* B_2 + a_{12} & \frac{4}{3}B_1 + a_{11} & 0 & -a_{11}B_2 \\ 0 & -\omega^* B_2 + 2a_{12} & B_1 & -a_{12}B_2 \\ 0 & -\frac{2}{3}B_1 + a_{22} & -\omega^* B_2 + a_{12} & -a_{22}B_2 \\ 0 & -B_3\omega^* & 0 & -B_3 a_{12} - 2B_4\omega^* \end{pmatrix} \tag{3.120}$$

evaluated at $\mathbf{q} = \mathbf{q}_0$ determine the stability properties of the respective fixed point. In the analytical derivation of the Jacobian, the coefficients B_i are treated as constants in analogy to the implicit treatment of the equations in the finite volume solver. The eigenvalues are computed using the computer algebra system Maple.

For both the LRR-ω and the JH-ω^h model, all real parts of the eigenvalues evaluated at the fixed points with finite A are negative, indicating that the fixed point is stable and initial values chosen within its convergence radius will result in this solution. The stability of the solution with vanishing A, on the other hand, distinguishes the two models. For the LRR-ω model, the two-component solution is unstable as expected, i.e. the system of equations will not converge towards this solution. However, all eigenvalues vanish if the coefficient functions of the JH-ω^h model are substituted into (3.120). Since the system of equations is non-linear, no definite statement on the stability of this solution for the JH-ω^h model can be made without further analysis. This finding motivated the phase space analysis presented in the following section.

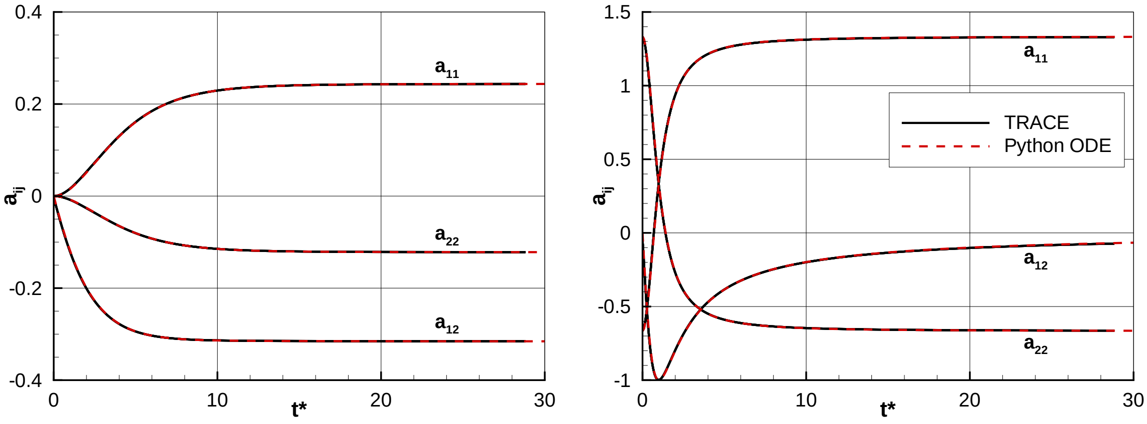

Figure 3.5: Validation of the JH-ω^h model implementation in the ODE solver against TRACE computations for homogeneous shear flow with isotropic (*left*) and one-component (*right*) initialisation.

3.4.3 Numerical phase space analysis

To gain deeper insight into the dynamical behaviour of the models, it is instructive to analyse phase space trajectories. For this purpose, the system of equations is coded in Python and solved by the standard SciPy ODE-solver (Oliphant, 2007). Its correct implementation is validated by comparison with solutions for the turbulence anisotropy tensor obtained with TRACE using the JH-ω^h model for initial conditions of isotropic turbulence (Figure 3.5 *left*) and one-component turbulence in 2-direction (Figure 3.5 *right*), respectively. It is interesting to note that the latter initialisation, contrary to the expected convergence towards more isotropic turbulence, is only rotated towards one-component turbulence in 1-direction. The production term, in this case, only generates energy in a second spatial direction and A remains zero for two-component turbulence. Hence, all redistribution terms are effectively zero as originally intended only close to a solid wall and no energy can be transferred to the third spatial direction.

To investigate the influence of the turbulent Reynolds number, two treatments are possible. On the one hand, Re_T can be treated as a fixed parameter in the coefficient function for the slow pressure-strain term. On the other hand, in addition to the system of equations (3.107)-(3.110) described above, an equation for the turbulent Reynolds number Re_T

$$\frac{dRe_T}{dt^*} = -Re_T\left(a_{12}(1-B_3) + \omega^*(1-B_4)\right), \tag{3.121}$$

derived from the equations for turbulent kinetic energy and dissipation rate, can be solved. Re_T increases exponentially for cases in which the term in brackets is negative. Because of the minimum function in the C_1 coefficient, it only influences the remaining JH-ω^h equations as long as $Re_T < 150$ while it has no effect at all in the LRR-ω context.

The general strategy to visualise the phase space trajectories is as follows. In contrast to two-equation models, the phase space for a DRSM for this problem is four-dimensional (three independent components of turbulence anisotropy, dissipation rate) or five-dimensional if the equation for Re_T is solved. Therefore, the trajectories will be plotted in the two-dimensional space of second and third invariants of the anisotropy tensor with the bounds of physically realisable turbulence (Lumley, 1979) shaded in grey. Time evolution will be plotted along the z-axis (not drawn to scale). The set of initial conditions is created by a linear distribution n values of anisotropy tensor components

Table 3.5: Initial conditions for phase space analysis of homogeneous shear flow. Non-realisable combinations of a_{ij} components are filtered.

Parameter	Range	n
a_{11}	[-0.6666, 1.3333]	10
a_{12}	[-1, 0]	10
a_{22}	[-0.6666, 1.3333]	10
ω^*	[0.001, 1]	10
Re_T	[0, 150]	16

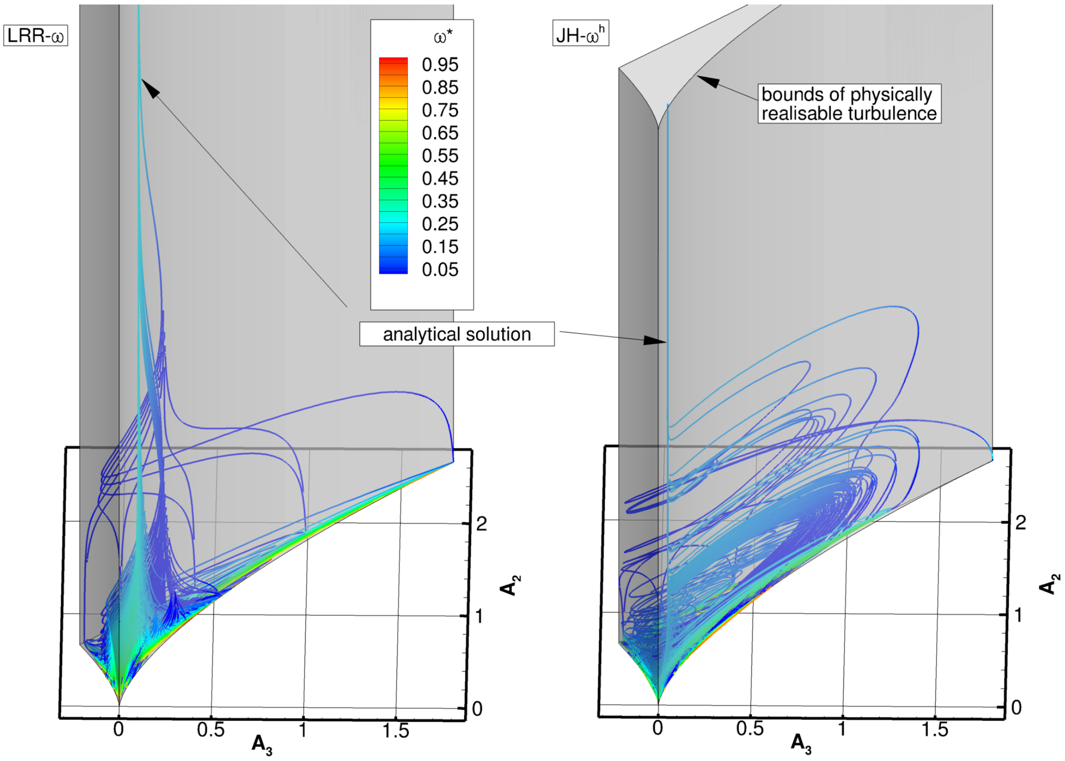

Figure 3.6: Phase space trajectories of LRR-ω (*left*) and JH-ω^h (*right*) in homogeneous shear flow initialised with different turbulence anisotropy states.

within the bounds of realisability and respective dissipation rates and turbulent Reynolds numbers as shown in Table 3.5. For ω^*, 0 is excluded from the range of initial conditions because it would result in $\omega^* = 0$ and $d\omega^*/dt = 0$ in the evolution equation (3.110). Furthermore, the solution has been found to be insensitive to initial values of ω^* much greater than 1 due to the negative quadratic term.

A first comparison in Figure 3.6 shows the phase space trajectories of the LRR-ω (*left*) and the JH-ω^h model (*right*) with a fixed $Re_T > 150$. Both models converge to the analytical steady-state solution with finite ω^* irrespective of initial conditions. In contrast to the LRR-ω model, however, there are trajectories of the JH-ω^h model which show a tendency towards the one-component limit ($A_2 = 8/3$, $A_3 = 17/9$, $A = 0$) before they finally converge to the steady-state solution. This raises the question what promotes convergence towards the degenerate solution. Different mechanisms that diminish stress redistribution in the JH-ω^h model will be analysed.

The turbulent Reynolds number Re_T directly controls the magnitude of the slow pres-

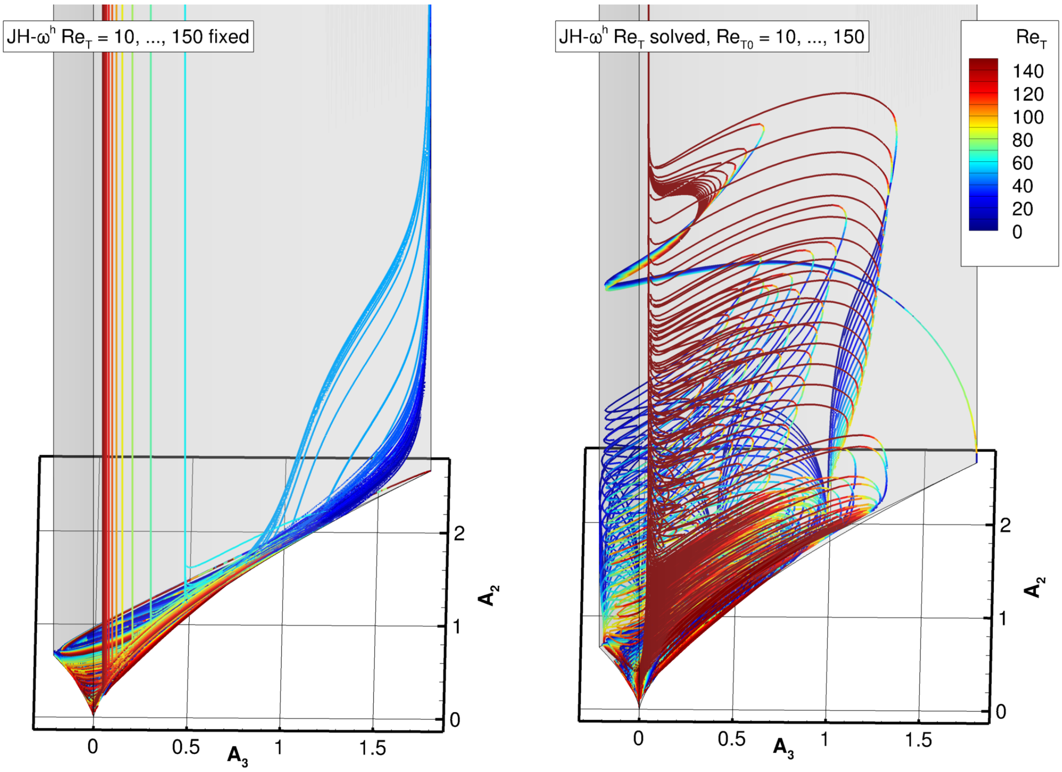

Figure 3.7: Phase space trajectories of JH-ω^h with the turbulent Reynolds number Re_T as fixed parameter (*left*) and with the Re_T equation solved (*right*) in homogeneous shear flow initialised with different turbulence anisotropy states.

sure-strain term via the coefficient function C_1. Its functional form was designed to drive turbulence towards the two-component limit close to the solid wall in turbulent channel flow. The effect of this low-Reynolds-number modification in homogeneous shear flow can be seen in Figure 3.7 (*left*) where Re_T was treated as fixed parameter. The same set of turbulence anisotropy states (Table 3.5), here with an initial specific dissipation rate of $\omega^* = 1$, is used as initial conditions. There is a threshold for Re_T below which the pressure-strain term is too small to prevent convergence towards one-component turbulence. All variants of the pressure-strain model with the parameter $Re_T < 60$ converge to the one-component limit irrespective of initial conditions. Once the solution is close to this limit, the pressure-strain term is diminished even further by its linear dependency on the two-component parameter A. For each remaining value of $Re_T \geq 60$, a separate, turbulent, steady-state solution corresponding to the formulation of C_1 is reached. If Re_T is determined by solving of its own evolution equation, the picture changes as demonstrated in Figure 3.7 (*right*). Due to the nature of the homogeneous shear flow problem, Re_T increases exponentially with time according to (3.121) if stresses and dissipation rate approach the equilibrium. Once it exceeds the value of 150, there is no more back coupling to the evolution of the anisotropy tensor. The figure shows that states initialised close to the two-component limit tend towards one-component turbulence as long as Re_T is small. This behaviour is reversed once Re_T reaches a value of about 100.

To further investigate this behaviour, the time evolution of turbulence initialised as isotropic ($a_{11} = 0$, $a_{12} = 0$, $a_{22} = 0$, $\omega^* = 1$) is analysed. Figure 3.8 shows the logarithmic time history of various parameters for three different cases. The first and third columns were computed with a fixed turbulent Reynolds number of $Re_T = 50$ and 150, respectively. In contrast, the second column shows results obtained by additional solu-

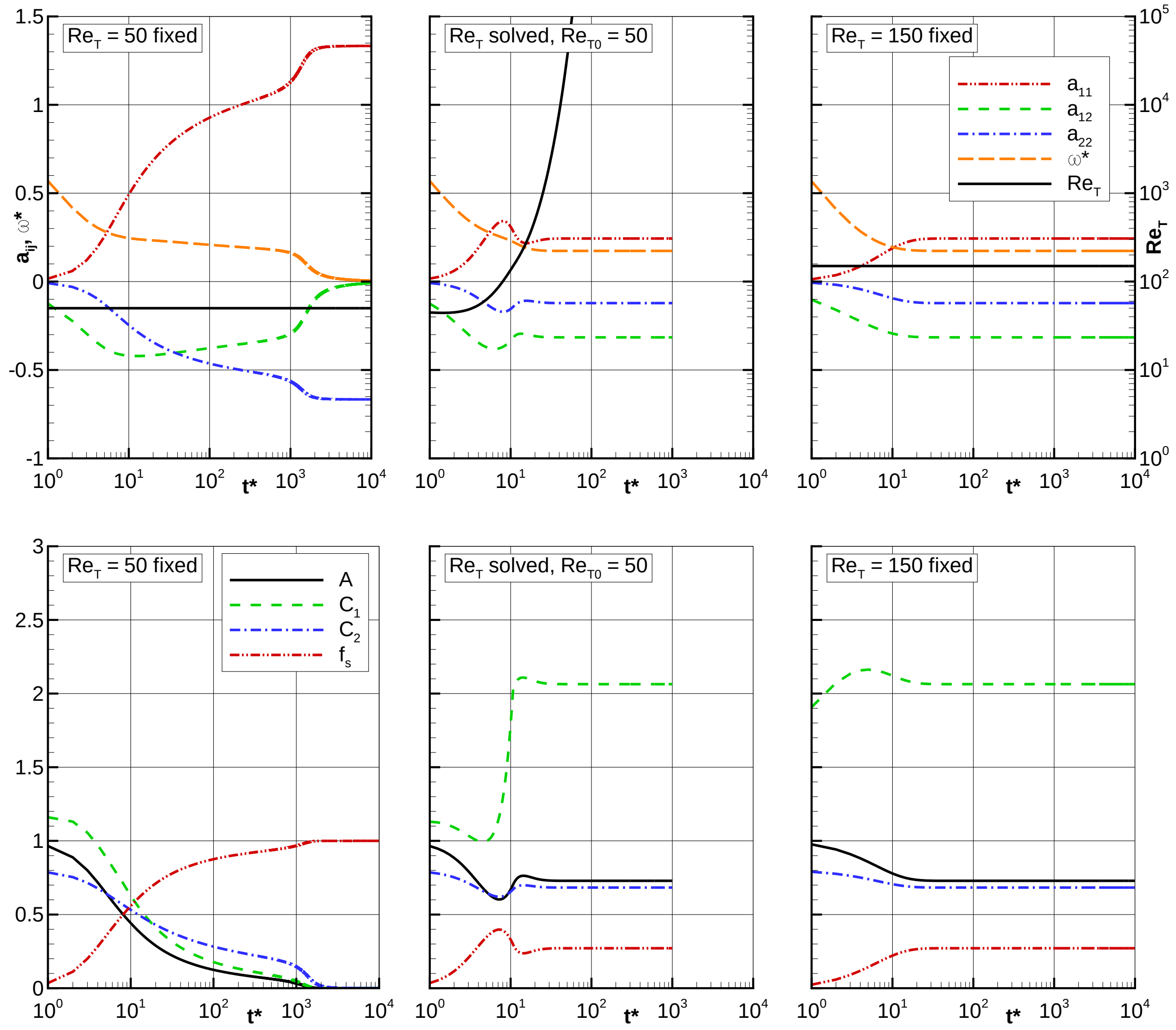

Figure 3.8: Logarithmic time history of solution variables a_{ij}, ω^* and Re_T (*first row*), model coefficients C_1, C_2, f_s and two-component parameter A (*second row*) for fixed $Re_T = 50$ (*first column*), solved Re_T initialised with $Re_{T0} = 50$ (*second column*) and fixed $Re_T = 150$ (*third column*).

tion of the equation for Re_T initialised with $Re_{T0} = 50$. In the first row, the components of the anisotropy tensor as well as the dissipation rate are plotted on the left axis while the turbulent Reynolds number is plotted on the right axis in logarithmic scaling. Both the $Re_T = 150$ case and the case in which the Re_T equation is solved converge to the same solution because the set of equations for the anisotropy tensor and the dissipation rate is the same once Re_T exceeds 150 due to the minimum function in C_1. In case of fixed $Re_T = 50$, both the shear stress and the dissipation rate eventually converge to zero. Instead, there is a rather sharp transition at $t^* > 1000$, where a_{12} and ω^* decay rapidly and a_{11} and a_{22} tend towards their physically realisable limiting values of $4/3$ and $-2/3$, respectively. This corresponds to a turbulence state where all turbulent kinetic energy is in the 11-component and all other entries of the Reynolds stress tensor vanish. Due to the direct dependency of the redistribution term coefficients C_1 and C_2 on the two-component parameter A, these also tend to zero as shown in the second row of plots. The second column supports the findings deduced from the phase space analysis: As long as Re_T is small, the system of equation tends towards the same solution as the system with small fixed turbulent Reynolds number. Once it exceeds a critical value, this trend is reversed and the system converges to the steady-state solution of high turbulent Reynolds number.

Figure 3.9 shows the source terms of the Reynolds stress equations

$$P^*_{ij} = \frac{P_{ij}}{Sk}, \quad \Pi^*_{ij,1} = \frac{\Pi_{ij,1}}{Sk}, \quad \Pi^*_{ij,2} = \frac{\Pi_{ij,2}}{Sk}, \quad -\epsilon^*_{ij} = -\frac{\epsilon_{ij}}{Sk} \tag{3.122}$$

normalised by turbulent kinetic energy k and shear rate S and their budget for each relevant component of the Reynolds stress tensor for the cases considered above. For the case of fixed $Re_T = 50$, the pressure-strain redistribution terms reach zero as indicated by their coefficient functions in Figure 3.8 (*bottom*). The 22-component is not produced directly and is, hence, dependent on active redistribution mechanisms. Once the latter are diminished by the decreasing two-component parameter, this stress component cannot be prevented from vanishing. Consequently, production of the (negative) shear stress 12-component vanishes and its budget changes sign from negative (production) to positive (destruction). This way, also the last active production term in the 11-component is affected and only dissipation terms remain active in the set of equations. The chain of events illustrates how pressure-strain redistribution is necessary to sustain turbulence and how its disappearance can lead to laminarisation of the flow. As described above, the additional solution of the Re_T-equation shown in the second column prevents the redistribution coefficients from going to zero and leads to convergence to the high Reynolds solution as shown with fixed $Re_T = 150$ in the third column. The distinctive discontinuity in the slope of the slow pressure-strain term appears exactly at $Re_T = 150$. It can be explained by the use of the minimum function in C_1. Below the critical turbulent Reynolds number the increase in C_1 is determined by the increase in Re_T. From there on, it is only dependent on A_2 and through A on A_3 resulting in the discontinuity in the slope.

To better understand the transition between the turbulent and the laminar solution type, a highly resolved variation of the turbulent Reynolds number Re_T between 45 and 55 with a step size of 0.1 was conducted using the equation set with fixed Re_T. The result is plotted in Figure 3.10, which shows the time history of the two-component parameter A over non-dimensional time t^* for the given range of turbulent Reynolds numbers indicated by line colour. $Re_T = 50.8$ labels the last solution with a stable finite value of A while all solutions with Re_T smaller than that converge to one-component turbulence with vanishing A. The JH-ω^h model does not seem to be able to sustain a turbulent solution for $Re_T \leq 50.7$ in this case. This is consistent with the results visualised in Figure 3.7 (*left*).

There are publications employing the Jakirlić/Hanjalić model with $C_2 = 0.6\sqrt{A}$ as the coefficient for the rapid pressure-strain term (Jakirlić *et al.*, 2007; Jakirlić & Maduta, 2014). The effect of choosing this formulation in homogeneous shear flow is demonstrated in Figure 3.11. On the left it is shown that a substantial number of initial conditions lead to phase space trajectories approaching the one-component limit. Figure 3.11 (*right*) shows a scatter plot of initial conditions which converge to the one-component limit. Their initial non-dimensional rate of dissipation ω^* is colour-coded. It can be deduced that the area of attraction scales with initial ω^*. For large ω^*, initial turbulence anisotropy needs to be rather close to the one-component limit, while for smaller values of ω^* (i.e. high rates of shear) a substantial part of the invariant map is attracted to one-component turbulence. The turbulence anisotropy of turbulent plane channel flow at $Re_\tau = 180$ predicted by the JH-ω^h model is plotted for reference. The low values of ω^* representing the ratio of turbulent dissipation rate to the rate of shear in the lower part of the boundary layer indicate potential problematic model behaviour. Indeed, if the

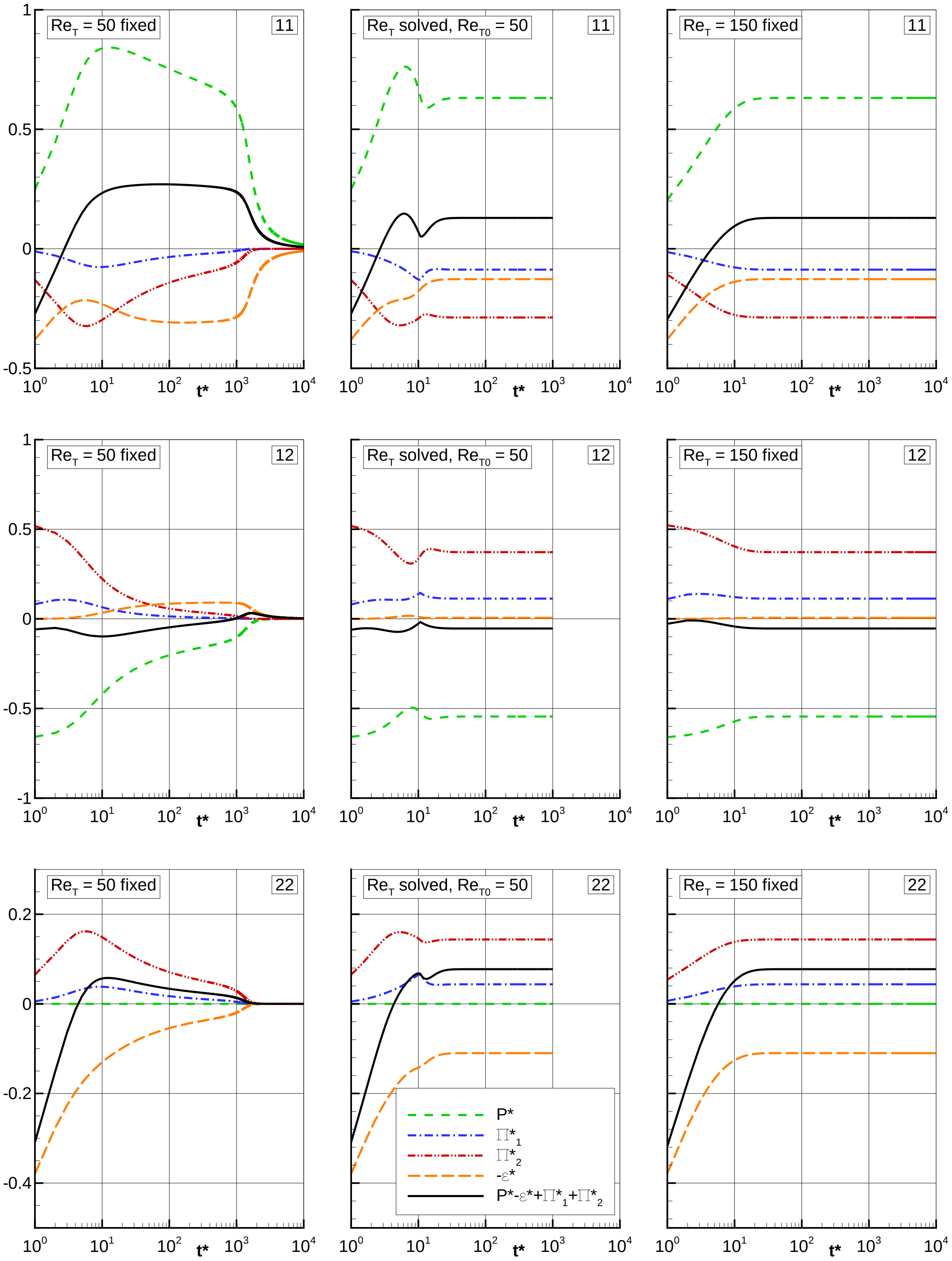

Figure 3.9: Logarithmic time history of normalised production P^*_{ij}, slow pressure-strain $\Pi^*_{ij,1}$, rapid pressure-strain $\Pi^*_{ij,2}$, dissipation term $-\epsilon^*_{ij}$ and total budget of 11- (*top*), 12- (*middle*) and 22-component (*bottom*) for fixed $Re_T = 50$ (*first column*), solved Re_T initialised with $Re_{T0} = 50$ (*second column*) and fixed $Re_T = 150$ (*third column*).

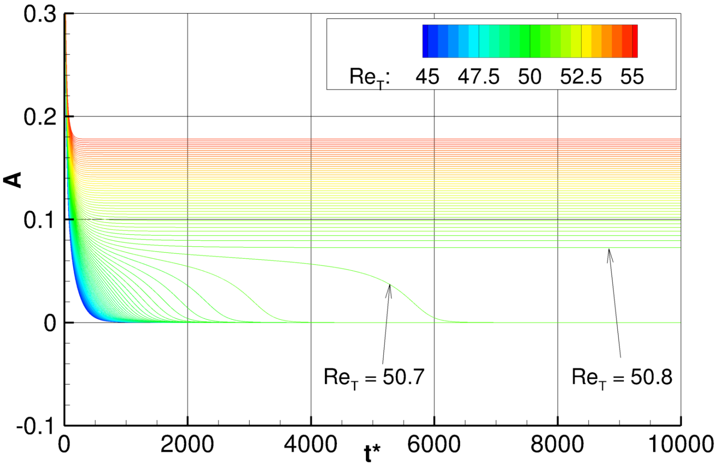

Figure 3.10: Time history of two-component parameter A for fixed values of Re_T between 45 and 55 indicated by line colour. $Re_T = 50.8$ labels the last solution with stable finite value of A while A goes to zero for all Re_T smaller than that.

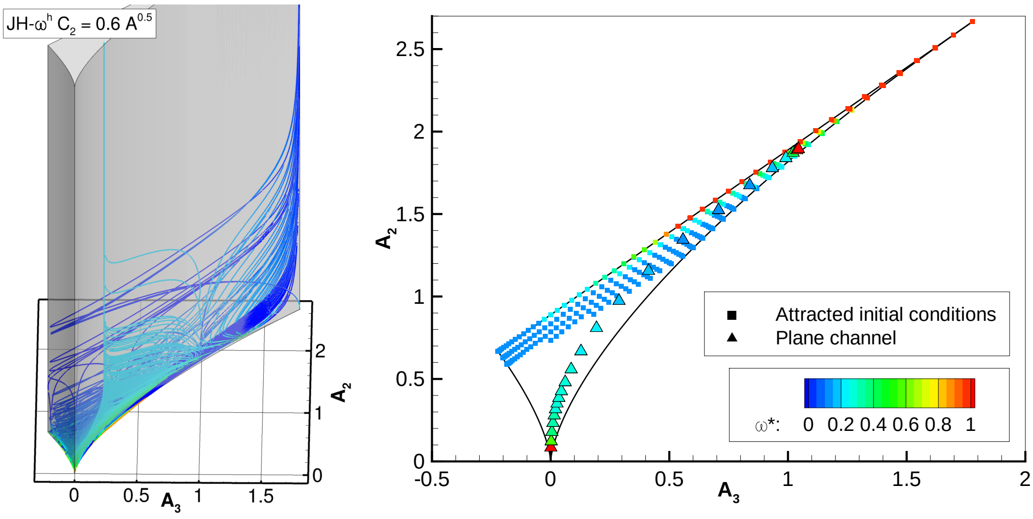

Figure 3.11: Phase space trajectories of JH-ω^h with $C_2 = 0.6\sqrt{A}$ in homogeneous shear flow initialised with different turbulence anisotropy states (*left*) and map of initial conditions attracted to one-component turbulence (*right*). The turbulent channel flow solution with JH-ω^h computed with TRACE is plotted for reference.

JH-ω^h model with $C_2 = 0.6\sqrt{A}$ is applied to turbulent plane channel flow, the model shows a tendency towards a laminar solution with Reynolds stresses approaching the one-component limit. Proper initialisation of the turbulence field prevents the laminar solution. These problems do not occur with $C_2 = 0.8\sqrt{A}$. This example demonstrates the transferability of the homogeneous shear flow findings to a boundary layer flow.

In summary, the JH-ω^h model's tendency towards laminar solutions has been investigated. It can be explained by the property of the model that redistribution can vanish under certain conditions. This is the case in two-component turbulence when A goes to zero - a state from which the model cannot recover because both redistribution terms scale with some power of A. Especially at low turbulent Reynolds numbers, the model has been shown to converge towards the degenerate solution. A possible solution could be a lower limit of the non-dimensional dissipation rate ω/S.

4 Numerical method

The aim of this chapter is to briefly introduce the numerical framework and methods used to solve the RANS and turbulence model equations. All numerical simulations were performed in the framework of DLR's CFD solver for turbomachinery flows, TRACE. A comprehensive description of the methods implemented in TRACE can be found in the corresponding publications of the Numerical Methods department of the Institute of Propulsion Technology (e.g. Frey *et al.*, 2009; Becker *et al.*, 2010; Franke *et al.*, 2010; Kersken *et al.*, 2012; Ashcroft *et al.*, 2013).

4.1 Flow solver

TRACE solves the Favre-averaged Navier-Stokes equations using a cell centred finite volume method (see e.g. LeVeque, 2002) as schematically depicted in Figure 4.1. Structured as well as unstructured meshes are distributed to different blocks to allow for parallel computation. While the coordinates of the cells are given by their vertices, the flow solution is stored at the cell centres. Ghost cells are used to supply the flow state of adjacent blocks as well as to prescribe boundary values at interfaces or solid walls.

The finite volume method is based on the integral conservation formulation of the equations obtained by applying Gauß's theorem to convert volume integrals over divergences to surface integrals over fluxes. Contributions to the balance of each (finite) control volume can be split into fluxes over its faces and volume sources. The balance

$$\int_V \frac{\partial \mathbf{q}}{\partial t} dV + \oint_{\partial V} (\mathbf{F} \cdot \mathbf{n}) dA = \oint_{\partial V} (\mathbf{F}_v \cdot \mathbf{n}) dA + \int_V \mathbf{S} dV \tag{4.1}$$

has to be fulfilled for each control volume V with surface ∂V in the grid with the vector of conservative solution variables given by

$$\mathbf{q} = (\overline{\rho}, \overline{\rho}\widetilde{u}_1, \overline{\rho}\widetilde{u}_2, \overline{\rho}\widetilde{u}_3, \overline{\rho}\widetilde{E}, \overline{\rho}\phi_1, \ldots, \overline{\rho}\phi_N)^T. \tag{4.2}$$

In TRACE, $\tilde{u}_i$ denotes the relative velocity in a rotating frame of reference. The dynamics of the fluid flow are governed by the inviscid $\mathbf{F}$ and viscous $\mathbf{F}_v$ flux vectors as well as the volume source term $\mathbf{S}$. Besides the continuity, momentum and energy equations, an arbitrary set of convection-diffusion equations for generic scalar variables ϕ_i is solved. These can be, for example, turbulence quantities such as the turbulent kinetic energy k, components of the Reynolds stress tensor $\widetilde{u_i''u_j''}$ or concentrations of tracer-particles.

In a finite volume scheme, the discretised version of the integral equation (4.1) is solved for each control volume. Volume integrals are approximated by a constant integrand over the control volume, whereas the surface integrals are evaluated as a sum over all

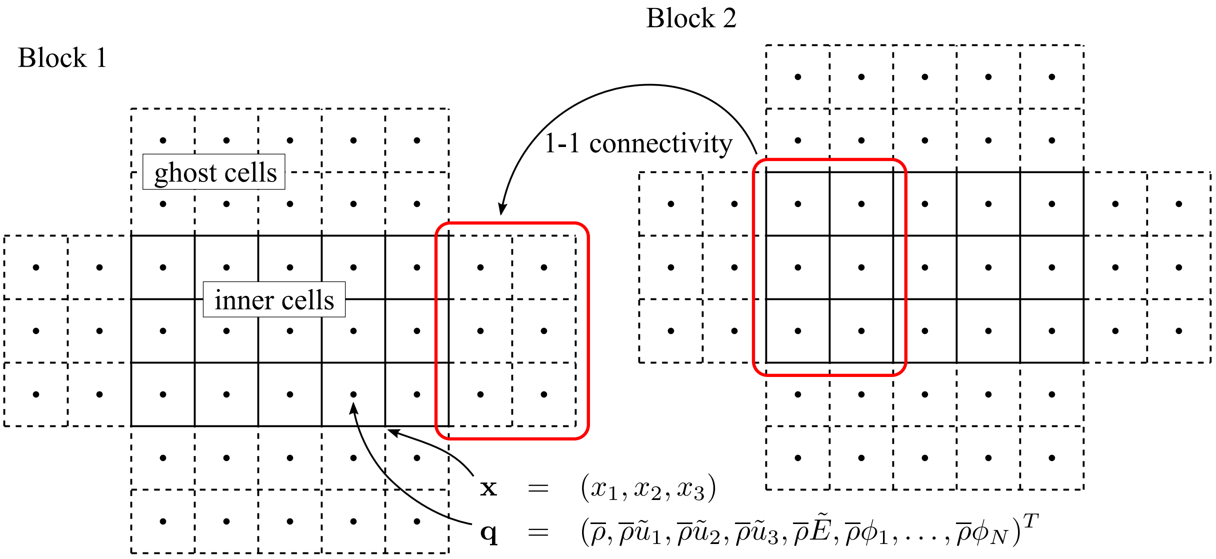
Block 1
Block 2
1-1 connectivity
ghost cells
inner cells
$\mathbf{x} = (x_1, x_2, x_3)$
$\mathbf{q} = (\overline{\rho}, \overline{\rho}\tilde{u}_1, \overline{\rho}\tilde{u}_2, \overline{\rho}\tilde{u}_3, \overline{\rho}\tilde{E}, \overline{\rho}\phi_1, \ldots, \overline{\rho}\phi_N)^T$

Figure 4.1: Schematic of multi-block cell centred finite volume method.

N_F cell faces with a constant value for each face.

$$\oint_{\partial V} (\mathbf{F} \cdot \mathbf{n}) dA = \sum_{f=1}^{N_F} (\mathbf{F} \cdot \mathbf{n}_f) A_f \tag{4.3}$$

The cell face f is represented by the face normal vector $\mathbf{n}_f$ and the face area A_f. A flux difference splitting method is employed to discretise the inviscid convection terms making use of a second order accurate Roe (1981) scheme. Gradients of velocity and temperature used in viscous terms are computed using second order accurate central differences.

Turbomachinery components typically consist of both stationary parts such as guide vanes and ducts and rotating parts such as rotor blades. For the latter, it can be convenient to solve the equations in a frame of reference which rotates at a constant rate $\mathbf{\Omega}$. Centrifugal and Coriolis forces then appear in the momentum equations through the source term

$$\mathbf{S} = \begin{pmatrix} S_{\overline{\rho}} \\ \mathbf{S}_{\overline{\rho}\widetilde{\mathbf{u}}} \\ S_{\overline{\rho}\widetilde{E}} \\ S_{\overline{\rho}\phi_i} \end{pmatrix} = \begin{pmatrix} 0 \\ -\overline{\rho}\mathbf{\Omega} \times (\mathbf{\Omega} \times \mathbf{x}) - 2\overline{\rho}\mathbf{\Omega} \times \widetilde{\mathbf{u}} \\ 0 \\ S_{\overline{\rho}\phi_i} \end{pmatrix} . \tag{4.4}$$

The contribution of the centrifugal force to the energy equation is accounted for by solving for the relative total energy defined by

$$\widetilde{E} = \widetilde{e} + \frac{\widetilde{u}_i \widetilde{u}_i}{2} - \frac{1}{2}\Omega^2 r_\perp^2 \tag{4.5}$$

with the internal energy $\widetilde{e}$, the norm of the rotation rate Ω and the distance from the axis of rotation $r_\perp$. In contrast to the general formulation of the energy equation (3.22), neither the convective nor the diffusive transport of turbulent kinetic energy k are considered here.

For a solution of the steady RANS equations, the time derivative of the residual $\mathbf{R}(\mathbf{q})$, which contains the fluxes and source terms, must go to zero

$$\frac{\partial \mathbf{q}}{\partial t} = \mathbf{R}(\mathbf{q}) \to 0. \tag{4.6}$$

The equations are solved by an implicit time-marching algorithm with local time stepping in pseudo-time $\partial\mathbf{q}/\partial t \rightarrow \partial\mathbf{q}/\partial\tau$ allowing for CFL numbers greater than unity. For the pseudo-time derivative $\partial\mathbf{q}/\partial\tau$, a simple finite difference of first order is employed. The unknown residual at time step $m+1$ is evaluated by a Taylor series expansion about time step m

$$\frac{\Delta\mathbf{q}^m}{\Delta\tau} = \mathbf{R}(\mathbf{q}^{m+1}) = \mathbf{R}(\mathbf{q}^m) + \left.\frac{\partial\mathbf{R}}{\partial\mathbf{q}}\right|^m \Delta\mathbf{q}^m + \mathcal{O}(\Delta\mathbf{q}^2). \tag{4.7}$$

This leads to a matrix equation for the update $\Delta\mathbf{q}$ of the conservative variables $\mathbf{q}$

$$\left(\frac{1}{\Delta\tau}\mathbf{1} - \left.\frac{\partial\mathbf{R}}{\partial\mathbf{q}}\right|^m\right)\Delta\mathbf{q}^m = \mathbf{R}(\mathbf{q}^m). \tag{4.8}$$

Unsteady problems with finite $\partial\mathbf{q}/\partial t$, on the other hand, require higher order discretisation in the temporal domain. Time discretisation schemes are available from second order accurate Euler over Crank-Nicolson to various implicit Runge-Kutta schemes (Ashcroft *et al.*, 2013). Unsteady solutions in this work were obtained by the second order accurate Euler backward scheme (Nürnberger, 2004). Then, the physical time derivative at physical time step $n+1$ is approximated by

$$\left.\frac{\partial\mathbf{q}}{\partial t}\right|^{n+1} = \frac{1}{2\Delta t}\left(3\mathbf{q}^{n+1} - 4\mathbf{q}^n + \mathbf{q}^{n-1}\right) + \mathcal{O}(\Delta t^2). \tag{4.9}$$

Again, the equations are solved numerically by the above implicit pseudo-time marching method. In contrast to the steady approach (4.7), the physical time derivative occurs on the right hand side

$$\frac{\Delta\mathbf{q}^m}{\Delta\tau} = \mathbf{R}(\mathbf{q}^{m+1}) - \left.\frac{\partial\mathbf{q}}{\partial t}\right|^{m+1} \tag{4.10}$$

using values of the next pseudo-time step $m+1$ for the update $\Delta\mathbf{q}^m$ of conservative variables at pseudo-time step m. In the physical time derivative, $\mathbf{q}^{n+1}$ is substituted by the solution $\mathbf{q}^{m+1}$ at pseudo-time step $m+1$. If the pseudo-time marching method converges, $\mathbf{q}^{m+1}$ will approach the value of the next physical time step $\mathbf{q}^{n+1}$. Linearising the residual $\mathbf{R}(\mathbf{q})$ and the approximated physical time derivative $\partial\mathbf{q}/\partial t$ about pseudo-time step m and re-arranging yields the equation which determines the update $\Delta\mathbf{q}^m$:

$$\left(\frac{1}{\Delta\tau}\mathbf{1} + \frac{3}{2\Delta t}\mathbf{1} - \left.\frac{\partial\mathbf{R}}{\partial\mathbf{q}}\right|^m\right)\Delta\mathbf{q}^m = \mathbf{R}(\mathbf{q}^m) - \frac{1}{2\Delta t}\left(3\mathbf{q}^m - 4\mathbf{q}^n + \mathbf{q}^{n-1}\right). \tag{4.11}$$

This is equivalent to the steady equation (4.8) for $\Delta t \rightarrow \infty$.

The treatment of inflow and outflow boundaries distinguishes turbomachinery from external aerodynamics problems in CFD. In contrast to flows in external aerodynamics, the domain extends only up to one chord length beyond the blade geometry at best. Using standard boundary conditions based on 1D Riemann invariants, the position of the boundary can influence the potential field by unwanted reflections. It is, however, desirable to be able to obtain results independent of the exact position of the boundary. For turbomachinery applications, which exhibit rotationally periodic domains, it is possible to formulate 2D non-reflecting boundary conditions (Giles, 1990; Robens *et al.*, 2013). These are the standard treatment for turbomachinery test cases in TRACE. For the basic validation test cases, in which potential perturbations do not approach the boundary, standard 1D non-reflecting boundary conditions (Riemann) are used.

This gives a crude overview of the flow solver TRACE. Turbulence models are implemented as scalar transport equations with respective fluxes and source terms. The following sections will deal with extensions of flow solver implemented to enable simulations with DRSMs. First, the consistent discretisation of transport equations with respect to conservation of the scalar quantities will be derived. Second, the implicit treatment of various parts of the set of equations is explained. These are the Reynolds stress terms in the RANS equations, on the one hand, and the diffusive fluxes and source terms in the turbulence model equations, on the other hand. Finally, turbulence boundary conditions will be established.

4.2 Discretisation of transport equations

This section will address the discretisation of the transport equations for turbulence and other scalar quantities with respect to their conservation properties and source terms. While a fully separated solution of scalar equations can be attractive as it reduces computational overhead, it can, in contrast to a coupled solution, lead to severe conservation errors. These can result in unphysical overshoots in physically bounded quantities (Reynolds normal stresses and consequently turbulent kinetic energy as well as turbulent dissipation rate) which affect the stability of the solution method. The goal is to avoid these effects and still maintain a high code modularity as well as computational efficiency. Therefore, a correction of the scalar convective fluxes has been derived, which restores full consistency with the discretisation of the corresponding terms in the Navier-Stokes equations and, hence, with a coupled solution method. The convective fluxes in TRACE are formulated using Roe's method (Roe, 1981), which uses the left and right states of a cell face. The latter are reconstructed using a MUSCL extrapolation (cf. Hirsch, 1990; van Leer, 1979), whose choice determines the spatial accuracy of the scheme. Parts of the following have already been published by the author (Morsbach & di Mare, 2012).

For reasons of readability, the flux correction is derived by investigation of the coupled solution of the 1D Euler equations and a generic transported scalar quantity ϕ. The extension to 3D and more equations is straightforward and leads to the same correction for each equation. The vectors of conservative variables $\mathbf{q}$, primitive variables $\mathbf{u}$ and the fluxes $\mathbf{F}$ of the coupled system of equations are defined as follows:

$$\mathbf{q} = \begin{pmatrix} \rho \\ \rho u \\ \rho E \\ \rho\phi \end{pmatrix} \quad \mathbf{u} = \begin{pmatrix} \rho \\ u \\ p \\ \phi \end{pmatrix} \quad \mathbf{F} = \begin{pmatrix} \rho u \\ \rho u^2 + p \\ (\rho E + p)u \\ \rho u \phi \end{pmatrix} \tag{4.12}$$

As a starting point, equation (4.1) is written in its differential form

$$\frac{\partial \mathbf{q}}{\partial t} + \frac{\partial \mathbf{F}}{\partial x} = 0, \tag{4.13}$$

neglecting the viscous fluxes $\mathbf{F}_v$ and source terms $\mathbf{S}$ without loss of generality. Introducing the flux Jacobian in conservative variables

$$\mathbf{A}_q = \frac{\partial \mathbf{F}}{\partial \mathbf{q}} \tag{4.14}$$

it can be written as

$$\frac{\partial \mathbf{q}}{\partial t} + \mathbf{A}_q \frac{\partial \mathbf{q}}{\partial x} = 0 \tag{4.15}$$

Roe's method (cf. LeVeque, 2002; Blazek, 2001) can then be used to obtain an exact solution for the linearised version of this equation using the flux at the cell face $I+1/2$ given by

$$\mathbf{F}_{I+1/2} = \begin{pmatrix} F_\rho \\ F_{\rho u} \\ F_{\rho E} \\ F_\phi \end{pmatrix} = \frac{1}{2}\left[\left(\mathbf{F}(\mathbf{u}^L) + \mathbf{F}(\mathbf{u}^R)\right) - \underbrace{|\mathbf{A}_q|\, \Delta\mathbf{q}}_{\hat{\mathbf{F}}} \right] \tag{4.16}$$

with a jump in conservative variables $\Delta\mathbf{q} = \mathbf{q}^R - \mathbf{q}^L$ and the left and right primitive face values $\mathbf{u}^L$ and $\mathbf{u}^R$.

An eigenvalue analysis of the flux Jacobian $\mathbf{A}_q$ is required to determine the stabilising term $\hat{\mathbf{F}}$. It is mathematically more convenient to perform this analysis in terms of the primitive variables for the matrix

$$\mathbf{A}_u = \left(\frac{\partial \mathbf{q}}{\partial \mathbf{u}}\right)^{-1} \mathbf{A}_q \frac{\partial \mathbf{q}}{\partial \mathbf{u}} = \left(\frac{\partial \mathbf{q}}{\partial \mathbf{u}}\right)^{-1} \frac{\partial \mathbf{F}}{\partial \mathbf{u}}. \tag{4.17}$$

This yields the diagonal matrix of eigenvalues

$$\mathbf{\Lambda} = \mathbf{R}_u^{-1}\mathbf{A}_u\mathbf{R}_u = \mathbf{R}_q^{-1}\mathbf{A}_q\mathbf{R}_q = \begin{pmatrix} u & 0 & 0 & 0 \\ 0 & u+a & 0 & 0 \\ 0 & 0 & u-a & 0 \\ 0 & 0 & 0 & u \end{pmatrix} \tag{4.18}$$

and the corresponding matrix of right eigenvectors in primitive variables

$$\mathbf{R}_u = \begin{pmatrix} 1 & \frac{\rho}{2a} & -\frac{\rho}{2a} & 0 \\ 0 & \frac{1}{2} & \frac{1}{2} & 0 \\ 0 & \frac{\rho a}{2} & -\frac{\rho a}{2} & 0 \\ 0 & 0 & 0 & 1 \end{pmatrix} \tag{4.19}$$

with the isentropic speed of sound for an ideal gas given by

$$a = \sqrt{\frac{\gamma p}{\rho}}. \tag{4.20}$$

The matrix of eigenvectors in conservative variables can be obtained by

$$\mathbf{R}_q = \frac{\partial \mathbf{q}}{\partial \mathbf{u}} \mathbf{R}_u. \tag{4.21}$$

With these results, the stabilising term $\hat{\mathbf{F}}$ can be expressed in terms of a jump in characteristic variables

$$\Delta\ell = \mathbf{R}_q^{-1}\Delta\mathbf{q} = \begin{pmatrix} \Delta\rho - \frac{\Delta p}{\hat{a}^2} \\ \Delta u + \frac{\Delta p}{\hat{\rho}\hat{a}} \\ \Delta u - \frac{\Delta p}{\hat{\rho}\hat{a}} \\ \Delta\phi \end{pmatrix}. \tag{4.22}$$

The final expression

$$\hat{\mathbf{F}} = |\mathbf{A}_q|\,\Delta\mathbf{q} = \mathbf{R}_q\,|\mathbf{\Lambda}|\,\mathbf{R}_q^{-1}\Delta\mathbf{q} = \frac{\partial\mathbf{q}}{\partial\mathbf{u}}\mathbf{R}_u\,|\mathbf{\Lambda}|\,\Delta\ell \tag{4.23}$$

is used to obtain the components for the density ρ and the generic transported scalar ϕ:

$$\hat{F}_\rho = |\lambda_1|\Delta\ell_1 + \frac{\hat{\rho}}{2\hat{a}}|\lambda_2|\Delta\ell_2 - \frac{\hat{\rho}}{2\hat{a}}|\lambda_3|\Delta\ell_3 \tag{4.24}$$

$$\hat{F}_\phi = \hat{\rho}|\lambda_4|\Delta\phi + \hat{\phi}\hat{F}_\rho = \hat{F}_{\phi,\,\text{separated}} + \hat{F}_{\phi,\,\text{correction}} \tag{4.25}$$

with all quantities evaluated at the cell face $I + 1/2$. A caret denotes Roe-averaged values (Roe, 1981). The scalar value $\hat{\phi}$ is evaluated as a simple arithmetic instead of a Roe average as it was seen that the difference between the two formulations is negligible. In the case of passive scalars, which do not influence the density, considered here, there only is a coupling term in one direction, i.e. the numerical fluxes of the scalar transport equation are influenced by the numerical fluxes of the continuity equation. For a homogeneous constant value scalar, the ϕ-flux has to reduce to the ρ-flux in order to guarantee the conservation of the scalar. It can be concluded that, if the scalar transport equation is solved in a separated manner, the correction term $\hat{F}_{\phi,\,\text{correction}}$ must be added in order to obtain a conservative scheme. With only this modification compared to the uncoupled formulation, the conservation of the transported scalar is restored if the numerical fluxes of the Navier-Stokes and generic transport equations are evaluated consistently at each cell face.

The volume source terms in the turbulence transport equations are evaluated at the cell centre of cell (I, J, K). Some of these terms require derivatives of variables ϕ such as velocity, turbulent kinetic energy, etc., which are computed as central differences in computational coordinates ξ_i using the values of neighbouring cells. They are transformed to physical coordinates x_i by the metric terms $\partial\xi_i/\partial x_j$.

$$\begin{aligned}\frac{\partial\phi}{\partial x_j} = \frac{\partial\xi_i}{\partial x_j}\frac{\partial\phi}{\partial\xi_i} = \;& \left.\frac{\partial\xi_1}{\partial x_j}\right|^{I,J,K} \frac{1}{2\Delta\xi_1}\left(\phi^{I+1,J,K} - \phi^{I-1,J,K}\right) \\ &+ \left.\frac{\partial\xi_2}{\partial x_j}\right|^{I,J,K} \frac{1}{2\Delta\xi_2}\left(\phi^{I,J+1,K} - \phi^{I,J-1,K}\right) \\ &+ \left.\frac{\partial\xi_3}{\partial x_j}\right|^{I,J,K} \frac{1}{2\Delta\xi_3}\left(\phi^{I,J,K+1} - \phi^{I,J,K-1}\right)\end{aligned} \tag{4.26}$$

The velocity is evaluated in the absolute frame of reference for rotating components. The computational space is designed such that $\Delta\xi_i = 1$. If an unstructured mesh is used, these gradients are computed based on the selected method which can be Green-Gauß or Least-Squares (Becker & Ashcroft, 2014). Second velocity derivatives are computed by repeated application of the first derivative method.

4.3 Linearisation of the residual

While the general approach of the implicit pseudo-time marching algorithm was introduced in Section 4.1, the formulation of the Jacobian $\partial\mathbf{R}/\partial\mathbf{q}$ (or the linearisation) of the residual $\mathbf{R}(\mathbf{q})$ was left for this section. The RANS Equations for the conservative variables $\mathbf{q} = (\overline{\rho}, \overline{\rho}\widetilde{u}_1, \overline{\rho}\widetilde{u}_2, \overline{\rho}\widetilde{u}_3, \overline{\rho}\widetilde{E})$ are solved in a fully coupled manner resulting in a dense

Jacobian matrix. In contrast, the Jacobian matrices are scalars for the transported turbulence variables since these equations are solved separately from the RANS equations and each other. For convective and diffusive terms in the RANS equations, the residual is linearised as described in (Kügeler, 2005). Since the application of an LEVM only affects the main equations through an increased effective viscosity, the same methods can be used in this context. However, if a DRSM is employed, no turbulent viscosity appears in the RANS equations. This does not only require a modification of the solver, but can also negatively affect the stability of the scheme because of decreased diffusivity compared to a LEVM approach.

To address this stability problem, the coupling of the Reynolds stress equations to the Navier-Stokes equations is performed according to the strategy outlined by Basara (2004); Hadzić (1999) and Durbin & Pettersson Reif (2000). The residual $\mathbf{R}(\mathbf{q})$ is split into an explicitly and an implicitly treated part

$$\mathbf{R}(\mathbf{q}) = \mathbf{R}^{\mathrm{imp}}(\mathbf{q}) + \mathbf{R}^{\mathrm{exp}}(\mathbf{q}) \tag{4.27}$$

with equation (4.8) replaced by

$$\left(\frac{1}{\Delta \tau} \mathbf{1} - \left. \frac{\partial \mathbf{R}^{\mathrm{imp}}}{\partial \mathbf{q}} \right|^{m} \right) \Delta \mathbf{q}^{m} = \mathbf{R}(\mathbf{q}^{m}). \tag{4.28}$$

This is done for both the momentum and energy equations and shown here exemplarily for the momentum equations in an inertial frame of reference. The complete momentum residual in a DRSM scheme reads

$$\mathbf{R}(\overline{\rho}\widetilde{u}_i) = -\frac{\partial(\overline{\rho}\widetilde{u}_i\widetilde{u}_j)}{\partial x_j} - \frac{\partial P}{\partial x_i} + \frac{\partial}{\partial x_j}\left[2\mu S^{*}_{ij} - \overline{\rho u''_i u''_j}\right] \tag{4.29}$$

with no eddy viscosity μ_T. The implicitly treated part

$$\mathbf{R}^{\mathrm{imp}}(\overline{\rho}\widetilde{u}_i) = -\frac{\partial(\overline{\rho}\widetilde{u}_i\widetilde{u}_j)}{\partial x_j} - \frac{\partial P}{\partial x_i} + \frac{\partial}{\partial x_j}\left[2(\mu + \mu_T) S^{*}_{ij}\right], \tag{4.30}$$

however, is chosen to be equivalent to that used in an LEVM scheme with the eddy viscosity μ_T determined from the DRSM. This increased viscosity on the left hand side (LHS) is the key to the stabilization of the scheme. When the solution reaches convergence, the update $\Delta \mathbf{q}$ vanishes. Hence, there will be no effect of this approach on the accuracy of a converged solution. In summary, to implement a DRSM scheme in the existing RANS solver, only the right hand side of the equations was modified compared to an LEVM scheme. There, the Boussinesq approximation is replaced by the Reynolds stresses obtained from the DRSM.

The linearisation of the different source terms of the Reynolds stress equations is another crucial factor for stability of the solution method. It has been developed within this work and parts of the following have already been published by the present author (Morsbach *et al.*, 2015*a*). Since no coupling between the Reynolds stress equations is considered, only derivatives of the source term component by the respective Reynolds stress component have to be calculated, i.e.

$$\frac{\partial R_{\alpha\beta}}{\partial \overline{\rho u''_\gamma u''_\delta}} = 0 \quad \text{if}\, \alpha \neq \gamma,\ \beta \neq \delta. \tag{4.31}$$

For the production term $\overline{\rho}P_{ij}$ given by equation (3.26) the derivatives are straightforward

$$\frac{\partial\left(\overline{\rho}P_{\alpha\beta}\right)}{\partial\left(\overline{\rho u''_\alpha u''_\beta}\right)} = -(S_{\alpha\alpha} + S_{\beta\beta}). \tag{4.32}$$

No summation is implied over Greek indices. For the rotation term $\frac{1}{2}\overline{\rho}R_{ij}$ all derivatives vanish.

The following derivatives are based on the general formulation of the modelled terms. All derivatives are obtained with $\epsilon^h = C_\mu k \omega^h$ substituted into the models. Simplifications are allowed because, as argued above, the LHS has no effect on the converged solution, only on stability. Both the isotropic and anisotropic parts of the dissipation model $\overline{\rho}\epsilon_{ij}$ (3.51) are linearised

$$\frac{\partial\left(\overline{\rho}\epsilon_{\alpha\beta}\right)}{\partial\left(\overline{\rho u''_\alpha u''_\beta}\right)} = \frac{1}{3}C_\mu\omega^h\delta_{\alpha\beta} + f_s C_\mu\omega^h\left(1-\frac{1}{3}\delta_{\alpha\beta}\right) \tag{4.33}$$

with $f_s = 0$ in case of the SSG/LRR-ω model.

The non-linear terms in the pressure strain models $\overline{\rho}\Pi_{ij,1}$ (3.46) and $\overline{\rho}\Pi_{ij,2}$ (3.48) complicate the derivatives. They can appear in the model itself as tensor products or in the coefficient functions hidden in anisotropy invariants. As a major simplification, all coefficient functions were held constant in the following derivatives. For the slow pressure-strain term $\overline{\rho}\Pi_{ij,1}$, $\mu_T = \overline{\rho}k/\omega$ was held constant in the derivative to simplify the resulting expressions

$$\begin{aligned}\frac{\partial\left(\overline{\rho}\Pi_{\alpha\beta,1}\right)}{\partial\left(\overline{\rho u''_\alpha u''_\beta}\right)} &= -C_\mu C_1\left(1-\frac{1}{3}\delta_{\alpha\beta}\right) \\ &\quad +\frac{2}{3}C_\mu C_1'\frac{\omega}{k}\left[2k-\frac{3}{2}\left(\widetilde{u''_\alpha u''_\alpha}+\widetilde{u''_\beta u''_\beta}\right)\right]\left(1-\frac{2}{3}\delta_{\alpha\beta}\right).\end{aligned} \tag{4.34}$$

The most complex expression was obtained for the Jacobian of the rapid pressure-strain term $\overline{\rho}\Pi_{ij,2}$

$$\begin{aligned}\frac{\partial\left(\overline{\rho}\Pi_{\alpha\beta,2}\right)}{\partial\left(\overline{\rho u''_\alpha u''_\beta}\right)} &= \frac{1}{2}C_3 S_{\alpha\beta}\delta_{\alpha\beta} + C_4\left[S_{\alpha\alpha}+S_{\beta\beta}-\frac{2}{3}\left(2S_{\alpha\beta}-\frac{1}{3}S_{qq}\right)\delta_{\alpha\beta}\right] \\ &\quad -\frac{C_2'}{k}\left[P_k-4\widetilde{u''_\alpha u''_\beta}S_{\alpha\beta}+\left(2k+\widetilde{u''_\alpha u''_\beta}\right)S_{\alpha\beta}\delta_{\alpha\beta}\right]\left(1-\frac{1}{3}\delta_{\alpha\beta}\right).\end{aligned} \tag{4.35}$$

Here, in the term including P_k, numerator and denominator were multiplied by k while k in the denominator was held constant in the derivative.

According to Wilcox (2006), only negative source terms are linearised while positive source terms are treated explicitly. This decision is evaluated on a cell-by-cell basis depending on the local value of the source term Jacobian. The increased diagonal dominance of the LHS matrix leads to a more stable scheme. Especially the linearisation of the slow pressure-strain term has proven to be a crucial factor for stability.

In contrast to LEVMs, the production term of turbulent kinetic energy P_k can become negative in a DRSM. Hence, not only the destruction term but also the production term in the ω^h equation need to be linearised. Furthermore, the linearisations of the cross diffusion term as well as the $P^i_{\epsilon 3}$ term can be negative due to the occurrence of ω^h in the denominator. The linearisation of these three terms denoted by $R^{\mathrm{imp}}(\overline{\rho}\omega^h)$ yields:

$$\frac{\partial\left(R^{\mathrm{imp}}(\overline{\rho}\omega^h)\right)}{\partial(\overline{\rho}\omega^h)} = \frac{\alpha}{k}P_k - 2\beta k\omega^h - \frac{2\sigma_d}{(\omega^h)^2}\frac{\partial k}{\partial x_i}\frac{\partial \omega^h}{\partial x_i} - \frac{1}{\overline{\rho}\omega^h}P^i_{\epsilon 3}. \tag{4.36}$$

The eddy viscosity defined as $\mu_T = \overline{\rho}k/\omega^h$ was used to derive the Jacobians. Since only negative contributions to the Jacobian are considered, the linearisation of the cross diffusion term is the same for limited and unlimited cross derivatives (see Section 3.3).

4.4 Boundary conditions for turbulent flows

In this section, boundary conditions which are specific to DRSMs are discussed. In addition to the model specific boundary condition for the turbulent dissipation rate at the wall, both DRSMs share the boundary treatment for solid walls, inlet boundaries, mixing planes, rotationally periodic boundaries and symmetry planes.

4.4.1 Solid walls

The solid wall boundary condition for the Reynolds stress tensor is the most trivial: If the mesh resolves the viscous sublayer, all components vanish

$$\widetilde{u_i''u_j''} = 0 \tag{4.37}$$

because of the no slip condition for all DRSMs.

The boundary equation for the scale-determining variable, however, is specific to each individual model. The SSG/LRR-ω model employs Menter's ω-boundary condition (Menter, 1992) in the same form as most k-ω models do. The dissipation rate at the wall is computed as

$$\omega|_w = 10 \frac{6\mu}{\beta_\omega \bar{\rho} y_1^2} \tag{4.38}$$

with the distance y_1 of the first cell centre from the wall. Since wall values cannot be directly set in the cell centred scheme (see Section 4.1), the value of the ghost cell is determined by linear extrapolation to ensure the correct wall value.

The boundary condition for the ϵ^h-equation is treated differently from the SSG/LRR-ω model. It is based on the Taylor microscale λ (Jakirlić & Jovanović, 2010), which is used to derive the following formulation for ϵ^h for the first cell away from the wall and its known gradient at the wall:

$$\epsilon^h\Big|_{\text{first cell}} = \frac{\nu k}{y_1^2}, \quad \frac{\partial \epsilon^h}{\partial \mathbf{n}}\bigg|_w = 0. \tag{4.39}$$

The corresponding solid wall boundary condition for ω^h is given by

$$\omega^h\Big|_{\text{first cell}} = \frac{\mu}{C_\mu \bar{\rho} y_1^2}, \quad \frac{\partial \omega^h}{\partial \mathbf{n}}\bigg|_w = 0. \tag{4.40}$$

Here, the gradient is also set to zero which is physically incorrect; however, since ω^h is fixed in the first cell, this choice has no influence as long as the diffusion of ω^h is computed using only directly neighbouring cells.

4.4.2 Rotationally periodic boundaries

As rotating machinery often exhibits rotational symmetry it is desirable for reasons of computational efficiency to simulate the flow through as few blade passages as possible. Periodic boundary conditions are employed in this case as schematically shown in Figure 4.2. For scalar quantities, no additional treatment is required. Tensor quantities, however, require a base transformation between the corresponding boundary panels.

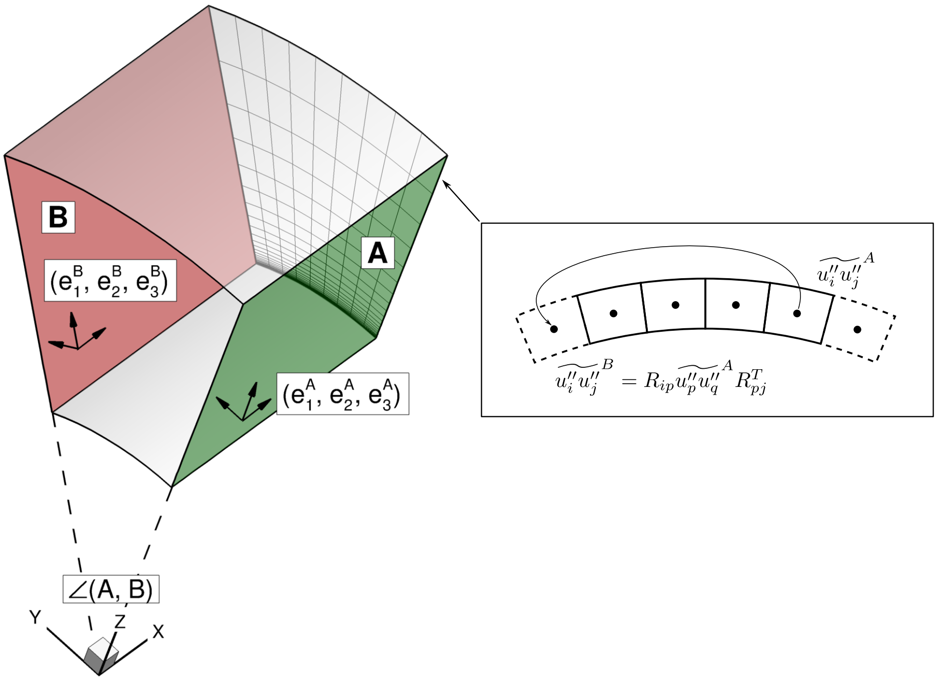
B
(e1B, e2B, e3B)
A
(e1A, e2A, e3A)
∠(A, B)
Y
Z
X
$\widetilde{u_i''u_j''}^A$
$\widetilde{u_i''u_j''}^B = R_{ip}\widetilde{u_p''u_q''}^A R^T_{pj}$

Figure 4.2: Schematic of rotationally periodic boundary. Flow state in ghost cell is the state in the corresponding inner cell rotated about x-axis by angle $\angle(A, B)$.

For solution variables, this applies to the velocity vector and the Reynolds stress tensor. The transformation matrix $\mathbf{R}$ with the following property

$$\mathbf{R}^{-1}\mathbf{R} = \mathbf{R}^T\mathbf{R} = \mathbf{1} \tag{4.41}$$

is defined by rotation axis and angle. It can also be interpreted the transformation matrix

$$\mathbf{R}^{A\to B} = \begin{pmatrix} \mathbf{e}_1^B\cdot\mathbf{e}_1^A & \mathbf{e}_1^B\cdot\mathbf{e}_2^A & \mathbf{e}_1^B\cdot\mathbf{e}_3^A \\ \mathbf{e}_2^B\cdot\mathbf{e}_1^A & \mathbf{e}_2^B\cdot\mathbf{e}_2^A & \mathbf{e}_2^B\cdot\mathbf{e}_3^A \\ \mathbf{e}_3^B\cdot\mathbf{e}_1^A & \mathbf{e}_3^B\cdot\mathbf{e}_2^A & \mathbf{e}_3^B\cdot\mathbf{e}_3^A \end{pmatrix} \tag{4.42}$$

between bases $(\mathbf{e}_1^A, \mathbf{e}_2^A, \mathbf{e}_3^A)$ and $(\mathbf{e}_1^B, \mathbf{e}_2^B, \mathbf{e}_3^B)$ corresponding to panels A and B.

In a cell centred code, ghost cells, drawn with dashed lines in Figure 4.2, are used to ensure appropriate boundary values. At the periodic boundary, the value in the ghost cell is computed from the value in the corresponding inner cell using the transformation described above. While the velocity vector transforms as

$$\widetilde{u}_i^B = R_{ij}^{A\to B}\widetilde{u}_j^A \tag{4.43}$$

the Reynolds stress tensor transforms as

$$\widetilde{u_i''u_j''}^B = R_{ip}^{A\to B}\widetilde{u_p''u_q''}^A \left(R^{A\to B}\right)_{qj}^T . \tag{4.44}$$

4.4.3 Mixing planes

At the interface between rotating and non-rotating components, a circumferentially mixed-out state is usually exchanged between adjacent blocks in steady simulations

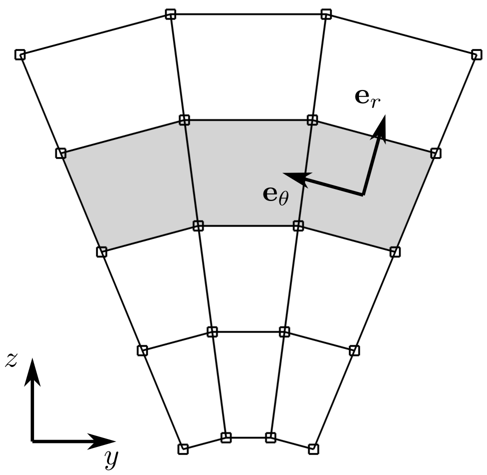

Figure 4.3: Schematic of mixing plane boundary at x = const. Reynolds stresses are averaged cylindrical coordinate system.

(Denton, 1992). This so-called mixing plane approach is schematically shown in Figure 4.3. The mixed-out state is obtained by a circumferential average, which needs to be performed in a cylindrical coordinate system at defined radial positions called bands (shaded in grey). In structured meshes these are simply given by constant radial face index.

The cylindrical coordinate system used in TRACE is given by the base $(\mathbf{e}_x, \mathbf{e}_r, \mathbf{e}_\theta)$ with

$$\mathbf{e}_\theta = -\sin\theta \cdot \mathbf{e}_y + \cos\theta \cdot \mathbf{e}_z \tag{4.45}$$

$$\mathbf{e}_r = \cos\theta \cdot \mathbf{e}_y + \sin\theta \cdot \mathbf{e}_z \tag{4.46}$$

yielding the transformation matrix from $(\mathbf{e}_x, \mathbf{e}_y, \mathbf{e}_z)$ to $(\mathbf{e}_x, \mathbf{e}_r, \mathbf{e}_\theta)$

$$\mathbf{R}^{xyz\to xr\theta} = \begin{pmatrix} 1 & 0 & 0 \\ 0 & \cos\theta & \sin\theta \\ 0 & -\sin\theta & \cos\theta \end{pmatrix} \tag{4.47}$$

according to (4.42). The basis vectors are sketched in Figure 4.3. With this base transformation, the procedure at a mixing plane is as follows: The Reynolds stresses are transformed to the cylindrical coordinate system and an area average is performed for each radial band. The averaged values are communicated to the downstream row and transformed back to Cartesian coordinates for each individual face of the corresponding band.

4.4.4 Inflow

There are a number of ways to specify turbulence quantities at inlet boundaries. Traditionally, when LEVMs are used, both turbulence intensity Tu and turbulent length scale L_T are specified. Without additional information on turbulence anisotropy, a reasonable assumption in a DRSM framework is isotropic turbulence. Given the velocity magnitude U at the inlet, the Reynolds stress tensor is given by

$$\widetilde{u_i''u_j''} = \frac{2}{3}k\delta_{ij}, \quad \text{with} \quad k = \frac{3}{2}Tu^2U^2. \tag{4.48}$$

The specific turbulent dissipation rate ω or its homogeneous counterpart ω^h can then be computed by

$$\omega = \omega^h = \frac{\sqrt{k}}{L_T}. \tag{4.49}$$

Alternatively, the turbulent kinetic energy and dissipation rate can be specified directly resulting also in isotropic turbulence at the inlet. The third option is to specify components of the Reynolds stress tensor and the dissipation rate directly. For rotationally symmetric cases, this needs to be done in cylindrical coordinates. For translational cases, on the other hand, Cartesian components are used.

4.4.5 Symmetry plane

At a symmetry plane boundary condition, the Reynolds stress tensor is transformed from the Cartesian basis $(\mathbf{e}_x, \mathbf{e}_y, \mathbf{e}_z)$ to a basis of two tangential vectors and the face normal vector $(\mathbf{e}_{t1}, \mathbf{e}_{t2}, \mathbf{e}_n)$ by the transformation matrix

$$\mathbf{R}^{xyz \to t_1 t_2 n} = \begin{pmatrix} \mathbf{e}_{t1} \cdot \mathbf{e}_x & \mathbf{e}_{t1} \cdot \mathbf{e}_y & \mathbf{e}_{t1} \cdot \mathbf{e}_z \\ \mathbf{e}_{t2} \cdot \mathbf{e}_x & \mathbf{e}_{t2} \cdot \mathbf{e}_y & \mathbf{e}_{t2} \cdot \mathbf{e}_z \\ \mathbf{e}_n \cdot \mathbf{e}_x & \mathbf{e}_n \cdot \mathbf{e}_y & \mathbf{e}_n \cdot \mathbf{e}_z \end{pmatrix}. \tag{4.50}$$

The basis vectors on the opposite side of the symmetry plane $\mathbf{e}'_i$ are given in terms of the basis vectors on the inner side $\mathbf{e}_i$ by (cf. Durbin & Pettersson Reif, 2000)

$$\mathbf{e}'_{t1} = \mathbf{e}_{t1}, \quad \mathbf{e}'_{t2} = \mathbf{e}_{t2}, \quad \text{and} \quad \mathbf{e}'_n = -\mathbf{e}_n. \tag{4.51}$$

This results in a zero gradient condition for all diagonal components and the correlation involving only tangential velocities. The Reynolds stress components which correlate tangential and normal velocity fluctuations go to zero at the symmetry plane.

4.5 Numerical performance

Since DRSMs solve 5 additional equations compared to LEVMs and since these equations employ more sophisticated source terms, it is interesting to quantify the additional computational effort required to obtain a solution. This effort is, on the one hand, determined by the CPU time per iteration and, on the other hand, by the number of iterations required for convergence. While the former scales simply with problem size, the latter can vary greatly for different cases.

The performance of the models used in this thesis will be evaluated using the simple test case of a duct segment of 90 degrees with two blocks of 10584 cells. The case features rotationally periodic boundaries and a mixing plane between the blocks to account for increased effort at boundaries where stresses have to be rotated. About 4% of the cells are located at the mixing plane and 22% of the cells are located at the periodic boundaries. Each block is computed on a single process and the wall clock time per time step is reported by the solver.

For analysis, the median out of 10^5 time steps is used because the average is influenced by spikes. It should be interpreted as an upper bound for the additional computational effort needed for DRSMs because the implementation has not yet been optimised for

Table 4.1: Iterative convergence of turbulence models for duct segment testcase.

Model	$n_{\text{steps}}/n_{\text{ref}}$	$t_{\text{step}}/t_{\text{ref}}$
Menter SST k-ω	1.000	1.00
Hellsten EARSM k-ω	0.992	1.09
SSG/LRR-ω	0.986	1.36
JH-ω^h	1.027	1.49

performance. The number of time steps required for convergence is determined by the first time the residual falls below a threshold close to machine zero for double precision.

The results are summarised in Table 4.1. The number of time steps n_{steps} and time per iteration t_{step} are normalised to the value obtained for the Menter SST k-ω model. In this case, the number of time steps is practically insensitive to the type of model. However, in more complex situations, more sophisticated models tend to require more time steps for iterative convergence. The additional algebraic equations introduced by the Hellsten EARSM k-ω model increase the effort by about 9%. Compared to that, the solution of 5 additional transport equations for DRSMs scales rather well. While the SSG/LRR-ω model requires 36% more CPU time, the JH-ω^h model requires 49% due to the various non-linear functions used in the source terms.

5 Model validation in generic flows

In this chapter, five building block flows with increasing complexity will be analysed in great detail. The simulation results will be compared to experimental and DNS data. As a reference models, the Menter SST k-ω LEVM (see Section A.1) and the Hellsten EARSM k-ω (see Section A.2) will be used. Finally, differences between the DRSMs will be analysed. No residual plots will be shown, since it could be ensured that the computations in this chapter converged to machine zero. If not mentioned otherwise, all 2D computations in this chapter were performed as 3D computations using one cell in spanwise direction with symmetry boundary conditions.

5.1 Channel flow

Since all flows in turbomachinery are wall-bounded, the correct prediction of turbulent boundary layers is essential for a successful evaluation of the configuration. The simplest version of a turbulent boundary layer is the fully developed turbulent flow through a plane channel as sketched in Figure 5.1. The flow is confined by two infinitely stretched parallel planes and, therefore, homogeneous in the streamwise direction x and the spanwise direction z. Variations in the flow variables only occur along the wall-normal direction y. A constant pressure gradient $\partial P/\partial x$ is applied to balance the skin friction. Periodic boundary conditions are set up in the streamwise direction while symmetry is enforced in the spanwise direction. The characteristic Reynolds number for this flow

$$Re_\tau = \frac{\rho_0 u_\tau \delta}{\mu_0} \tag{5.1}$$

is based on the friction velocity u_τ (introduced below) and the channel half-width δ. To simulate the incompressible flow using a compressible solver without a low-Mach preconditioning, it is scaled to an essentially incompressible Mach number of about 0.3 while preserving the Reynolds number Re_τ. This is achieved by adapting the channel

Table 5.1: Test case setup and DNS data sources for turbulent plane channel flow.

Re_τ	δ [mm]	$\partial P/\partial x$ [Pa/m]	DNS data source
180	1.5	8320	Kim *et al.* (1987)
395	3.0	4915	Iwamoto *et al.* (2002)
590	6.0	1408	Moser *et al.* (1999)
2003	16.5	747	Hoyas & Jimenez (2006)

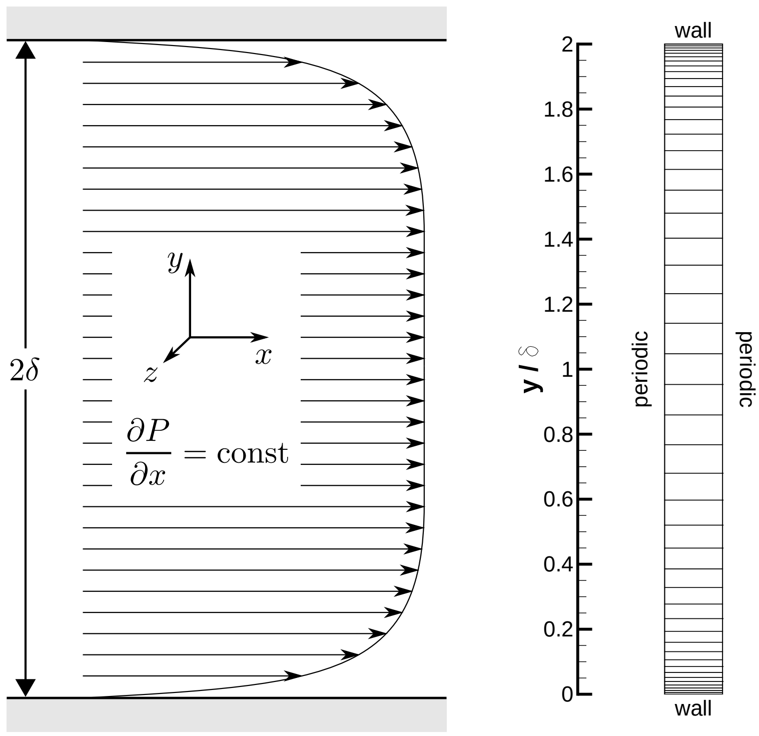
2δ
y
x
z
∂P/∂x = const
y / δ
0
0.2
0.4
0.6
0.8
1
1.2
1.4
1.6
1.8
2
wall
wall
periodic
periodic

Figure 5.1: Sketch of fully developed turbulent flow through a plane channel (*left*) and mesh with 48 nodes in y-direction and boundary conditions (*right*).

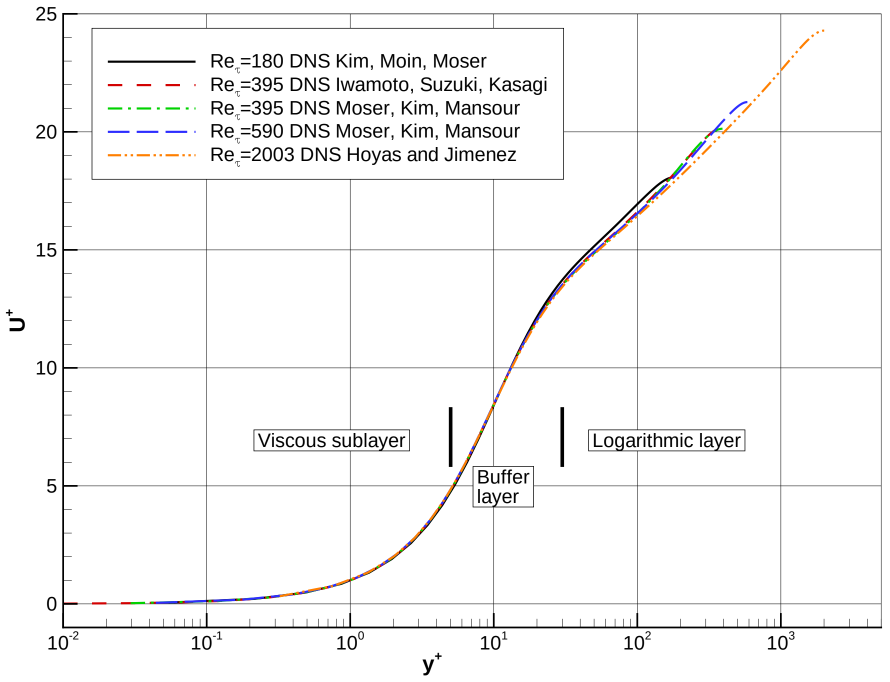

Figure 5.2: Normalised boundary layer velocity profile computed by DNS for fully developed turbulent flow through a plane channel.

half-width δ and the pressure gradient $\partial P/\partial x$. Table 5.1 summarises the setup for the investigated Reynolds numbers.

The case offers a number of advantages over the zero pressure gradient flat plate flow. First, there exists a wide range of DNS data readily available for validation of turbulence models. They offer not only velocity and Reynolds stress profiles but also data on Reynolds stress budgets. Table 5.1 summarises the data used in this work. Although the computations have been performed by independent authors, Figure 5.2 shows that all velocity profiles collapse to the logarithmic law of the wall as expected. Furthermore, this test case is physically simpler since it does not cover the development of the boundary layer. It reduces to an essentially one dimensional problem. Finally, because of that, only a number of the order of 100 cells are required and allow for very fast computation. This makes the test case ideal for model development and calibration.

In a one dimensional boundary layer, the momentum budget is determined by the single Reynolds shear stress $\overline{\rho u_x'' u_y''}$. If the turbulence model adequately predicts the profile of $\overline{\rho u_x'' u_y''}$, the velocity profile will be computed correctly. Here, the Reynolds shear stress is, in fact, proportional to the mean strain rate. This explains why LEVMs can be used to predict boundary layer flows successfully even though they do not incorporate the production and redistribution mechanisms of the normal Reynolds stress tensor components. A closer look at DNS data of turbulent plane channel flow, however, reveals anisotropic normal stresses. Since $\overline{\rho u_x'' u_x''}$ is, as $\overline{\rho u_x'' u_y''}$, directly produced by the mean velocity gradient $\partial U/\partial y$, this stress component dominates the turbulence energy with a peak close to the wall that becomes more defined as the Reynolds number increases. The remaining normal stresses $\overline{\rho u_y'' u_y''}$ and $\overline{\rho u_z'' u_z''}$ are fed by pressure-strain redistribution. Due to the blocking effect of the solid wall, velocity fluctuations normal to the wall are damped stronger than those parallel to the wall. This results in the order $\overline{\rho u_x'' u_x''}$, $\overline{\rho u_z'' u_z''}$, $\overline{\rho u_y'' u_y''}$ by decreasing value. Even though LEVMs suffice to produce an adequate description of the velocity profile in a simple turbulent boundary layer, it is desirable to also be able to predict the normal stresses correctly. They contribute to the turbulence production term and are responsible for the sensitivity of the turbulence model to extra strain rates.

The boundary layer is analysed using wall units obtained by normalisation with the friction velocity u_τ

$$U^+ = \frac{U}{u_\tau}, \quad y^+ = \frac{\overline{\rho} u_\tau}{\mu} y \quad \text{with} \quad u_\tau = \sqrt{\frac{\tau_w}{\overline{\rho}}}, \quad \tau_w = \mu \frac{\partial U}{\partial y}\bigg|_{y=0} . \tag{5.2}$$

For each turbulence model, a mesh convergence study including three subsequently refined meshes with y^+ values ranging from 1 (48 nodes) down to 0.25 (192 nodes) has been performed. The coarsest mesh is shown in Figure 5.1. All models employing Menter's ω-boundary condition (4.38) show a significant dependence of the non-dimensional velocity profile on the mesh. This is not the case, however, for the JH-ω^h model which sets the specific turbulent dissipation rate in the first cell according to the Taylor microscale λ. The velocity profiles for all meshes for the SSG/LRR-ω as a representative of models using Menter's boundary condition and the JH-ω^h are shown in Figure 5.3. For the latter, the lines for all meshes coincide. In the following only results for the finest mesh are presented.

Figure 5.4 (*top*) shows the normalised boundary layer velocity profile. The curves for $Re_\tau = 395$ and $Re_\tau = 2003$ are shifted in y-direction by 5 and 10 units, respectively. All ω-based turbulence models are able to reproduce the characteristic boundary layer velocity profile to a reasonable degree of accuracy. Both the Menter SST k-ω and the

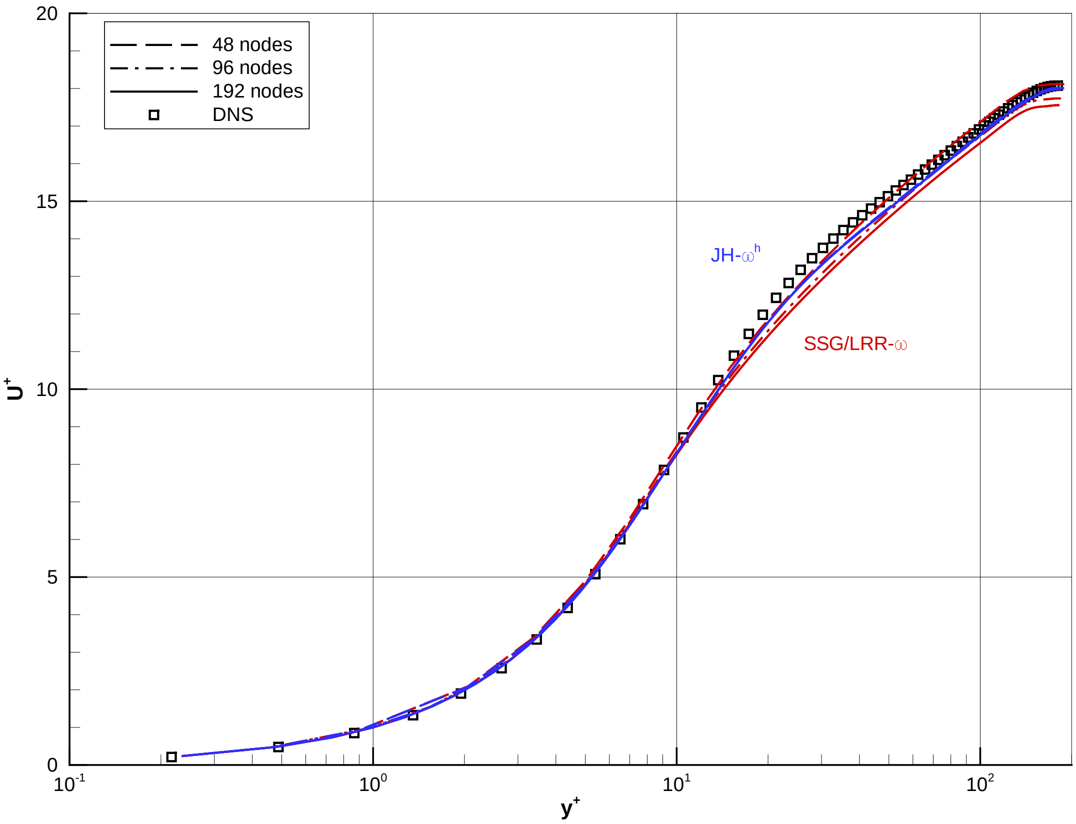

Figure 5.3: Mesh dependence of SSG/LRR-ω and JH-ω^h model in turbulent plane channel flow. The meshes have 48, 96 and 192 nodes in wall-normal direction.

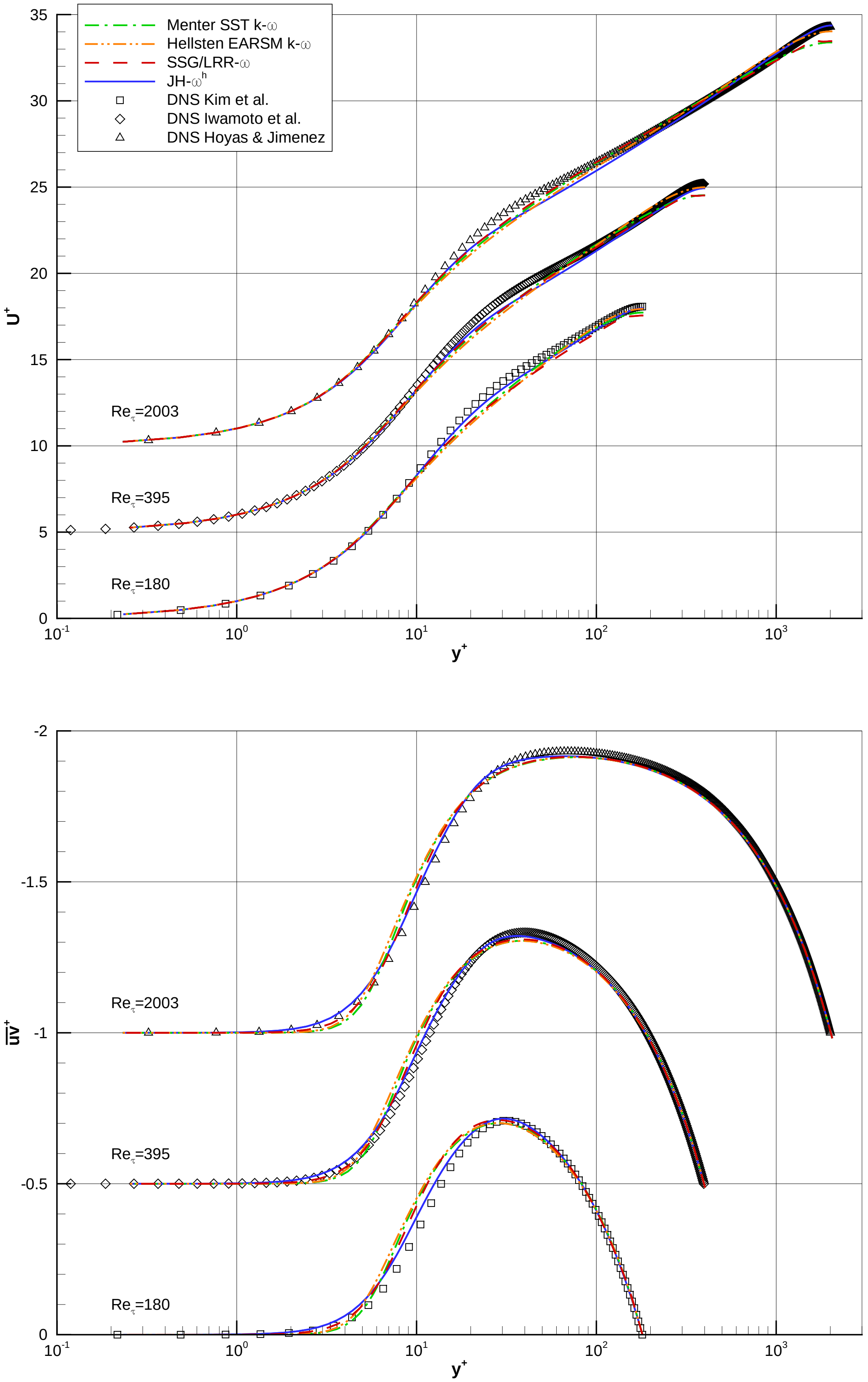

Figure 5.4: Comparison of Menter SST k-ω, Hellsten EARSM k-ω, SSG/LRR-ω and JH-ω^h results for turbulent plane channel flow at $Re_\tau = 180$ (Kim *et al.*, 1987), $Re_\tau = 395$ (Iwamoto *et al.*, 2002) (offset U^+ by 5, $\overline{uv}^+$ by 0.5) and $Re_\tau = 2003$ (Hoyas & Jimenez, 2006) (offset U^+ by 10, $\overline{uv}^+$ by 1): Normalised velocity U^+ (*top*) and Reynolds shear stress $\overline{uv}^+$ (*bottom*).

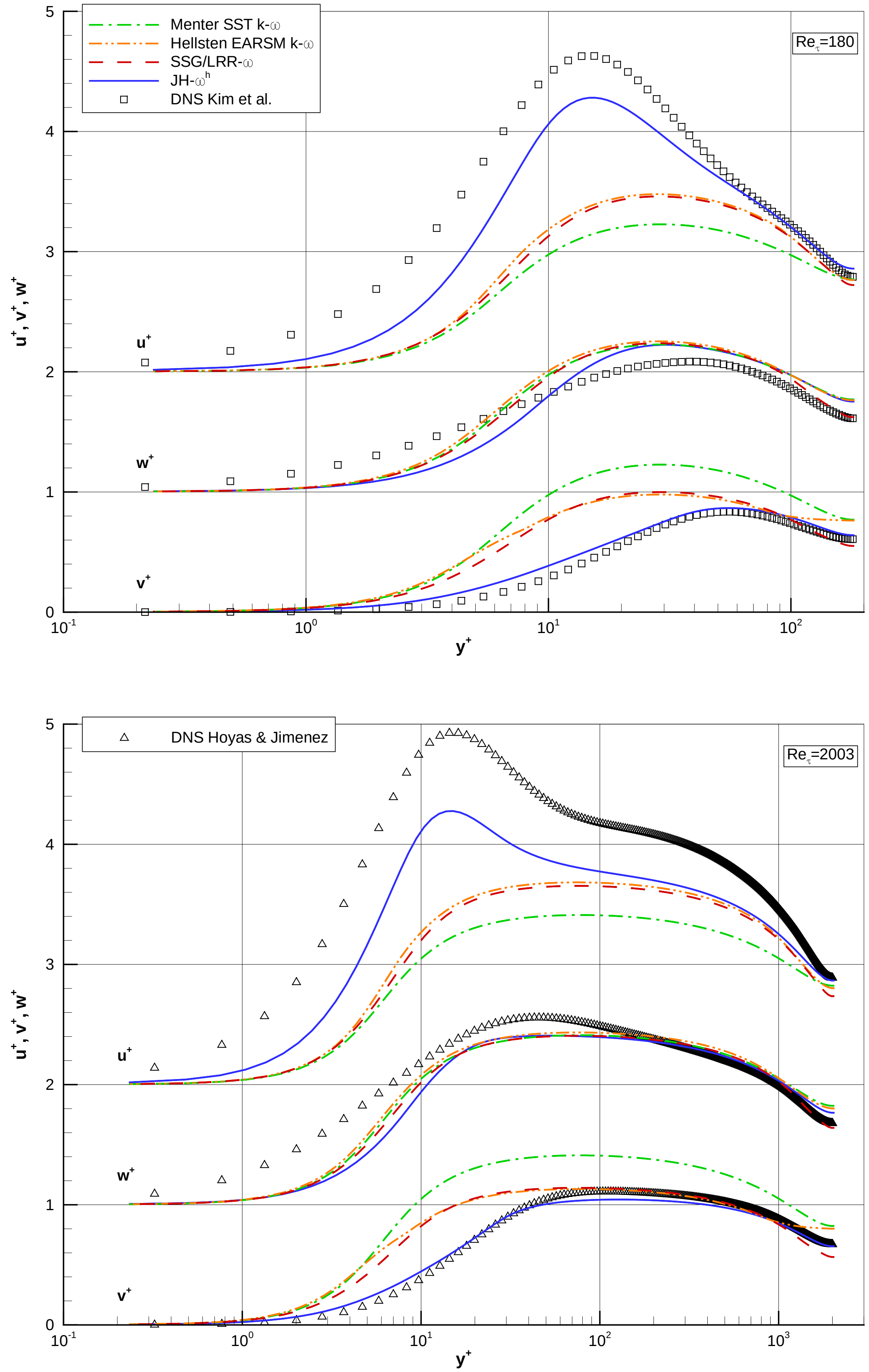

Figure 5.5: Comparison of Menter SST k-ω, Hellsten EARSM k-ω, SSG/LRR-ω and JH-ω^h results for turbulent plane channel flow: Normalised velocity fluctuations u^+ (offset by 2), v^+ and w^+ (offset by 1) for $Re_\tau = 180$ (Kim *et al.*, 1987) (*top*) and $Re_\tau = 2003$ (Hoyas & Jimenez, 2006) (*bottom*).

SSG/LRR-ω model underpredict the mean velocity U^+ in the centre of the channel. Both models also agree on the slope in the logarithmic part of the boundary layer ($y^+ > 30$) and follow the same profile down to the wall. This can partly be attributed to the ω-equation they share. In contrast, the centre line velocity is well predicted by the Hellsten EARSM k-ω and the JH-ω^h model. While the slope of the velocity profile in the logarithmic layer is slightly overpredicted by Hellsten's model, the JH-ω^h model results closely follow the profile of DNS data for all Reynolds numbers. All models underpredict the velocity in the buffer region between the logarithmic and the viscous sublayer ($5 < y^+ < 30$). Here, the JH-ω^h model shows the closest agreement. This behaviour is reflected in the normalised shear stress

$$\overline{uv}^+ = \frac{\widetilde{u''_x u''_y}}{u_\tau^2} \tag{5.3}$$

as shown in Figure 5.4 (*bottom*). The curves for $Re_\tau = 395$ and $Re_\tau = 2003$ are shifted in y-direction by 0.5 and 1 units, respectively.

The normalised root mean square fluctuating velocities given by

$$u^+ = \frac{\sqrt{\widetilde{u''_x u''_x}}}{u_\tau}, \quad v^+ = \frac{\sqrt{\widetilde{u''_y u''_y}}}{u_\tau}, \quad w^+ = \frac{\sqrt{\widetilde{u''_z u''_z}}}{u_\tau} \tag{5.4}$$

are shown for in Figure 5.5 for $Re_\tau = 180$ (*top*) and $Re_\tau = 2003$ (*bottom*). For reasons of clarity, u^+ is shifted by 2 and w^+ is shifted by 1 units in y-direction of the plot. This plot clearly reveals the differences between the types of models and also between the different DRSMs. Since the Menter SST k-ω model is based on the Boussinesq assumption, it is not able to reproduce the normal stress anisotropy that can be seen in the DNS data. The Hellsten EARSM k-ω and the SSG/LRR-ω model show very similar results. This can be attributed to the fact that Hellsten's model has been derived from the LRR pressure-strain model which is active in the SSG/LRR-ω model in turbulent channel flow. Both models predict increased streamwise and decreased wall-normal velocity fluctuations, respectively. Although this is correct in principle, two important qualitative features are not reproduced. First, there is the peak in the streamwise velocity fluctuation at $y^+ \sim 20$ which becomes more pronounced with increasing Reynolds number. Second, the wall-normal velocity fluctuations decrease much faster towards the wall than the respective wall-parallel components. Both features can be found in the results obtained with JH-ω^h model. While the peak in u^+ is reproduced only qualitatively, excellent quantitative agreement between the model predictions and the DNS data is achieved for v^+. Significant additional modelling effort was necessary compared to the SSG/LRR-ω model to produce this behaviour close to the wall. A feature that both DRSMs miss is the fact that both w^+ and v^+ take the same value on the centre line as predicted by the DNS.

Figures 5.6 and 5.7 compare the different versions of the JH model. For the velocity profile (Figure 5.6, *top*), the solution computed with the JH-ϵ^h model shows a strong dependency on the Reynolds number. While the model is calibrated very well for the low-Reynolds-number case $Re_\tau = 180$, the normalised velocity outside the viscous sublayer is significantly underestimated for the higher Reynolds numbers. This can be attributed to an overestimation of friction velocity due to overestimation of shear stress in the immediate wall vicinity (Figure 5.6, *bottom*). Maduta's version of the JH-ω^h model consistently underestimates the normalised velocity in the logarithmic layer and the shear stress close to the wall independent of Reynolds number. Further differences between the model versions can be found in the Reynolds normal stresses. It

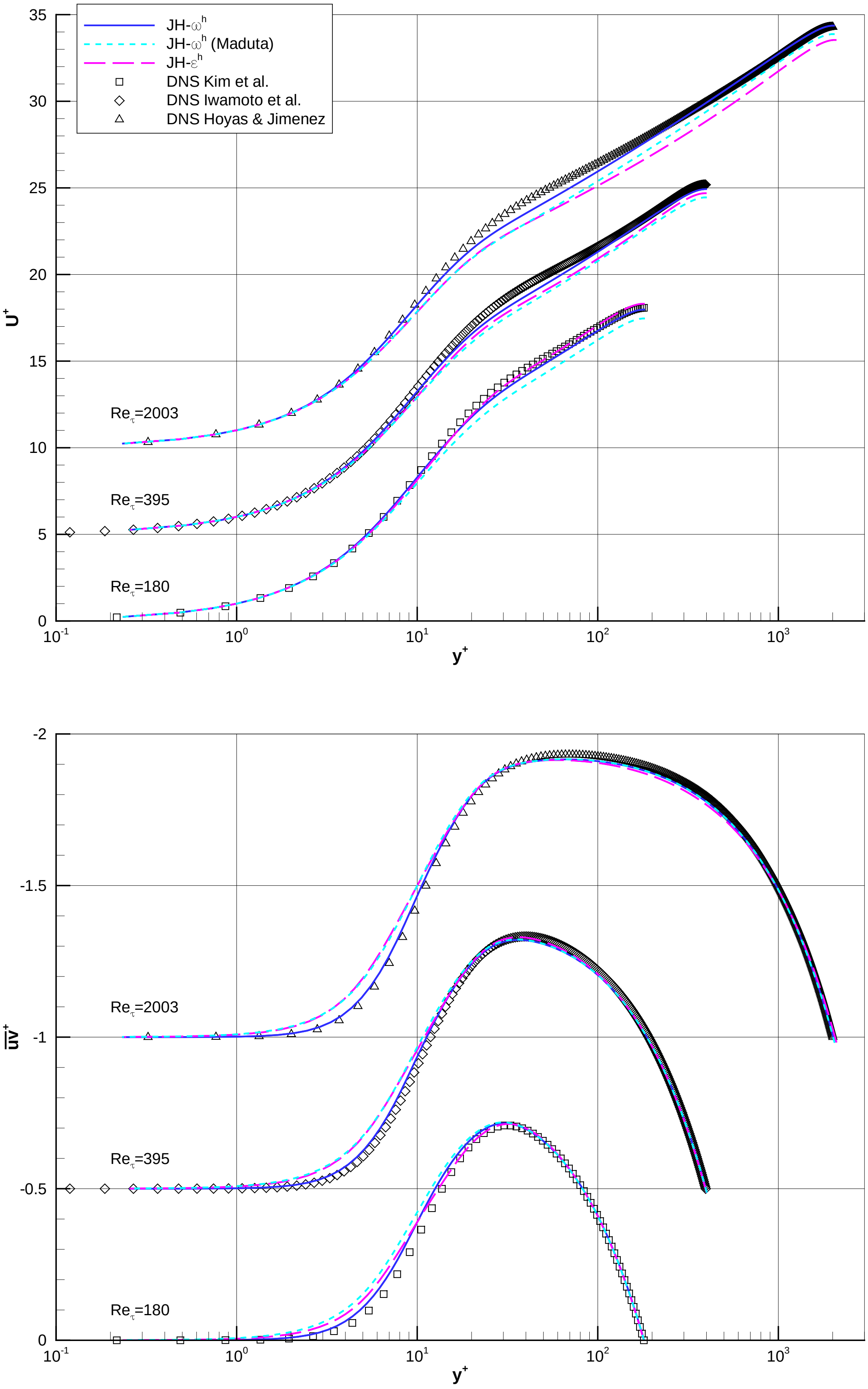

Figure 5.6: Comparison of JH-ω^h, JH-ω^h (Maduta) and JH-ϵ^h results for turbulent plane channel flow at $Re_\tau = 180$ (Kim *et al.*, 1987), $Re_\tau = 395$ (Iwamoto *et al.*, 2002) (offset U^+ by 5, $\overline{uv}^+$ by 0.5) and $Re_\tau = 2003$ (Hoyas & Jimenez, 2006) (offset U^+ by 10, $\overline{uv}^+$ by 1): Normalised velocity U^+ (*top*) and Reynolds shear stress $\overline{uv}^+$ (*bottom*).

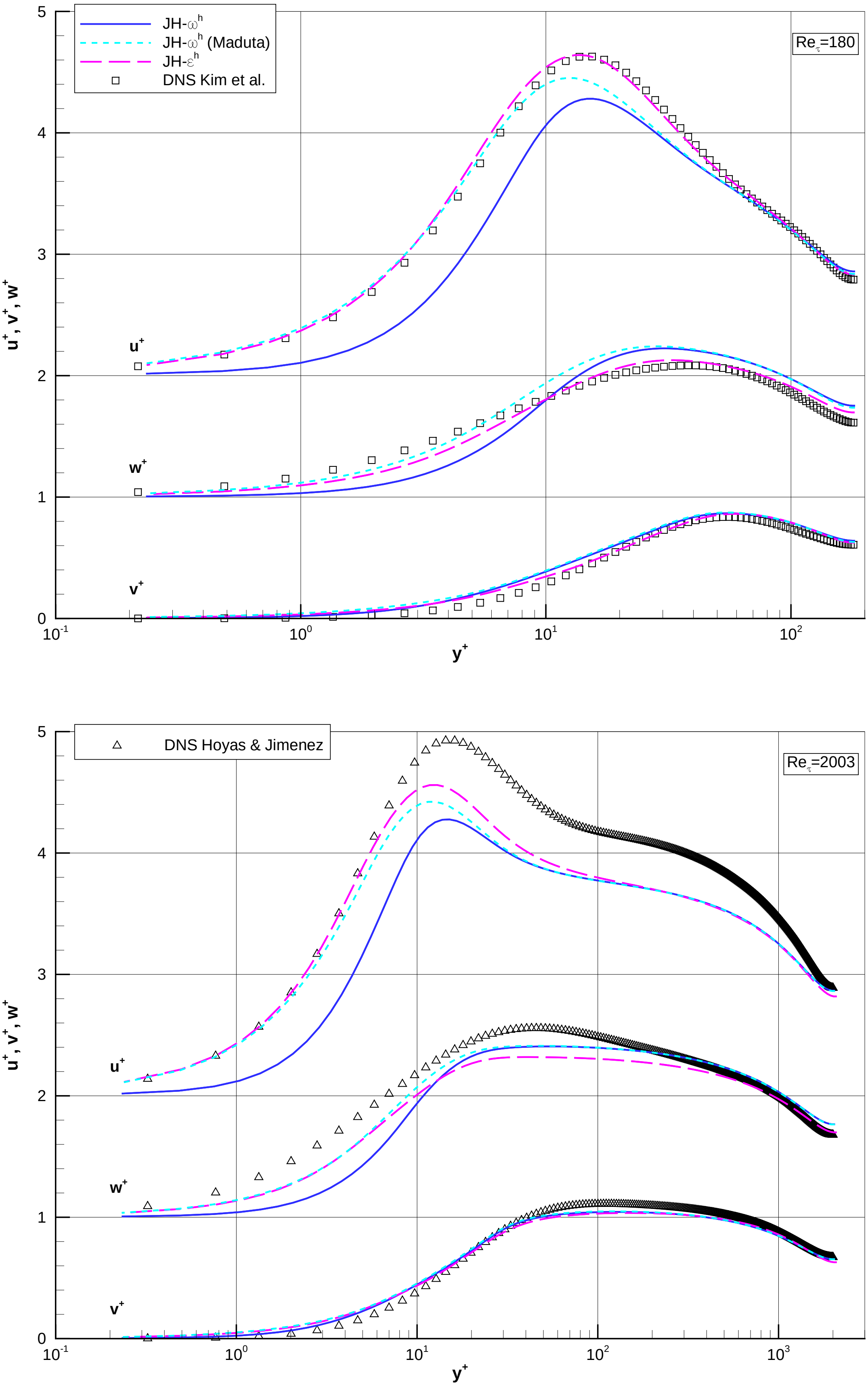

Figure 5.7: Comparison of JH-ω^h, JH-ω^h (Maduta) and JH-ϵ^h results for turbulent plane channel flow: Normalised velocity fluctuations u^+ (offset by 2), v^+ and w^+ (offset by 1) for $Re_\tau = 180$ (Kim *et al.*, 1987) (*top*) and $Re_\tau = 2003$ (Hoyas & Jimenez, 2006) (*bottom*).

can be clearly seen that the JH-ϵ^h model was calibrated using DNS data at $Re_\tau = 180$ (Figure 5.7, *top*) with which its results agree nearly perfectly. At $Re_\tau = 2003$ (Figure 5.7, *bottom*), the levels of u^+ and w^+ are underestimated especially in the logarithmic layer. While the JH-ϵ^h and the JH-ω^h (Maduta) variant produce better quantitative agreement of the velocity fluctuations u^+ and w^+ for the wall asymptotic behaviour compared to the JH-ω^h model, the wall-normal velocity fluctuations v^+ agree with the DNS data for all model versions. In summary, when the improved predictive accuracy of the mean velocity and shear stress are considered, the deficiency of the JH-ω^h model concerning the normal stresses can be tolerated.

The turbulence structure can also be visualised using the anisotropy invariant map introduced in Section 3.2.2. Figure 5.8 shows the invariant map for $Re_\tau = 180$ in three dimensions to illustrate the dependence of turbulence anisotropy on the coordinate y^+. The DNS data show axisymmetric, nearly isotropic turbulence in the centre of the channel. It approaches the one-component limit with its closest point at $y^+ \sim 8$ before it reaches the two-component limit at the wall. Both the Menter SST k-ω and Hellsten EARSM k-ω model erroneously predict isotropic turbulence at the wall and in the centre, which does not reflect the DNS data. Only a slight improvement can be attributed to the SSG/LRR-ω model as it predicts some anisotropy on the channel centre line. The low-Reynolds JH-ω^h and JH-ϵ^h models are clearly superior and are able to produce results which follow the trend in the DNS data at least down through the logarithmic layer. Deviations can be seen in the viscous sublayer at $y^+ < 10$ where the JH-ω^h and the JH-ϵ^h models show different trends. While the former does not reach the two-component limit at the wall, the latter approaches the one-component limit much closer than the DNS. The anisotropy invariants reach their maximum value at the wall instead of showing a reduction as can be found in the DNS data. Maduta's version can be seen as a compromise between the two models. In an SAS-type scale-resolving simulation, the "instability-sensitive" version of the JH-ω^h (Maduta) model, on the other hand, is able to capture the peak in anisotropy invariants away from the wall (Jakirlić & Maduta, 2015). This comes, however, at the expense of significantly increased computing time. Figure 5.9 shows the two-component factor A as a function of y^+ and underlines the previous conclusions. In the cells directly at the wall, models based on the Boussinesq assumption violate realisability.

An alternative presentation of turbulence anisotropy is shown in Figure 5.10 using the barycentric map (*left*) and the respective RGB colouring (*right*) as introduced in Section 3.2.2. While it is debatable if using the colouring in this simple geometry brings clarity or obscures the data, it is, nevertheless, introduced here to become acquainted with this method before applying it to more complex flows. The linearity of the barycentric map allows for a better comparison of the results close to the extreme states. The DNS results clearly show axisymmetric turbulence in the centre of the channel; a result that is obscured by the invariant map due to its non-linear axes, which weight one- and two-component turbulence more heavily than isotropic turbulence. Turbulence in the centre of the channel is found not to be as close to isotropy as the invariant map suggests (Banerjee *et al.*, 2007). All four DRSMs are quite far away from reproducing this feature. Apart from the SSG/LRR-ω model's anomaly of isotropic turbulence at the solid wall, subtle differences become visible for the different versions of the JH-model. As already observed using the invariant map, neither model can follow the DNS data's trend towards two-component turbulence. Both JH-ϵ^h and JH-ω^h (Maduta) seem to tend towards the one-component corner. It is only using this map that the JH-ω^h model's tendency towards axisymmetric turbulence very close to the solid wall becomes visible. As the combination of limited cross diffusion

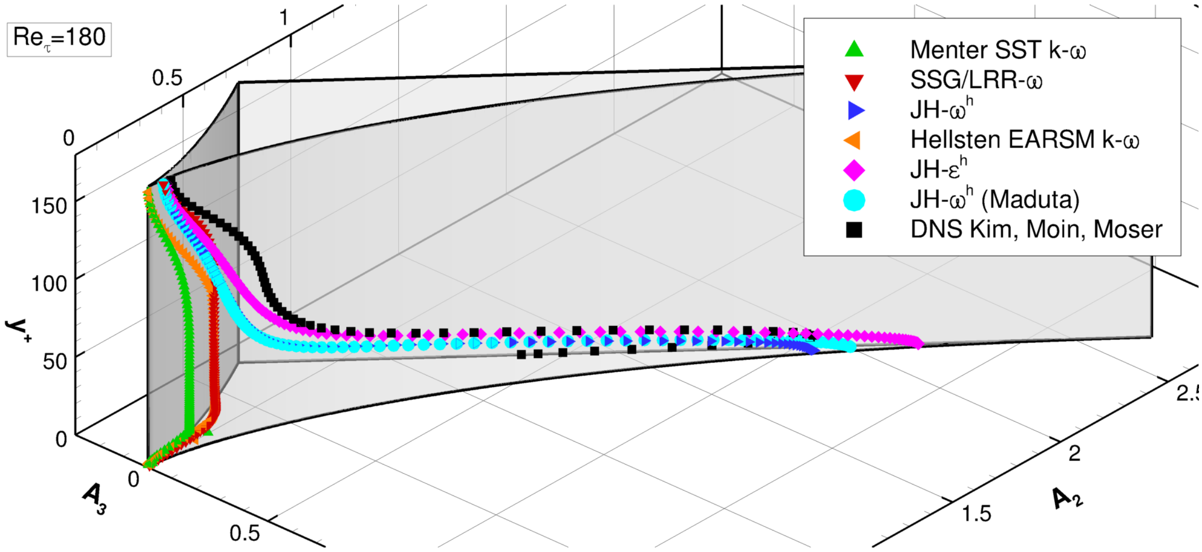

Figure 5.8: Reynolds stress anisotropy invariant map of turbulent plane channel flow at $Re_\tau = 180$ (Kim *et al.*, 1987) for $y/\delta \in [0, 1]$.

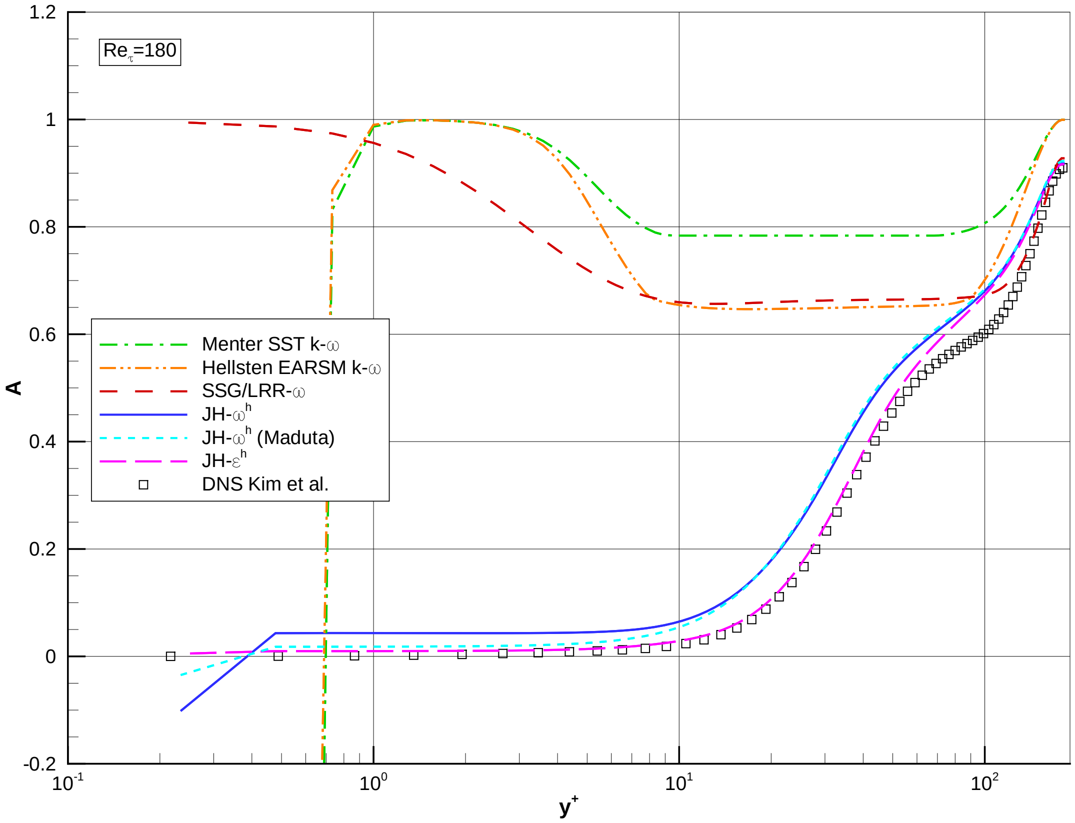

Figure 5.9: Reynolds stress anisotropy two component factor A of turbulent plane channel flow at $Re_\tau = 180$ (Kim *et al.*, 1987).

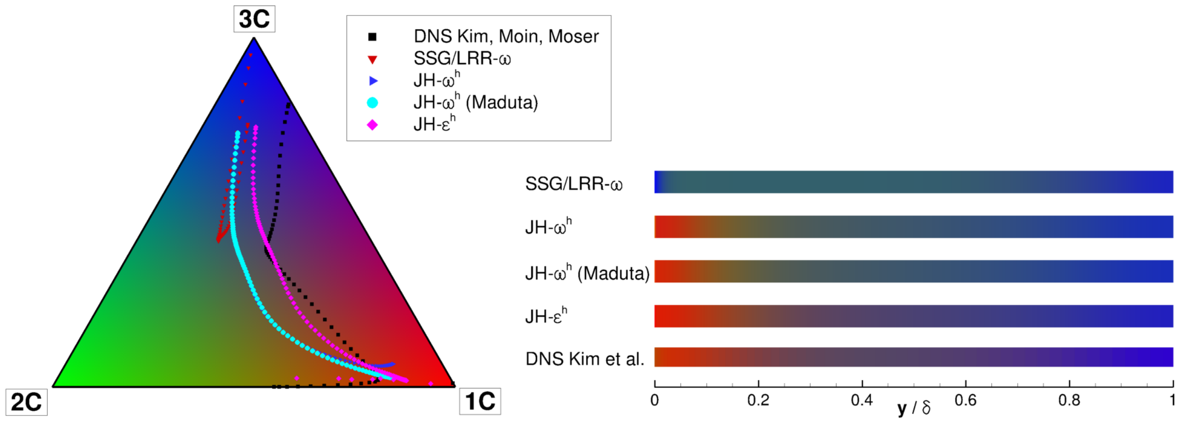

Figure 5.10: Turbulence anisotropy of all four DRSMs in turbulent plane channel flow at $Re_\tau = 180$ (Kim *et al.*, 1987) plotted to barycentric map (*left*) and as colours (*right*).

term and the choice of $P_{\epsilon 3}$ form the only difference between the JH-ω^h and the JH-ω^h (Maduta) model, this effect can be purely attributed to the choice of terms in the scale-determining equation. The unlimited cross diffusion term in case of the latter model leads to a significant decrease in ω^h for $y^+ < 20$. All the above observations are mirrored in the RGB colouring, e.g. the JH-ϵ^h model following more closely the DNS data in the interval $y/\delta \in [0.1, 0.5]$. Especially the differences in near-wall behaviour become obvious and can be distinguished by colours for isotropic, one-component and two-component turbulence.

The budget of source terms of turbulent kinetic energy k is shown in Figure 5.11. Again, the production and homogeneous dissipation

$$P^+ = \frac{\mu}{\bar{\rho} u_\tau^4} P_k \quad \text{and} \quad \epsilon^{h+} = -\frac{\mu}{\bar{\rho} u_\tau^4} \epsilon^h \tag{5.5}$$

are normalised by the friction velocity. All ω-based models except for Maduta's formulation erroneously predict zero dissipation at the wall because k goes to zero and ω goes toward a large but finite value at the wall. Only the JH-ϵ^h and the JH-ω^h (Maduta) models are able to correctly predict the trend and wall value of the homogeneous dissipation rate. This comes at the expense of an overprediction of turbulent kinetic energy production near the wall.

In summary, the JH-ϵ^h and the JH-ω^h (Maduta) models are clearly superior in the prediction of the turbulence structure especially close to the wall. However, the former exhibits a strong dependency on Reynolds number and the latter is numerically less stable than the JH-ω^h model. Both models underestimate the velocity in the logarithmic layer, especially at higher Reynolds numbers. Despite its theoretical advantages, the JH-ϵ^h model was not investigated further because its Reynolds number dependence is seen as problematic for general applications. On the other hand, the JH-ω^h model provides the best predictive accuracy concerning the turbulent shear stress and the mean flow field. Furthermore, the numerical stability is enhanced, which is a decisive advantage in view of application to complex 3D flows.

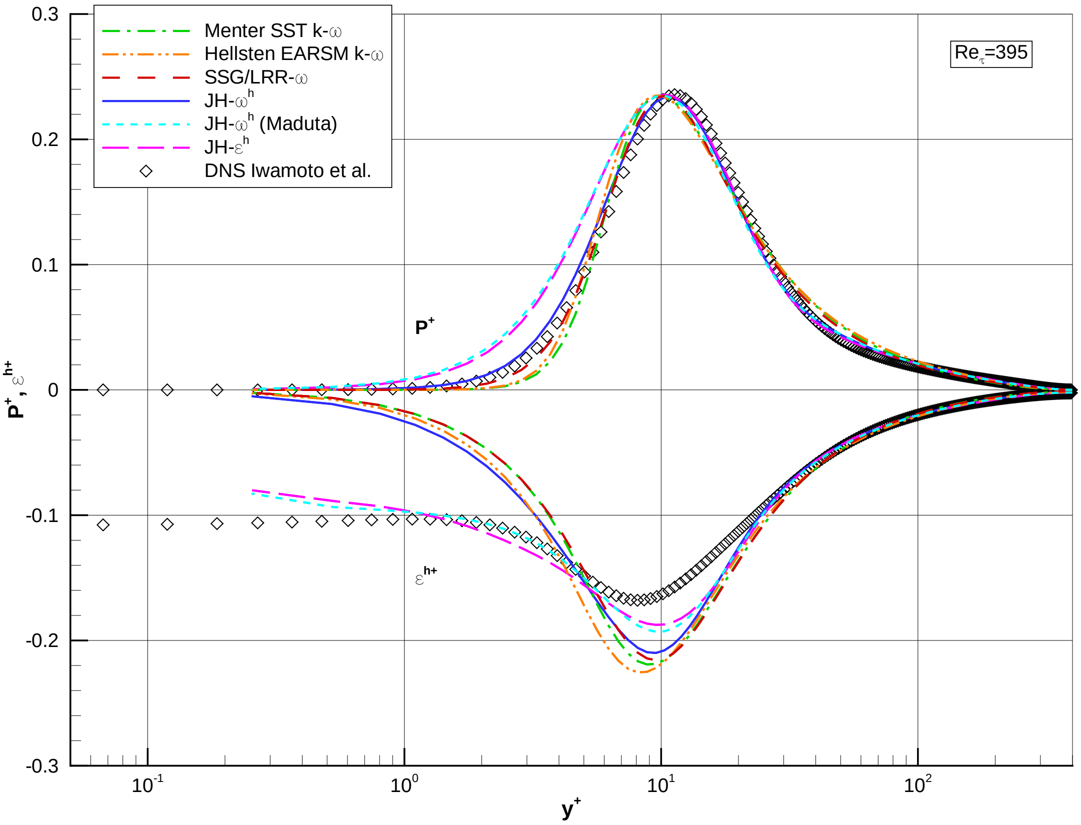

Figure 5.11: Production and homogeneous dissipation of turbulent kinetic energy of turbulent plane channel flow at $Re_\tau = 395$ (Iwamoto *et al.*, 2002).

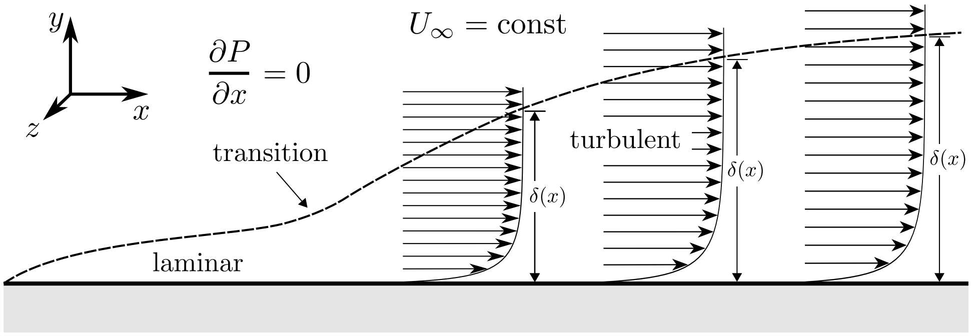
y
x
z
$\frac{\partial P}{\partial x} = 0$
U_∞ = const
transition
laminar
turbulent
δ(x)
δ(x)
δ(x)

Figure 5.12: Sketch of zero pressure gradient flow over flat plate.

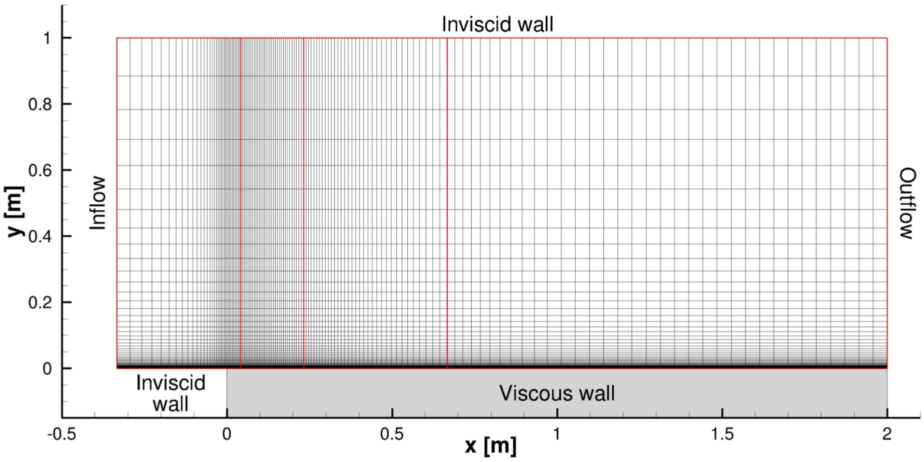

Figure 5.13: Mesh of zero pressure gradient flat plate test case.

5.2 Boundary layer

While the turbulent plane channel flow is homogeneous in the streamwise and spanwise directions, the boundary layer over a flat plate with no pressure gradient develops in the streamwise direction and increases in thickness. Its development can be parametrised by the Reynolds number based on the boundary layer momentum thickness θ

$$Re_\theta = \frac{\overline{\rho}_\infty U_\infty \theta}{\mu_\infty} \quad \text{with} \quad \theta = \int_0^\infty \frac{\overline{\rho} U(y)}{\overline{\rho}_\infty U_\infty} \left(1 - \frac{U(y)}{U_\infty}\right) dy. \tag{5.6}$$

As sketched in Figure 5.12, the boundary layer is initially laminar. At a critical Reynolds number, the instabilities in the flow lead to a transition from the laminar to a turbulent boundary layer, which is significantly thicker (Schlichting, 1982). For the latter, various correlations derived from experimental data exist for the skin friction coefficient c_f as function of Re_θ (Schoenherr, 1932; Kays & Crawford, 1980). Furthermore, a recent DNS data base provides skin friction data in the range of $Re_\theta \in [2500, 6500]$ (Sillero *et al.*, 2013). This data base also contains velocity and stress profiles for various stations specified by Re_θ and is complemented by the classic DNS data obtained by Spalart (1988).

The coordinate directions for this case are chosen as in the plane channel with the y-direction perpendicular to the wall. The mesh is taken from the series of flat plate meshes supplied by the TMBWG (Rumsey *et al.*, 2010). It is sketched, along with the boundary conditions, in Figure 5.13. As the upper boundary is far away from the wall compared to the boundary layer thickness, an inviscid wall boundary condition was chosen. The accelerating effect of the thickening boundary layer is negligible in this case. For the same reason as in the channel flow, the test case at a Reynolds number based on unit length of $Re/L = 5 \cdot 10^6$ is scaled to a free stream Mach number of $M = 0.2$. This setup results in a value of $y^+ \approx 0.5$ for the first cell from the wall.

Figure 5.14 shows the skin friction coefficient

$$c_f = \frac{\tau_w}{\frac{1}{2}\overline{\rho}_\infty U_\infty^2} \tag{5.7}$$

over Re_θ. As in the channel test case, the Menter SST k-ω and SSG/LRR-ω models predict nearly the same curve, which can be attributed to the ω-equation they share.

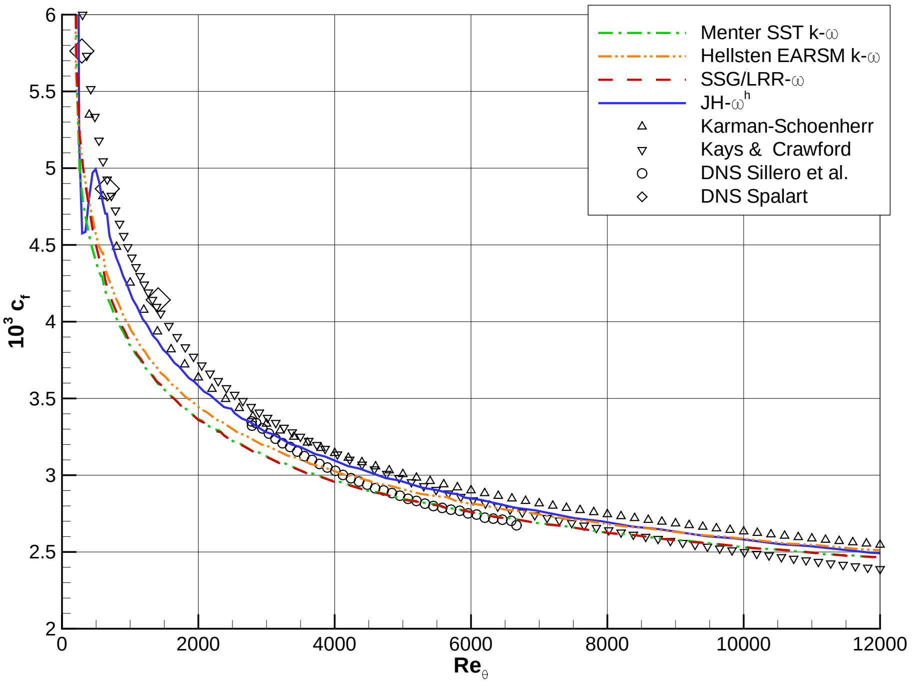

Figure 5.14: Friction coefficient c_f of zero pressure gradient flat plate flow over Reynolds number based on momentum thickness Re_θ. DNS data by Spalart (1988), Sillero *et al.* (2013), correlations by Kays & Crawford (1980) and Schoenherr (1932).

Both models, as well as the Hellsten EARSM k-ω, develop a turbulent boundary layer starting directly at the plate's leading edge while the JH-ω^h model shows a laminar range up to $Re_\theta = 300$ although no transition model is employed. Over the remaining length of the plate, however, the latter model matches the correlation of Karman and Schönherr.

The velocity profiles in wall units are shown in Figure 5.15 (*top*). From the wall up to the defect layer, the Menter SST k-ω, Hellsten EARSM k-ω and SSG/LRR-ω models show a very similar behaviour. Significant improvements in the logarithmic layer and especially in the defect layer are achieved by the JH-ω^h model at lower Reynolds numbers up to about 2000. It produces U^+ closer to the DNS in the free-stream which can be attributed to an improved prediction of wall shear stress. As the Reynolds number increases, especially the Menter SST k-ω and SSG/LRR-ω models show good agreement in this region. These results can be linked to the prediction of shear stress as shown in Figure 5.15 (*bottom*). The JH-ω^h model overpredicts the shear stress for $Re_\theta > 2000$ while the SSG/LRR-ω model underpredicts it for $Re_\theta < 2000$. Figure 5.16 shows the computed velocity fluctuations at $Re_\theta = 1551$ (*top*) and $Re_\theta = 6000$ (*bottom*) compared with the DNS data of Sillero *et al.* (2013). Spalart's results at $Re_\theta = 1410$ (Spalart, 1988) are plotted for reference. The model performance agrees very well with the findings obtained for the turbulent plane channel. The JH-ω^h model provides the best prediction of all components of the velocity fluctuations while deficiencies remain in the asymptotic behaviour of the u^+- and w^+-components.

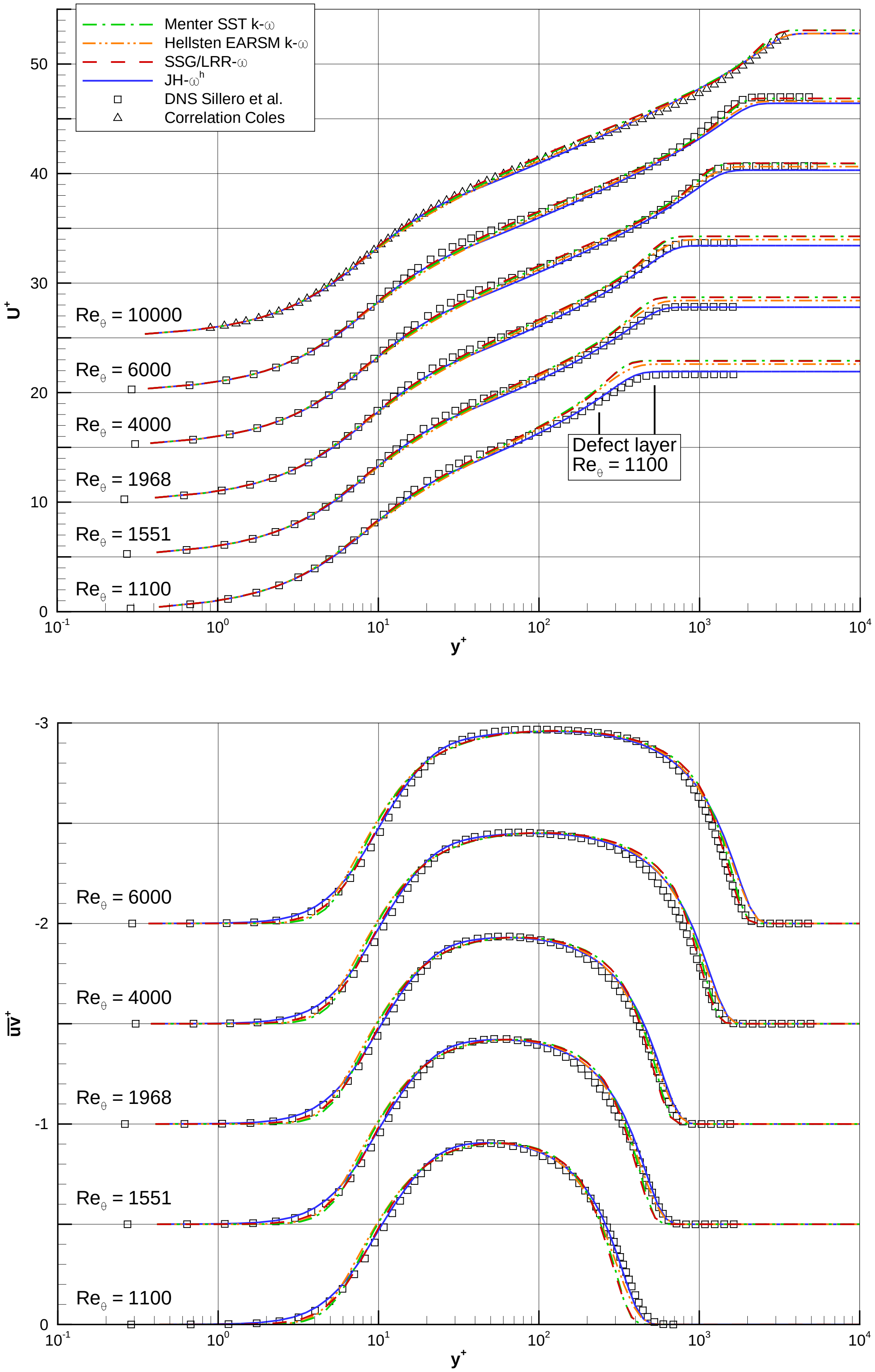

Figure 5.15: Normalised velocity U^+ (*top*) and Reynolds shear stress $\overline{uv}^+$ (*bottom*) profiles of zero pressure gradient flat plate flow at varying Re_θ (offset U^+ by 5 each, $\overline{uv}^+$ by 0.5 each) compared with DNS (Sillero *et al.*, 2013) and a correlation at $Re_\theta = 10000$ (Coles, 1956).

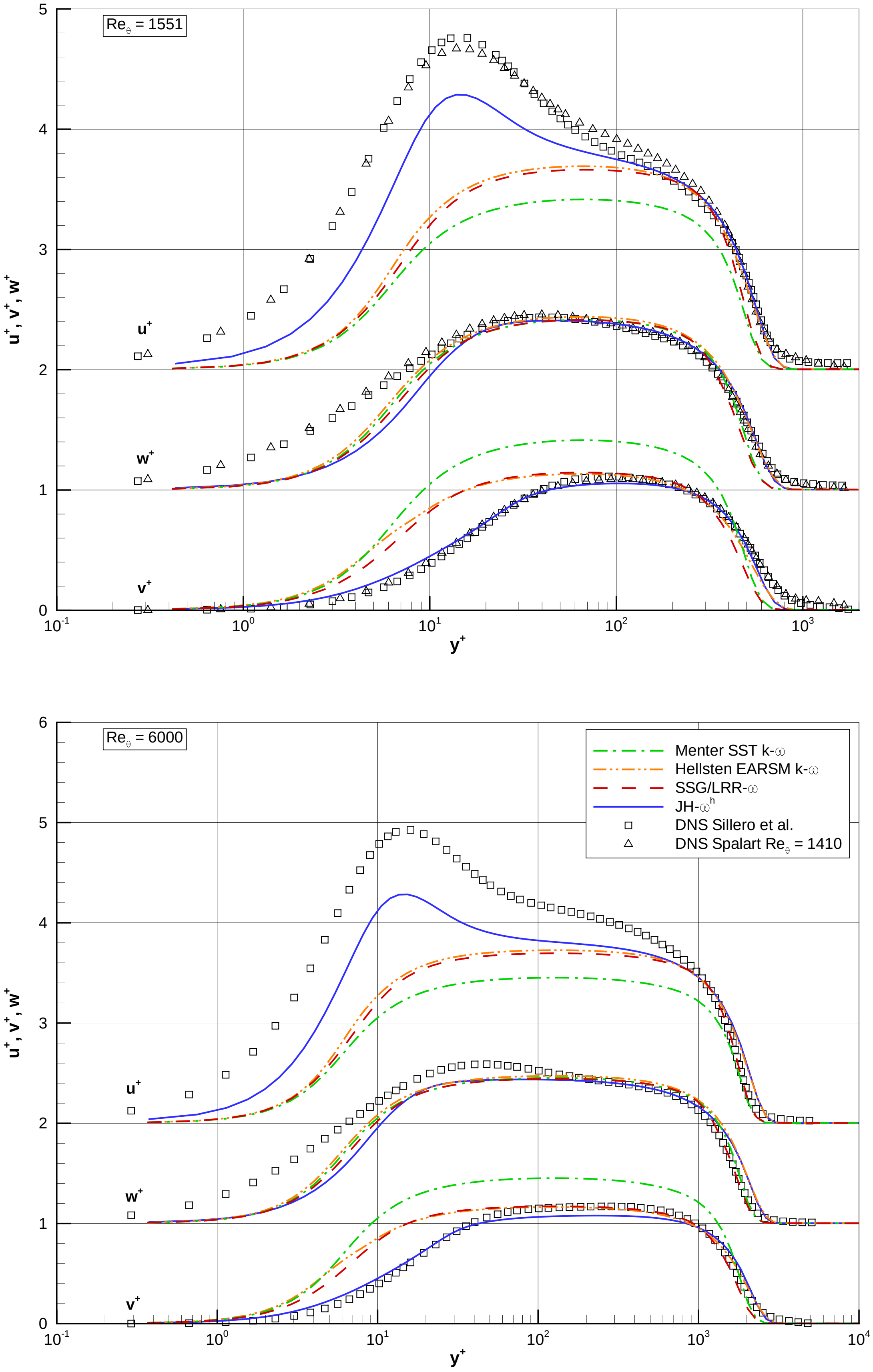

Figure 5.16: Normalised velocity fluctuations u^+ (offset by 2), v^+ and w^+ (offset by 1) of zero pressure gradient flat plate flow at $Re_\theta = 1551$ (*top*) and $Re_\theta = 6000$ (*bottom*) compared with DNS data (Sillero *et al.*, 2013). Spalart's results at $Re_\theta = 1410$ (Spalart, 1988) are plotted for reference.

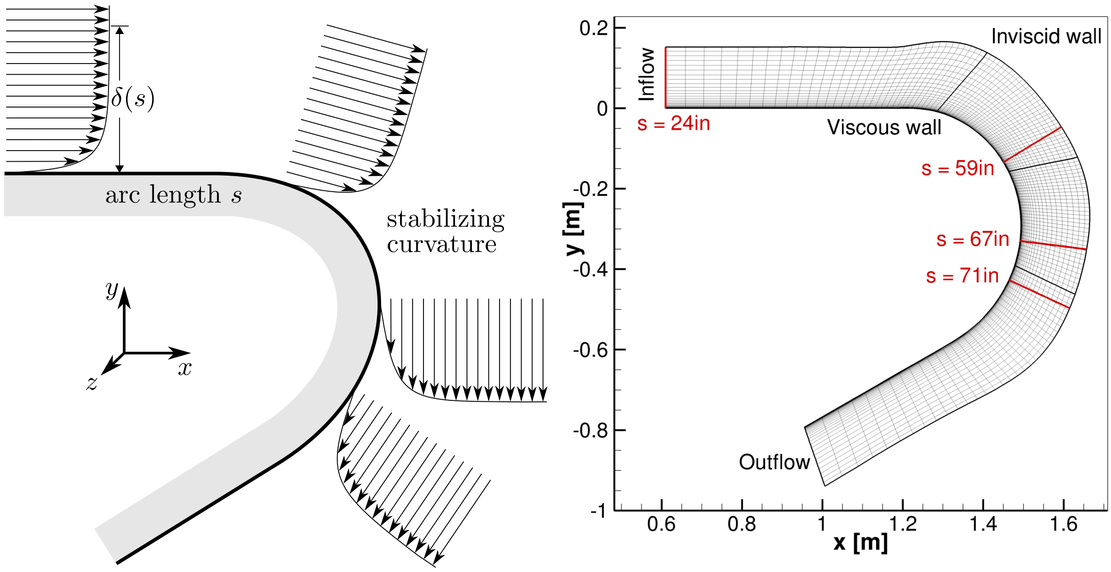

Figure 5.17: Sketch of flow around curved bend (So & Mellor, 1973) (*left)* and computational mesh (every second line shown in streamwise direction, every fourth line shown in direction normal to the wall), boundary conditions and positions of boundary layer profiles at stations $s = 24\text{in}, 59\text{in}, 67\text{in}, 71\text{in}$ (*right*).

5.3 Curved boundary layer

The first real validation test case for Reynolds stress turbulence models is the flow around a curved bend with a convex boundary layer. Figure 5.17 (*left*) shows the configuration, which was experimentally investigated by So & Mellor (1973). In contrast to a straight boundary layer, where the strain rate tensor has only one non-vanishing component $S_{12} = \frac{1}{2}\partial U/\partial y$, the remaining components of S_{ij} have finite values in a flow with streamline curvature. In this case it does not suffice to describe the turbulence energy production by a Boussinesq approach since each component of the strain rate tensor can have a different and significant effect on the budget (Hanjalić & Jakirlić, 2002). The exact production term in a DRSM context enables the models to capture these effects appropriately. Over a convex wall, turbulence is damped and the flow can eventually laminarise. The aim of So and Mellor's study was to investigate this stabilising effect of convex curvature. In order to be able to investigate the effect in isolation, the shape of the opposite wall was specifically chosen to ensure a vanishing pressure gradient around the bend.

Rumsey & Gatski (2001) designed the computational mesh to reproduce the experimental conditions by optimisation of the inviscid wall opposite to the convex wall. It is shown in Figure 5.17 (*right*) and consists of 256 cells in streamwise and 100 cells in wall-normal direction resulting in a non-dimensional wall distance of $y^+ = 0.25$ at the first cell centre. At the inlet, a boundary layer profile which matches the measured skin friction coefficient c_f is prescribed from a preliminary boundary layer calculation and a constant pressure is applied at the outlet. With the experimental free stream velocity of $U_\infty = 22\,\text{m/s}$ and ISA (International Standard Atmosphere) sea level conditions, a Mach number of $M = 0.064$ and a Reynolds number based on unit length $Re/L = 1.5 \cdot 10^6$ are obtained.

So and Mellor measured mean and turbulent quantities in boundary layer profiles at different stations along the bend, which are specified by their respective arc length

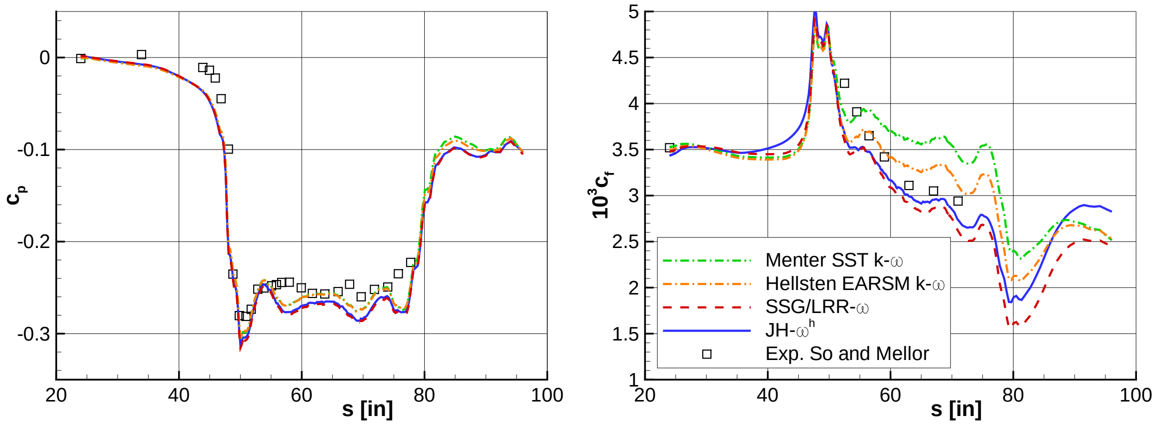

Figure 5.18: Pressure coefficient c_p (*left*) and friction coefficient c_f (*right*) for curved bend flow (So & Mellor, 1973).

s and shown in Figure 5.17 (*right*). At each of these stations, all vector and tensor quantities were measured in a coordinate system aligned with the wall-parallel and normal directions. Therefore, a basis transformation was applied to the computational results from the computational basis $(\mathbf{e}_1, \mathbf{e}_2, \mathbf{e}_3)$ to the experimental basis $(\mathbf{e}_u, \mathbf{e}_v, \mathbf{e}_w)$ where u is wall-parallel in streamwise direction, v is wall-normal and w is wall-parallel in spanwise direction. The base transformation of the Reynolds stresses is performed in analogy to the description in Section 4.4.

Figure 5.18 shows the pressure coefficient

$$c_p = \frac{\overline{p} - \overline{p}_\infty}{\frac{1}{2}\overline{\rho}_\infty U_\infty^2} \tag{5.8}$$

and friction coefficient c_f over the arc length s along the curved wall. In the region of curvature, c_p remains on a nearly constant level for all turbulence models in agreement with the experimental data confirming the suitability of the mesh to reproduce the flow conditions of the experiment. The damping of turbulence manifests itself in the drop of c_f along the curved region. Due to the insensitivity of its production term to streamline curvature and since LEVMs do not model stress redistribution processes, the Menter SST k-ω model cannot reproduce the measured data. Since the Hellsten EARSM k-ω model uses the extra anisotropy a_{ij}^{ex} in addition to the Boussinesq approximation, its production term reacts to individual strain rate components. However, without curvature corrections, the trend in the experimental data cannot be predicted satisfactorily. While both Reynolds stress models are able to predict the experimental level of skin friction, only the JH-ω^h model can reproduce its slope.

The boundary layer profiles of normalised mean velocity U/U_∞ and Reynolds stresses $\overline{uu}/U_\infty^2$, $-\overline{uv}/U_\infty^2$ and $\overline{vv}/U_\infty^2$ in the coordinate system aligned with the wall, as described above, are plotted over the normalised distance from the wall d/δ in Figure 5.19 and confirm the above trend. The boundary layer thickness in this case is defined as $\delta = \delta^{0.99}$ meaning the distance from the wall, where the velocity equals 99 % of the velocity outside the boundary layer. According to the predicted skin friction coefficient, the boundary layer profiles show differences in the velocity gradient directly at the wall. While the differences in velocity between the Reynolds stress models are rather subtle, more information can be obtained from the Reynolds stresses. Unfortunately, the experiment does not provide data down to the wall. The peak in $\overline{uu}/U_\infty^2$, which is only predicted by the low-Reynolds JH-ω^h model, is clearly damped with increasing arc length s as expected. In contrast to the computational results, the experiments

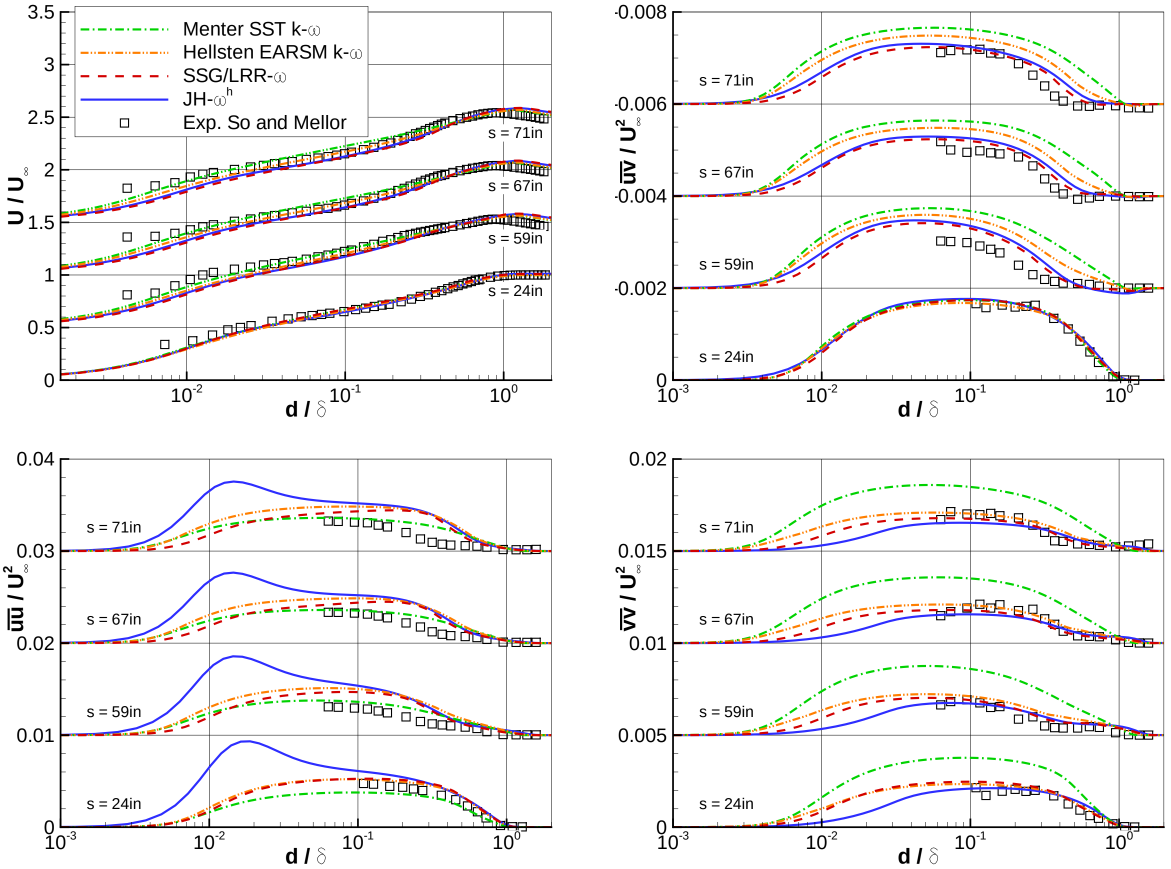

Figure 5.19: Normalised velocity magnitude U/U_∞, Reynolds shear stress $\overline{uv}/U_\infty^2$ and normal stresses $\overline{uu}/U_\infty^2$ and $\overline{vv}/U_\infty^2$ for curved bend flow in basis of experiment (So & Mellor, 1973).

show a significantly reduced $\overline{uu}/U_\infty^2$ in the bend. Stresses in the wall-normal direction $\overline{vv}/U_\infty^2$ are reproduced in good agreement with experimental data by all models except for the Menter SST k-ω model. The shear stress $\overline{uv}/U_\infty^2$, which determines the momentum budget in the boundary layer, shows that only the DRSMs are able to correctly predict the damped turbulence. In summary, if no ad hoc modifications of LEVMs or curvature corrections in EARSMs are applied, DRSMs are necessary to correctly predict flows with streamline curvature.

Figure 5.20 compares the turbulence anisotropy predicted by the SSG/LRR-ω (*left*) and JH-ω^h (*right*) models with measured values. At the three measurement stations in the bend, the measured values scaled with the local boundary layer thickness δ are plotted as squares. The measured Reynolds stresses show a non-negligible scatter, as can be seen in Figure 5.19. This measurement uncertainty can, therefore, also be found in the derived turbulence anisotropy. However, a qualitative assessment is possible. Both turbulence models predict a trend towards isotropic turbulence in the outer part of the boundary layer, soon after the wall curvature has started. This trend can also be seen in the measured data. As in the plane turbulent boundary layer, the JH-ω^h model predicts turbulence close to the one-component limit very close to the wall, whereas the SSG/LRR-ω model shows a trend towards isotropy in this region. This example also shows the potential of the method to qualitatively assess turbulence anisotropy as a field quantity. However, it also requires high quality measurement data for quantitative comparisons.

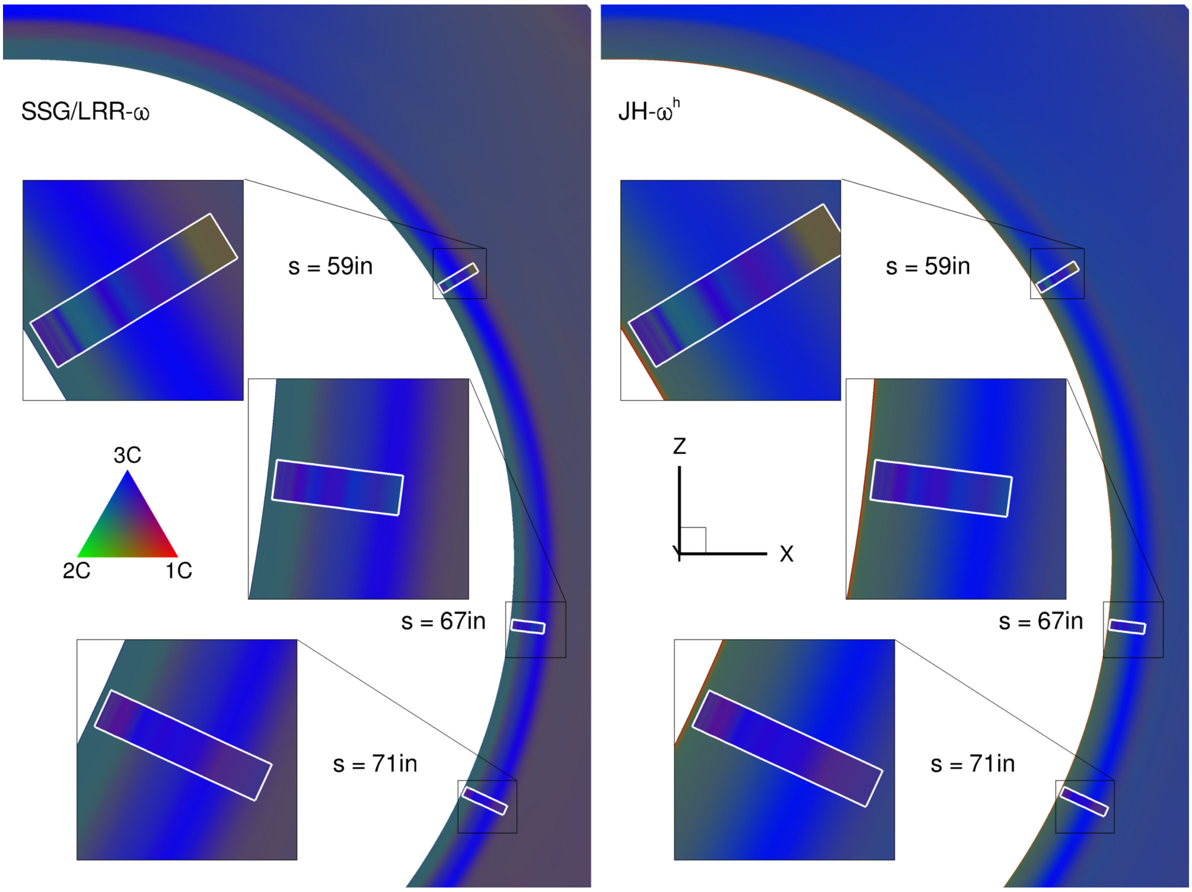

Figure 5.20: Turbulence anisotropy of curved bend flow in RGB colours for SSG/LRR-ω (*right*) and JH-ω^h (*left*). Experimental data by So & Mellor (1973) scaled to computational coordinates are plotted within white boxes.

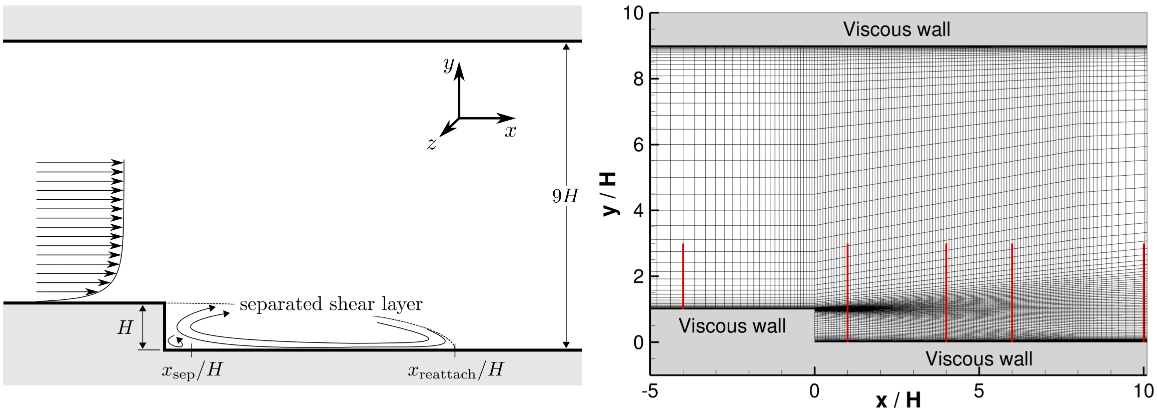

Figure 5.21: Sketch of flow over backward facing step (Driver & Seegmiller, 1985) (*left*) and computational mesh (every fourth line shown in streamwise direction, every second line shown in direction normal to the wall), boundary conditions and positions of boundary layer profiles (red) at stations $x/H = -4, 1, 4, 6, 10$ (*right*). Inflow and outflow boundaries are not shown as the mesh extends 130 step heights upstream and 50 step heights downstream.

5.4 Separated boundary layer

Flow separation is a phenomenon which is encountered in most, if not all, turbomachinery flows. While it is the rule going towards surge conditions, even at the design point separated flow can be found at blade/side-wall junctions in the form of horseshoe vortices and corner separations (Langston, 2001). Therefore, the performance of a turbulence model in separating flows is rather important for the application in view. The backward facing step flow offers separation at a well-defined position, so the development of the separated shear layer, the primary recirculation zone and the reattachment and recovery of the boundary layer can be investigated. A secondary vortex forms in the corner behind the step where the reversed flow separates from the bottom wall. Figure 5.21 (*left*) shows the geometry of the channel with a step of height H. The channel expands by 1/8 from $8H$ to $9H$. Often the DNS data of step flow at $Re_H = 5,100$ based on the step height with an expansion ratio of 1.2 (Le *et al.*, 1997) is used for model validation (e.g. Jakirlić & Maduta, 2015). As the models are supposed to be used in higher Reynolds number applications, the backward facing step flow at $Re_H = 36,000$ (Driver & Seegmiller, 1985) was chosen for validation.

Figure 5.21 (*right*) shows the computational mesh, which is again supplied by the TMBWG (Rumsey *et al.*, 2010), with every fourth line in streamwise direction and every second line in wall-normal direction. The inflow and outflow boundaries are located at $130H$ upstream and $50H$ downstream of the step, respectively. All walls are viscous, except for the area $x/H = -130$ to -110 which is treated as an inviscid wall. The inflow total temperature and pressure and the outflow static pressure are chosen, such that $M = 0.128$ is reached at $x/H = -4$. The latter and the remaining positions where experimental profile data are available are plotted in red.

In addition to the JH-ω^h model, the flow is also computed with the version JH-ω^h (Maduta). However, this version resulted in a completely laminar boundary layer upstream of the step and the computation crashed at some point due to instabilities irrespective of mesh density or numerical setup. To show the effect of the unlimited cross diffusion term anyway, a converged solution was obtained by changing the ve-

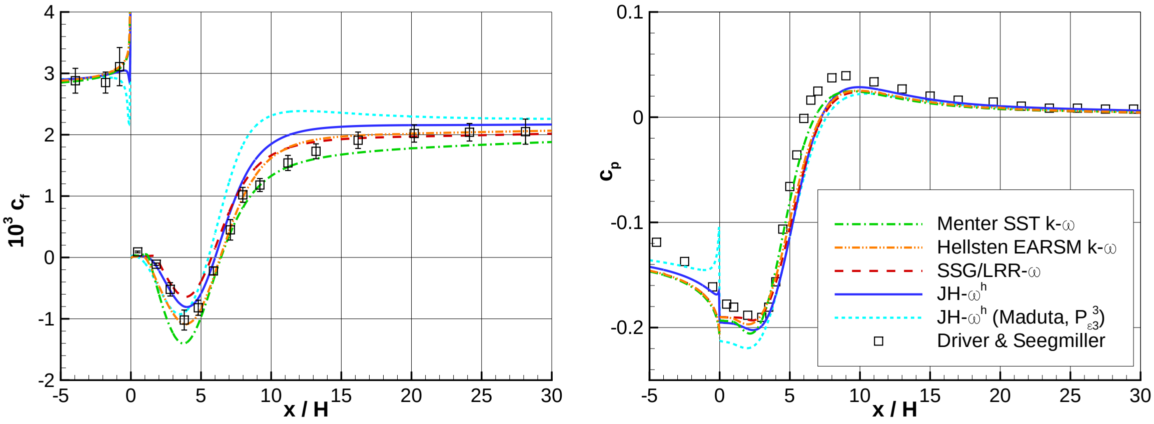

Figure 5.22: Skin friction coefficient c_f (*left*) and pressure coefficient c_p (*right*) for backward facing step flow.

locity gradient source term of the ω^h equation from $P^2_{\epsilon 3}$ to $P^3_{\epsilon 3}$ (3.86). This means that $\mu_T = C_\mu \bar{\rho} k^2/\epsilon^h$ instead of (3.69) is used to compute $P_{\epsilon 3}$ and the coefficient $C_{\epsilon 3}$ is modified accordingly. The version of the model is called JH-ω^h (Maduta, $P^3_{\epsilon 3}$) and used only for this case.

A number of features will be investigated in the following. First, the skin friction coefficient c_f, which shows a recirculation zone, the point of reattachment and recovery of the boundary layer, and the respective pressure coefficient c_p are shown in Figure 5.22. The reference velocity needed to compute the coefficients using (5.7) and (5.8) is the centre-line velocity at $x/H = -4$. The reference pressure was chosen such that $c_p = 0$ at $x/H = 40$ as in the experiment. The pressure coefficient is mostly unaffected by the choice of turbulence model showing greater scatter only around the reattachment point, except for the JH-ω^h (Maduta, $P^3_{\epsilon 3}$) model. It shows a spurious drop in pressure over the recirculation zone, which can be explained by the streamlines showing positive y-velocity directly at separation leading to a slight contraction of the channel (see Figure 5.24). Furthermore, it predicts the shortest reattachment length of all models and a peak in c_f in the recovering boundary layer, which is not in line with the experiment. The JH-ω^h model shows a significant improvement, giving a reasonable agreement of c_f in the recirculation zone as well as with position of the reattachment point. In the recovering boundary layer, however, c_f deviates from the measured values. In contrast, the skin friction after reattachment is reproduced well by the SSG/LRR-ω model, which predicts slightly premature reattachment. While the Hellsten EARSM k-ω model gives nearly perfect agreement with the experiments, the Menter SST k-ω model overestimates the undershoot in skin friction in the recirculation zone and slightly underpredicts c_f in the recovering boundary layer. Table 5.2 quantitatively compares the computed reattachment lengths with the experimental data.

Figure 5.23 shows normalised velocity profiles U/U_{ref} (*top left*) and Reynolds stress profiles $\overline{uv}/U^2_{\text{ref}}$ (*top right*), $\overline{uu}/U^2_{\text{ref}}$ (*bottom left*) and $\overline{vv}/U^2_{\text{ref}}$ (*bottom right*) at the stations $x/H = -4, 1, 4, 6, 10$. For readability, the downstream profiles are shifted in the plot x-direction. All turbulence models satisfactorily reproduce the measured upstream velocity profile at $x/H = -4$. Downstream of the step, however, the picture changes. While the prediction is still quite accurate at $x/H = 1$, the x-velocity below step height is underpredicted by all used turbulence models. Again, the JH-ω^h model shows a slight improvement compared to the JH-ω^h (Maduta, $P^3_{\epsilon 3}$) version. This also applies for the Reynolds stress components. Around and downstream of reattachment, the shear

Table 5.2: Reattachment and secondary separation points in backward facing step flow at $Re_H = 36,000$ with expansion ratio 1.125 (Driver & Seegmiller, 1985).

Dataset	x_{reattach}/H	x_{sep}/H
Menter SST k-ω	6.43	1.27
Hellsten EARSM k-ω	6.37	0.99
SSG/LRR-ω	5.75	1.79
JH-ω^h	6.01	1.20
JH-ω^h (Maduta, $P_{\epsilon 3}^3$)	5.53	0.53
Driver & Seegmiller	6.26 ± 0.10	

stress as well as the streamwise normal stress are overpredicted by all but the Menter SST k-ω model. The peak of all Reynolds stress components is too far away from the wall.

A well-known deficiency of many DRSMs is the spurious back bending of the dividing streamline at reattachment in this kind of flow. This is often remedied by introducing an additional source term in the scale-determining equation. Hanjalić & Jakirlić (1998) call this term, which is based on gradients of the turbulent length scale, S_l. Figure 5.24 shows streamlines in the region of separated flow with the reattachment point magnified for clarity for the JH-ω^h model (*top*), the JH-ω^h (Maduta, $P_{\epsilon 3}^3$) model (*middle*) and the SSG/LRR-ω model (*bottom*). The latter two models clearly show the back bending problem while the JH-ω^h model does not seem to have this problem although no extra source term has been introduced. Major differences can be found in the size of the secondary recirculation bubble as summarised in Table 5.2 by positions of the secondary separation points. The skin friction measurements contain only one point with positive value in this region, which lies within the predicted range of all turbulence models. Only the velocity profile at $x/H = 1$ suggests that at a distance of $y/H = 0.1$ from the wall, there should be no flow in positive x-direction which is in contrast to the prediction by the SSG/LRR-ω model and indicates that it predicts too large a bubble. Information about turbulence anisotropy can be deduced by the RGB colours in Figure 5.24. Qualitative differences between the JH-ω^h and SSG/LRR-ω models can be seen around the secondary separation point. There the former model shows that turbulence close to the two-component limit (green) is transported from the immediate wall vicinity into the flow field. Since not all relevant stress components were available from the experiment, no comparison with measured data can be shown here.

In summary, in this case the classic modelling approaches already provide satisfactory agreement with the experiment. The SSG/LRR-ω and the JH-ω^h (Maduta, $P_{\epsilon 3}^3$) models show the spurious back bending at reattachment which needs to be addressed by an additional term in the ω-equation. On the other hand, the JH-ω^h model emerges as a good compromise since it produces acceptable agreement with the measured data without the need for additional modelling.

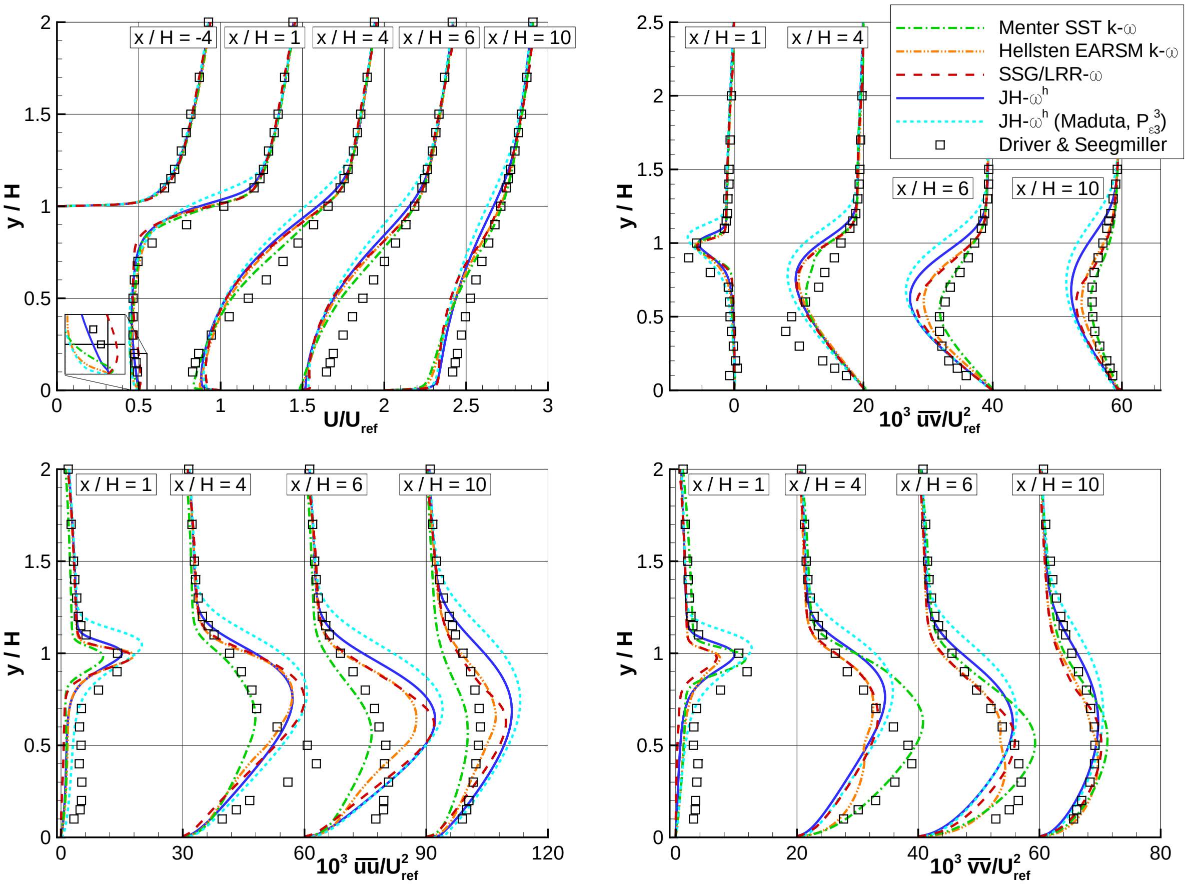

Figure 5.23: Normalised velocity profiles U/U_{ref} (*top left*) and Reynolds stress profiles $\overline{uv}/U^2_{\mathrm{ref}}$ (*top right*), $\overline{uu}/U^2_{\mathrm{ref}}$ (*bottom left*) and $\overline{vv}/U^2_{\mathrm{ref}}$ (*bottom right*) of backward facing step flow at $Re_H = 36,000$ (Driver & Seegmiller, 1985) at stations $x/H = -4, 1, 4, 6, 10$ (offset in x-direction).

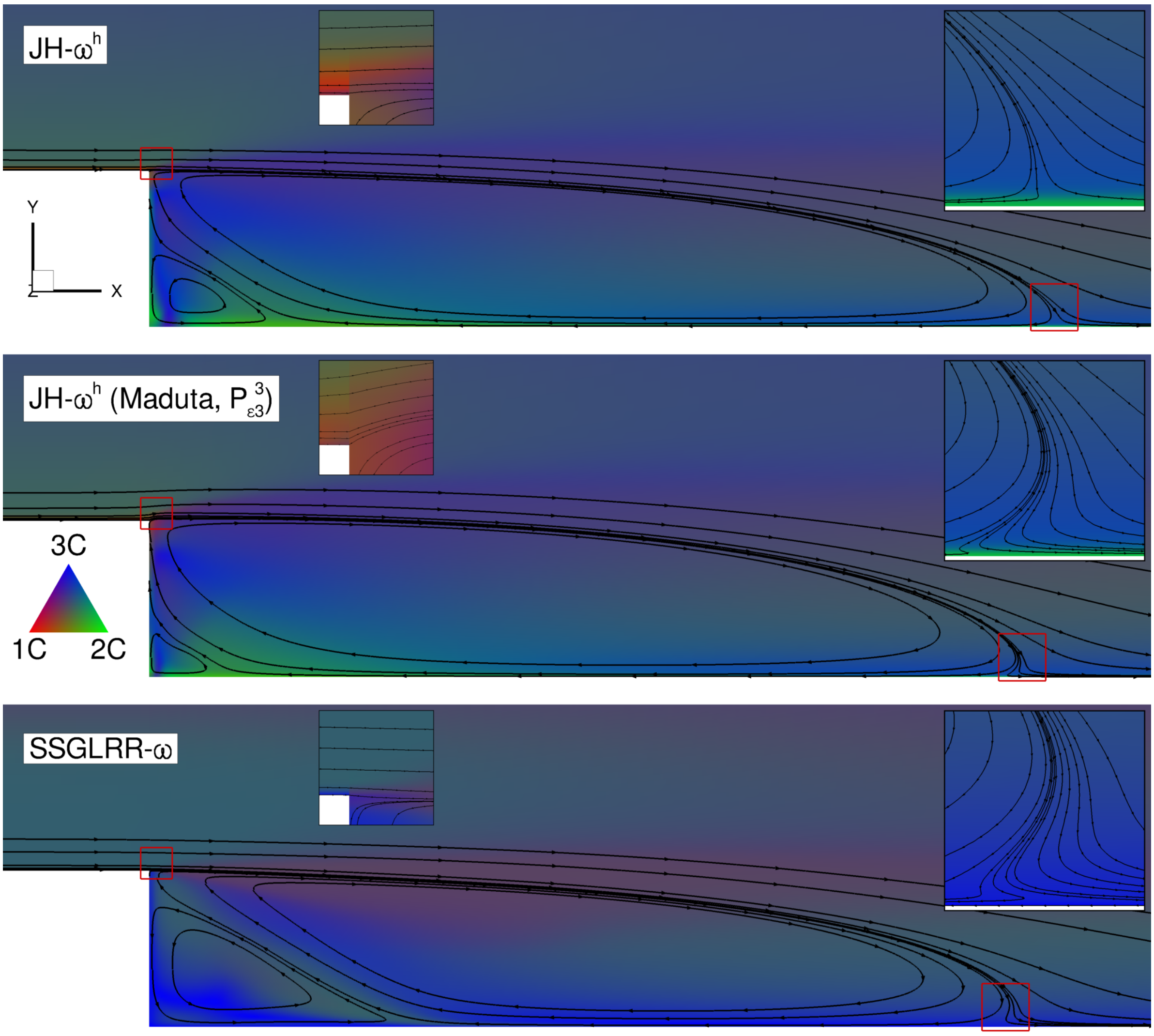

Figure 5.24: Streamlines of backward facing step flow at $Re_H = 36,000$ (Driver & Seegmiller, 1985) computed by JH-ω^h (*top*), JH-ω^h (Maduta, $P_{\epsilon 3}^3$) (*middle*) and SSG/LRR-ω (*bottom*) with separation and reattachment points magnified. The turbulence anisotropy is coloured in RGB.

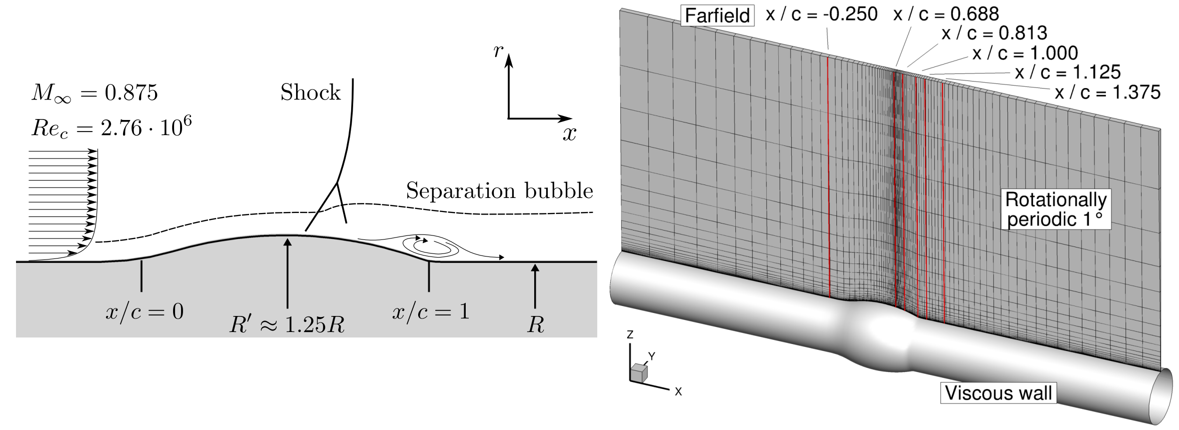

Figure 5.25: Sketch of transonic flow over axisymmetric bump (Bachalo & Johnson, 1986) (*left*) and computational mesh (every eighth line shown), boundary conditions and positions of boundary layer profiles at stations $x/c = -0.250, 0.688, 0.813, 1.000, 1.125, 1.375$ (*right*).

5.5 Shock wave/boundary layer interaction

Since transonic flows are often found in present day turbomachines, it is important to test the turbulence model's ability to predict effects of shock waves interacting with turbulent boundary layers. One classic example of a detailed study devoted to this phenomenon is the transonic flow over an axisymmetric bump investigated experimentally by Bachalo & Johnson (1986). The case is sketched in Figure 5.25 (*left*). The bump is a circular arc with chord length c mounted on a cylinder of radius R with fillets at both leading and trailing edges. At its thickest point, the radius is $R' \approx 1.25R$. In the case of a free stream Mach number of $M = 0.875$ and Reynolds number based on chord length of $Re_c = 2.76 \cdot 10^6$, a shock forms, which, in combination with the adverse pressure gradient near the trailing edge, causes the flow to separate and reattach downstream of the bump.

A series of meshes is provided by the TMBWG (Rumsey *et al.*, 2010). Only one cell spanning 1° of the full 360° configuration is meshed as shown in Figure 5.25 (*right*) with 720 cells in axial and 320 cells in radial direction. The symmetry is exploited by application of rotationally periodic boundary conditions (see 4.4). All other boundaries are treated as farfield boundaries, at which total pressure, total temperature, Mach number, flow angles and turbulence quantities are specified. The positions at which radial profiles are extracted are plotted in red.

Figure 5.26 shows the pressure coefficient c_p (*top left*) and the skin friction coefficient c_f (*top right*) computed using equations (5.8) and (5.7). For the former, experimental data was available and is plotted as symbols. The choice of turbulence model clearly influences the predicted shock position. All DRSMs are in very good agreement with the experiment. However, all models fail to predict the measured pressure coefficient in the region of separation between the shock and the reattachment point. The size of the separation can be judged by the skin friction coefficient and is compared to the measured size. Both the Menter SST k-ω and the Hellsten EARSM k-ω models predict a separation bubble about 20% bigger than found in the experiment with early separation and late reattachment. In contrast, a very short bubble of about 40% the measured size is predicted by the JH-ω^h (Maduta) model. The SSG/LRR-ω agrees very well in terms of the length of the separation bubble but predicts too early separation and reattachment. The skin friction coefficient predicted by the JH-ω^h model shows the correct separation location but a bubble that is about 10% too short.

The following parts of Figure 5.26 show the normalised turbulent kinetic energy k/U_∞^2 (*middle left*), the normalised turbulent shear stress $\overline{uv}/U_\infty^2$ (*middle right*) and the normalised axial velocity U/U_∞ (*bottom*) at various axial positions. Station $x/c = -0.250$ represents the incoming boundary layer, which all turbulence models reproduce satisfactorily. The profile at $x/c = 0.688$ cuts through the shock resulting in very pronounced differences in velocity outside of the boundary layer depending on the predicted shock position. Both Menter SST k-ω and Hellsten EARSM k-ω underpredict the velocity in the boundary layer due to premature separation. This also holds true for the rest of the profiles. The DRSMs, on the other hand, provide an overall accurate representation of mean velocity, except for the magnitude of reverse flow at $x/c = 1.000$ which they all underestimate. Agreement with experimental data is better for JH-ω^h than for the SSG/LRR-ω model. A look at the turbulence quantities shows further differences. The Hellsten EARSM k-ω systematically shows k and $\overline{uv}$ maxima further away from the wall than the experiment. The Menter SST k-ω model underestimates the shear stress at all positions downstream of the shock. Again, the DRSMs show improved agreement with experimental data for turbulence quantities. Because only k instead of the single diagonal components of the Reynolds stress tensor are given, differences between the JH-ω^h and SSG/LRR-ω model are rather subtle in this case.

In Figure 5.27, the shock is visualised by the $M = 1$ isoline plotted in white and turbulence anisotropy is represented by RGB colours. It is evident that the strong normal straining at the shock greatly influences the turbulence anisotropy, especially in case of the SSG/LRR-ω model and more subtly in case of the JH-ω^h model. Furthermore, the shock leads to a thickening of the boundary layer and subsequent flow separation as illustrated by the streamlines plotted in black. The effects in this case are very similar to the backward facing step flow although the separation is much weaker. Strong back bending can be found in case of the SSG/LRR-ω model but it is almost non-existent in case of JH-ω^h. In summary, except for the exact length of the separation bubble, the JH-ω^h model is able to properly predict this case of shock wave/boundary layer interaction.

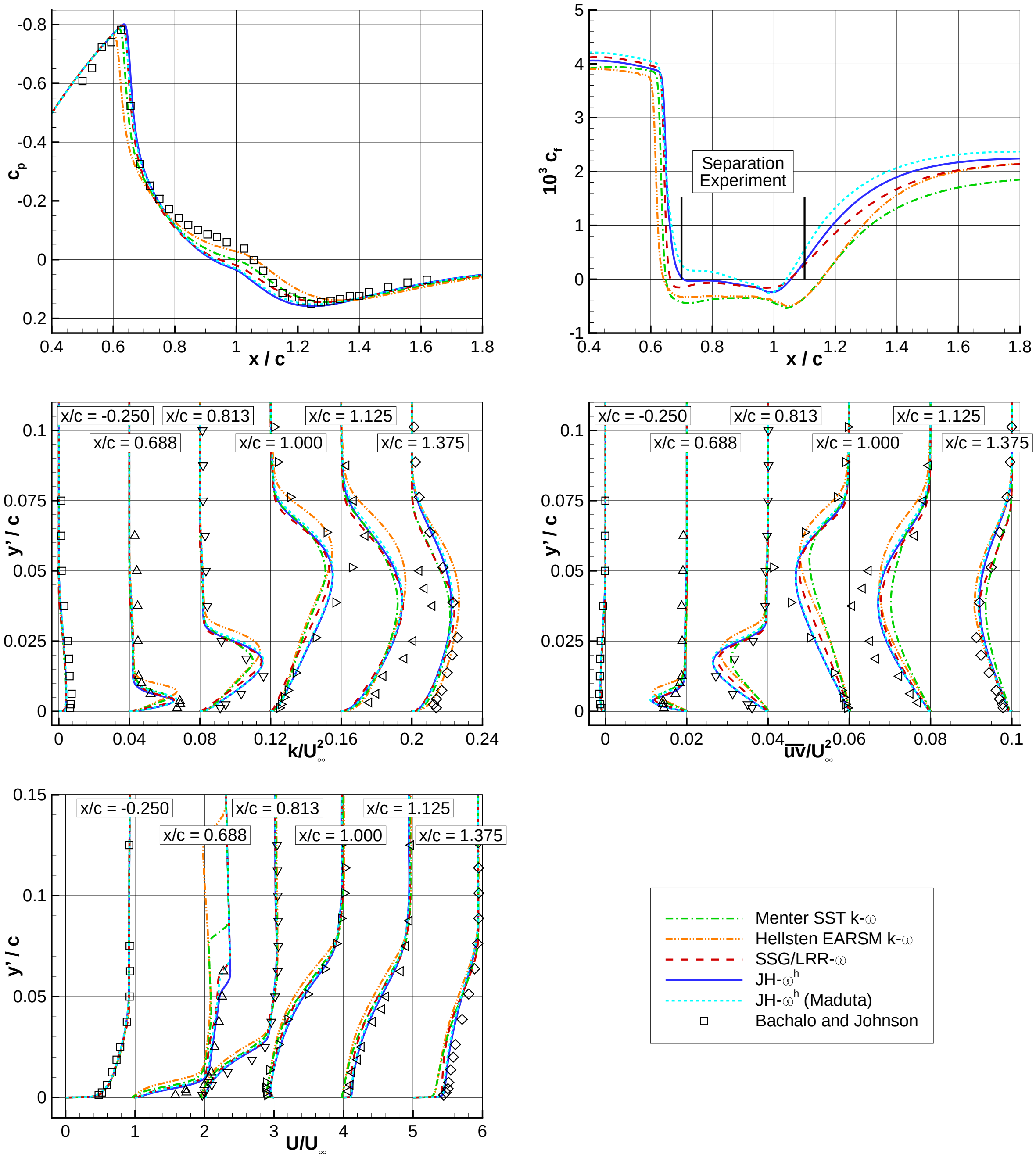

Figure 5.26: Transonic flow over axisymmetric bump (Bachalo & Johnson, 1986). Pressure coefficient c_p (*top left*), skin friction coefficient c_f (*top right*); profiles of normalised turbulent kinetic energy k/U_∞^2 (*middle left*), shear stress $\overline{uv}/U_\infty^2$ (*middle right*) and normalised mean velocity U/U_∞ (*bottom left*) at axial stations $x/c = -0.250, 0.688, 0.813, 1.000, 1.125, 1.375$ (offset in x-direction).

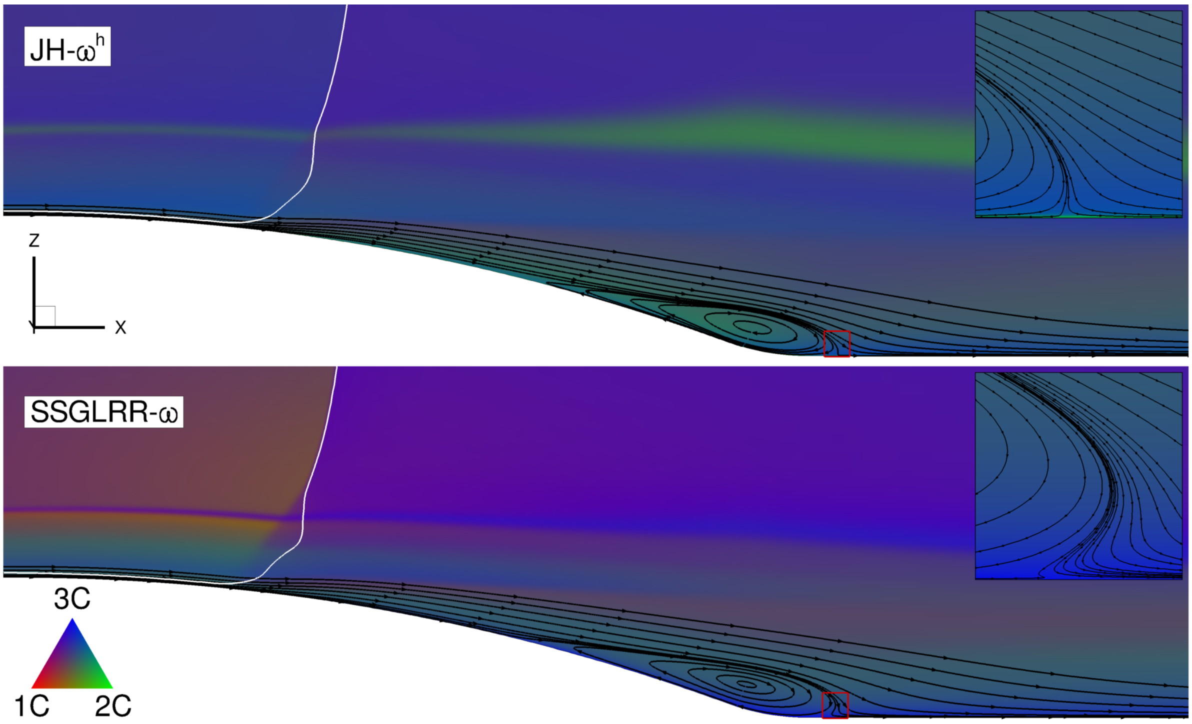

Figure 5.27: Streamlines of flow over axisymmetric transonic bump (Bachalo & Johnson, 1986) computed by JH-ω^h (*top*) and SSG/LRR-ω (*bottom*) with reattachment point magnified in respective top right corner. The turbulence anisotropy is coloured in RGB and the shock is visualised by the $M = 1$ isoline (white).

6 Model application to turbomachinery flows

In this chapter, the DRSMs shall be applied to industrially relevant turbomachinery configurations. Their predictions will be compared to the reference turbulence models as well as experimental data. The chapter serves to demonstrate the feasibility of this turbulence modelling approach to predict complex 3D flows through complex 3D geometries including numerous fluid dynamic effects.

6.1 Compressor cascade

6.1.1 Description

The low speed compressor cascade investigated experimentally by Muthanna (2002) and Tang (2004) is representative of a turbomachinery flow characterised by complex 3D flow features. It is operated at a Mach number of $M = 0.07$ and a Reynolds number of $Re = 400,000$. Tang investigated the flow in the tip gap with Laser Doppler Velocimetry (Tang, 2004) while Muthanna employed a hot wire probe to scan the passage flow (Muthanna & Devenport, 2004). Both delivered averaged velocities as well as Reynolds stresses. The geometric properties of the cascade and the inflow conditions are summarised in Table 6.1. Parts of this section have already been published by the author (Morsbach *et al.*, 2014, 2015*a*).

6.1.2 Numerical setup

An overview of the numerical setup is given in Figure 6.1. The mesh has already been used in previous studies to investigate the performance of LEVMs and EARSMs (Kainz & Kozulovic, 2007; Franke, 2010). To achieve an appropriate representation of the tip gap flow, 34 cells were placed between the blade tip and the casing. One passage of the compressor cascade was computed on a mesh with 2.7 million cells distributed to 19 blocks and low-Reynolds resolution ($y^+ < 1$) at all solid walls. Non-reflecting boundary conditions were used at inlet and outlet, and periodic boundary conditions were used in the pitchwise direction. The turbulence at the inflow was specified as isotropic given by turbulence intensity and length scale for all turbulence models. Due to the low Mach number, a local low Mach preconditioning of the type proposed by Turkel was employed (Fiedler & di Mare, 2012).

Table 6.1: Properties of Virginia Tech compressor cascade and inflow conditions.

Property		Value	
Aerofoil		GE Rotor B	
Chord	c	254	mm
Blade height	h	254	mm
Pitch		236	mm
Stagger angle		56.9	°
Axial chord	c_a	138.68	mm
Relative tip gap		1.65	%
Inflow velocity	U_{ref}	24.5	m/s
Inflow angle		65.1	°
Inflow turbulence intensity	Tu	5.0	%
Inflow turbulent length scale	L_T	0.01	m
Mach number	M	0.073	
Reynolds number	Re	$400,000$	

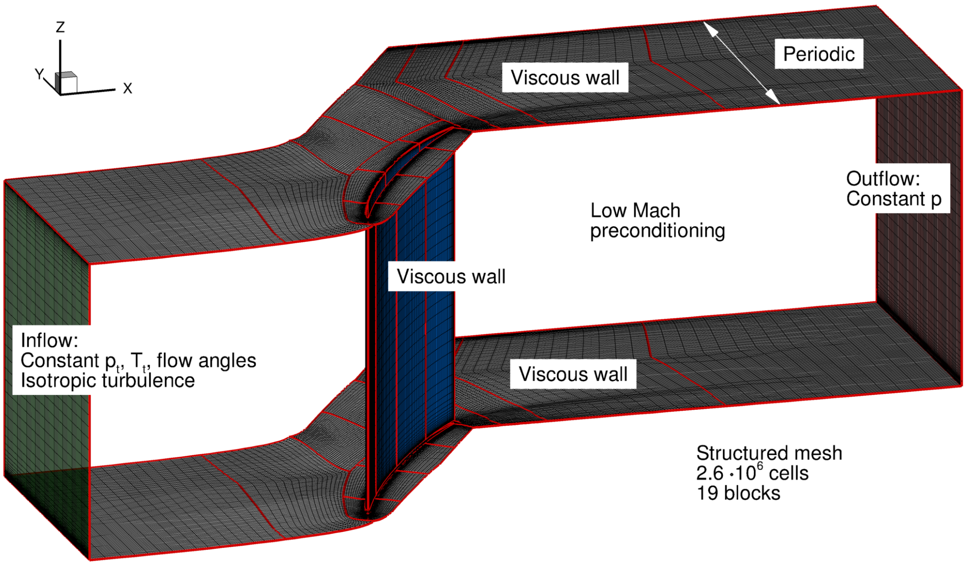
Z
Y
X
Viscous wall
Periodic
Outflow: Constant p
Low Mach preconditioning
Viscous wall
Inflow: Constant p_t, T_t, flow angles Isotropic turbulence
Viscous wall
Structured mesh
2.6 ·10^6 cells
19 blocks

Figure 6.1: Summary of numerical setup of Virginia Tech compressor cascade computation.

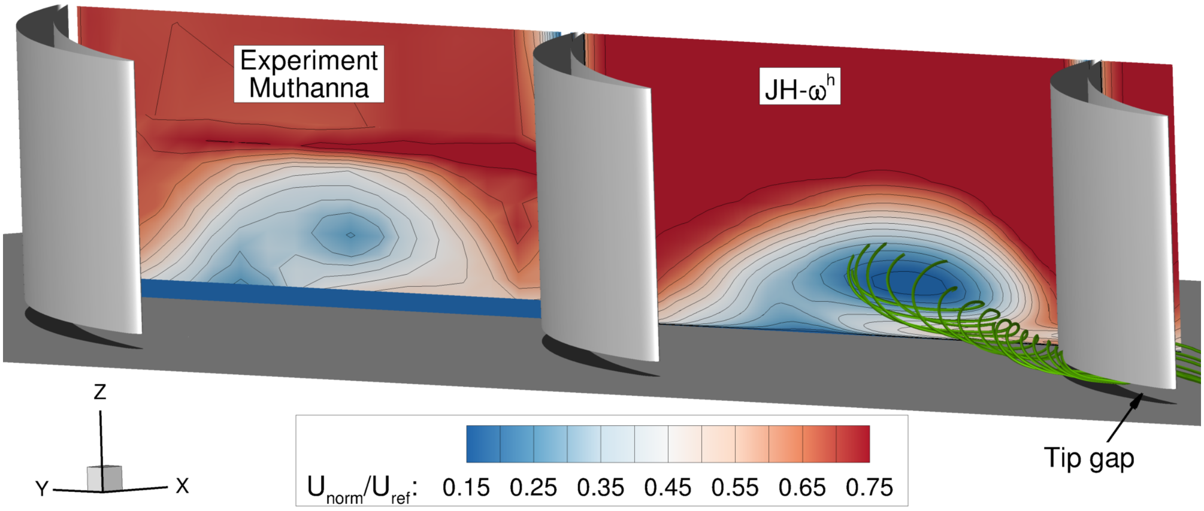

Figure 6.2: Illustration of tip-leakage flow in the Virginia Tech compressor cascade. The measured mean velocity in blade passage is compared to the prediction by the JH-ω^h DRSM.

6.1.3 Discussion

The flow topology, shown in Figure 6.2, is dominated by the flow through the tip gap, which leads to the development of the tip gap vortex visualised by the streamlines. Qualitatively, the velocity deficit in the vortex core predicted with the JH-ω^h model is compared to the measured data at $x/c_a = 0.98$. Figure 6.3 (*left*) shows the measurement positions used for comparison. The pressure distribution on the blade at midspan, predicted by the different turbulence models (Figure 6.3, *right*), lies within the experimental scatter, confirming that the boundary conditions were chosen appropriately to match the measured operating point. To ensure the proper turbulent inflow conditions, the predicted boundary layer velocity distribution upstream of the blade row at $x/c_a = -0.33$ is compared with measured data in Figure 6.4 (*left*). All turbulence models match the measured profile in the logarithmic layer and wake region with the JH-ω^h model giving the best agreement. The scatter of the predicted velocity profiles is comparable to that of the generic turbulent boundary layer described in Section 5.2. Deviations are visible in the buffer and viscous sublayers where the experimental data do not show the expected asymptotic behaviour. The turbulence two-component parameter A is plotted in Figure 6.4 (*right*) as a simplified measure to represent the Reynolds stress prediction. Since the flow is essentially a flat plate boundary layer at this position, results are comparable to Figure 5.9. The JH-ω^h model is the only one that is able to approach the two-component limit near the wall. As in case of the velocity, the measured data show a return towards isotropy in the wall vicinity; this is not in line with theoretical expectations, indicating a systematic measurement error.

In the following, the performance of the DRSMs compared to the Hellsten EARSM k-ω and the Menter SST k-ω model will be assessed. The focus will be on global flow features, such as the end wall separation line or the trajectory of the vortex core, as well as local quantitative comparisons between measured and computed mean flow and turbulence quantities.

Muthanna (2002) determined the centre of the vortex as the location of the maximum streamwise vorticity. From the simulation data, the vortex core was determined us-

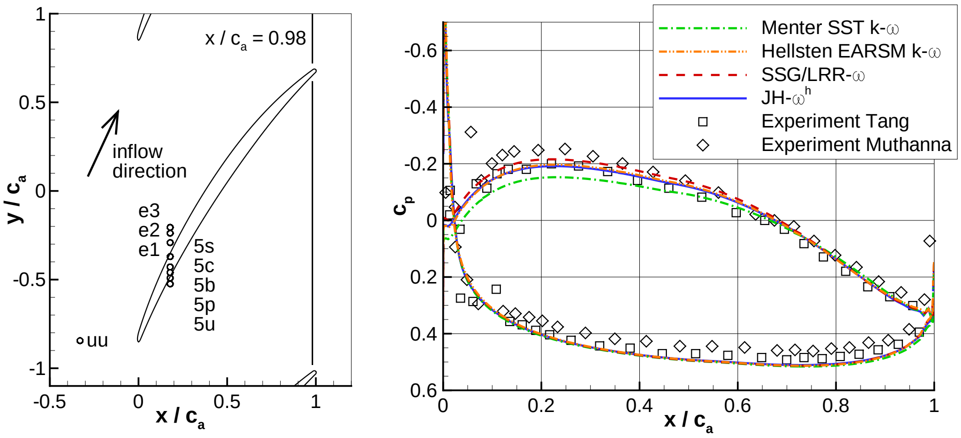

Figure 6.3: Measurement positions (*left*) and pressure coefficient c_p at midspan (*right*) of Virginia Tech compressor cascade (Muthanna, 2002; Tang, 2004).

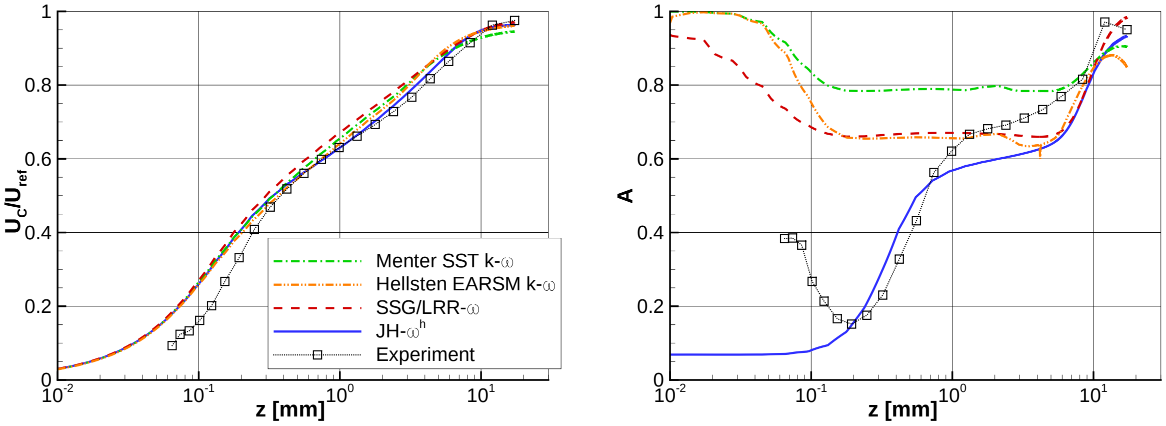

Figure 6.4: Normalised chordwise velocity U_c/U_{ref} (*left*) and turbulence two-component parameter A (*right*) compared with measurements (Tang, 2004) upstream of the blade row at $x/c_a = -0.33$.

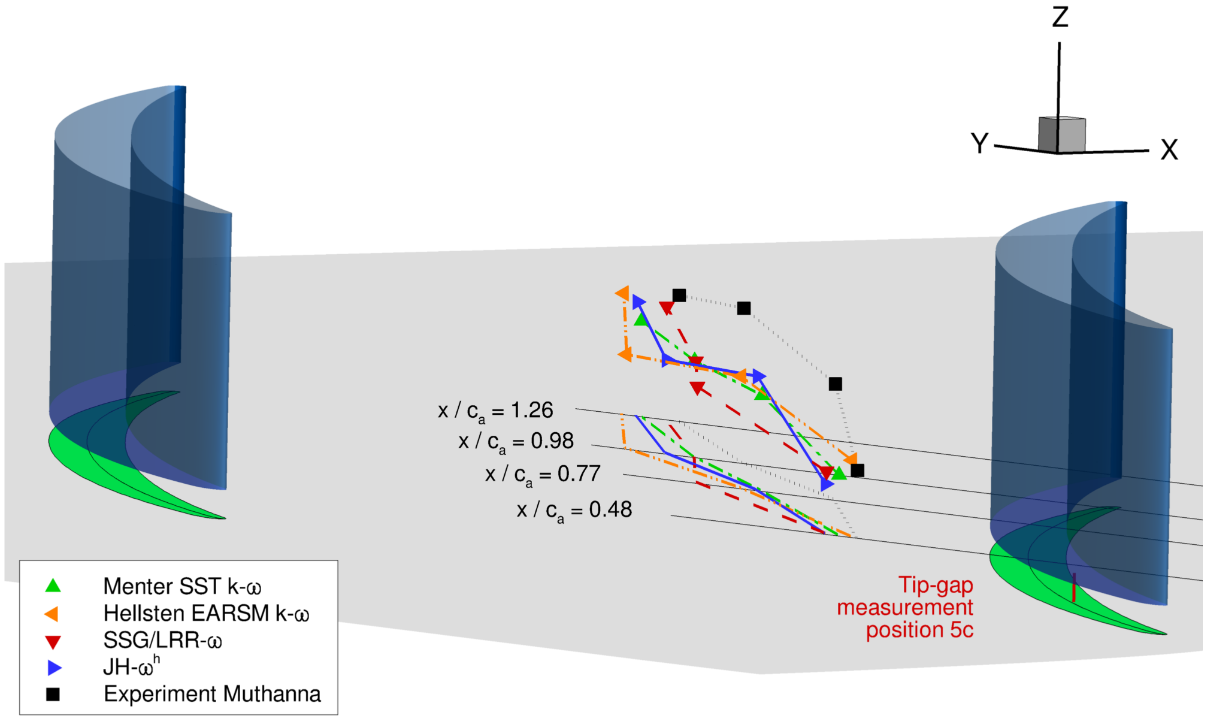

Figure 6.5: Prediction of tip gap vortex centre. The symbols represent vortex centre at different measurement planes. Its trajectory is projected to x-y plane for better comparability. The position for the examined tip gap measurements at $x/c_a = 0.18$, is shown in red.

ing the λ_2-criterion (Jeong & Hussain, 1995), interpreting its minimum value as vortex core. The position of the vortex core (spheres) at four measurement planes is shown in Figure 6.5. To facilitate comparison, its path is also projected onto the side wall (corresponding lines without symbols). From these results it can be argued that none of the employed turbulence models shows a clear advantage over the others and that all of them predict a path that is comparable to the experiment. Similar conclusions can be drawn from the prediction of the separation line on the end wall plotted in Figure 6.6. The limiting streamlines obtained from the wall shear stress vector

$$\tau_{w,i} = \mu n_j \left. \frac{\partial U_i}{\partial x_j} \right|_w \tag{6.1}$$

with the wall-normal vector n_j are coloured with surface pressure. While differences between the models are rather subtle, some improvements can be seen from the simplest to the most complex model. Going from the Menter SST k-ω to the SSG/LRR-ω model yields an improvement in separation prediction close to the blade. Downstream of the blade, the Hellsten EARSM k-ω and the JH-ω^h model produce the best agreement with the experimental separation line.

Tang (2004) measured the mean velocities and Reynolds stresses at various stations in the tip gap. A representative station close to the region where the passage flow separates from the end wall was selected for analysis. It is termed station 5c and its location at $x/c_a = 0.18$ is illustrated in Figure 6.5. To obtain a representation which is independent of the selected coordinate system, invariants of the Reynolds stress anisotropy tensor a_{ij} instead of the Reynolds stress tensor components themselves are plotted in Figure 6.7. Close to a solid wall, turbulence is expected to tend towards

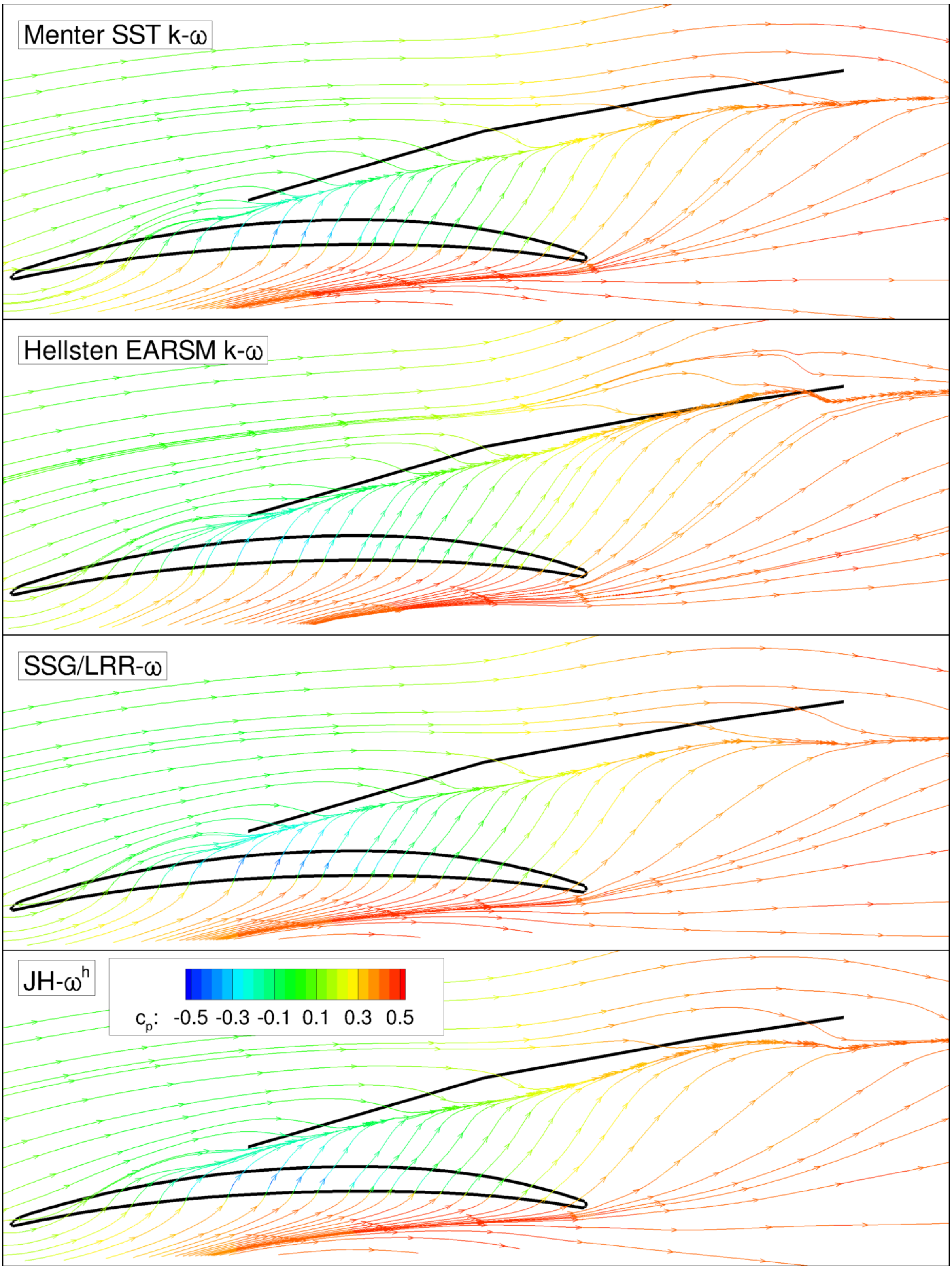

Figure 6.6: Prediction of separation line on the end wall. The blade profile and the separation line from oil flow visualisation (Muthanna, 2002) are plotted in black. The limiting streamlines are coloured with surface pressure coefficient c_p.

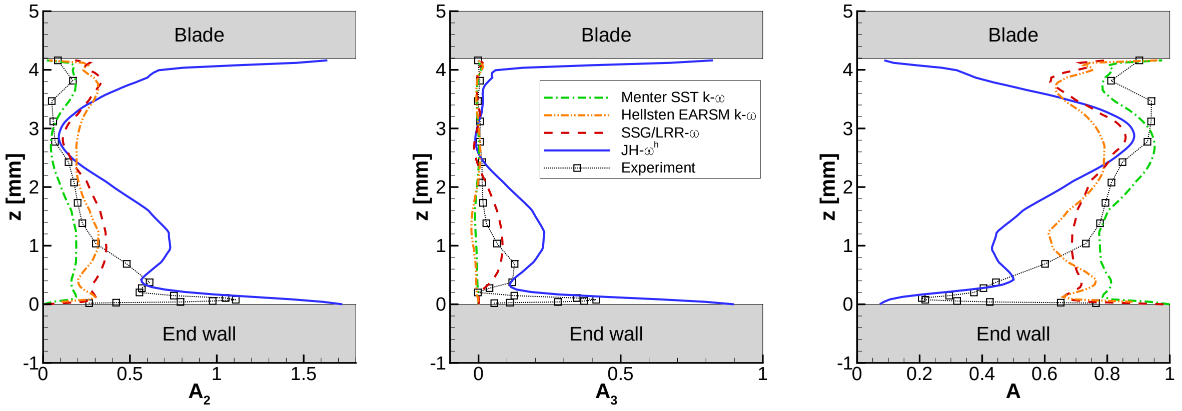

Figure 6.7: Reynolds stress anisotropy invariants in the tip gap at measurement position 5c.

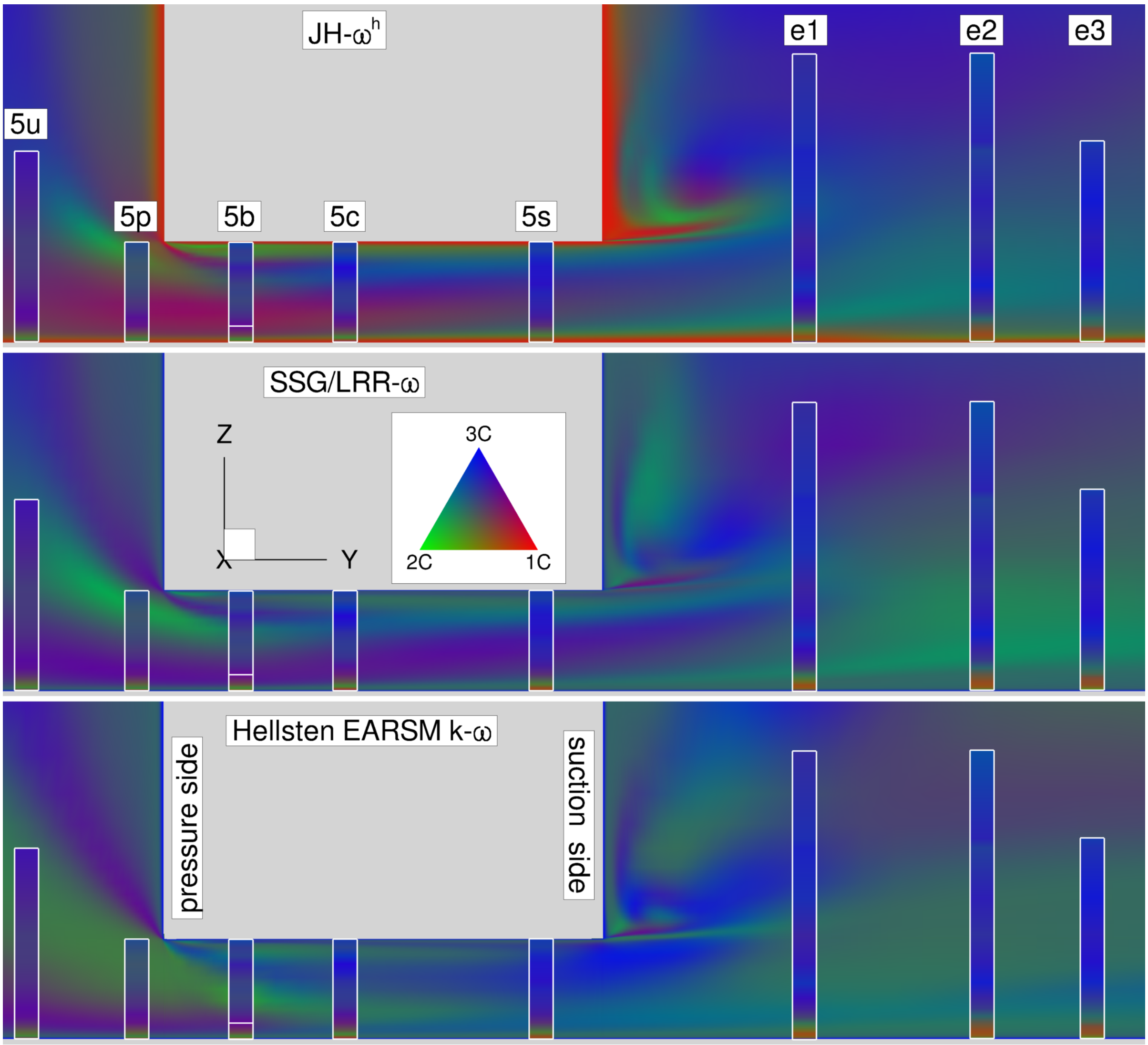

Figure 6.8: Turbulence anisotropy indicated by RGB colours in measurement plane 5 as computed by JH-ω^h (*top*), SSG/LRR-ω (*middle*) and Hellsten EARSM k-ω (*bottom*) models compared with experimental data (Tang, 2004) plotted in white boxes. Solid walls are shaded in grey.

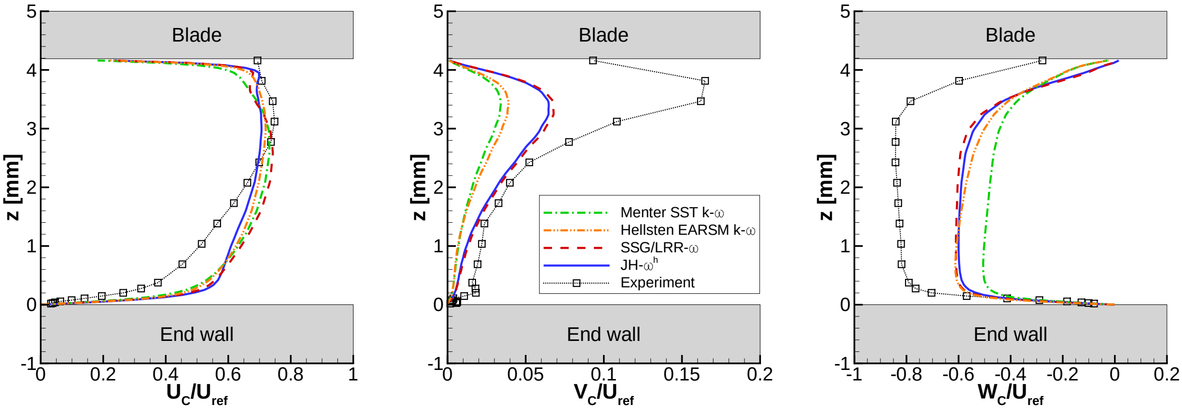

Figure 6.9: Velocity components in the tip gap at measurement position 5c in the coordinate system aligned with the chord.

the two-component limit with $A = 0$. Towards the end wall, experiments show such a trend except for the points closest to the wall, again indicating the systematic measurement error. In contrast, no such trend can be observed towards the blade tip wall, suggesting that the velocities were possibly not measured down to the wall. As shown in Section 5.2 for the generic turbulent boundary layer, it cannot be expected from the LEVM to correctly predict turbulence anisotropy but also the Hellsten EARSM k-ω and the high Reynolds SSG/LRR-ω DRSM are not able to capture the peak of anisotropy at the end wall. The low-Reynolds JH-ω^h DRSM formulation, on the contrary, can predict this peak and qualitatively displays the correct two-component turbulence behaviour at both solid walls in the tip gap. Below the blade-tip boundary layer, turbulence reaches a nearly isotropic state with $A \rightarrow 1$, which is predicted by both DRSMs. Figure 6.8 extends this analysis to the whole plane at $x/c_a = 0.18$ and shows the turbulence anisotropy in RGB colours for the JH-ω^h (*top*), SSG/LRR-ω (*middle*) and Hellsten EARSM k-ω (*bottom*) models. The experimental results are shown as coloured lines at their respective positions. The qualitative difference between the two DRSMs in the lower boundary layer is again evident. In the tip gap, even further away from walls, the JH-ω^h model predicts turbulence closer to the one component limit than the SSG/LRR-ω model. Away from the tip gap and at some distance from solid walls, both DRSMs predict very similar turbulence anisotropy. This finding can also be extended to the Hellsten EARSM k-ω model, which produces results very close to the SSG/LRR-ω model, as seen in Section 5.2. The experiments generally show turbulence much closer to the isotropic state. This can particularly be seen at stations $e1$, $e2$ and $e3$ on the suction side of the blade. For a more comprehensive comparison, high quality planar measurements of all Reynolds stress tensor components would be advantageous.

The mean velocity is shown in a coordinate system aligned with the chord of the blade. U_C is in the direction of the chord, V_C points in the spanwise direction and W_C is the blade-to-blade direction. Figure 6.9 shows the mean velocity components in the specified coordinate system normalised by the inflow velocity U_{ref}. The measured velocities do not vanish at the blade tip wall which is in line with the findings concerning the turbulence anisotropy. Whilst an almost symmetric chordwise velocity profile is predicted by the LEVM, experiments show a higher velocity near the blade tip than near the end wall. This asymmetry is predicted qualitatively by the JH-ω^h and partly by the Hellsten EARSM k-ω and the SSG/LRR-ω DRSM. Furthermore, improvements of the results obtained with DRSMs as compared to LEVM and EARSM results can be seen especially in the secondary flow directions. However, although the structure of the

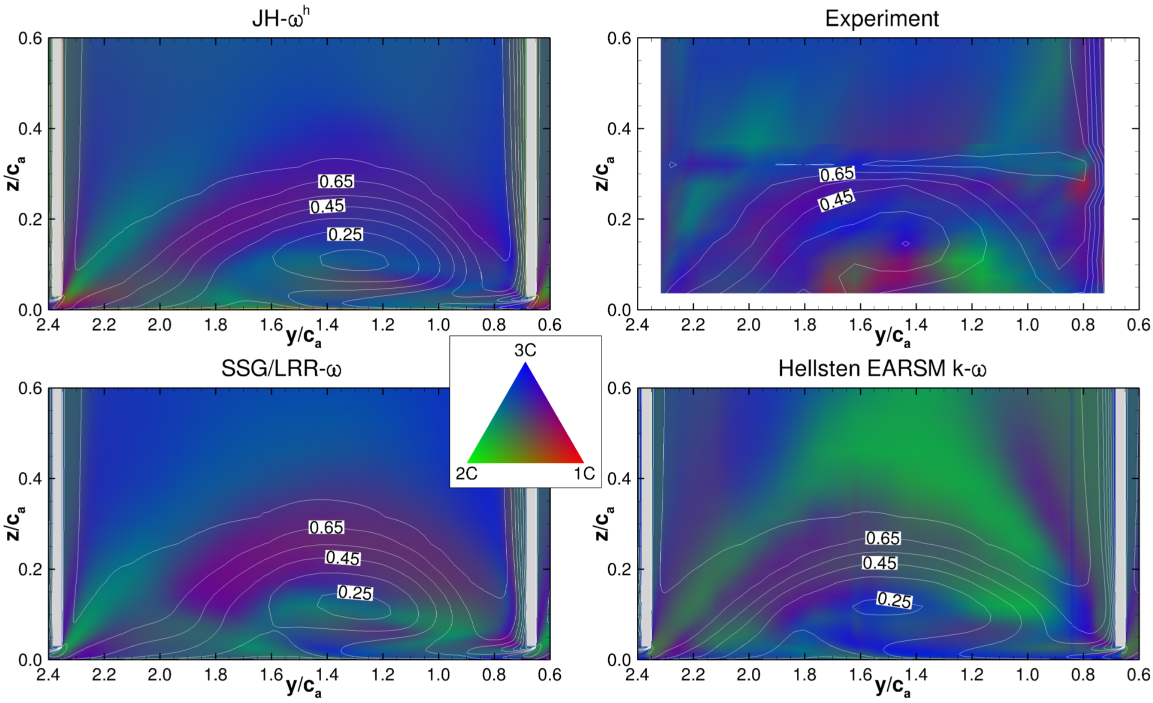

Figure 6.10: Turbulence anisotropy plotted as RGB colours and normalised mean velocity magnitude plotted as white contour lines on a slice through the passage flow at $x/c_a = 0.98$ compared with measured data (Muthanna, 2002).

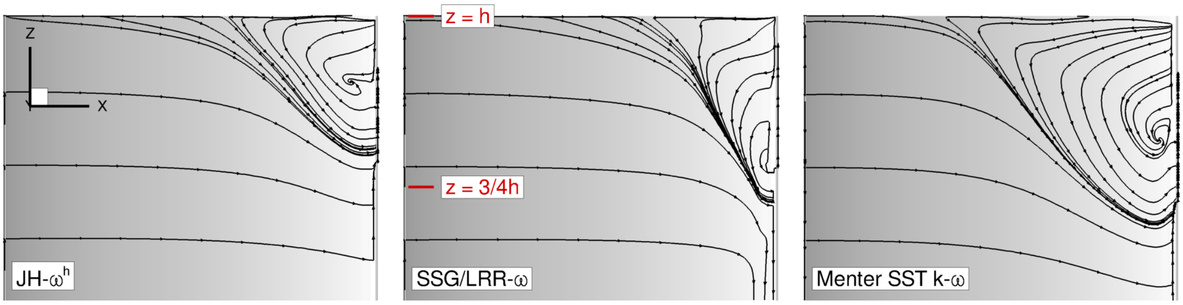

Figure 6.11: Comparison of the corner separation on the blade wall opposite to the tip gap predicted by JH-ω^h (*left*), SSG/LRR-ω (*middle*) and Menter SST k-ω (*right*).

turbulence is predicted much better when DRSMs are employed, the improvement in quantitative agreement of mean velocity data is still far from optimal.

Figure 6.10 shows the turbulence anisotropy of the passage flow coloured by RGB on the slice $x/c_a = 0.98$. The normalised mean velocity magnitude U/U_{ref} is plotted as white contour lines and blade sections are shaded in grey. All turbulence models and the measured data show a region of turbulence close to the two-component limit emanating from the tip gap at an angle of about 45°. The upper edge of the vortex, which features the greatest velocity gradients, is characterised by axisymmetric turbulence. The DRSMs are able to reproduce the general picture as found in the experiments. Only the Hellsten EARSM k-ω predicts a large part of the passage flow as nearly two-component turbulence, which is not in line with the measurements. Turning to the mean velocity field, it can be said that all numerical simulations overestimate the velocity deficit in the vortex core, where there is only a very small region with $U/U_{\text{ref}} < 0.25$ in the measured data. The JH-ω^h model exhibits the greatest deviation in this case.

While vortex breakdown is one mechanism resulting in blockage of the blade passage towards off-design operating conditions, corner separation at the end wall/blade junction can also be a limiting factor. Figure 6.11 shows limiting streamlines obtained by the three turbulence models JH-ω^h (*left*), SSG/LRR-ω (*middle*) and Menter SST k-ω (*right*). LEVMs notoriously predict excessive corner separation bubbles (Spalart, 2010). It is expected that DRSMs can more precisely predict corner separations due to the improved representation of Reynolds stress anisotropy. Unfortunately, only few experiments are available documenting such flow topology features, which are of prime importance for turbomachinery performance prediction. This underlines the need for more, highly accurate measurements specifically addressing topological issues in realistic configurations.

To summarise, it was demonstrated that both the high Reynolds SSG/LRR-ω and the near-wall JH-ω^h DRSMs can be applied to simulate a flow representative of an industrially relevant turbomachinery component. Especially as far as turbulence structure is concerned, they offer improvements over the classical LEVMs or EARSMs. However, it was also seen that these improvements do not always extend to the mean flow quantities.

6.2 Ranque-Hilsch vortex tube

6.2.1 Description

To achieve designs of turbomachinery components with even higher efficiencies, it becomes necessary to consider aerodynamic, thermal, mechanical and acoustical phenomena in a coupled way. With the increasing robustness and accuracy of numerical simulations, a tendency towards multidisciplinary design can be observed. One example is the cooling of thermally loaded turbine blades, for which an accurate description of the internal cooling flows is essential. The cooling ducts are mostly angular, which results in turbulence driven secondary flows. Standard eddy viscosity approaches fail to resolve this kind of secondary flow and hence to accurately predict the heat transfer between the flow and solid structure. Furthermore, the turbulent heat flux, which is usually modelled with a constant turbulent Prandtl number approach, can be computed more accurately by using information about Reynolds stresses. These higher order heat flux models require an appropriate description of Reynolds stresses (Younis *et al.*, 2012).

Another concept to increase the cooling efficiency is to use round cooling pipes with cyclone cooling (Kobiela, 2013). The Ranque-Hilsch vortex tube represents one such flow. It features a swirling flow with the additional effect of temperature separation, whose origin could not yet satisfactorily be explained by the community. The effect was first observed by Ranque (1933) and the tube was optimized with respect to cooling efficiency by Hilsch (1947). Figure 6.12 shows the investigated geometry with the main flow features schematically drawn as streamlines. Gas at constant total pressure and temperature is injected through the four inlet tubes which are attached tangentially to the vortex tube. Before it is expanded into the vortex tube, the flow passes a critical contraction. From there, the gas spirals along the outer wall towards the hot exit which consists of three radially attached outflow tubes. A throttle downstream of the latter is used to set the mass flow. Part of the flow reverses its direction in the inner part of the tube and is directed towards the orifice at the cold exit where it exits at atmospheric pressure. Figure 6.13 shows the vortex tube at the hot end illuminated

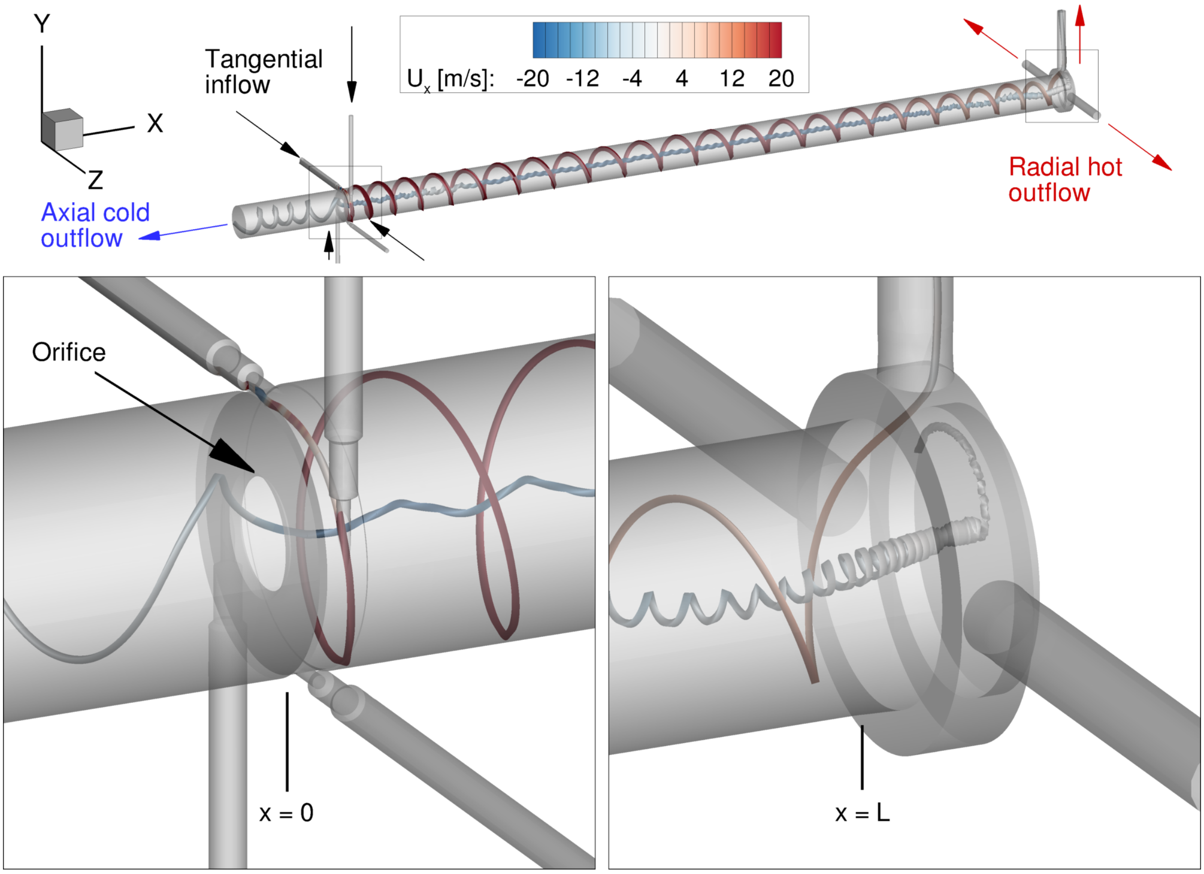

Figure 6.12: Vortex tube geometry and boundary conditions.

by the laser sheet while the vortex core appears dark. Various theories exist about the origin of the temperature separation effect (Doll *et al.*, 2015). They have been reviewed by Eiamsa-ard & Promvonge (2008) and Xue *et al.* (2010). The radial adiabatic compression and expansion driven by the turbulent flow field is one of the explanations which is why it is interesting to investigate how the measured physical effects can be described by the various turbulence models. The vortex tube was investigated within the DLR internal project *TurboVaLd* in collaboration with the *Institute of Propulsion Technology*'s department of *Engine Measurement Systems*. At the time of the project, only the SSG/LRR-ω model was available for the simulation. Due to the significant computational resources required for the unsteady simulation, no results were obtained using the JH-ω^h model after the project was finished. Parts of this section have already been published by the present author (Morsbach *et al.*, 2015*b*).

The model tube has a radius of $R = 15\,\text{mm}$, a length of $L = 700\,\text{mm}$ and an orifice diameter of $R_{\text{cold}} = 6\,\text{mm}$. It was investigated with different optical measurement methods. Velocity profiles were obtained by the Laser-2-Focus (L2F) method (Doll *et al.*, 2014). In addition, filtered Rayleigh scattering (FRS) was used to obtain 2D temperature information as well as velocity information through the measured Doppler shift (Doll *et al.*, 2015). Pressure taps and a flow metre were used to determine the operating point, which is defined by the fraction of gas leaving the cold exit as

$$\epsilon = \frac{\dot{m}_{\text{cold}}}{\dot{m}}. \tag{6.2}$$

All the above experimental data are time-averaged because of the employed measurement methods. For the assessment of the unsteady flow effects, piezoelectric pressure

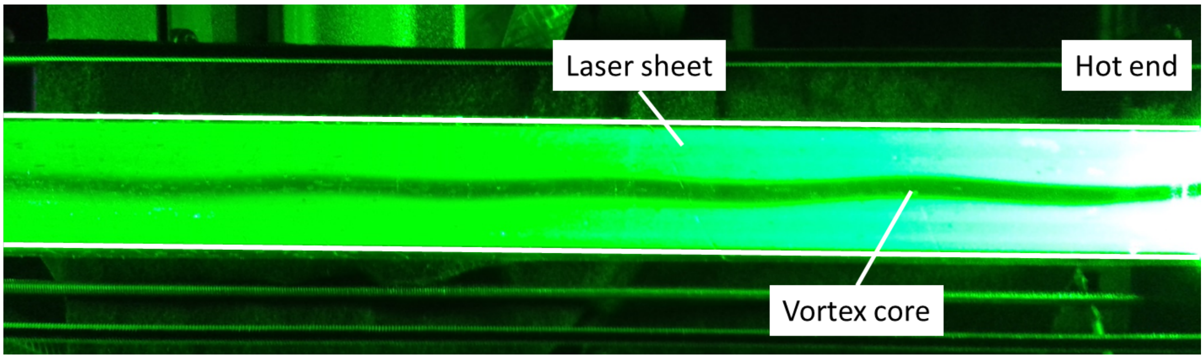

Figure 6.13: Photo of vortex tube experiment showing the part of the tube at the hot end illuminated by the laser sheet with a dark core vortex.

sensors were installed at different axial positions at the tube wall and used to sample the pressure signal at a rate of $50\,\mathrm{kHz}$ (Doll *et al.*, 2015).

6.2.2 Numerical setup

Geometrically, the case can be described simply by intersecting cylindrical and conical elements. However, the tangential connections, especially in the inflow region, pose a significant challenge to the meshing process. If the tubes were meshed with structured topologies, this could only be solved by a non-matching (zonal) interface (Yang *et al.*, 2002), possibly with mixed solid/fluid cells. This would have introduced additional uncertainty about the accuracy in a region of the flow with large gradients. Therefore, the geometry was meshed with a completely unstructured topology without the need for non-matching interfaces using the commercial software Centaur (Schlüß, 2013) Centaur uses the CAD data, which was created in the design of the experiments, as geometry for the mesh. Figure 6.14 shows the resulting mesh in the region of the inflow tubes. The surfaces of all tubes were generally meshed with quadrilateral elements; areas which are geometrically more complex, such as the connection of the inflow tubes to the main tube, were meshed with triangles. Boundary layers were the resolved with hexahedra and prisms, respectively, with the first distance from the wall ensuring the low-Reynolds condition. Finally, the remaining volume was filled with tetrahedra. All inflow and outflow boundaries are treated as Riemann boundaries. The direction of the inflow is along the respective tube. The turbulence intensity is chosen rather arbitrarily because the pipe flow is fully developed when it enters the contraction. While the pressure at the cold outlet is set, it is controlled at the hot outlet to achieve a mass flow of $\dot{m}_{\mathrm{hot}} = 2.33\,\mathrm{g/s}$ per tube. The conditions summarised in Table 6.2 define an operating point of a cold fraction of $\epsilon = 0.3$.

6.2.3 Discussion

A mesh convergence study was conducted to evaluate the influence of the mesh resolution on the flow quantities. Three meshes with 4.0, 5.8 and 12.6 million cells were created and global quantities such as temperature difference between hot and cold outlet and profile data within the vortex tube were compared. The simulations were conducted using the Menter SST k-ω model and the results are summarised in Table 6.3. The variation refers to the difference between minimum and maximum values normalised with the average value. In the outer region of the radial profiles, the velocity

Table 6.2: Boundary conditions for Ranque-Hilsch vortex tube.

Property		Value	
Inflow total pressure	p_t	700.0	kPa
Inflow total temperature	T_t	293.0	K
Inflow turbulence intensity	Tu	5.0	%
Inflow turbulent length scale	L_T	0.7	mm
Cold outflow static pressure	p	103.0	kPa
Hot outflow mass flow	$\dot{m}_{\text{cold}}$	2.33	g/s

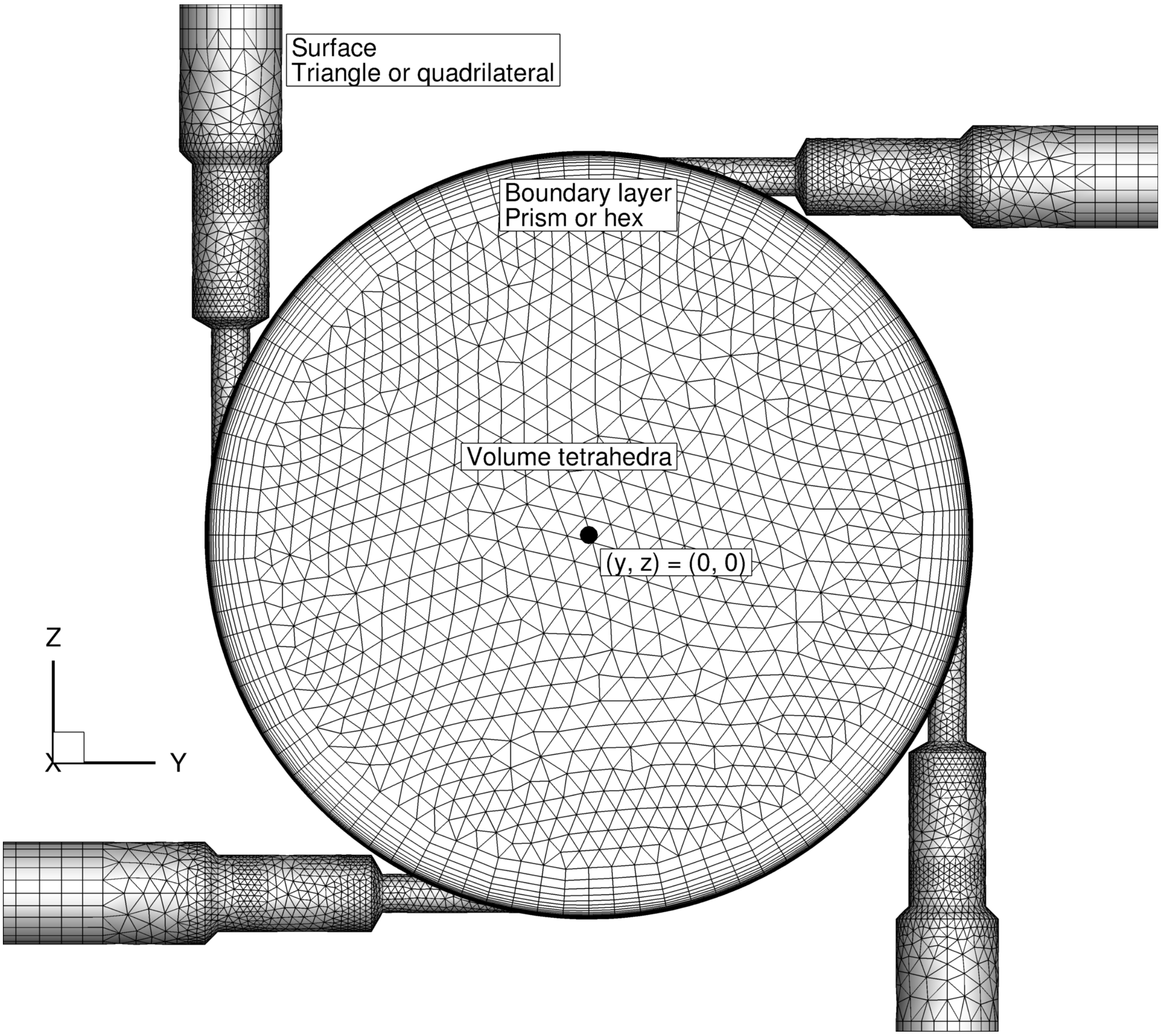
Surface
Triangle or quadrilateral
Boundary layer
Prism or hex
Volume tetrahedra
(y, z) = (0, 0)
Z
X
Y

Figure 6.14: Vortex tube mesh.

Table 6.3: Uncertainty due to the computational mesh for the Ranque-Hilsch vortex tube computed with the Menter SST k-ω model.

Position	Property	Value	Variation
Radial profile, outer region	U	200 m/s	5%
Radial profile, core region	U_x	30 m/s	25%
Radial profile	T	280 K	1%
Outlet hot and cold	ΔT	20 K	20%

U showed a variation of 5%. In the core region, however, the axial velocity U_x could vary by up to 25% due to the small absolute velocity. In contrast, the temperature T was rather robust and showed a variation of only 1% (Schlüß, 2013; Morsbach *et al.*, 2015*b*). The relatively low error in absolute temperature translates into a 20% error in temperature difference ΔT between the hot and cold outlet. All following results were obtained with the mesh of 5.8 million cells as a compromise between the available computational resources and time and the accuracy of the results. They have to be interpreted considering the uncertainties evaluated above.

Experiments have shown that the flow inside the vortex tube is inherently unsteady (Liew *et al.*, 2012). Both visual clues as well as unsteady pressure measurements have confirmed this (Doll *et al.*, 2015). While a converged steady-state solution could be obtained using the Menter SST k-ω and Hellsten EARSM k-ω models, the simulation using the SSG/LRR-ω model did not converge. This was the starting point for the study to investigate if an unsteady RANS (URANS) simulation with a DRSM can reproduce the unsteady features seen in the experiments. The physical time step has to be chosen such that the unsteady phenomena of interest can be resolved. Since the vortex tube has no moving parts, the characteristic frequencies are determined by the flow only. One measure is the frequency based on the circumferential velocity and the radius of the tube. It varies from about $5000\,\mathrm{Hz}$ in the vortex chamber to about $500\,\mathrm{Hz}$ at the hot end of the tube. The time step size Δt was chosen such that the highest frequency was resolved with about 100 time steps. To reduce the computing time of the unsteady simulation, the steady result was used to initialise the solver. It was run until the integral boundary data such as mass flow, temperature and pressure showed statistical patterns. The sum of the mass flow over all four inlets and all four outlets is shown in Figure 6.15. All fluctuations can be attributed to the cold outlet at which the pressure is held constant.

Data sets of different temporal and spatial resolution were recorded in the following time steps. Their positions in the vortex tube are sketched in Figure 6.16. To reduce the amount of storage required, a 2D surface in the $z = 0$ plane over the complete length of the vortex tube was generated in the pre-process by intersection with the 3D mesh and the flow solution was interpolated to this surface on output. Point probes (0D) were introduced at the positions of the pressure sensors in the experiment which allowed recording the complete unsteady simulation. The 2D and 0D time series were evaluated in the frequency domain by a Fast Fourier Transform (FFT) and compared with experimental data.

Quantitative differences between the unsteady time-averaged results of the SSG/LRR-ω model and the steady results of the Menter SST k-ω and Hellsten EARSM k-ω models

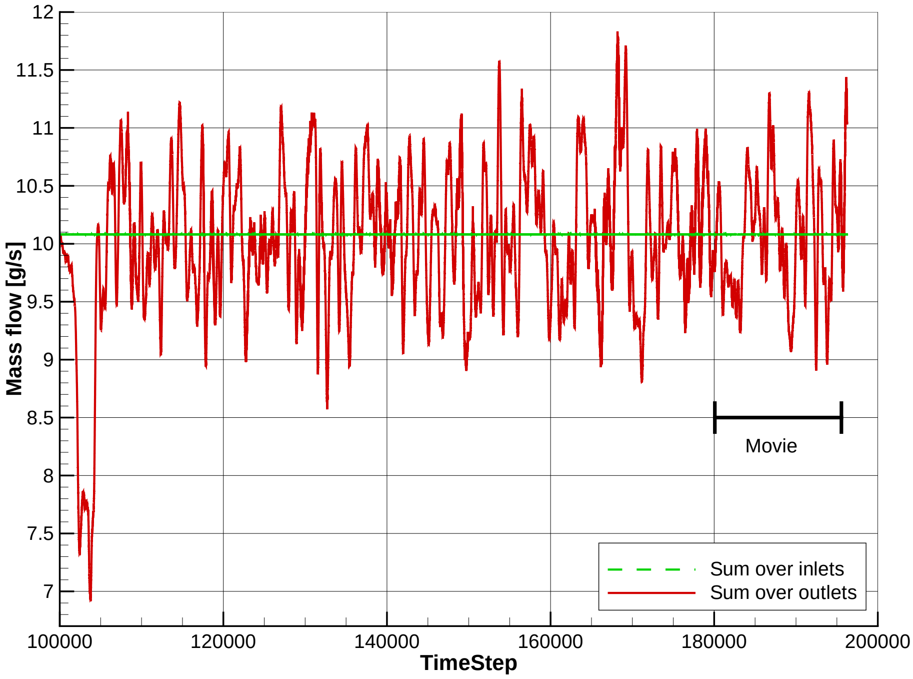

Figure 6.15: Mass flow convergence of the unsteady simulation of the Ranque-Hilsch vortex tube using the SSG/LRR-ω model. The sum over all inlets is shown against the sum over all outlets.

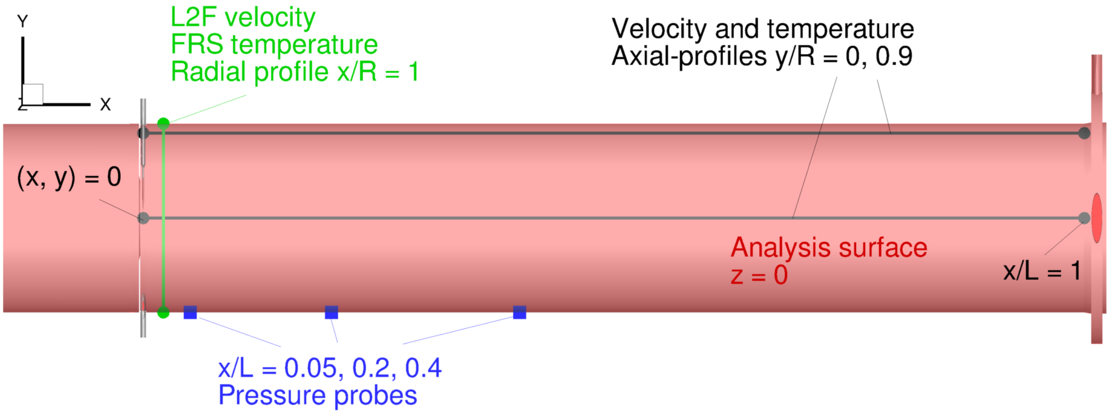
Y
X
Z
L2F velocity
FRS temperature
Radial profile x/R = 1
Velocity and temperature
Axial-profiles y/R = 0, 0.9
(x, y) = 0
Analysis surface
z = 0
x/L = 1
x/L = 0.05, 0.2, 0.4
Pressure probes

Figure 6.16: Sketch of analysis and measurement positions in the Ranque-Hilsch vortex tube. The axes have been rescaled.

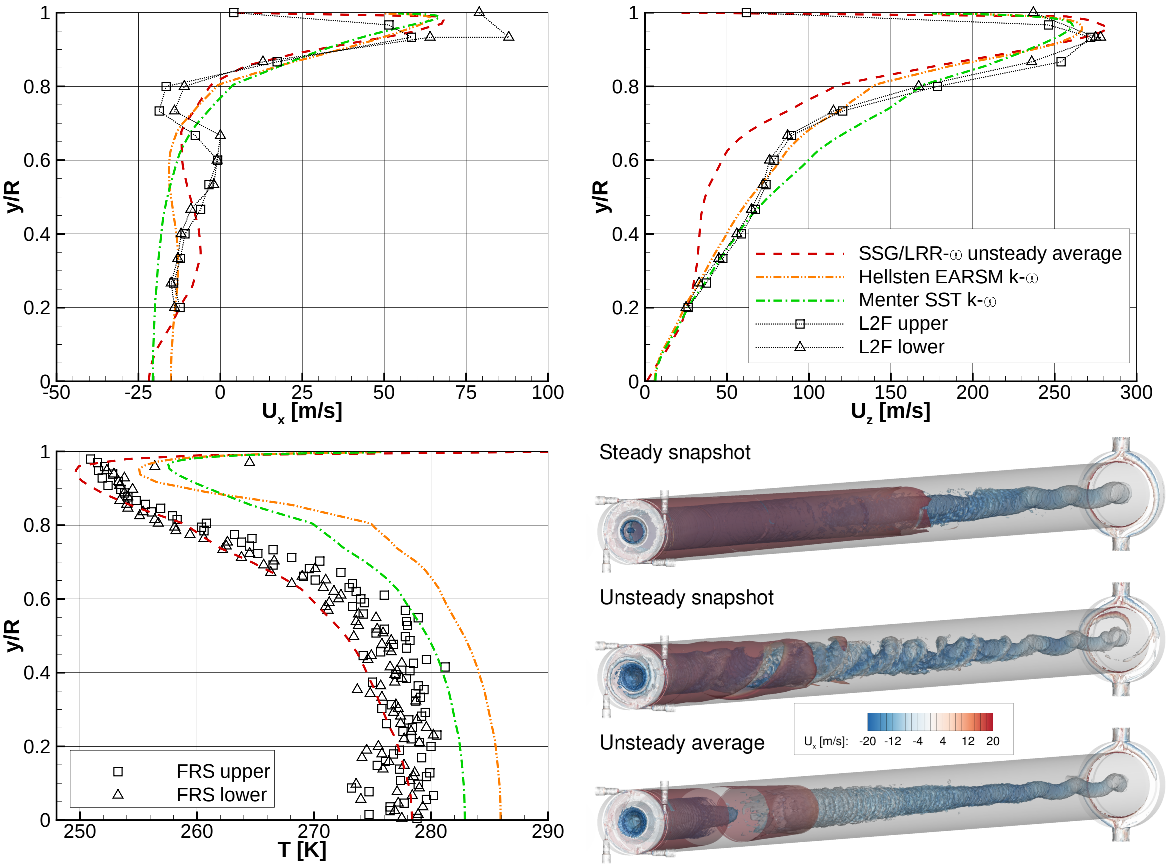

Figure 6.17: Comparison of axial and circumferential velocity U_x (*top left*) and U_z (*top right*) radial profiles with L2F data and temperature T (*bottom left*) radial profile with FRS data at $x/R = 1$. Vortex visualisation using the $\lambda_2 = -1$ isosurface of the steady snapshot, the unsteady snapshot and the unsteady averaged solution obtained with SSG/LRR-ω model (*bottom right*).

are shown in Figure 6.17. The measurements were performed for one diameter of the tube. Due to the rotational symmetry, two measurement points (lower and upper) correspond to the same radius. The predicted axial (*top left*) and circumferential (*top right*) velocities U_x and U_z at $x/R = 1$ are compared to experimental data of the mean flow obtained by the L2F method. A local minimum in U_x (flow towards cold outlet) at $y/R = 0.75$ is evident in the experimental data. In contrast, the Menter SST k-ω model predicts monotonously increasing U_x from the centre to the maximum at the edge of the wall boundary layer. Anisotropy resolving models seem to be required to produce this S-shape, although it is far less pronounced in the steady Hellsten EARSM k-ω solution than in the experiment. However, for the time-averaged URANS solution with the SSG/LRR-ω model, a local extremum appears at $y/R \approx 0.7$ in the averaged solution. The second extremum, a local maximum in U_x is found at $y/R \approx 0.35$ in contrast to $y/R \approx 0.6$ in the experiment. Similar conclusions can be drawn for the circumferential velocity U_z. The experimental data confirm the solid body like rotation in the core flow reported by several authors (e.g. Liew *et al.*, 2012)) up to $y/R \approx 0.4$. A short region of decreased velocity gradient follows up to $y/R \approx 0.6$. This feature is reproduced by neither the Menter SST k-ω nor the Hellsten EARSM k-ω model. Only the averaged unsteady solution with the SSG/LRR-ω model can reproduce the solid body like rotation followed by the region of reduced gradient. Although the experimental data are not matched quantitatively, the qualitative prediction of the trends in velocity is improved if the DRSM is applied in URANS mode.

The measured global temperature separation amounts to $\Delta T = T_h - T_c = 23.8\,\mathrm{K}$. The Menter SST k-ω and the Hellsten EARSM k-ω model underestimate ΔT by $5\,\mathrm{K}$ and $12\,\mathrm{K}$, respectively. In contrast, ΔT is overpredicted by the SSG/LRR-ω model by $8\,\mathrm{K}$. The trend in ΔT is also expressed in the radial temperature profiles at $x/R = 1$ shown in Figure 6.17 (*bottom left*). While both Menter SST k-ω and Hellsten EARSM k-ω models overestimate the temperature near the cold outlet by up to $10\,\mathrm{K}$, it can be reproduced by the averaged unsteady solution of the SSG/LRR-ω model.

Figure 6.17 (*bottom right*) shows the flow topology computed with the latter model using a $\lambda_2 = -1$ isosurface. A snapshot of the unsteady RANS solution (*middle*) shows clear evidence of large scale unsteady effects. The vortical structures rotate around the core flow towards the cold outlet. On average (*bottom*), a straight vortex core is detected in the first 70% of the tube, while a helical structure occurs towards the hot end. It can be seen in the experiment (Figure 6.13) as well as in the snapshot of the not-converged steady state computation (*top*) and might, therefore, be attributed to a steady flow feature induced by the asymmetry of the hot end.

Figure 6.18 shows the averaged velocity components U_x, U_y, U_z and temperature T computed with the SSG/LRR-ω model in the $z = 0$ plane plotted from the orifice at the cold outlet to the hot end. For quantitative comparison, profiles at constant $y = 0$ and $y/R = 0.9$ are plotted in Figure 6.19. The computed flow in the vortex tube can be divided into three regions distinguished by axial temperature gradient, radial temperature gradient, axial velocity and secondary flow structures. The following analysis attempts to link these observations.

The first region extends from the cold outlet to approximately $x/L = 0.25$. There, the radial temperature minimum can be found at about $y/R = 0.95$ instead of the core region resulting from the expansion of the injected gas. At all radial positions, the axial temperature gradient is at its maximum value in this part of the vortex tube. The region exhibits a conical structure of nearly vanishing negative axial velocity. It is confirmed experimentally by the L2F measurements as shown in Figure 6.17 for

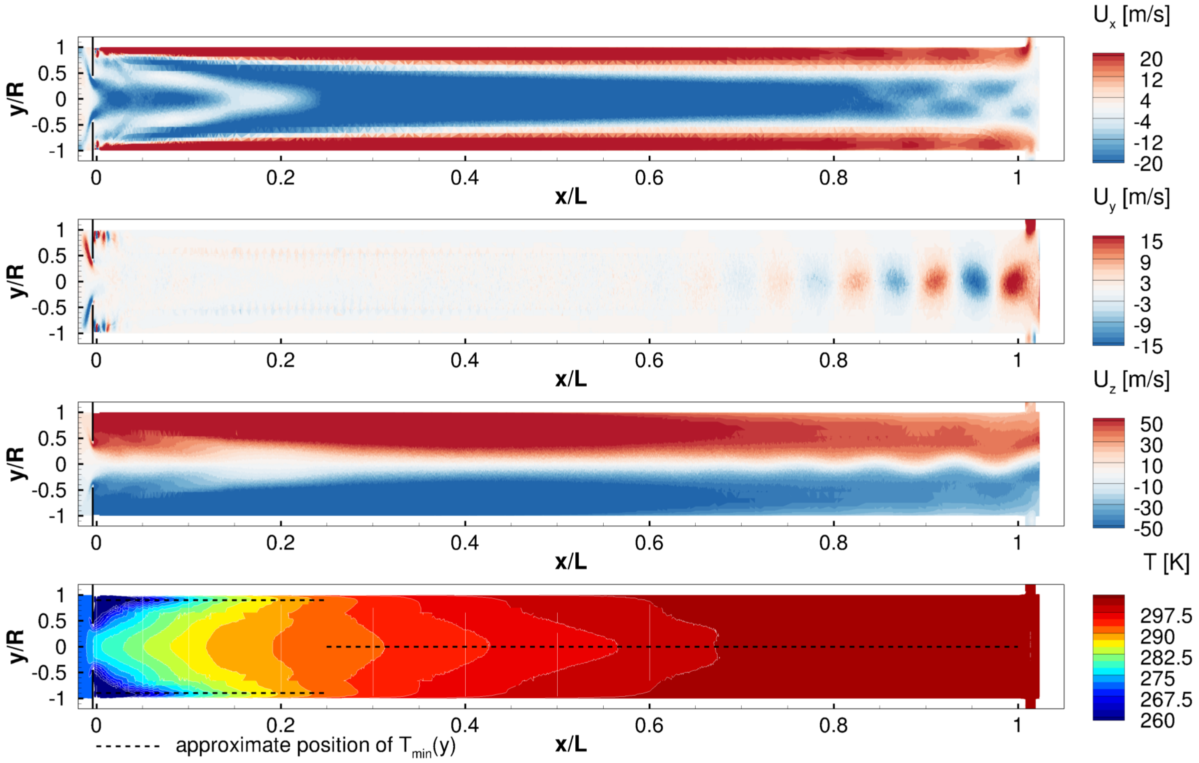

Figure 6.18: Contours of average velocity components U_x, U_y, U_z and temperature T in the $z = 0$ plane from the 2D data set computed with the SSG/LRR-ω model.

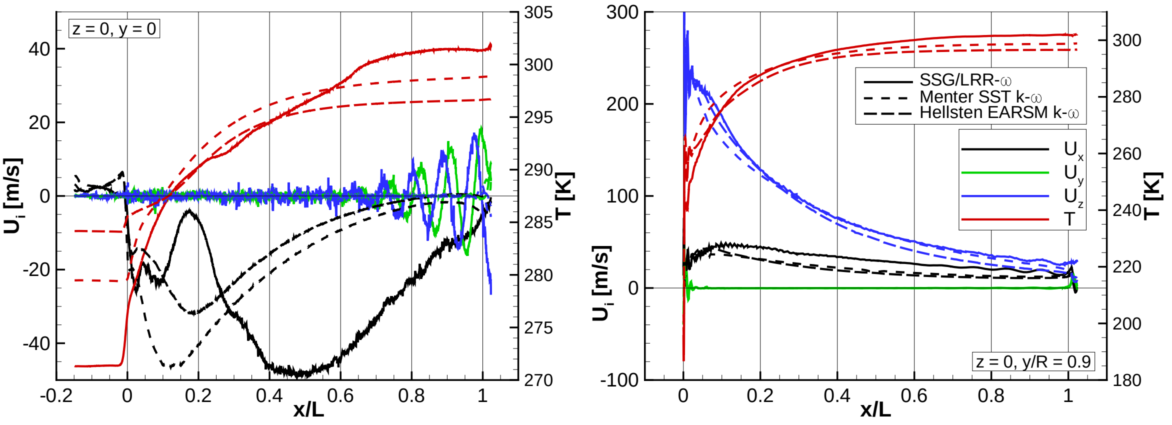

Figure 6.19: Velocity U_x, U_y, U_z and temperature T profiles in the $z = 0$ plane at $y = 0$ (*left*) and $y/R = 0.9$ (*right*) extracted from the steady solutions computed with the Menter SST k-ω and Hellsten EARSM k-ω models, respectively, and the unsteady 2D data set computed with SSG/LRR-ω model.

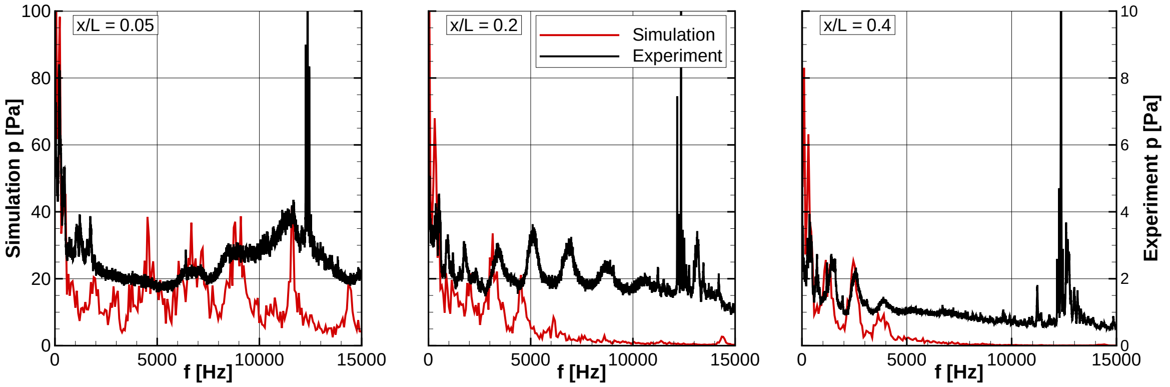

Figure 6.20: Fourier transform of pressure signal obtained from the unsteady computation with the SSG/LRR-ω model from the 0D data set compared to measured data at $x/L = 0.05, 0.2$ and 0.4.

a single axial position $x/R = 1$. This local axial velocity extremum does not occur beyond $x/L > 0.15$. The direct effects of the injection play a major role in the flow topology up to about $x/L = 0.025$. Fluctuating horse shoe vortices develop around the four jets injected into the vortex chamber.

The second region is characterised by a moderate axial temperature gradient from $x/L = 0.25$ to $x/L = 0.65$. At the beginning of the region at $x/L = 0.25$ the temperature minimum moves from the outer region to the core region as indicated by the dashed line. From there to the hot end, the radial temperature minimum can be found at $y = 0$. While the axial and circumferential velocities decay monotonously in the peripheral region, the axial velocity in the core reaches its greatest negative value at $x/L = 0.5$. No significant secondary flow structures develop in this region.

From $x/L = 0.65$ to the hot end, the axial temperature gradient tends to and reaches zero at about $x/L = 0.9$. At $y = 0$, the axial velocity linearly tends to zero. Secondary flow structures start to develop and manifest themselves as the helical structure of the λ_2 isosurface (Figure 6.17, *bottom right*). They can be seen in all velocity components in Figure 6.18. Towards the hot end, the intensity of the vortices mixing the core flow with the peripheral flow increases. Figure 6.19 clearly shows increasing amplitudes of the oscillations in U_y and U_z at $y = 0$. Due to the enhanced convective mixing of fluid, also the radial temperature gradient nearly vanishes. It cannot be definitely concluded within this study if this is a flow feature due to the asymmetry of the hot outlet configuration or a general feature of the vortex tube.

The steady-state results obtained with the Menter SST k-ω and Hellsten EARSM k-ω models are plotted in Figure 6.19 for comparison. At $y/R = 0.9$ they only differ quantitatively from the averaged results obtained with the unsteady SSG/LRR-ω simulation. For the former, the temperature rises quicker while the axial velocity decays faster and both quantities reach a nearly constant level at about $x/L = 0.5$. On the centreline, however, the velocity and temperature fields differ qualitatively. No region of partial stagnation is predicted by the steady simulations. Furthermore, neither the LEVM nor the EARSM predict secondary flow structures or the linear decay of axial velocity at the hot end. These features are only predicted by the DRSM. Indirect evaluation of the velocity components by the Doppler shift from the FRS data (Doll *et al.*, 2015) show a strongly oscillating axial velocity at $y = 0$ contradicting the all above simulation results. Direct velocity measurements in this area are required to investigate the flow field in this region.

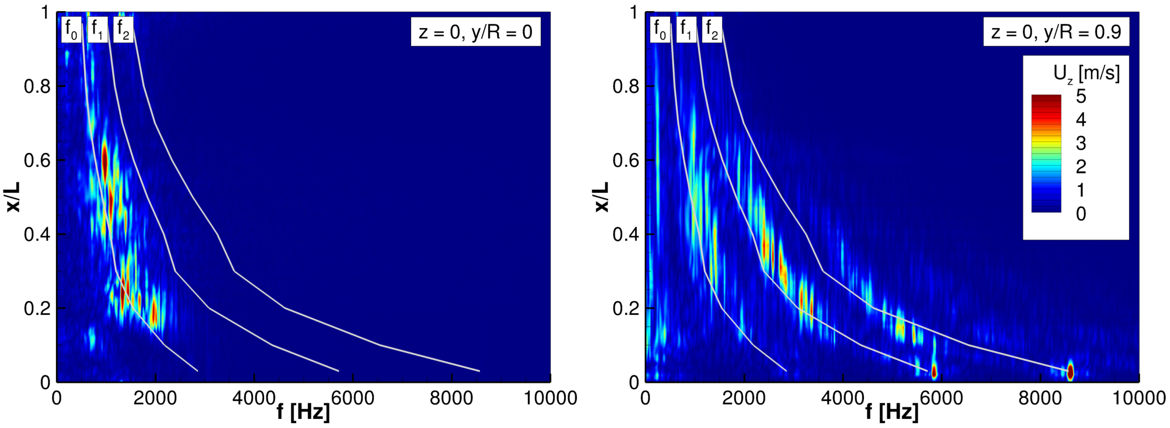

Figure 6.21: Fourier transform of the circumferential velocity U_z at $z = 0$ on the axis (*left*) and at $y/R = 0.9$ (*right*) from the 2D data set computed with the SSG/LRR-ω model.

Figure 6.20 shows the frequency content of the pressure signal at the axial positions $x/L = 0.05, 0.2$ and 0.4 measured at the wall of the tube. The experimental data show dominant peaks at a frequency of about $12.5\,\mathrm{kHz}$, which is not present at any station in the numerical results. The spectra also differ at lower frequencies in the first $20\,\%$ of the vortex tube. At $x/L = 0.4$, the dominant frequencies and its harmonics correspond to the circumferential velocity at this axial position of the simulation. The experimental data also show peaks at these frequencies. To investigate the relationship between circumferential velocity and dominant frequency it is instructive to look at the spatially resolved Fourier analysis. Figure 6.21 shows the amplitude of the circumferential velocity signal dependent on axial position and frequency for the radial positions $y/R = 0$ and 0.9. Liew *et al.* (2012) argue that the dominant frequency in their unsteady velocity signal correlates with the maximum vorticity. For this reason, the frequency

$$f_0 = \frac{U_{z,\max}}{2\pi r(U_{z,\max})} \tag{6.3}$$

of the main vortex, defined by the maximum circumferential velocity and the corresponding radius, is computed at discrete stations $x/L \in [0.03, 0.97]$. The resulting base frequency f_0 and its first two harmonics f_1 and f_2 are also plotted in Figure 6.21. In the outer tube ($y/R = 0.9$, (*right*)), all three frequencies are dominant over large parts of the vortex tube. They correspond to the maximum circumferential velocity at the respective axial position. Especially in the vortex chamber, where the high pressure gas is injected into the tube, the two harmonics dominate. On the axis ($y/R = 0$, (*left*)), however, only the base frequency has a significant contribution. This supports the experimental findings of Liew *et al.* (2012), who stated that contributions to the base frequency are found mainly on the centre line while higher harmonics become visible at greater radii.

This section demonstrates that a DRSM can be successfully used in URANS mode to reproduce unsteady features in a complex swirling flow. While the quantitative agreement with experimental results still leaves room for improvement, the DRSM shows qualitatively improved results compared to the other two models. In terms of turbulent transport of heat, future studies could include the investigation of the influence of different turbulent heat flux models.

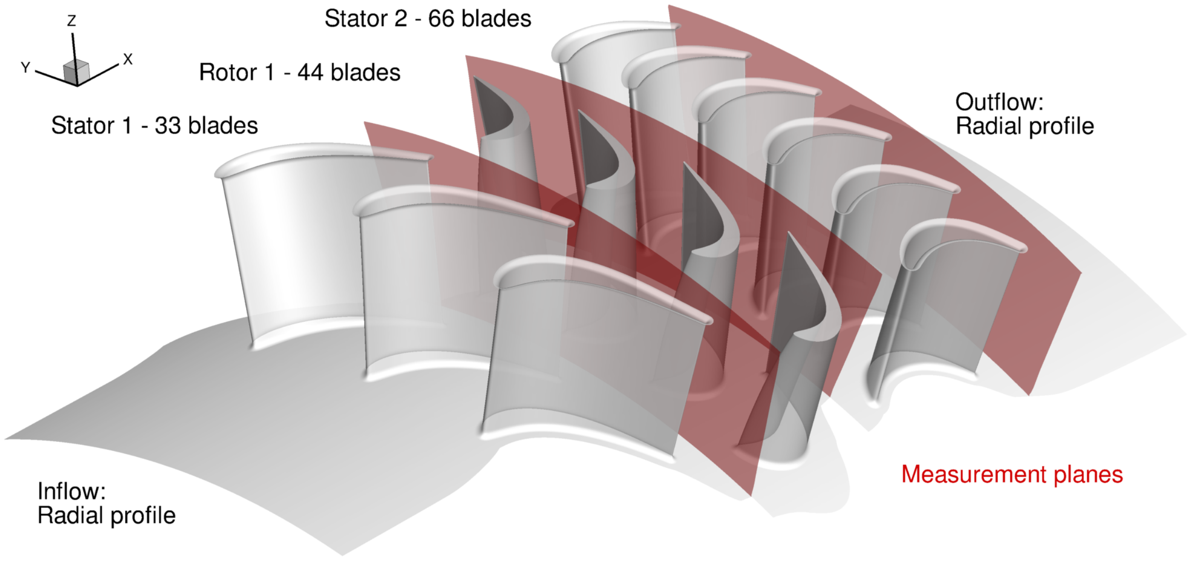

Figure 6.22: 1.5 stage cold air turbine test rig of the *Institute of Jet Propulsion and Turbomachinery* at the *RWTH Aachen University*. Measurement planes of five hole probes are shaded in red.

6.3 One and a half stage cold air turbine

6.3.1 Description

The aim of this section is to investigate the performance of the DRSMs in a case that is representative of a practical turbomachinery application. A realistic configuration consists of several stator and rotor blade rows. Both downstream and upstream interaction between the rows can be found due to wakes and potential effects. Furthermore, secondary flows, for which DRSMs are expected to yield a superior predictive accuracy, develop due to the interacting end wall and blade boundary layers. A phenomenon which shall not be investigated in this thesis is laminar to turbulent transition. Therefore the configuration should be computable in fully turbulent mode without losing too much accuracy. Finally, and most importantly, high quality measurement data which allow for the assessment of turbulence models through more than global data or radial traverses should be available. Considering all the above requirements, the 1.5 stage cold air turbine rig operated by the *Institute of Jet Propulsion and Turbomachinery* at the *RWTH Aachen University* was selected to serve for this purpose.

An overview of the configuration is given in Figure 6.22 and global properties of the turbine are summarised in Table 6.4. The annulus has a constant cross section with constant hub and shroud radii at 245 mm and 300 mm (shroud not plotted). In this document, the blade rows are referred to as stator 1, rotor 1 and stator 2. All stator blades are equipped with fillets of radius 2 mm at hub and tip, while the rotor blade has a hub fillet of the same radius and a radial tip gap of 0.3 mm. Transition is enforced on the suction side of stator 1 to avoid a laminar separation bubble. Compared to the chord length, the height of the blades is relatively small. Hence, secondary flows and 3D effects are more pronounced. The basics of secondary flows encountered in turbomachinery are described in detail by Langston (2001) and Poehler *et al.* (2015) have revisited them in the context of this case. Compared to the compressor cascade (see Section 6.1), the Mach numbers are increased but the Reynolds number is in the

Table 6.4: Properties of RWTH Aachen cold air turbine rig (Niewoehner *et al.*, 2015).

Property		Value	Unit
Rotor speed	Ω	3500	1/min
Torque	τ	450	Nm
Inlet total temperature	$T_{t,\text{in}}$	329.15	K
Inlet total pressure	$p_{t,\text{in}}$	163.250	kPa
Total pressure ratio	Π	1.294	
Mass flow	$\dot{m}$	8.1	kg/s
Radius at hub	r_{hub}	245	mm
Radius at shroud	r_{shroud}	300	mm
Channel height	h	55	mm

Table 6.5: Blade properties of RWTH Aachen cold air turbine rig (Niewoehner *et al.*, 2015).

Property		Stator 1	Rotor 1	Stator 2	Unit
Number of blades	N_{blades}	33	44	66	
Pitch /chord	t/c	0.9	0.98	0.71	
Height /chord	h/c	0.95	1.40	1.51	
Height / axial chord	h/l_{ax}	1.45	1.77	1.57	
Radial tip gap		–	0.3	–	mm
Fillet radius	r_{fillet}	2	2	2	mm
Reynolds number	Re	810	520	330	10^3
Inflow Mach number (midspan)	M_{in}	0.145	0.22	0.26	
Outflow Mach number (midspan)	M_{out}	0.47	0.50	0.38	

same order of magnitude.

Various studies about this turbine configuration were performed both numerically and experimentally. An issue was the influence of axial spacing between the blade rows. Behre *et al.* (2012) performed a numerical study employing unsteady simulations with the Wilcox (1988) k-ω model. They found an increasing isentropic efficiency with decreasing axial spacing. Furthermore, they concluded that the trends could also be observed if transition was neglected. Restemeier *et al.* (2012) compared the numerical results to experimental data obtained by five hole probes in planes between the blade rows. Unsteady simulations were found to improve the agreement between numerical and experimental results. The effect of non-axisymmetric end wall contouring and 3D aerofoil design on losses and secondary flows was investigated in a two-part paper (Poehler *et al.*, 2015; Niewoehner *et al.*, 2015). A purely numerical study was focussed on the effect of platform misalignment (Kluxen *et al.*, 2014). For a detailed description of experimental setup, the reader is referred to the literature cited above. In order to assess the performance of different turbulence models, the base configuration of the above studies has been selected (Niewoehner *et al.*, 2015).

6.3.2 Numerical setup

The block structured mesh was created using the template based in-house tool PyMesh (Weber & Sauer, 2016). An S2m mesh defines the annulus and the radial resolution. Each blade row is meshed separately with interfaces introduced at roughly half the axial gap. The geometry of the blade is supplied by CAD data without fillets, which are created during the meshing process. All solid walls are resolved with $y^+ \sim 1$.

For steady computations, the configuration consists of one blade passage per row with mixing planes at the interfaces between stator and rotor systems. Due to the different numbers of blades, the periodicity is different for each blade row. This is acceptable in a mixing plane approach because the information exchanged between blade rows is circumferentially averaged. In unsteady computations, on the other hand, no such averaging is performed and the periodicity is required to be the same for the whole configuration. The turbine has been designed with this restriction in mind and the blade numbers were chosen, such that rotational periodicity with 11 segments in total can be obtained. For this purpose, 3 blade passages of stator 1, 4 blade passages of rotor 1 and 6 blade passages of stator 2 are generated as one segment as shown in Figure 6.22. The exchange of information between the blade rows is realised using a fully conservative method for non-matching (zonal) interfaces (Yang *et al.*, 2002). 768 physical time steps were used to resolve one segment passing.

There are methods to reduce the computational overhead for unsteady simulations due to duplicated blades. One such method is the phase lag approach (Schnell & Nürnberger, 2004) which is limited to the coupling of 2 blade rows and, hence, cannot be applied in this case. Another option would be a computation in the frequency domain using the harmonic balance method (Hall *et al.*, 2002). This method, however, requires *a priori* knowledge about the involved frequencies of periodic flow field. Only unsteady effects with energy in these frequencies and their harmonics are then resolved. This is not desirable when unsteady effects with no direct relation to the blade passing frequency are of interest. Hence, to rule out uncertainties concerning the solution method and to focus on the effect of the turbulence model, the increased computational effort of a time domain solution was invested.

With one blade per row for the steady simulations, the mesh has a total number of 7.6 million cells. The structured blocks have been split to achieve a 90% parallel efficiency on 48 processes. The mesh for the unsteady simulations with duplicated blades has 33.2 million cells with a 90% parallel efficiency on 144 processes. To evaluate the influence of the mesh on the steady solution, a fine mesh was created by doubling the resolution in all three index directions resulting in a mesh with 61.1 million cells. While the original mesh resolution is already high for overnight design computations in an industrial context, the fine mesh requires too many resources for a practical RANS computation. Therefore, after evaluation of the mesh dependence, all subsequent computations were performed on the original mesh.

Inflow and outflow boundary conditions were available in the form of measured radial traverses. At the inflow, total pressure, total temperature and flow angles were specified for the mean flow quantities. The turbulence intensity and length scale were given for the turbulence equations to generate isotropic turbulence. At the outflow, the static pressure was prescribed. All interfaces except for the zonal ones were computed using 2D non-reflecting boundary conditions (Giles, 1990).

The steady computations using the Menter SST k-ω and the Hellsten EARSM k-ω models were initialised with an S2m averaged solution. To accelerate the convergence and minimise reasons for numerical instability, both RSM simulations were initialised with the solution obtained with the Menter SST k-ω model. All unsteady computations were set up as restart from the respective steady result.

Two measures were taken to enhance the numerical stability of the DRSMs in this complex configuration. First, the SSG/LRR-ω model was run with SGD instead of GGD for the Reynolds stresses for both steady and unsteady simulations. As pointed out in Section 3.2.5, the diffusion model has only minor influence but greatly enhances stability. Second, problems occurred with the JH-ω^h in the unsteady simulation, which crashed where the wake of the rotor hit the downstream stator due to spurious values of ω^h. The stability analysis in Section 3.4 showed that a lower limit of ω^h/S could help prevent spurious solutions. Following this conclusion, the value of ω^h was explicitly limited after the update as

$$\omega^h \to \max\left[\omega^h, \sqrt{\frac{3}{2}S_{ij}S_{ij}}\right] \quad \Leftrightarrow \quad \frac{\omega^h}{S} \geq \frac{\sqrt{3}}{2}. \tag{6.4}$$

This limiter was originally derived in an eddy viscosity context for realisability reasons (see e.g. Durbin, 2009) and is used to remedy the stagnation point anomaly. When it is used in conjunction with the JH-ω^h model, no influence on the results of the validation cases could be detected. It was found crucial to make the unsteady simulation possible. It has to be mentioned, though, that this is an *ad hoc* fix, which stands in contrast to the idea of a more general modelling foundation of DRSMs. Unsteady computations with the Hellsten EARSM k-ω model, on the other hand, could not be done successfully with same number of time steps and CFL number as the other models and are not considered here.

6.3.3 Post-processing

The steady and unsteady simulation results are post-processed to obtain data which can be compared to experimental results. Five hole probe data obtained in planes at half the axial gap behind the respective trailing edges as shown in Figure 6.22 are used for this comparison. The probes were fixed in the stator frame of reference and traversed to obtain radially and circumferentially resolved data. By nature of this measurement method, the data are time-averaged over many rotor blade passings. Hence, from the unsteady simulation an average was computed for one passing of the complete segment.

The in-house post-processing tool POST is used to place analysis planes in the 3D solution at the locations specified by the experiment and to interpolate the flow solution to these planes. They are placed in the stationary frame of reference which is the natural choice behind the stators. The analysis plane of the rotor, on the other hand, is placed in the stator frame of reference of stator 2. In the unsteady averaged results, this plane sees the circumferentially averaged rotor wakes and vortex effects in the stator system. Flow structures generated by the upstream stator, on the other hand, are resolved circumferentially. This is exactly what was measured by the five hole probe. The mixing plane in the steady simulation, however, prohibits a direct comparison with the experiments. The steady results could either show rotor flow features in the rotor frame of reference or the mixed out state behind mixing plane. In any case, no structures from the upstream stator 1 would show because of the mixing plane between stator 1 and rotor 1. Hence, the analysis planes are only evaluated for unsteady simulations. Radial distributions, on the other hand, are computed by circumferential mass averaging on the extracted planes using radial bands. Therefore, they can be compared for rotor as well as stator rows for both steady and unsteady simulations. In this comparison, the influence of the mixing plane approximation can be seen.

Secondary flow features in the 3D flow field are visualised by isosurfaces of λ_2 (Jeong & Hussain, 1995). By doing so, 3D secondary flow structures can be associated with features on the analysis planes. In the rotor row, all velocity gradients are evaluated in the rotating frame of reference. The streamwise vorticity ω_{sw}, defined by

$$\omega_{\mathrm{sw}} = \frac{U_i \epsilon_{ijk} \frac{\partial U_k}{\partial x_j}}{\sqrt{U_q U_q}} \tag{6.5}$$

is computed to characterise the vortices and visualise the structures on the analysis planes. While this is straightforward from the numerical results, the missing information about the axial derivative of the measurements at constant axial position needs to be addressed. This was done under certain assumptions as described in Appendix B.2.

6.3.4 Discussion

The discussion of results starts with an evaluation of the convergence of the steady simulations. Figure 6.23 shows mass the flow convergence and the average residual of the RANS equations (*bottom right*). Machine zero would be 10^{-16} in double precision or 10^{-8} in single precision. All computations were performed with double precision. It can, hence, be stated that, in contrast to the validation cases, machine zero is not reached for any model. This behaviour is in line with experience in this kind of configuration. Only the simulation using the Menter SST k-ω model converged well below single precision machine zero. On the fine mesh, the convergence rate is expectedly much slower but eventually the simulation converges below single precision machine zero. Simulations using the Hellsten EARSM k-ω and SSG/LRR-ω models level out at 10^{-6} still showing low frequency oscillations. For the JH-ω^h the residual levels out even one order of magnitude higher. This indicates that all RSMs try to resolve unsteady effects within the single blade rows, which are dissipated or do not occur with an LEVM.

The conclusion is reflected in the respective mass flow convergence plots in Figure 6.23 for Menter SST k-ω (*top left*), Menter SST k-ω on the fine mesh (*top right*), SSG/LRR-ω (*middle left*), Hellsten EARSM k-ω (*middle right*) and JH-ω^h (*bottom left*). All zoomed boxes have the same scaling of the mass flow axis except for the JH-ω^h model. No steady convergence could be obtained for the latter with a mass flow variation of 0.25%. The other models show a variation below 0.01% and the Menter SST k-ω model actually converged to machine zero with a variation of 10^{-5}%. On the fine mesh, the Menter SST k-ω model initially shows a similar degree of unsteadiness as the other models but eventually converges towards a steady-state solution with a variation of 10^{-4}% after 10^5 time steps. Another quantity to judge the convergence is the variation of the isentropic efficiency (Bräunling, 2009) measured between the inlet and the outlet of the complete configuration. Since typical design improvements are on the order of 0.1%, the JH-ω^h cannot be regarded as converged with a variation in the same order of magnitude. Both the SSG/LRR-ω and the Hellsten EARSM k-ω results can be regarded as converged since they show variations smaller by two orders of magnitude. For a fair comparison of between the DRSMs and the other models, averaged results from unsteady computations need to be obtained.

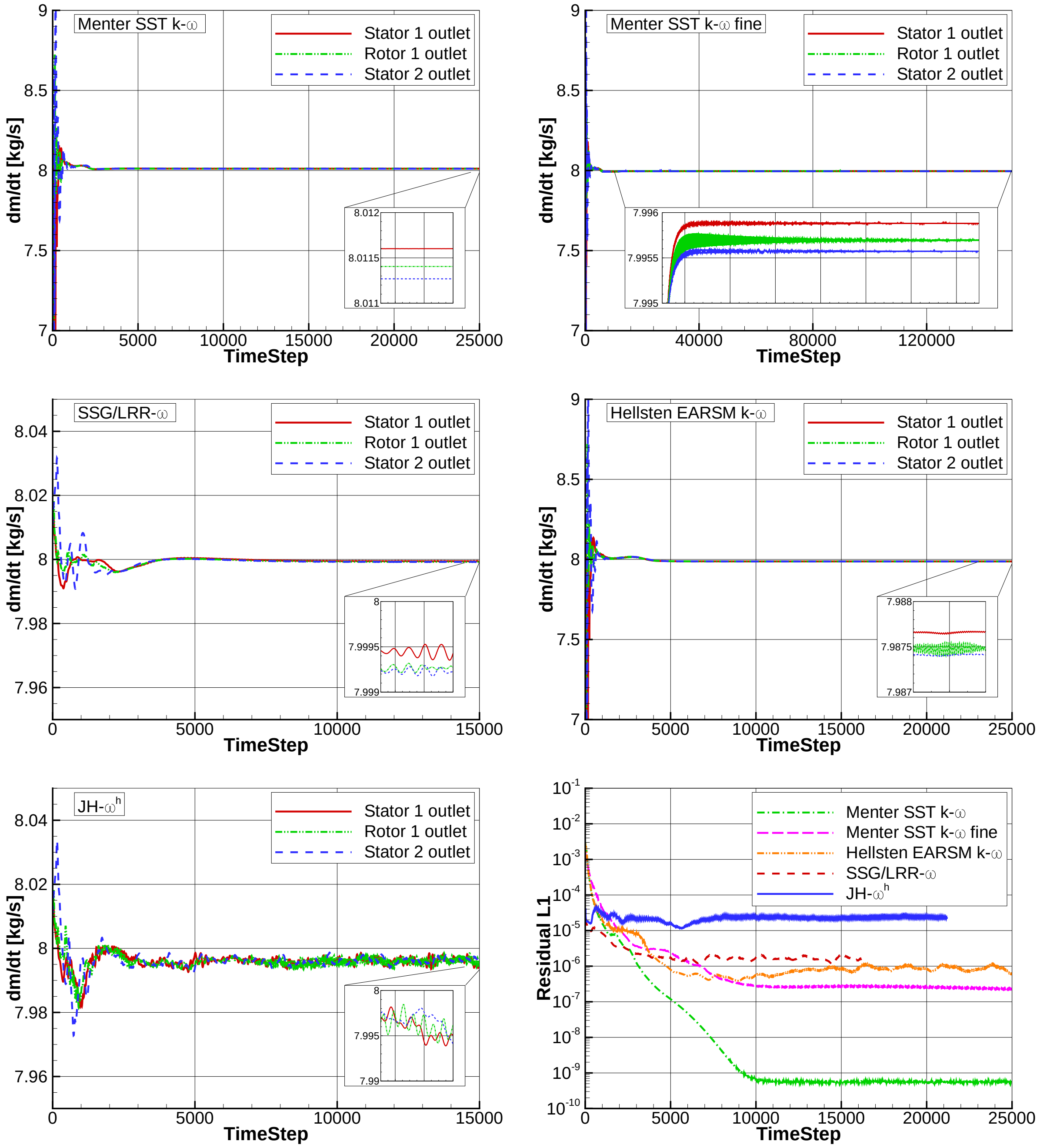

Figure 6.23: Mass flow convergence Menter SST k-ω (*top left*), Menter SST k-ω on refined mesh (*top right*), SSG/LRR-ω (*middle left*), JH-ω^h (*middle right*) and Hellsten EARSM k-ω (*bottom left*), RANS residuals for all models (*bottom right*).

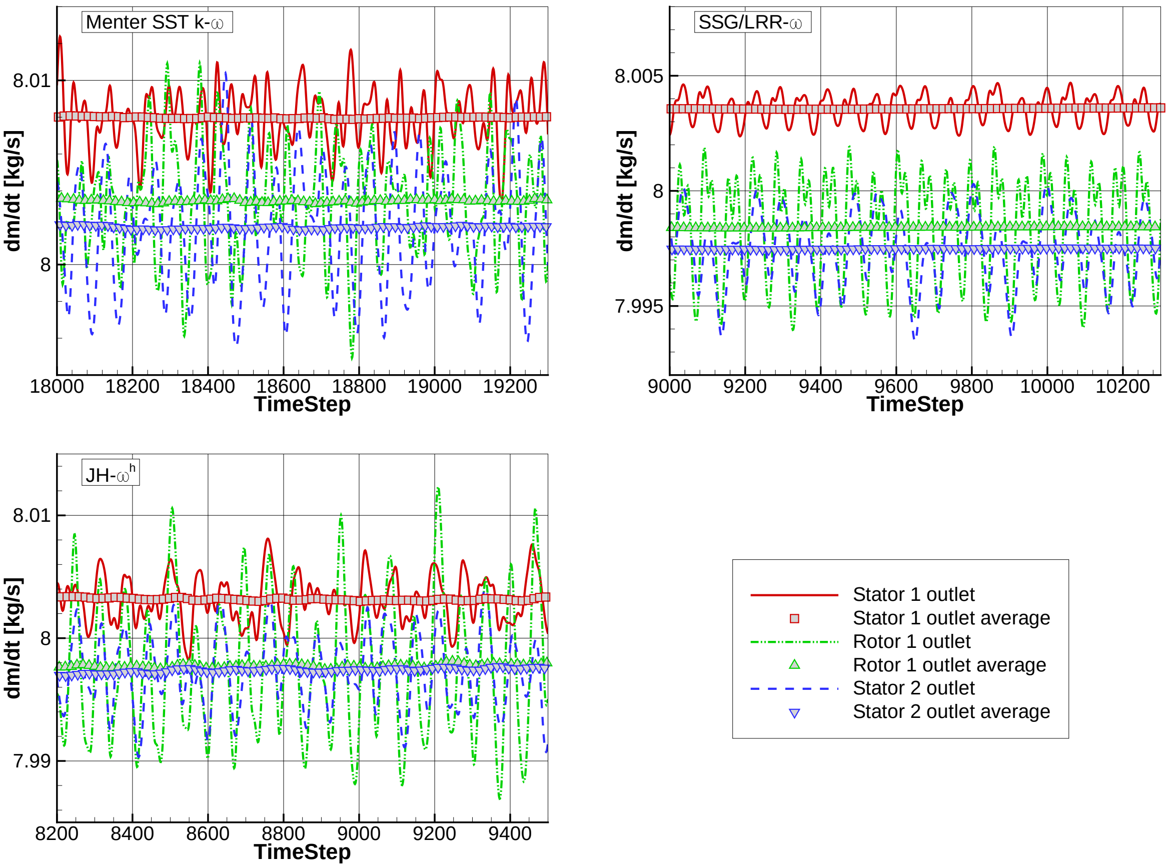

Figure 6.24: Unsteady mass flow convergence Menter SST k-ω (*top left*), SSG/LRR-ω (*top right*) and JH-ω^h (*bottom left*).

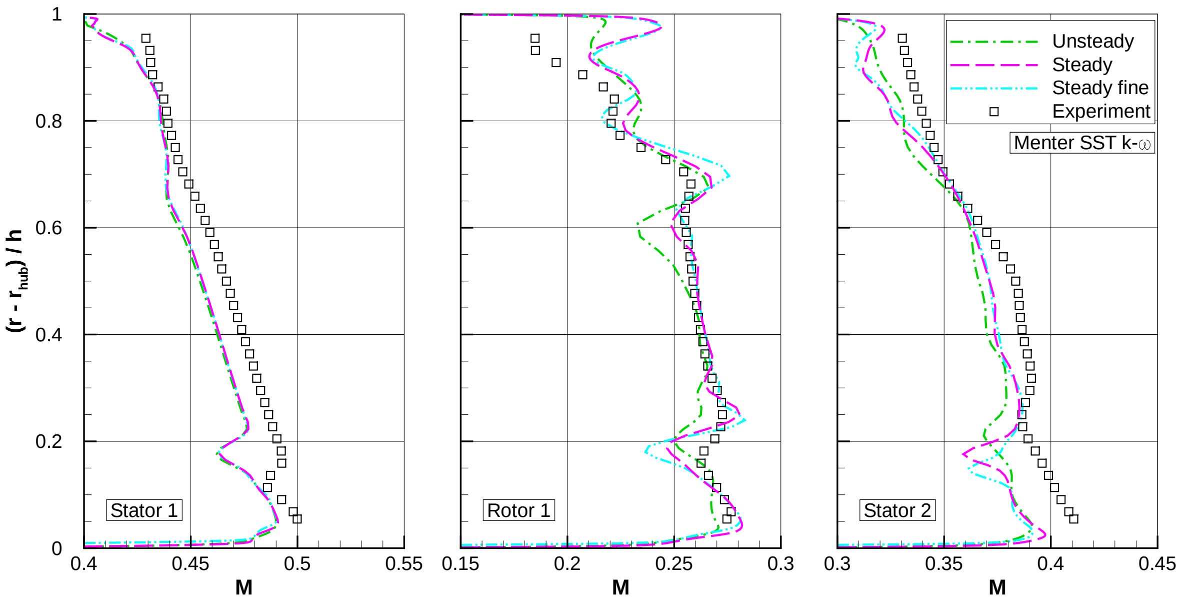

Figure 6.25: Radial traverses behind stator 1 (*left*), rotor 1 (*middle*) and stator 2 (*right*) obtained with the Menter SST k-ω model comparing steady and unsteady averaged results with steady results on the refined mesh.

The mass flow convergence of the unsteady simulations is shown in Figure 6.24. They all exhibit a transient phase following the restart on the steady solution (not shown) because the mixing plane interfaces have been changed to zonal interfaces. Wakes and vortices are no longer mixed out but convected to the downstream row and potential effects reach the upstream row. Unsteady convergence is judged by the variation of the average mass flow. After 10000 time steps, it has fallen below 0.01% as in the steady simulations using the RSMs and a reasonably periodic signal with a period of 768 time steps has been obtained. The computation using the Menter SST k-ω model was run for 20000 time steps to allow for damping of low frequency oscillations in the averaged mass flow. As already seen in the steady mass flow convergence, the JH-ω^h model shows the greatest amplitude in instantaneous mass flow. This is reflected in the variation of the average isentropic efficiency of 0.04% in contrast to 0.02% for the Menter SST k-ω and SSG/LRR-ω models.

Simulations with the Menter SST k-ω model are used to show the influence of the mesh and the difference between (converged) steady and unsteady simulations. Figure 6.25 shows radial traverses behind the three blade rows (from left to right) comparing the results for the two meshes. In the first stator row, basically no difference between the two meshes can be spotted. The decreased dissipation due to the finer mesh can be seen in the rotor row, where the amplitude of peaks due to secondary flow structures is increased. Only in the second stator row, a significant difference occurs in the minimum in averaged Mach number due to the hub trailing edge separation at a relative channel height of 0.15. This feature is shifted towards the hub on the fine mesh. As argued above, the aim of this chapter is to test models on meshes that will become standard in practical applications soon and on which simulations can be performed in realistic time frames with the existing computational resources. Therefore, the original mesh was used for all subsequent simulations.

Figure 6.25 also shows the difference between the steady and unsteady RANS results obtained with the Menter SST k-ω model. As argued above, interaction effects between

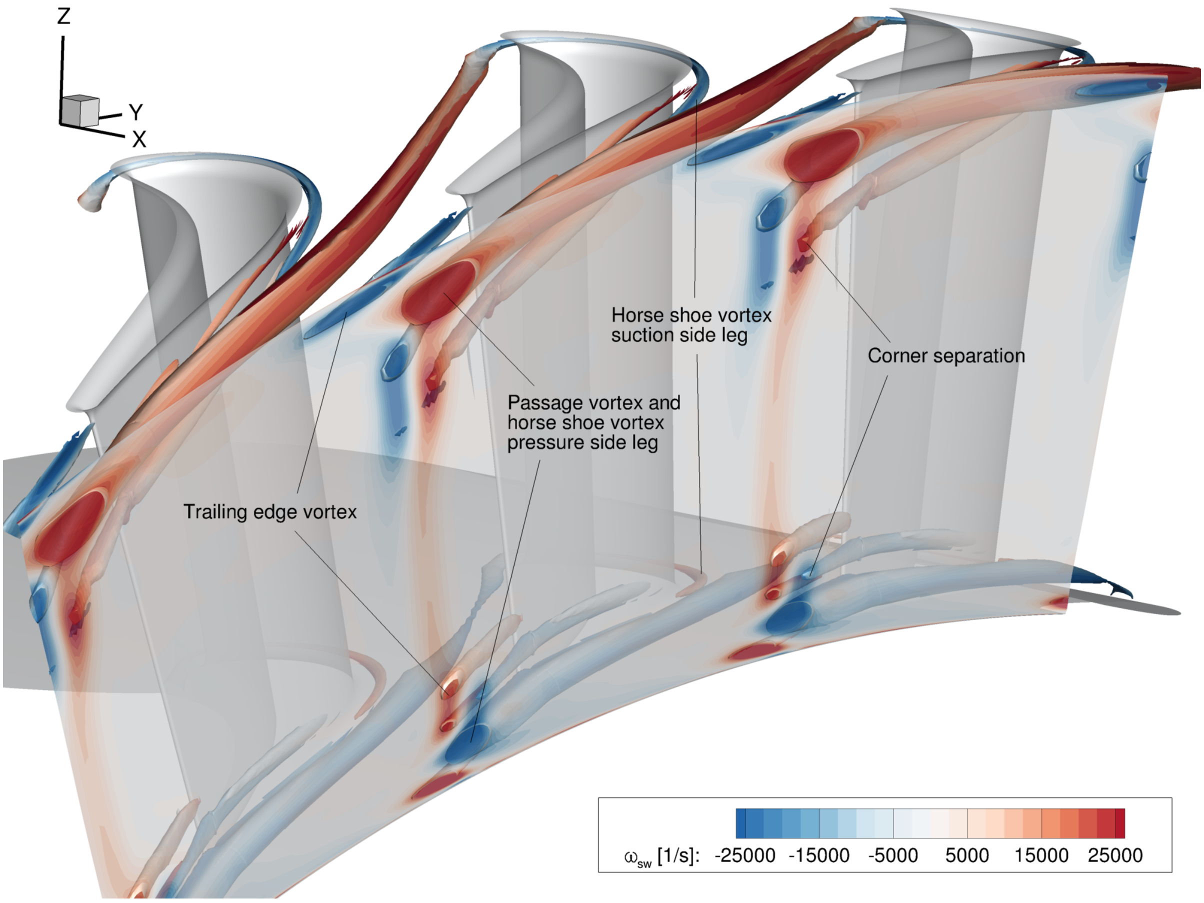
Z
Y
X
Horse shoe vortex suction side leg
Corner separation
Passage vortex and horse shoe vortex pressure side leg
Trailing edge vortex
ωsw [1/s]: -25000 -15000 -5000 5000 15000 25000

Figure 6.26: Visualisation of the vortex system in stator 1 by a $\lambda_2 = -1.5$ isosurface coloured with streamwise vorticity ω_{sw}.

the blade rows are now resolved. Practically no change of the radial traverse downstream of stator 1 can be detected. This indicates that the upstream influence of rotor 1 can be neglected and that the flow in stator 1 can be regarded as steady when a LEVM is employed. The traverses behind rotor 1 and stator 2 are generally smoother for the unsteady average than for the steady result indicating that the main influence of the upstream blade row is an increased radial mixing. An exception is the increased peak at relative channel height 0.6 behind rotor 1 which can be attributed to the trailing edge vortex (see also Figure 6.28). The same conclusions can be drawn for the comparison of steady and unsteady results obtained with the SSG/LRR-ω model (not plotted).

In the following, the streamwise vorticity and the Mach number on the analysis planes behind the blade rows will be compared to experimental data. To understand the features on these 2D planes and in the corresponding radial distributions, it is instructive to analyse the 3D wake and vortex systems in both the stator and rotor rows. This analysis will be performed based on the unsteady averaged solution obtained with the SSG/LRR-ω model. Figure 6.26 shows the stator 1 blade row segment without the tip wall for clarity. The vortex structures are visualised by a $\lambda_2 = -1.5$ isosurface coloured with streamwise vorticity ω_{sw}. The analysis surface downstream of the blade is also coloured with ω_{sw}. At both end wall/blade junctions, the horse shoe vortex develops. Its pressure side leg merges with passage vortex to become the dominant vortex in the stator system both at hub and shroud. The corner separations lift from the blade close to the end walls. Finally, trailing edge vortices leave the blade rotating in opposite direction to the corner separations. All these features can be found clearly in the streamwise vorticity on the analysis plane. Their effects on the Mach number are, however, more subtle.

Figure 6.27 shows the streamwise vorticity ω_{sw} (*top*) and the Mach number M distribution (*bottom*) on the analysis plane behind stator 1 compared to experimental data. One pitch is plotted in polar coordinates with the relative pitch defined as $(\theta-\theta_0)/\Delta\theta$ where θ_0 is the reference circumferential position and $\Delta\theta = 360°/N_{\text{blades}}$ refers to the angle covered by one blade passage. The experiment did not resolve the end wall boundary layer so data is only available from about 5-95% of relative channel height $(r - r_{\text{hub}})/h$. The streamwise vorticity has the same scaling as in Figure 6.26. The 2D flow field in the central part of the blade, namely the passage flow and the wake, shows no significant difference between the models and experiment. Differences in the prediction of the 3D flow close to the end walls generally occur rather between the two turbulence model types than between the two DRSMs. First, in contrast to the Menter SST k-ω model, the DRSMs show a clear distinction between the passage vortex and corner separation near the shroud. Furthermore, they predict a slightly more compact corner separation. Both features show an improved agreement with the experiment. Also the shape and relative position of passage vortex is improved although it is computed as too strong by the DRSMs. The same trend can be observed at the hub. There, the corner vortices are predicted too far away from the end wall by all models. The trends are reflected in the Mach number distribution (*bottom*), which indicates that especially the corner separation at the hub is predicted as too large. No big difference can be detected in the depth and width of the wake between the models. It can be said, though, that the wake seems slimmer and deeper in the experimental data.

A qualitatively different flow field prevails in the rotor row as shown in Figure 6.28. The vortex visualisation is based on the velocity averaged in the rotor frame of reference. As argued above, the analysis plane is placed in the stator frame of reference; hence the flow features which are at a distinct circumferential location relative to the rotor frame of reference appear circumferentially averaged. All strong vortices show up as circumferential streaks on the plane. Effects of the upstream stator row can be seen as circumferential variation. The horse shoe and passage vortex system develops in analogy to the stator flow. However, owing to the fact that the pressure and suction sides are inverted, the direction of rotation of the passage vortices is inverted as well. The passage vortex appears weaker and broader than in the stator flow. What clearly distinguishes the rotor row from the stator rows is the tip gap vortex at a relative channel height of about 95% rotating in the opposite direction to the shroud passage vortex. After the shroud trailing edge vortex, this is the strongest vortex at the exit of the rotor. It greatly influences the corner flow of the blade and passage vortex at the shroud.

The flow field downstream of rotor 1 is compared to experiments in Figure 6.29 again showing streamwise vorticity ω_{sw} (*top*) and Mach number M (*bottom*). Because the measurement was performed in the stator system, 4/3 rotor pitches equivalent to one pitch of the upstream stator 1 are shown. The relative circumferential position of the extracted simulation data has been adjusted such that the wake of stator 1, which can be seen in the Mach number distribution at a relative pitch of about 1, coincides with the experimental data. In the shroud region, the circumferential variation in both ω_{sw} and M is rather small, implying that this region is dominated by the rotor flow features. The tip gap vortex is, unfortunately, not completely resolved by the experiment. The data suggest, however, that the vortex is stronger than predicted by the Menter SST k-ω model. Furthermore, it is modulated by the wake of stator 1, as can be seen in the Mach number. The radial position of the peak vorticity corresponding to the shroud passage

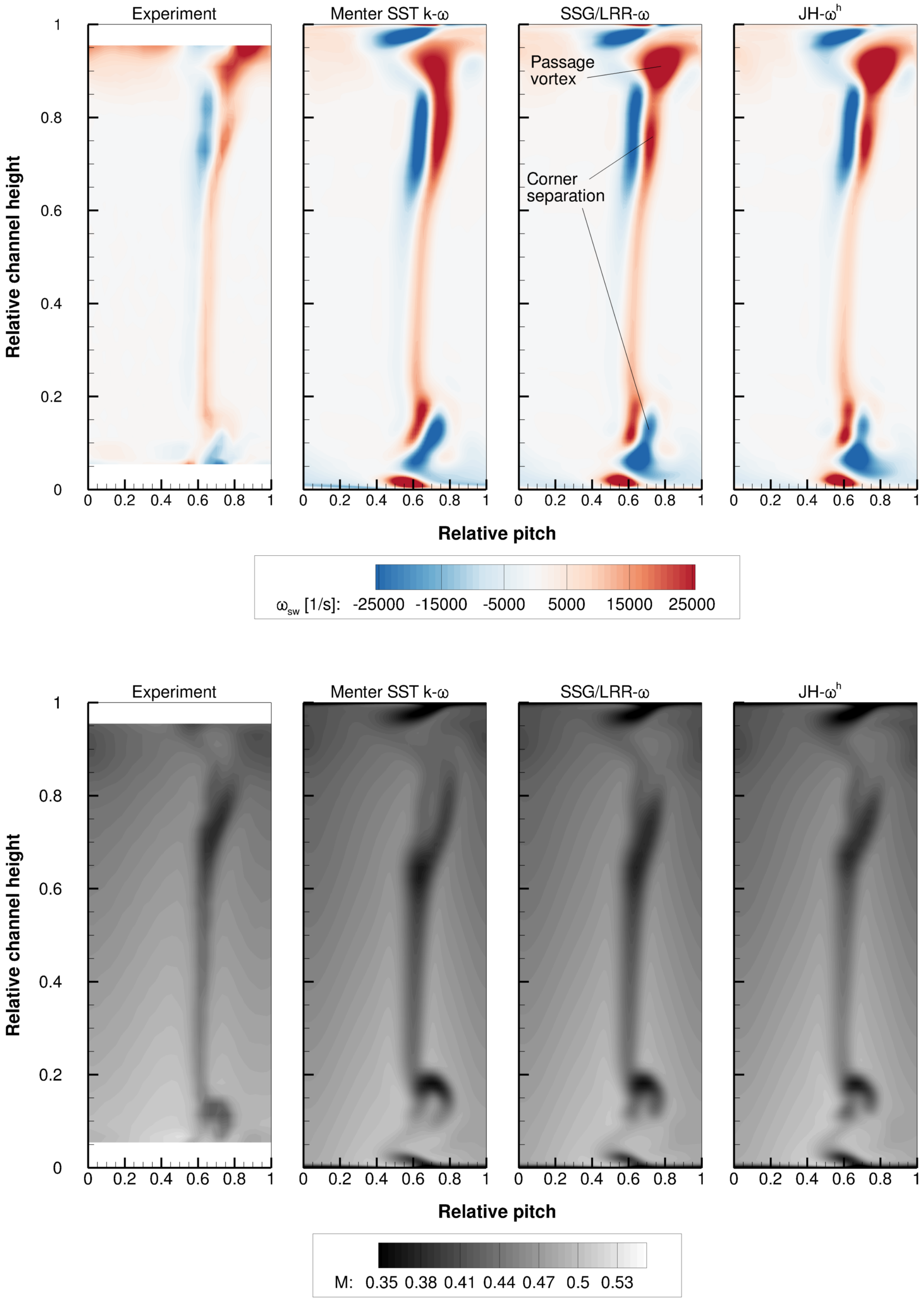

Figure 6.27: Streamwise vorticity ω_{sw} (*top*) and Mach number M (*bottom*) downstream of stator 1.

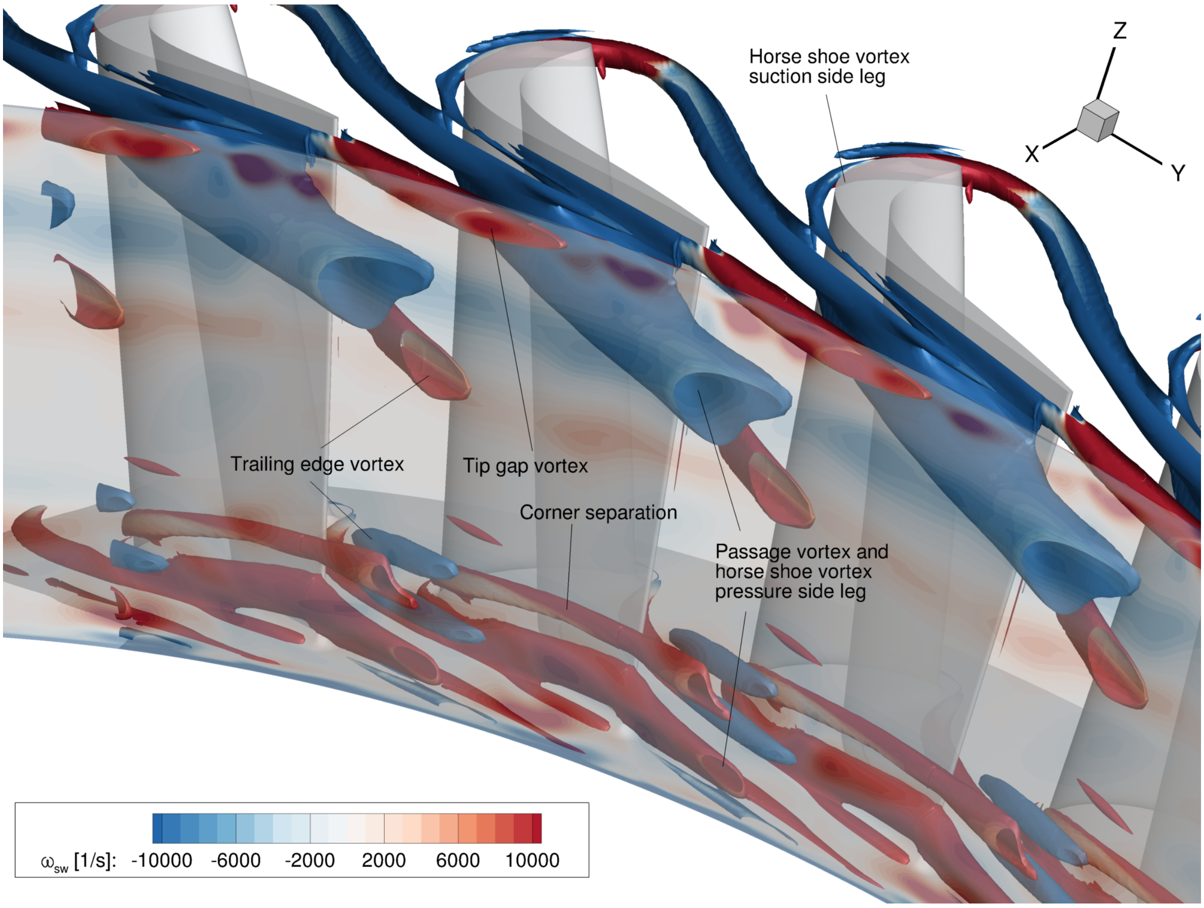
Horse shoe vortex
suction side leg
Z
X
Y
Trailing edge vortex
Tip gap vortex
Corner separation
Passage vortex and
horse shoe vortex
pressure side leg
ω_sw [1/s]: -10000 -6000 -2000 2000 6000 10000

Figure 6.28: Visualisation of the vortex system in rotor 1 by a $\lambda_2 = -1.5$ isosurface coloured with streamwise vorticity ω_{sw}.

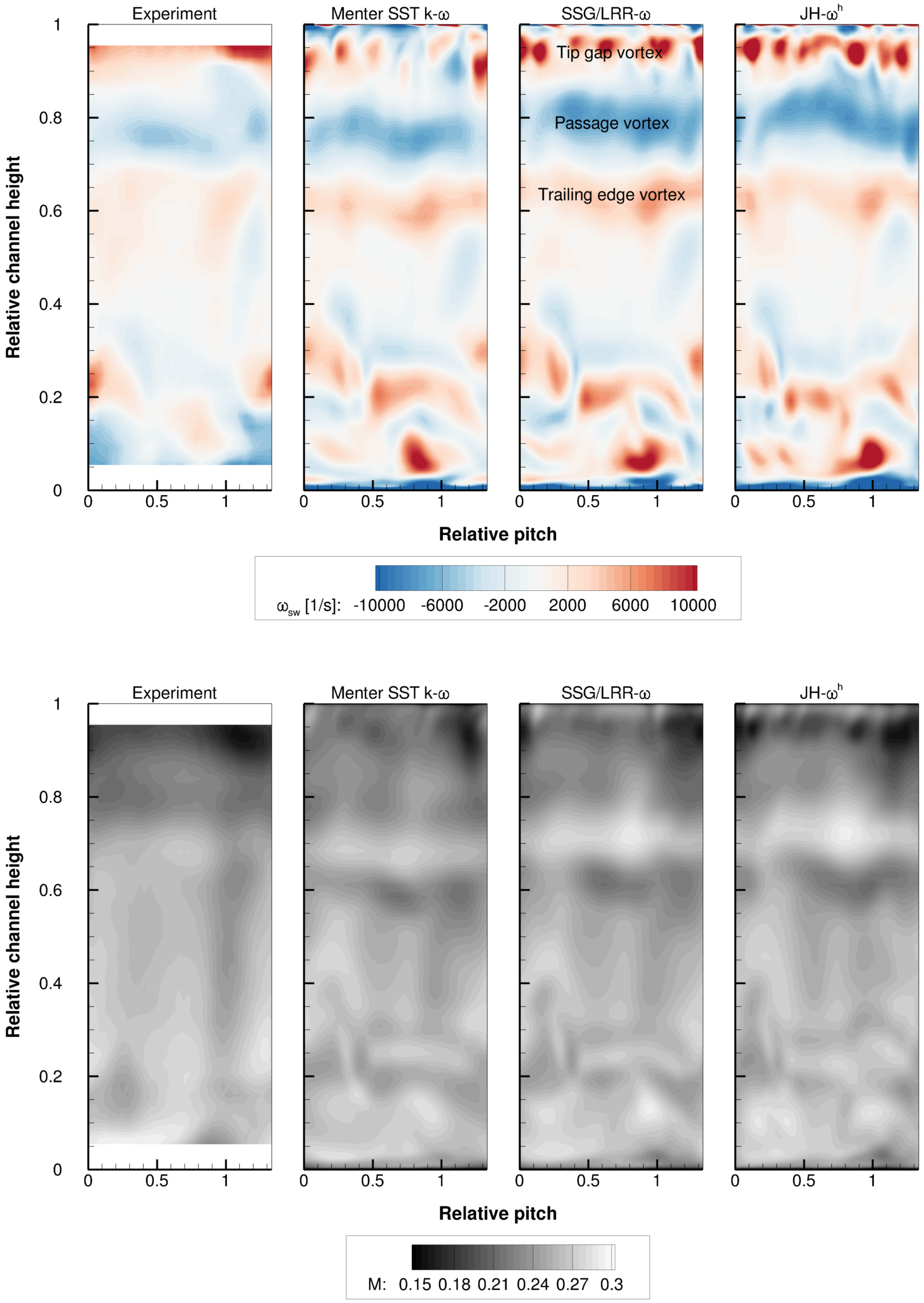

Figure 6.29: Streamwise vorticity ω_{sw} (*top*) and Mach number M (*bottom*) downstream of rotor 1.

vortex and trailing edge separation is predicted in agreement with the experiment. The hub flow, in contrast, shows a significant circumferential variation due to the influence of the upstream stator 1. While the turbulence models basically agree with each other, the comparison with the experiment is limited to a very qualitative way in the hub region.

The final measurement plane analysed in this section is placed behind stator 2 and shown in Figure 6.30. Two stator 2 pitches are equivalent to one pitch of the upstream stator 1. The secondary flow structures in stator 2 are dominated by the upstream blade rows. The Menter SST k-ω model, in contrast to the DRSMs, shows strong positive streamwise vorticity very close to the shroud corresponding to a corner separation. As Figure 6.29 (*top*) shows, the strong secondary flow structures associated with the rotor tip gap and passage flow have dissipated more than in the DRSM solutions when they enter the stator passage. A possible explanation could be that the stator's corner separation is suppressed by these features in the DRSM solution, which is in line with the experiment. Remnants of the trailing edge vortex of rotor 1 at 80% relative channel height can be seen in every other blade passage. As the tip vortex, the DRSMs convect this vortex downstream much stronger than the LEVM, which corresponds to the measured values. In the hub region, the picture is, again, rather noisy because structures from both upstream rows appear here. The wakes predicted by the simulation are deeper than in the experiment. Furthermore, there is a strong minimum in Mach number in the region of the hub corner separation in every other stator 2 passage. In contrast, the experiments show less variation from one stator 2 passage to the other.

To summarise the discussions above, a quantitative comparison is presented in Figure 6.31. It shows radial traverses of circumferentially mass averaged streamwise vorticity ω_{sw} (*top*) and Mach number M (*bottom*) computed from the averaged unsteady simulations with the Menter SST k-ω, SSG/LRR-ω and JH-ω^h models compared with experiments. For the Mach number, the measurement uncertainty is equivalent to roughly the size of the symbols. As seen above in the discussion of the 2D plots, the differences between the models are more pronounced in the streamwise vorticity than in the Mach number. For the latter, especially in stator 1 there are only marginal differences between the models; a similar conclusion can be drawn for stator 2. The general trends of the experimental data are followed rather well by all models. The only major differences can be seen in the rotor tip region. There, the passage vortex is predicted closer to shroud wall by the DRSMs, which does not agree as well with the measured data as the result obtained with the Menter SST k-ω model. The tip gap vortex, however, dissipates too quickly in the LEVM simulation. Both DRSMs capture the peak in streamwise vorticity which corresponds to this vortex both in position and amplitude. In the upstream row, the peak vorticity of the shroud passage vortex is predicted better than with the LEVM. As argued above, the numerical data in stator 2 show numerous peaks and only qualitatively agree with the measurements.

In contrast to all cases used for validation of the models, laminar boundary layer problems in spite of a fully turbulent simulation occur for the JH-ω^h model due to the low turbulence intensity. This can be seen in Figure 6.32, which shows the wall shear stress at midspan where it differs from all other models. Unfortunately no experimental data are available. Furthermore it shows a separation and reattachment on the stator 1 suction surface as opposed to all other models. As suggested in Section 3.4, additional computations were performed with a lower limit of ω^h/S introduced in the numerical procedure. However, as in the original model, no healthy turbulent boundary layer could be found in these results. This finally reveals that the ω^h-version of the model

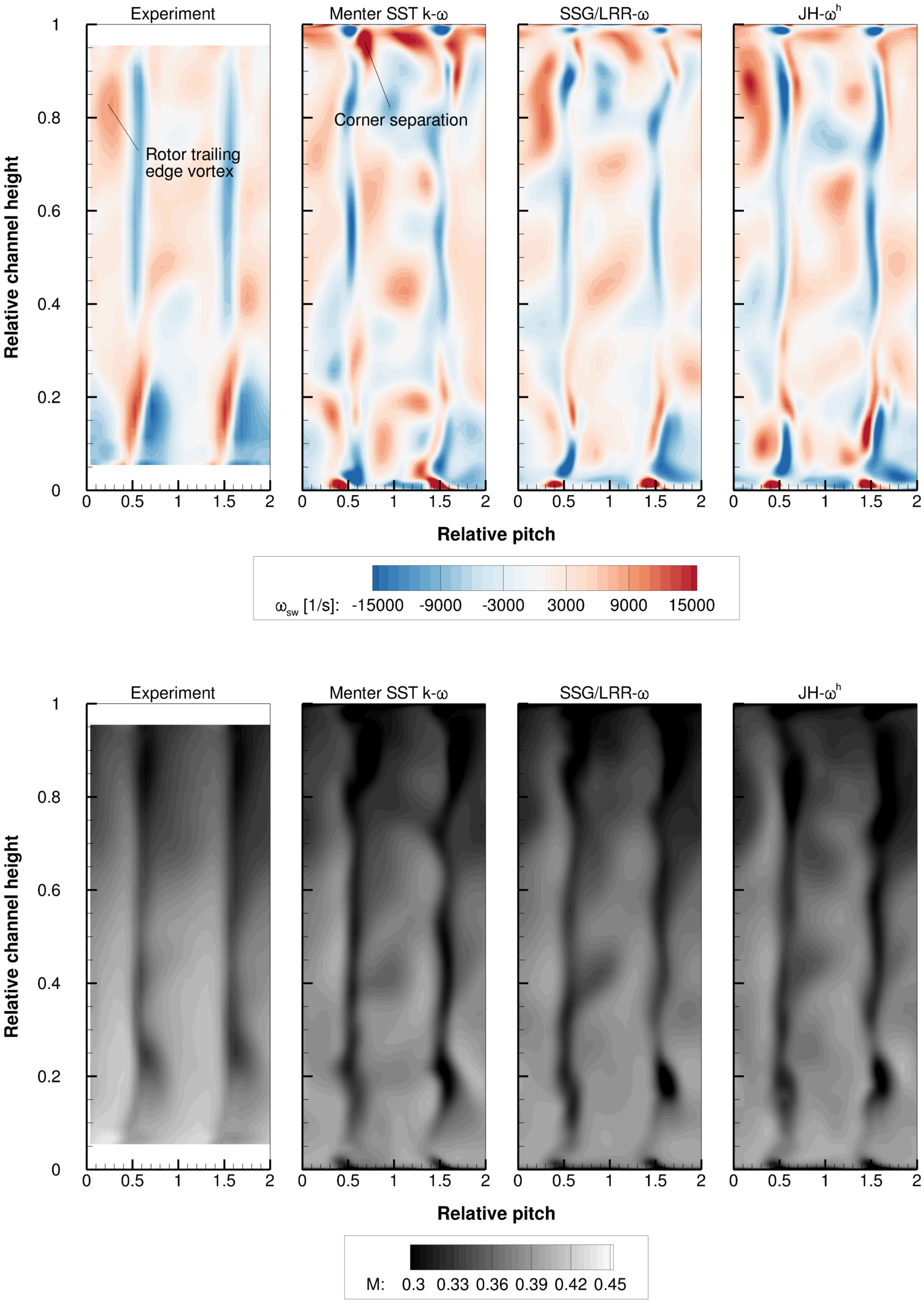

Figure 6.30: Streamwise vorticity ω_{sw} (*top*) and Mach number M (*bottom*) downstream of stator 2.

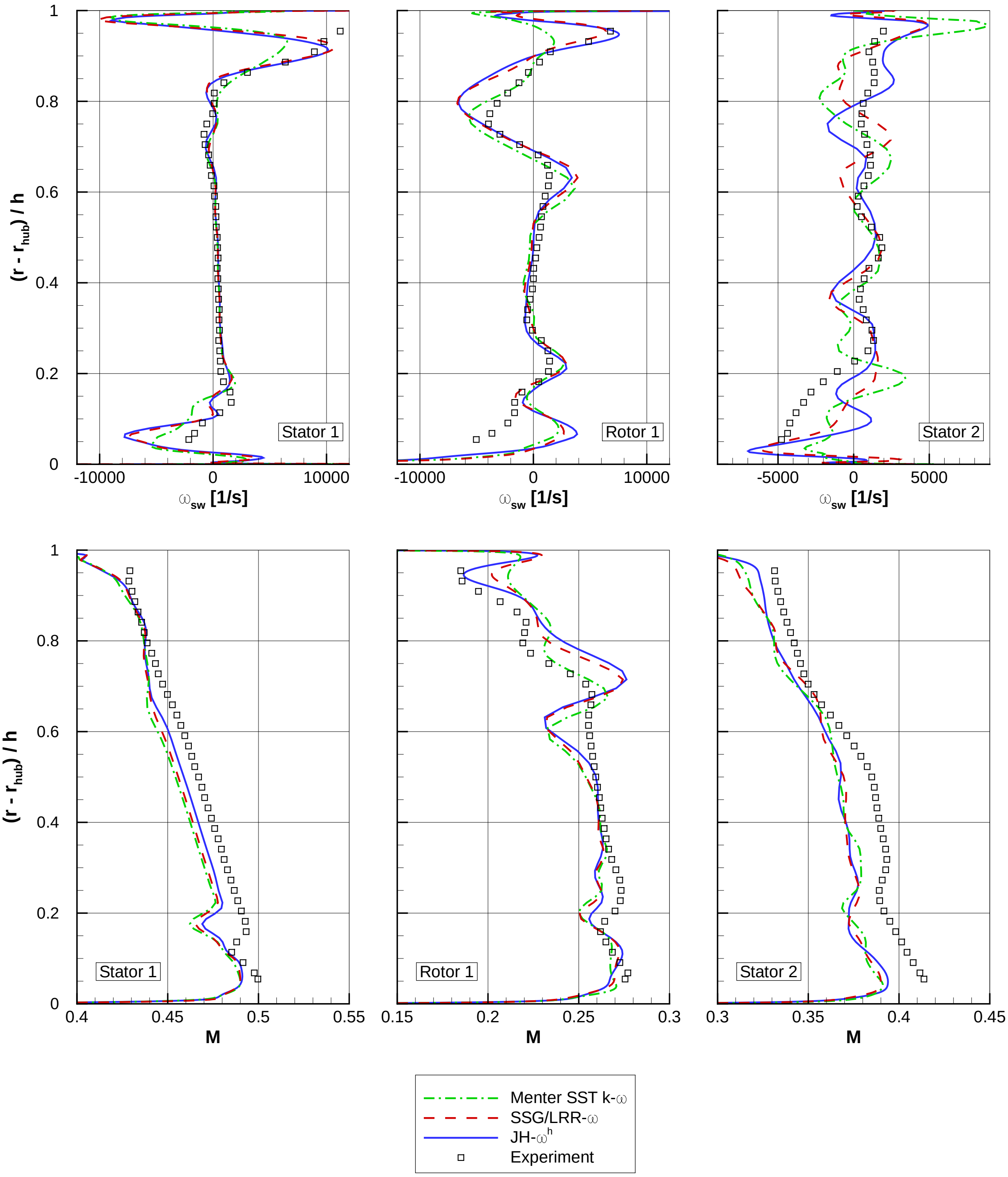

Figure 6.31: Radial traverses of streamwise vorticity ω_{sw} (*top*) and Mach number M (*bottom*) behind stator 1 (*left*), rotor 1 (*middle*) and stator 2 (*right*) averaged from the unsteady simulations with Menter SST k-ω, SSG/LRR-ω and JH-ω^h models compared to experimental data.

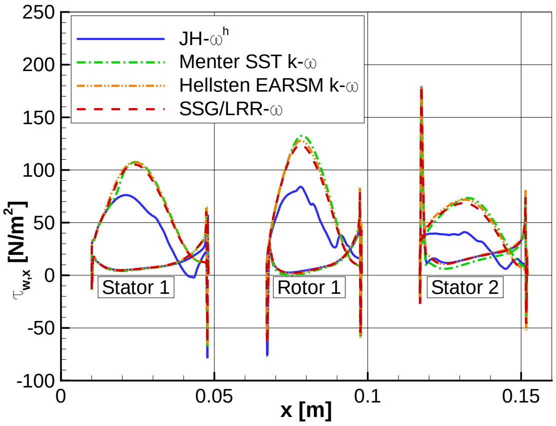

Figure 6.32: Wall shear stress $\tau_{w,x}$ for stator 1, rotor 1, stator 2 (from left to right) from steady simulation.

suffers from the same deficiency concerning the transition behaviour as the ϵ^h-version (Probst, 2013). It is possible that a treatment which forces transition through additional source terms, as Probst derived for the ϵ^h-version, is also necessary for the general applicability of the JH-ω^h model.

The general picture deduced from the above test case is very similar to that obtained for the Virginia Tech cascade in Section 6.1. DRSMs show improvements in the prediction of secondary flow effects but a near-wall model does not significantly improve predictions any further. In general, the application of a DRSM can be recommended if secondary flow effects are of primary interest. Especially the SSG/LRR-ω model can be run without stability problems. The JH-ω^h needs further investigation possibly in combination with a suitable transition model.

7 Summary and Outlook

The performance of differential Reynolds stress models (DRSM) in turbomachinery flows has been investigated. DLR's in-house solver for turbomachinery applications, TRACE, was used as a vehicle for the study. The solver is used in productive industrial design environments. Hence, quality management plays a major role in the development. After the infrastructure for the computations of DRSMs had been created, two DRSMs of different complexity were implemented. Whereas the SSG/LRR-ω model is a high Reynolds model, developed with focus on its application to complex 3D flows, the JH-ω^h model has been built up from the bottom by careful analysis of direct numerical simulation (DNS) data in building block flows. The latter model includes near-wall effects explicitly in the pressure-strain term and through the use of the specific homogeneous dissipation rate as scale-determining variable. While it has various theoretical advantages, problems of spurious laminar solutions have been reported. A theoretical analysis of the model's behaviour identified possible causes.

The stability of the numerical method is of prime importance if complex 3D flows relevant in industrial applications have to be computed. Two aspects have been taken care of. The first is the stability of the solution method for the Reynolds stress transport equations. A method has been developed to solve the additional transport equations in a separated yet conservative manner. As the equations are solved in an implicit algorithm, the linearisation of the source and diffusion terms for DRSMs has been derived and implemented. The second aspect is the coupling of the DRSM to the Reynolds averaged Navier-Stokes (RANS) equations, for which an existing strategy has been employed. As a final point in this respect, the Reynolds stress boundary conditions specific to turbomachinery flows solved in rotating frames of reference have been developed.

The implementation of the models has been carefully validated using a number of building block flows. Experimental and DNS data as well as well-established turbulence models such as the Menter SST k-ω and the Hellsten EARSM k-ω model were used as references. The test cases included the features of a boundary layer, streamline curvature, separation and shock wave/boundary layer interaction. As expected, the theoretically superior JH-ω^h model proved to be superior in the prediction of these flows. This holds true for both the prediction of the turbulence structure, analysed in terms of turbulence anisotropy and its invariants, and the prediction of mean flow quantities. It has to be mentioned, though, that the differences between the DRSMs in the latter were much smaller.

After the successful validation, the models were applied in the simulation of a compressor and a turbine flow as well as to a flow relevant to internal cooling. The flow through the Virginia Tech compressor cascade was analysed with focus on the tip gap flow and the development of the passage vortex. Both DRSMs showed improvements compared to both the reference LEVM and EARSM, especially in the prediction of secondary flow features. The JH-ω^h model was found to be superior in the prediction of Reynolds stress anisotropy. However, only marginal differences in the in mean flow quantities distinguished the two DRSMs. The flow in the Ranque-Hilsch vortex tube was investigated in collaboration with the *Engine Measurement Systems* department of DLR's *Institute of Propulsion Technology*. At the time of the project, only the SSG/LRR-ω model was available for the simulation. No steady solution could be obtained with the DRSM because the model is inherently less dissipative than eddy viscosity models. The subsequent computationally expensive unsteady RANS simulation produced qualitatively reasonable results for unsteady effects and showed good agreement with measured temperature data. The most advanced turbomachinery application was the 1.5 stage cold air turbine test rig operated by the *Institute of Jet Propulsion and Turbomachinery* at the *RWTH Aachen University*. This case involved all features present in real turbomachines such as rotating frames of reference and the interaction of blade rows. Due to the aspect ratio of the blades, the focus was on the strong secondary flows. Again, an unsteady RANS simulation was required both from a flow physics point of view and due to the convergence behaviour of the DRSMs. It could be shown that the prediction of secondary flow structures was improved by both DRSMs. While the SSG/LRR-ω model ran without problems both in steady and unsteady mode, the JH-ω^h model computed a transitional solution similar to the reported behaviour of its ϵ^h-version.

In the investigated cases, the DRSMs showed superior prediction of secondary flow features. When the flow is very complex and many different effects interfere with each other, the prediction of intricate details of the inner boundary layer seems to become less important for the overall result. Here, a compromise between the accuracy in the details and the stability of the solution method has to be found. While the JH-ω^h model appears to be clearly superior to the SSG/LRR-ω model in the prediction of building block flows, this advantage cannot be recognised as pronounced in complex 3D flows and comes at the expense of decreased numerical stability. This raises the question of the appropriate level of complexity of DRSMs for practical simulations of such flows. From the current knowledge, the SSG/LRR-ω model can be recommended for practical applications although it has some theoretical shortcomings such as the pressure-strain model close to a solid wall. While these can be criticised, on the one hand, they can be viewed in terms of a different rationale, on the other hand. The model employs simpler formulations in parts of the flow which are critical from a stability point of view and, hence, ensures that a solution can be obtained. The JH-ω^h model, in contrast, shows a lot of theoretical potential but needs further investigations, especially of its transition behaviour.

This leads to the real dilemma of turbulence modelling. In order to gain insight into turbulence mechanisms and derive appropriate models, highly idealised flows focusing on very few isolated effects have to be studied: basically all turbulence models are calibrated using such flows. What distinguishes the various models is how accurately the flow features of building block flows can be reproduced. However, almost all flows to which the models are applied are highly complex and feature combinations of various effects. Since the governing equations are non-linear it can *per se* not be expected that a model calibrated for a number of idealised flows yields satisfying results in a complex flow. An approach to overcome this dilemma would be the use of automated optimisation methods to calibrate the models in relevant flows.

The results from this thesis can be built upon to further advance the application of DRSMs in practical turbomachinery applications. Since transition plays an important role in many parts of a turbomachinery flow, the coupling with an appropriate transition model and the transition properties of the JH-ω^h models should be investigated. In view of applications involving heat transfer, the models should be coupled to advanced turbulent heat flux models. The DRSMs could also serve as advanced background models for scale adaptive simulations. Finally, as the potential of the models to improve the prediction of relevant secondary flow features was proved, they should be incorporated in future turbomachinery design projects.

Nomenclature

Abbreviations

ACARE	Advisory Council for Aviation Research and Innovation in Europe
BSL	Baseline
CAD	Computer Aided Design
CFD	Computational Fluid Dynamics
CFL	Courant, Friedrichs, Lewy
DES	Detached Eddy Simulation
DLR	Deutsches Zentrum für Luft- und Raumfahrt (German Aerospace Center)
DNS	Direct Numerical Simulation
DRSM	Differential Reynolds Stress Model
EARSM	Explicit Algebraic Reynolds Stress Model
FFT	Fast Fourier Transform
FRS	Filtered Rayleigh Scattering
GGD	Generalised Gradient Diffusion
HL	Hanjalić, Launder
IP	Isotropisation of production
ISA	International Standard Atmosphere
JH	Jakirlić, Hanjalić
L2F	Laser-2-Focus
LES	Large Eddy Simulation
LEVM	Linear Eddy Viscosity Model
LHS	Left Hand Side
LRR	Launder, Reece, Rodi
MUSCL	Monotonic Upstream-centered Scheme for Conservation Laws
NLEVM	Non-linear Eddy Viscosity Model
ODE	Ordinary Differential Equation
ONERA	Office National d'Etudes et de Recherches Aérospatiales
PANS	Partially Averaged Navier-Stokes
RAE	Royal Aircraft Establishment
RANS	Reynolds-averaged Navier-Stokes
RGB	Red Green Blue
RSM	Reynolds Stress Model
RWTH	Rheinisch-westfälische technische Hochschule
SAS	Scale Adaptive Simulation
SciPy	Scientific Computing Tools for Python
SGD	Simple Gradient Diffusion

SMC	Second Moment Closure
SSG	Speziale, Sarkar, Gatski
SST	Shear Stress Transport
TMBWG	Turbulence Model Benchmarking Working Group
TRACE	Turbomachinery Research Aerodynamic Computational Environment
TurboVaLd	Turbulenzmodellvalidierung mittels Laserdiagnostik (DLR internal project)

Symbols

a	Speed of sound
a_{ij}	Reynolds stress anisotropy tensor
a_{ij}^{ex}	Extra Reynolds stress anisotropy in EARSM context
A	Reynolds stress two-component factor
A	Area
$\mathbf{A}$	Flux Jacobian
A_2, A_3	Second and third invariant of Reynolds stress anisotropy tensor
B_i	Coefficients of homogeneous shear model problem
c	Chord length
c_f	Skin friction coefficient
c_p	Pressure coefficient
c_p	Specific heat at constant pressure
c_v	Specific heat at constant volume
C_i	Coefficients of turbulence models
$CD_{k\omega}$	k-ω cross diffusion term
$D_{ij,k}^{\mu}$	Viscous diffusion of Reynolds stresses
$D_{ij,k}^{T}$	Turbulent diffusion of Reynolds stresses
e	Internal energy
$\mathbf{e}_i^A$	Basis vector in base A
e_{ij}	Dissipation anisotropy tensor
E	Dissipation two-component factor
$\widetilde{E}$	Favre-averaged relative total energy
E_2, E_3	Second and third invariant of dissipation anisotropy tensor
f	JH model function
f	Frequency
$\mathbf{f}$	Arbitrary vector function
F	JH model function
$\mathbf{F}$	Inviscid flux
$\mathbf{F}_v$	Viscous flux
F_1	Menter's blending function
f_s	Model function for dissipation anisotropy
h	Enthalpy
h	Blade height, channel height
H	Step height
k	Turbulent kinetic energy
l_{ax}	Axial chord length
L	Length, RANS length scale

L_T	RANS length scale used in boundary conditions
$\dot{m}$	Mass flow
M	Mach number
M_{ij}	Reynolds stress budget contribution of turbulent mass flux due to density fluctuations
n	Number
n_i, $\mathbf{n}$	(Wall) normal vector
p	Pressure
P	Reynolds-averaged pressure
P_{ij}	Reynolds stress production tensor
$P_{\epsilon 3}$	Gradient production term
P_k	Production term of turbulent kinetic energy $\frac{1}{2}P_{ii}$
Pr	Prandtl number
$\mathbf{q}$	Solution vector, conservative state vector
q_i	Heat flux vector
q_i^T	Turbulent heat flux vector
$r_\perp$	Distance from rotation axis
R	Radius
$\mathbf{R}$	Residual vector
$\mathbf{R}^{A\to B}$	Transformation matrix from base A to base B
R_{ij}	Reynolds stress rotation term
Re	Reynolds number
s	Arc length
s_{ij}	Strain rate tensor
S	Shear rate
$\mathbf{S}$	Volume source term
S_{ij}	Favre averaged strain rate tensor
t	Time
t	Pitch
T	Temperature
Tu	Turbulence intensity
$\mathbf{u}$	Primitive state vector
u, v, w; u_x, u_y, u_z	Cartesian velocity components
u_i	Velocity vector
u_τ	Friction velocity
U	Favre averaged velocity norm
U_i	Favre averaged velocity vector
V	Control volume
W_{ij}	Favre averaged vorticity tensor
x_B, y_B	Barycentric coordinates
x_i, $\mathbf{x}$	Coordinate vector
x, y, z	Cartesian coordinates
x, r, θ	Cylindrical coordinates
y_n	Distance to nearest wall
α	Coefficient of production term in ω-equation
β	Coefficient of destruction term in ω-equation
γ	Adiabatic index
δ	Channel half height, boundary layer thickness
δ_{ij}	Kronecker delta
ϵ	Cold fraction (vortex tube)

ϵ	Turbulent dissipation rate
ϵ_{ij}	Reynolds stress dissipation tensor
ϵ_{ijk}	Levi-Civita symbol
η_K	Kolmogorov length scale
θ	Boundary layer momentum thickness
λ	Thermal conductivity
$\mathbf{\Lambda}$	Diagonal matrix of eigenvalues
λ_i	Eigenvalues (Reynolds stress anisotropy tensor, flux Jacobian, vortex visualisation)
μ	Dynamic viscosity
μ_T	Turbulent or eddy viscosity
ν	Kinematic viscosity
ξ_i	Computational coordinates
Π_{ij}	Reynolds stress pressure-strain tensor
Π_{ij}^w	Reynolds stress pressure-strain tensor wall model
ρ	Density
σ_d	Coefficient of cross-diffusion term in ω-equation
σ_ω	Turbulent diffusion coefficient in ω-equation
σ_{ij}	Viscous stress tensor
τ	Pseudo-time
τ_w	Wall shear stress
ϕ	Generic quantity
ω_{sw}	Streamwise vorticity
ω	Specific turbulent dissipation rate
Ω	Norm of system rotation rate vector
Ω_i, $\mathbf{\Omega}$	System rotation rate vector
Ω_{ij}	System rotation rate tensor $\epsilon_{ijk}\Omega_k$
ℓ	Characteristic variables

Subscripts / Superscripts

0	Reference value, initial value
$1C$, $2C$, $3C$	One-component, two-component, three-component
a, ax	Axial
C	Referring to chord
f	Cell face
h	Homogeneous
q	Based on conservative variables
ref	Reference value
t	Total or stagnation values
T	Turbulent, transposed
u	Based on primitive variables
w	Wall
μ	Viscous, based on dynamic viscosity
ν	Viscous, based on kinematic viscosity
τ	Based on wall shear stress
∞	Free stream

Decorations

$\overline{\phi}$	Reynolds average
ϕ'	Fluctuating part of Reynolds-averaged quantity
$\widetilde{\phi}$	Favre average
ϕ''	Fluctuating part of Favre-averaged quantity
ϕ^*_{ij}	Trace free tensor $\phi_{ij} - \frac{1}{3}\phi_{kk}\delta_{ij}$
ϕ^*	Non-dimensional quantity
$\hat{\phi}$	Roe-averaged value
ϕ^+	Non-dimensional based on friction velocity u_τ

Bibliography

Ashcroft, G., Frey, C., Heitkamp, K. & Weckmüller, C. 2013 Advanced numerical methods for the prediction of tonal noise in turbomachinery–part I: Implicit Runge-Kutta schemes. *J. Turbomach.* **136** (2), 021002–021002.

Bachalo, W. D. & Johnson, D. A. 1986 Transonic, turbulent boundary-layer separation generated on an axisymmetric flow model. *AIAA J.* **24** (3), 437–443.

Banerjee, S., Krahl, R., Durst, F. & Zenger, C. 2007 Presentation of anisotropy properties of turbulence, invariants versus eigenvalue approaches. *J. Turbul.* **8**, N32.

Barre, S., Bonnet, J.-P., Gatski, T. & Sandham, N. 2002 Compressible, high-speed flows. In *Closure Strategies for Turbulent and Transitional Flows*, 1st edn. (ed. B. E. Launder & N. D. Sandham), chap. 19, pp. 522–581. Cambridge, UK: Cambridge University Press.

Basara, B. 2004 Employment of the second-moment turbulence closure on arbitrary unstructured grids. *Int. J. Numer. Meth. Fl.* **44** (4), 377–407.

Batten, P., Craft, T. J. & Leschziner, M. A.and Loyau, H. 1999 Reynolds-stress transport modelling for compressible aerodynamics applications. *AIAA J.* **37** (7), 785–797.

Becker, K., Heitkamp, K. & Kügeler, E. 2010 Recent progress in a hybrid-grid CFD solver for turbomachinery flows. In *V European Conference on Computational Fluid Dynamics ECCOMAS CFD 2010*. Lisbon, Portugal.

Becker, K. C. & Ashcroft, G. 2014 A comparative study of gradient reconstruction methods for unstructured meshes with application to turbomachinery flows. In *AIAA SciTech*. American Institute of Aeronautics and Astronautics.

Behre, S., Restemeier, M. S., Jeschke, P., Guendogdu, Y. & Engel, K. 2012 Time-resolved numerical investigation of the effects of blade-row spacing on the turbine efficiency. In *Proceedings of the ASME Turbo Expo 2012*, pp. 1621–1631. Copenhagen, Denmark: ASME.

Blazek, J. 2001 *Computational fluid dynamics: principles and applications*. Elsevier Science.

Borello, D., Hanjalić, K. & Rispoli, F. 2007 Computation of tip-leakage flow in a linear compressor cascade with a second-moment turbulence closure. *Int. J. Heat Fluid Fl.* **28** (4), 587 – 601.

Bradshaw, P. 1971 *An Introduction to Turbulence and its Measurement*. Pergamon Press.

Bradshaw, P. 1996 Turbulence modeling with application to turbomachinery. *Prog. Aerosp. Sci.* **32** (6), 575 – 624.

Bräunling, W. J. G. 2009 *Flugzeugtriebwerke*, 3rd edn. Berlin: Springer.

Cécora, R.-D., Radespiel, R., Eisfeld, B. & Probst, A. 2014 Differential Reynolds-stress modeling for aeronautics. *AIAA J.* pp. 1–17.

Cécora, R.-D., Eisfeld, B., Probst, A., Crippa, S. & Radespiel, R. 2012 Differential Reynolds stress modeling for aeronautics. In *50th AIAA Aerospace Sciences Meeting*. Nashville, TN, USA.

Chou, P. Y. 1945 On velocity correlations and the solutions of the equations of turbulent fluctuation. *Q. Appl. Math.* **111** (1), 38–54.

Coles, D. 1956 The law of the wake in the turbulent boundary layer. *J. Fluid Mech.* **1**, 191–226.

Craft, T. J. & Launder, B. E. 1996 A Reynolds stress closure designed for complex geometries. *Int. J. Heat Fluid Fl.* **17** (3), 245 – 254.

Daly, B. J. & Harlow, F. H. 1970 Transport equations in turbulence. *Phys. Fluids* **13** (11), 2634–2649.

Denton, J. D. 1992 The calculation of three-dimensional viscous flow through multistage turbomachines. *J. Turbomach.* **114** (1), 18–26.

Doll, U., Beversdorff, M., Stockhausen, G., Willert, C., Schlüß, D. & Morsbach, C. 2014 Characterization of the flow field inside a Ranque-Hilsch vortex tube using filtered Rayleigh scattering, laser-2-focus velocimetry and numerical methods. In *17th Int Symp on Applications of Laser Techniques to Fluid Mechanics*. Lisbon, Portugal.

Doll, U., Burow, E., Beversdorff, M., Stockhausen, G., Willert, C., Morsbach, C., Schlüß, D. & Franke, M. 2015 The flow field inside a Ranque-Hilsch vortex tube part I: Experimental analysis using planar filtered Rayleigh scattering. In *Ninth International Symposium on Turbulence Shear Flow Phenomena (TSFP-9)*. Melbourne, Australia.

Driver, D. M. & Seegmiller, H. L. 1985 Features of a reattaching turbulent shear layer in divergent channel flow. *AIAA J.* **23** (2), 163–171.

Durbin, P. A. 2009 Limiters and wall treatments in applied turbulence modeling. *Fluid Dyn. Res.* **41** (1), 012203.

Durbin, P. A. & Pettersson Reif, B. A. 2000 *Statistical Theory and Modeling for Turbulent Flows*. Chichester, UK: John Wiley & Sons, LTD.

Eiamsa-ard, S. & Promvonge, P. 2008 Review of Ranque-Hilsch effects in vortex tubes. *Renewable and Sustainable Energy Reviews* **12** (7), 1822 – 1842.

Einstein, A. 1916 Die Grundlage der allgemeinen Relativitätstheorie. *Annalen der Physik* **49** (7), 769–822.

Eisfeld, B. 2006 Computation of complex compressible aerodynamic flows with a Reynolds stress turbulence model. In *International Conference on Boundary and Interior Layers (BAIL)*. Göttingen, Germany.

Eisfeld, B. 2010*a* The influence of the length scale equation on the simulation results of aerodynamic flows using differential Reynolds stress models. In *New Results in Numerical and Experimental Fluid Mechanics VII* (ed. A. Dillmann, G. Heller, M. Klaas, H.-P. Kreplin, W. Nitsche & W. Schröder), *Notes on Numerical Fluid Mechanics and Multidisciplinary Design*, vol. 112, pp. 83–90. Springer Berlin / Heidelberg.

Eisfeld, B. 2010*b* Reynolds stress modelling for complex aerodynamic flows. In *V European Conference on Computational Fluid Dynamics ECCOMAS CFD 2010*. Lisbon, Portugal.

Eisfeld, B. 2014 The influence of the diffusion model on the separation sensitivity of differential Reynolds stress models. In *New Results in Numerical and Experimental Fluid Mechanics IX* (ed. A. Dillmann, G. Heller, E. Krämer, H.-P. Kreplin, W. Nitsche & U. Rist), *Notes on Numerical Fluid Mechanics and Multidisciplinary Design*, vol. 124, pp. 113–121. Springer International Publishing.

Emory, M. & Iaccarino, G. 2014 Visualizing turbulence anisotropy in the spatial domain with componentality contours. Annual research briefs 2014. Center for Turbulence Research, Stanford University, Stanford, CA, USA.

European Commission, Directorate-General for Research and Innovation & Directorate-General for Mobility and Transport 2011 *Flightpath 2050: Europe's Vision for Aviation : Maintaining Global Leadership and Serving Society's Needs*. Luxembourg: Publications Office of the European Union.

Fiedler, J. & di Mare, F. 2012 Generalised implementation of low-Mach preconditioning for arbitrary three-dimensional geometries. In *6th European Congress on Computational Methods in Applied Sciences and Engineering (ECCOMAS 2012)*. Vienna, Austria.

Franke, M. 2010 Application of advanced turbulence models in turbomachinery flows. In *XIX Polish National Fluid Dynamics Conference KKMP 2010*. Poznan, Poland.

Franke, M., Röber, T., Kügeler, E. & Ashcroft, G. 2010 Turbulence treatment in steady and unsteady turbomachinery flows. In *V European Conference on Computational Fluid Dynamics ECCOMAS CFD 2010*. Lisbon, Portugal.

Frey, C., Nürnberger, D. & Kersken, H.-P. 2009 The discrete adjoint of a turbomachinery RANS solver. In *Proceedings of ASME-GT2009*.

Gatski, T. & Jongen, T. 2000 Nonlinear eddy viscosity and algebraic stress models for solving complex turbulent flows. *Prog. Aerosp. Sci.* **36** (8), 655 – 682.

Gerolymos, G. A., Joly, S., Mallet, M. & Vallet, I. 2010 Reynolds-stress model flow prediction in aircraft-engine intake double-s-shaped duct. *J. Aircraft* **47** (4), 1368–1381.

Gerolymos, G. A., Neubauer, J., Sharma, V. C. & Vallet, I. 2002 Improved prediction of turbomachinery flows using near-wall Reynolds-stress model. *J. Turbomach.* **124** (1), 86–99.

Gerolymos, G. A. & Vallet, I. 1997 Near-wall Reynolds-stress three-dimensional transonic flow computation. *AIAA J.* **35** (2), 228–236.

Gerolymos, G. A. & Vallet, I. 2002 Wall-normal-free Reynolds-stress model for rotating flows applied to turbomachinery. *AIAA J.* **40** (2), 199–208.

Gerolymos, G. A. & Vallet, I. 2007 Robust implicit multigrid Reynolds-stress model computation of 3D turbomachinery flows. *J. Fluids Eng.* **129** (9), 1212–1227.

Giles, M. B. 1990 Nonreflecting boundary conditions for Euler calculations. *AIAA J.* **28** (12), 2050–2058.

Girimaji, S. S. 2006 Partially-averaged Navier-Stokes model for turbulence: A Reynolds-averaged Navier-Stokes to direct numerical simulation bridging method. *J. Appl. Mech.* **73** (3), 413–421.

Hadzić, I. 1999 Second-moment closure modelling of transitional and unsteady turbulent flows. Dissertation, Technische Universiteit Delft.

Hall, K. C., Thomas, J. P. & Clark, W. S. 2002 Computation of unsteady nonlinear flows in cascades using a harmonic balance technique. *AIAA J.* **40** (5), 879–886.

Hanjalić, K. & Jakirlić, S. 1993 A model of stress dissipation in second-moment closures. *Apl. Sci. Res.* **51**, 513–518, 10.1007/BF01082584.

Hanjalić, K. & Jakirlić, S. 1998 Contribution towards the second-moment closure modelling of separating turbulent flows. *Comput. Fluids* **27** (2), 137 – 156.

Hanjalić, K. & Jakirlić, S. 2002 Second-moment turbulence closure modelling. In *Closure Strategies for Turbulent and Transitional Flows*, 1st edn. (ed. B. E. Launder & N. D. Sandham), chap. 2, pp. 47–101. Cambridge, UK: Cambridge University Press.

Hanjalić, K. & Launder, B. E. 1972 A Reynolds stress model of turbulence and its application to thin shear flows. *J. Fluid Mech.* **52**, 609–638.

Hanjalić, K. & Launder, B. E. 1976 Contribution towards a reynolds-stress closure for low-reynolds-number turbulence. *J. Fluid Mech.* **74** (04), 593–610.

Hellsten, A. 2005 New advanced k-ω tuburlence model for high-lift aerodynamics. *AIAA J.* **43** (9), 1857–1869.

Hilsch, R. 1947 The use of the expansion of gases in a centrifugal field as cooling process. *Rev. Sci. Instrum.* **18**, 108–113.

Hirsch, C. 1990 *Numerical Computation of Internal and External Flows – Computational Methods for Inviscid and Viscous Flows*, 1st edn. Wiley.

Hoyas, S. & Jimenez, J. 2006 Scaling of the velocity fluctuations in turbulent channels up to $\mathrm{Re}_\tau = 2003$. *Phys. Fluids* **18** (1), 011702.

Iwamoto, K., Suzuki, Y. & Kasagi, N. 2002 Reynolds number effect on wall turbulence: toward effective feedback control. *Int. J. Heat Fluid Fl.* **23** (5), 678 – 689.

Jakirlić, S. & Hanjalić, K. 2013 A direct numerical simulation-based re-examination of coefficients in the pressure–strain models in second-moment closures. *Fluid Dyn. Res.* **45** (5), 055509.

Jakirlić, S., Jovanović, J. & Maduta, R. 2013 On near-wall treatment in (U)RANS-based closure models. *Flow Turbul. Combus.* pp. 1–18.

Jakirlić, S. & Maduta, R. 2015 Extending the bounds of 'steady' RANS closures: Toward an instability-sensitive Reynolds stress model. *Int. J. Heat Fluid Fl.* **51**, 175 – 194, theme special issue celebrating the 75th birthdays of Brian Launder and Kemo Hanjalic.

Jakirlić, S. 2004 A DNS-based scrutiny of RANS approaches and their potential for predicting turbulent flows. Habilitation, TU Darmstadt.

Jakirlić, S., Eisfeld, B., Jester-Zürker, R. & Kroll, N. 2007 Near-wall, Reynolds-stress model calculations of transonic flow configurations relevant to aircraft aerodynamics. *Int. J. Heat Fluid Fl.* **28** (4), 602–615.

Jakirlić, S. & Hanjalić, K. 2002 A new approach to modelling near-wall turbulence energy and stress dissipation. *J. Fluid Mech.* **459**, 139–166.

Jakirlić, S., Hanjalić, K. & Tropea, C. 2002 Modeling rotating and swirling turbulent flows: A perpetual challenge. *AIAA J.* **40** (10), 1984–1996.

Jakirlić, S. & Jester-Zürker, R. 2010 Convective heat transfer in wall-bounded flows affected by severe fluid properties variation: A second-moment closure study. In *Proceedings of ASME 3rd Joint US-European Fluids Engineering Summer Meeting*. Montreal, Canada.

Jakirlić, S. & Jovanović, J. 2010 On unified boundary conditions for improved predictions of near-wall turbulence. *J. Fluid Mech.* **656**, 530–539.

Jakirlić, S. & Maduta, R. 2014 On "steady" RANS modeling for improved prediction of wall-bounded separations. In *AIAA SciTech*. American Institute of Aeronautics and Astronautics.

Jeong, J. & Hussain, F. 1995 On the identification of a vortex. *J. Fluid Mech.* **285**, 69–94.

Jovanović, J., Ye, Q.-Y. & Durst, F. 1995 Statistical interpretation of the turbulent dissipation rate in wall-bounded flows. *J. Fluid Mech.* **293**, 321–347.

Kainz, M. & Kozulovic, D. 2007 Untersuchung der Vorhersagegüte eines Zweigleichungs-Turbulenzmodells für Spaltströmungen in Turbomaschinen. Internal report IB-325-05-07. Institute of Propulsion Technology, Geman Aerospace Center (DLR).

Kays, W. M. & Crawford, M. E. 1980 *Convective heat and mass transfer*, 2nd edn. New York, USA: McGraw-Hill Inc.

Kersken, H.-P., Frey, C., Voigt, C. & Ashcroft, G. 2012 Time-linearized and time-accurate 3D RANS methods for aeroelastic analysis in turbomachinery. *J. Turbomach.* **134** (5), 051024–051024.

Kim, J., Moin, P. & Moser, R. 1987 Turbulence statistics in fully developed channel flow at low Reynolds number. *J. Fluid Mech.* **177**, 133–166.

Kluxen, R., Terstegen, M., Behre, S., Jeschke, P. & Guendogdu, Y. 2014 Effects of platform misalignment in a 3D designed 1.5 stage axial turbine. In *Proceedings of the ASME Turbo Expo 2014*. Düsseldorf, Germany: ASME.

Kobiela, B. 2013 Wärmeübertragung in einer Zyklonkühlkammer einer Gasturbinenschaufel. Dissertation, Universität Stuttgart.

Kügeler, E. 2005 Numerisches Verfahren zur genauen Analyse der Kühleffektivität filmgekühlter Turbinenschaufeln. Dissertation, Ruhr-Universität Bochum.

Langston, L. S. 2001 Secondary flows in axial turbines–a review. *Ann. N. Y. Acad. Sci.* **934**, 11–26.

Lardeau, S. & Manceau, R. 2014 Computations of complex flow configurations using a modified elliptic-blending Reynolds-stress model. In *10th International ERCOFTAC Symposium on Engineering Turbulence Modelling and Measurements*. Marbella, Spain.

Launder, B. E., Reece, G. & Rodi, W. 1975 Progress in the development of a Reynolds-stress turbulence closure. *J. Fluid Mech.* **68**, 537–566.

Le, H., Moin, P. & Kim, J. 1997 Direct numerical simulation of turbulent flow over a backward-facing step. *J. Fluid Mech.* **330**, 349–374.

van Leer, B. 1979 Towards the ultimate conservative difference scheme. V. A second-order sequel to Godunov's method. *J. Comput. Phys.* **32** (1), 101 – 136.

Leschziner, M. A., Batten, P. & Loyau, H. 2000 Modelling shock-affected near-wall flows with anisotropy-resolving turbulence closures. *Int. J. Heat Fluid Fl.* **21** (3), 239 – 251.

LeVeque, R. J. 2002 *Finite Volume Methods for Hyperbolic Problems*, 1st edn. New York, NY, USA: Cambridge University Press.

Liew, R., Zeegers, J., Kuerten, J. & Michałek, W. 2012 3D velocimetry and droplet sizing in the Ranque-Hilsch vortex tube. *Exp. Fluids* **54** (1).

Lumley, J. L. 1979 Computational modeling of turbulent flows. *Advances in Applied Mechanics*, vol. 18, pp. 123 – 176. Elsevier.

Maduta, R. 2013 An eddy-resolving Reynolds stress model for unsteady flow computations: development and application. Dissertation, TU Darmstadt.

Menter, F. 1992 Improved two-equation k-ω turbulence models for aerodynamic flows. Technical Memorandum 103975. NASA Ames Research Center, Moffett Field, CA, USA.

Menter, F., Kuntz, M. & Langtry, R. 2003 Ten years of industrial experience with the SST model. In *Turbulence, Heat and Mass Transfer 4* (ed. K. Hanjalić, Y. Nagano & M. Tummers).

Menter, F. R. 1994 Two-equation eddy-viscosity turbulence models for engineering applications. *AIAA J.* **32** (8), 1598–1605.

Menter, F. R. & Egorov, Y. 2005 A scale-adaptive simulation model using two-equation models. In *43rd AIAA Aerospace Sciences Meeting and Exhibit*. Reno, Nevada, USA.

Michelassi, V., Chen, L., Pichler, R. & Sandberg, R. 2014 Compressible direct numerical simulation of low-pressure turbines: Part II - effect of inflow disturbances. In *Proceedings of ASME Turbo Expo 2014*.

Morsbach, C. 2015 Analysis of a low Reynolds differential Reynolds stress model in homogeneous shear flow with respect to numerical stability. In *22nd AIAA Computational Fluid Dynamics Conference*. Dallas, TX, USA.

Morsbach, C., Franke, M. & di Mare, F. 2012 Towards the application of Reynolds stress transport models to 3D turbomachinery flows. In *7th International Symposium on Turbulence, Heat and Mass Transfer*. Palermo, Sicily, Italy.

Morsbach, C., Franke, M. & di Mare, F. 2014 Evaluation of a differential Reynolds stress model incorporating near-wall effects in a compressor cascade tip-leakage flow. In *6th European Conference on Computational Fluid Dynamics (ECFD VI)* (ed. E. Onate, X. Oliver & A. Huerta). International Center for Numerical Methods in Engineering.

Morsbach, C., Franke, M. & di Mare, F. 2015*a* Application of a low Reynolds differential Reynolds stress model to a compressor cascade tip-leakage flow. In *Differential Reynolds Stress Modeling for Separating Flows in Industrial Aerodynamics* (ed. B. Eisfeld), pp. 1–17. Springer International Publishing.

Morsbach, C. & di Mare, F. 2012 Conservative segregated solution method for turbulence model equations in compressible flows. In *6th European Congress on Computational Methods in Applied Sciences and Engineering (ECCOMAS 2012)*. Vienna, Austria.

Morsbach, C., Schlüß, D., Franke, M., Doll, U., Burow, E., Beversdorff, M., Stockhausen, G. & Willert, C. 2015*b* The flow field inside a Ranque-Hilsch vortex tube part II: Turbulence modelling and numerical simulation. In *Ninth International Symposium on Turbulence Shear Flow Phenomena (TSFP-9)*. Melbourne, Australia.

Moser, R. D., Kim, J. & Mansour, N. N. 1999 Direct numerical simulation of turbulent channel flow up to $Re_\tau = 590$. *Phys. Fluids* **11** (4), 943–945.

Muthanna, C. 2002 The effects of free stream turbulence on the flow field through a compressor cascade. Dissertation, Virginia Polytechnic Institute and State University.

Muthanna, C. & Devenport, W. J. 2004 Wake of a compressor cascade with tip gap, part 1: Mean flow and turbulence structure. *AIAA J.* **42** (11), 2320–2331.

Nguyen, T., Behr, M. & Reinartz, B. 2011 Near-wall extension of a non-equilibrium, omega-based Reynolds stress model. *J. Phys. Conf. Ser.* **318** (4), 042031.

Niewoehner, J., Poehler, T., Jeschke, P. & Guendogdu, Y. 2015 Investigation of nonaxisymmetric endwall contouring and three-dimensional airfoil design in a 1.5 stage axial turbine–part II: Experimental validation. *J. Turbomach.* **137** (8), 081010–081010.

Nürnberger, D. 2004 Implizite Zeitintegration für die Simulation von Turbomaschinenströmungen. Dissertation, Ruhr-Universität Bochum.

Oliphant, T. E. 2007 Python for scientific computing. *Comput. Sci. Eng.* **9** (3), 10–20.

Pettersson-Reif, B. A., Gatski, T. B. & Rumsey, C. L. 2006 On the behavior of two-equation models in nonequilibrium homogeneous turbulence. *Phys. Fluids* **18** (6).

Poehler, T., Niewoehner, J., Jeschke, P. & Guendogdu, Y. 2015 Investigation of nonaxisymmetric endwall contouring and three-dimensional airfoil design in a 1.5-stage axial turbine–part I: Design and novel numerical analysis method. *J. Turbomach.* **137** (8), 081009–081009.

Probst, A. 2013 Reynoldsspannungsmodellierung für das Überziehen in der Flugzeugaerodynamik. Dissertation, TU Braunschweig.

Probst, A. & Radespiel, R. 2008 Implementation and extension of a near-wall Reynolds-stress model for application to aerodynamic flows on unstructured meshes. In *Aerospace Sciences Meetings*. American Institute of Aeronautics and Astronautics.

Ranque, G. J. 1933 Expériences sur la détente giratoire avec productions simultanées d'un echappement d'air chaud et d'un echappement d'air froid. *Journal de Physique et Le Radium* **4** (7), 112–114.

Rautaheimo, P. P., Salminen, E. J. & Sikonen, T. L. 2003 Numerical simulation of the flow in the NASA low-speed centrifugal compressor. *Int. J. Turbo Jet. Eng.* **20**, 155–170.

Reinmöller, U. 2007 Experimentelle Untersuchung von instationären Strömungsphänomenen in Axialturbinen. Dissertation, RWTH Aachen.

Restemeier, M., Jeschke, P., Guendogdu, Y. & Gier, J. 2012 Numerical and experimental analysis of the effect of variable blade row spacing in a subsonic axial turbine. *J. Turbomach.* **135** (2), 021031–021031.

Reynolds, O. 1895 On the dynamical theory of incompressible viscous fluids and the determination of the criterion. *Phil. Trans. R. Soc. Lond. A* **186**, 123–164.

Robens, S., Frey, C., Jeschke, P., Kügeler, E., Bosco, A. & Breuer, T. 2013 Adaption of Giles non-local non-reflecting boundary conditions for a cell-centered solver for turbomachinery applications. In *Proceedings of ASME Turbo Expo 2013*.

Roe, P. L. 1981 Approximate Riemann solvers, parameter vectors, and difference schemes. *J. Comput. Phys.* **43** (2), 357 – 372.

Rotta, J. 1951 Statistische Theorie nichthomogener Turbulenz. *Z. Phys. A Hadron Nucl.* **129** (6), 547–572.

Rumsey, C. L. 2007 Apparent transition behavior of widely-used turbulence models. *International Journal of Heat and Fluid Flow* **28** (6), 1460 – 1471, revised and extended papers from the 5th conference in Turbulence, Heat and Mass Transfer 'The 5th conference in Turbulence, Heat and Mass Transfer.

Rumsey, C. L. & Gatski, T. B. 2001 Isolating curvature effects in computing wall-bounded turbulent flows. In *39th AIAA Aerospace Sciences Meeting & Exhibit*. Reno, NV, USA.

Rumsey, C. L., Pettersson Reif, B. A. & Gatski, T. B. 2006 Arbitrary steady-state solutions with the k-epsilon model. *AIAA J.* **44** (7), 1586–1592.

Rumsey, C. L., Smith, B. R. & Huang, G. P. 2010 Description of a website resource for turbulence modeling verification and validation. In *40th AIAA Fluid Dynamics Conference and Exhibit*. Chicago, IL, USA.

Sandberg, R. D., Michelassi, V., Pichler, R., Chen, L. & Johnstone, R. 2015 Compressible direct numerical simulation of low-pressure turbines–part I: Methodology. *J. Turbomach.* **137** (5), 051011–051011.

Schlüß, D. 2013 Untersuchung der Vorhersagequalität von Reynolds-Spannungs-Turbulenzmodellen in komplexen 3D-Strömungen. Master thesis, RWTH Aachen.

Schlichting, H. 1982 *Grenzschicht-Theorie*. Karlsruhe: Braun.

Schnell, R. & Nürnberger, D. 2004 Investigation of the tonal acoustic field of a transonic fanstage by time-domain CFD-calculation with arbitrary blade counts. In *Proceedings of the ASME Turbo Expo 2004*, , vol. 5, pp. 1763–1773. Vienna, Austria.

Schoenherr, K. E. 1932 Resistance of flat surfaces moving through a fluid. *Trans. SNAME* **40**, 279–313.

Sciberras, M. A. & Coleman, G. N. 2007 Testing of Reynolds-stress-transport closures by comparison with DNS of an idealized adverse-pressure-gradient boundary layer. *Eur. J. Mech. B Fluids* **26** (4), 551 – 582.

Shir, C. C. 1973 A preliminary numerical study of atmospheric turbulent flows in the idealized planetary boundary layer. *J. Atmos. Sci.* **30** (7), 1327–1339.

Sillero, J. A., Jiménez, J. & Moser, R. D. 2013 One-point statistics for turbulent wall-bounded flows at Reynolds numbers up to $\delta + \approx 2000$. *Phys. Fluids* **25** (10).

Simonsen, A. J. & Krogstad, P.-A. 2005 Turbulent stress invariant analysis: Clarification of existing terminology. *Phys. Fluids* **17** (8), 088103.

So, R. M. C. & Mellor, G. L. 1973 Experiment on convex curvature effects in turbulent boundary layers. *J. Fluid Mech.* **60** (01), 43–62.

Spalart, P. R. 1988 Direct simulation of a turbulent boundary layer up to $R_\theta = 1410$. *J. Fluid Mech.* **187**, 61–98.

Spalart, P. R. 2009 Detached-eddy simulation. *Annu. Rev. Fluid Mech.* **41** (1), 181–202.

Spalart, P. R. 2010 Reflections on RANS modelling. In *Progress in Hybrid RANS-LES Modelling* (ed. S.-H. Peng, P. Doerffer & W. Haase), *Notes on Numerical Fluid Mechanics and Multidisciplinary Design*, vol. 111, pp. 7–24. Springer Berlin / Heidelberg.

Spalart, P. R. 2015 Philosophies and fallacies in turbulence modeling. *Progress in Aerospace Sciences* **74**, 1 – 15.

Spalart, P. R. & Shur, M. 1997 On the sensitization of turbulence models to rotation and curvature. *Aerosp. Sci. Technol.* **1** (5), 297 – 302.

Speziale, C. G. & Mhuiris, N. M. G. 1989 On the prediction of equilibrium states in homogeneous turbulence. *J. Fluid Mech.* **209**, 591–615.

Speziale, C. G., Sarkar, S. & Gatski, T. B. 1991 Modelling the pressure-strain correlation of turbulence: An invariant dynamical systems approach. *J. Fluid Mech.* **227**, 245–272.

Tang, G. 2004 Measurements of the tip-gap turbulent flow structure in a low-speed compressor cascade. Dissertation, Virginia Polytechnic Institute and State University.

Tucker, P. 2011 Computation of unsteady turbomachinery flows: Part 2—LES and hybrids. *Prog. Aerosp. Sci.* **47** (7), 546 – 569.

Weber, A. & Sauer, M. 2016 Pymesh - template documentation. Technical report DLR-IB-AT-KP-2016-34. German Aerospace Center (DLR), Institute of Propulsion Technology, Linder Hoehe, Cologne, Germany.

Wilcox, D. C. 1988 Reassessment of the scale-determining equation for advanced turbulence models. *AIAA J.* **26** (11), 1299–1310.

Wilcox, D. C. 2006 *Turbulence Modeling for CFD*, 3rd edn. DCW Industries, La Cañada, USA.

Xue, Y., Arjomandi, M. & Kelso, R. 2010 A critical review of temperature separation in a vortex tube. *Experimental Thermal and Fluid Science* **34** (8), 1367 – 1374.

Yang, H., Nürnberger, D. & Weber, A. 2002 A conservative zonal approach with application to unsteady turbomachinery flows. In *DGLR Jahrestagung*.

Younis, B. A., Weigand, B. & Laqua, A. 2012 Prediction of turbulent heat transfer in rotating and nonrotating channels with wall suction and blowing. *J. Heat Transf.* **134** (7), 071702.

List of Figures

1.1 Hierarchy of RANS turbulence models. Reproduced after Gatski & Jongen (2000). 3

3.1 Invariant map of realisable turbulence states (Lumley, 1979). For orientation, DNS results of channel flow (Moser *et al.*, 1999) are plotted with nearly isotropic turbulence in the centre of the channel and two-component limit at the wall. 18

3.2 Barycentric map describing turbulence anisotropy tensor (Banerjee *et al.*, 2007). For orientation DNS of channel flow (Moser *et al.*, 1999) is plotted with nearly isotropic turbulence in the centre of the channel and two-component limit at the wall. It is filled with contours of two-component parameter A for comparison with the anisotropy invariant map (*left*) and with RGB colouring to allow for a contour plot field visualisation of turbulence anisotropy states (Emory & Iaccarino, 2014) (*right*). 18

3.3 Coefficient functions for the slow (*left*) and rapid (*right*) pressure-strain terms of the JH-ω^h model compared to the SSG/LRR-ω model in turbulent plane channel flow. 26

3.4 Motivation for the investigation of homogeneous shear model problem: Skin friction coefficient c_f of RAE2822 aerofoil. 31

3.5 Validation of the JH-ω^h model implementation in the ODE solver against TRACE computations for homogeneous shear flow with isotropic (*left*) and one-component (*right*) initialisation. 35

3.6 Phase space trajectories of LRR-ω (*left*) and JH-ω^h (*right*) in homogeneous shear flow initialised with different turbulence anisotropy states. 36

3.7 Phase space trajectories of JH-ω^h with the turbulent Reynolds number Re_T as fixed parameter (*left*) and with the Re_T equation solved (*right*) in homogeneous shear flow initialised with different turbulence anisotropy states. 37

3.8 Logarithmic time history of solution variables a_{ij}, ω^* and Re_T (*first row*), model coefficients C_1, C_2, f_s and two-component parameter A (*second row*) for fixed $Re_T = 50$ (*first column*), solved Re_T initialised with $Re_{T0} = 50$ (*second column*) and fixed $Re_T = 150$ (*third column*). 38

3.9 Logarithmic time history of normalised production P^*_{ij}, slow pressure-strain $\Pi^*_{ij,1}$, rapid pressure-strain $\Pi^*_{ij,2}$, dissipation term $-\epsilon^*_{ij}$ and total budget of 11- (*top*), 12- (*middle*) and 22-component (*bottom*) for fixed $Re_T = 50$ (*first column*), solved Re_T initialised with $Re_{T0} = 50$ (*second column*) and fixed $Re_T = 150$ (*third column*). 40

3.10 Time history of two-component parameter A for fixed values of Re_T between 45 and 55 indicated by line colour. $Re_T = 50.8$ labels the last solution with stable finite value of A while A goes to zero for all Re_T smaller than that. 41

3.11 Phase space trajectories of JH-ω^h with $C_2 = 0.6\sqrt{A}$ in homogeneous shear flow initialised with different turbulence anisotropy states (*left*) and map of initial conditions attracted to one-component turbulence (*right*). The turbulent channel flow solution with JH-ω^h computed with TRACE is plotted for reference. 41

4.1 Schematic of multi-block cell centred finite volume method. 44

4.2 Schematic of rotationally periodic boundary. Flow state in ghost cell is the state in the corresponding inner cell rotated about x-axis by angle $\angle(A, B)$. 52

4.3 Schematic of mixing plane boundary at $x =$ const. Reynolds stresses are averaged cylindrical coordinate system. 53

5.1 Sketch of fully developed turbulent flow through a plane channel (*left*) and mesh with 48 nodes in y-direction and boundary conditions (*right*). 58

5.2 Normalised boundary layer velocity profile computed by DNS for fully developed turbulent flow through a plane channel. 58

5.3 Mesh dependence of SSG/LRR-ω and JH-ω^h model in turbulent plane channel flow. The meshes have 48, 96 and 192 nodes in wall-normal direction. 60

5.4 Comparison of Menter SST k-ω, Hellsten EARSM k-ω, SSG/LRR-ω and JH-ω^h results for turbulent plane channel flow at $Re_\tau = 180$ (Kim *et al.*, 1987), $Re_\tau = 395$ (Iwamoto *et al.*, 2002) (offset U^+ by 5, $\overline{uv}^+$ by 0.5) and $Re_\tau = 2003$ (Hoyas & Jimenez, 2006) (offset U^+ by 10, $\overline{uv}^+$ by 1): Normalised velocity U^+ (*top*) and Reynolds shear stress $\overline{uv}^+$ (*bottom*). 61

5.5 Comparison of Menter SST k-ω, Hellsten EARSM k-ω, SSG/LRR-ω and JH-ω^h results for turbulent plane channel flow: Normalised velocity fluctuations u^+ (offset by 2), v^+ and w^+ (offset by 1) for $Re_\tau = 180$ (Kim *et al.*, 1987) (*top*) and $Re_\tau = 2003$ (Hoyas & Jimenez, 2006) (*bottom*). 62

5.6 Comparison of JH-ω^h, JH-ω^h (Maduta) and JH-ϵ^h results for turbulent plane channel flow at $Re_\tau = 180$ (Kim *et al.*, 1987), $Re_\tau = 395$ (Iwamoto *et al.*, 2002) (offset U^+ by 5, $\overline{uv}^+$ by 0.5) and $Re_\tau = 2003$ (Hoyas & Jimenez, 2006) (offset U^+ by 10, $\overline{uv}^+$ by 1): Normalised velocity U^+ (*top*) and Reynolds shear stress $\overline{uv}^+$ (*bottom*). 64

5.7 Comparison of JH-ω^h, JH-ω^h (Maduta) and JH-ϵ^h results for turbulent plane channel flow: Normalised velocity fluctuations u^+ (offset by 2), v^+ and w^+ (offset by 1) for $Re_\tau = 180$ (Kim *et al.*, 1987) (*top*) and $Re_\tau = 2003$ (Hoyas & Jimenez, 2006) (*bottom*). 65

5.8 Reynolds stress anisotropy invariant map of turbulent plane channel flow at $Re_\tau = 180$ (Kim *et al.*, 1987) for $y/\delta \in [0, 1]$. 67

5.9 Reynolds stress anisotropy two component factor A of turbulent plane channel flow at $Re_\tau = 180$ (Kim *et al.*, 1987). 67

5.10 Turbulence anisotropy of all four DRSMs in turbulent plane channel flow at $Re_\tau = 180$ (Kim *et al.*, 1987) plotted to barycentric map (*left*) and as colours (*right*). 68

5.11 Production and homogeneous dissipation of turbulent kinetic energy of turbulent plane channel flow at $Re_\tau = 395$ (Iwamoto *et al.*, 2002). 69

5.12 Sketch of zero pressure gradient flow over flat plate. 69

5.13 Mesh of zero pressure gradient flat plate test case. 70

5.14 Friction coefficient c_f of zero pressure gradient flat plate flow over Reynolds number based on momentum thickness Re_θ. DNS data by Spalart (1988), Sillero *et al.* (2013), correlations by Kays & Crawford (1980) and Schoenherr (1932). 71

5.15 Normalised velocity U^+ (*top*) and Reynolds shear stress $\overline{uv}^+$ (*bottom*) profiles of zero pressure gradient flat plate flow at varying Re_θ (offset U^+ by 5 each, $\overline{uv}^+$ by 0.5 each) compared with DNS (Sillero *et al.*, 2013) and a correlation at $Re_\theta = 10000$ (Coles, 1956). 72

5.16 Normalised velocity fluctuations u^+ (offset by 2), v^+ and w^+ (offset by 1) of zero pressure gradient flat plate flow at $Re_\theta = 1551$ (*top*) and $Re_\theta = 6000$ (*bottom*) compared with DNS data (Sillero *et al.*, 2013). Spalart's results at $Re_\theta = 1410$ (Spalart, 1988) are plotted for reference. 73

5.17 Sketch of flow around curved bend (So & Mellor, 1973) (*left)* and computational mesh (every second line shown in streamwise direction, every fourth line shown in direction normal to the wall), boundary conditions and positions of boundary layer profiles at stations $s = 24\text{in}, 59\text{in}, 67\text{in}, 71\text{in}$ (*right*). 74

5.18 Pressure coefficient c_p (*left*) and friction coefficient c_f (*right*) for curved bend flow (So & Mellor, 1973). 75

5.19 Normalised velocity magnitude U/U_∞, Reynolds shear stress $\overline{uv}/U_\infty^2$ and normal stresses $\overline{uu}/U_\infty^2$ and $\overline{vv}/U_\infty^2$ for curved bend flow in basis of experiment (So & Mellor, 1973). 76

5.20 Turbulence anisotropy of curved bend flow in RGB colours for SSG/LRR-ω (*right*) and JH-ω^h (*left*). Experimental data by So & Mellor (1973) scaled to computational coordinates are plotted within white boxes. 77

5.21 Sketch of flow over backward facing step (Driver & Seegmiller, 1985) (*left*) and computational mesh (every fourth line shown in streamwise direction, every second line shown in direction normal to the wall), boundary conditions and positions of boundary layer profiles (red) at stations $x/H = -4, 1, 4, 6, 10$ (*right*). Inflow and outflow boundaries are not shown as the mesh extends 130 step heights upstream and 50 step heights downstream. 78

5.22 Skin friction coefficient c_f (*left*) and pressure coefficient c_p (*right*) for backward facing step flow. 79

5.23 Normalised velocity profiles U/U_ref (*top left*) and Reynolds stress profiles $\overline{uv}/U_\text{ref}^2$ (*top right*), $\overline{uu}/U_\text{ref}^2$ (*bottom left*) and $\overline{vv}/U_\text{ref}^2$ (*bottom right*) of backward facing step flow at $Re_H = 36,000$ (Driver & Seegmiller, 1985) at stations $x/H = -4, 1, 4, 6, 10$ (offset in x-direction). 81

5.24 Streamlines of backward facing step flow at $Re_H = 36,000$ (Driver & Seegmiller, 1985) computed by JH-ω^h (*top*), JH-ω^h (Maduta, $P^3_{\epsilon 3}$) (*middle*) and SSG/LRR-ω (*bottom*) with separation and reattachment points magnified. The turbulence anisotropy is coloured in RGB. 82

5.25 Sketch of transonic flow over axisymmetric bump (Bachalo & Johnson, 1986) (*left*) and computational mesh (every eighth line shown), boundary conditions and positions of boundary layer profiles at stations $x/c = -0.250, 0.688, 0.813, 1.000, 1.125, 1.375$ (*right*). 83

5.26 Transonic flow over axisymmetric bump (Bachalo & Johnson, 1986). Pressure coefficient c_p (*top left*), skin friction coefficient c_f (*top right*); profiles of normalised turbulent kinetic energy k/U_∞^2 (*middle left*), shear stress $\overline{uv}/U_\infty^2$ (*middle right*) and normalised mean velocity U/U_∞ (*bottom left*) at axial stations $x/c = -0.250, 0.688, 0.813, 1.000, 1.125, 1.375$ (offset in x-direction). 85

5.27 Streamlines of flow over axisymmetric transonic bump (Bachalo & Johnson, 1986) computed by JH-ω^h (*top*) and SSG/LRR-ω (*bottom*) with reattachment point magnified in respective top right corner. The turbulence anisotropy is coloured in RGB and the shock is visualised by the $M = 1$ isoline (white). 86

6.1 Summary of numerical setup of Virginia Tech compressor cascade computation. 88

6.2 Illustration of tip-leakage flow in the Virginia Tech compressor cascade. The measured mean velocity in blade passage is compared to the prediction by the JH-ω^h DRSM. 89

6.3 Measurement positions (*left*) and pressure coefficient c_p at midspan (*right*) of Virginia Tech compressor cascade (Muthanna, 2002; Tang, 2004). . . . 90

6.4 Normalised chordwise velocity U_c/U_{ref} (*left*) and turbulence two-component parameter A (*right*) compared with measurements (Tang, 2004) upstream of the blade row at $x/c_a = -0.33$. 90

6.5 Prediction of tip gap vortex centre. The symbols represent vortex centre at different measurement planes. Its trajectory is projected to x-y plane for better comparability. The position for the examined tip gap measurements at $x/c_a = 0.18$, is shown in red. 91

6.6 Prediction of separation line on the end wall. The blade profile and the separation line from oil flow visualisation (Muthanna, 2002) are plotted in black. The limiting streamlines are coloured with surface pressure coefficient c_p. 92

6.7 Reynolds stress anisotropy invariants in the tip gap at measurement position 5c. 93

6.8 Turbulence anisotropy indicated by RGB colours in measurement plane 5 as computed by JH-ω^h (*top*), SSG/LRR-ω (*middle*) and Hellsten EARSM k-ω (*bottom*) models compared with experimental data (Tang, 2004) plotted in white boxes. Solid walls are shaded in grey. 93

6.9 Velocity components in the tip gap at measurement position 5c in the coordinate system aligned with the chord. 94

6.10 Turbulence anisotropy plotted as RGB colours and normalised mean velocity magnitude plotted as white contour lines on a slice through the passage flow at $x/c_a = 0.98$ compared with measured data (Muthanna, 2002). 95

6.11 Comparison of the corner separation on the blade wall opposite to the tip gap predicted by JH-ω^h (*left*), SSG/LRR-ω (*middle*) and Menter SST k-ω (*right*). 95

6.12 Vortex tube geometry and boundary conditions. 97

6.13 Photo of vortex tube experiment showing the part of the tube at the hot end illuminated by the laser sheet with a dark core vortex. 98

6.14 Vortex tube mesh. 99

6.15 Mass flow convergence of the unsteady simulation of the Ranque-Hilsch vortex tube using the SSG/LRR-ω model. The sum over all inlets is shown against the sum over all outlets. 101

6.16 Sketch of analysis and measurement positions in the Ranque-Hilsch vortex tube. The axes have been rescaled. 101

6.17 Comparison of axial and circumferential velocity U_x (*top left*) and U_z (*top right*) radial profiles with L2F data and temperature T (*bottom left*) radial profile with FRS data at $x/R = 1$. Vortex visualisation using the $\lambda_2 = -1$ isosurface of the steady snapshot, the unsteady snapshot and the unsteady averaged solution obtained with SSG/LRR-ω model (*bottom right*). 102

6.18 Contours of average velocity components U_x, U_y, U_z and temperature T in the $z = 0$ plane from the 2D data set computed with the SSG/LRR-ω model. 104

6.19 Velocity U_x, U_y, U_z and temperature T profiles in the $z = 0$ plane at $y = 0$ (*left*) and $y/R = 0.9$ (*right*) extracted from the steady solutions computed with the Menter SST k-ω and Hellsten EARSM k-ω models, respectively, and the unsteady 2D data set computed with SSG/LRR-ω model. 104

6.20 Fourier transform of pressure signal obtained from the unsteady computation with the SSG/LRR-ω model from the 0D data set compared to measured data at $x/L = 0.05, 0.2$ and 0.4. 105

6.21 Fourier transform of the circumferential velocity U_z at $z = 0$ on the axis (*left*) and at $y/R = 0.9$ (*right*) from the 2D data set computed with the SSG/LRR-ω model. 106

6.22 1.5 stage cold air turbine test rig of the *Institute of Jet Propulsion and Turbomachinery* at the *RWTH Aachen University*. Measurement planes of five hole probes are shaded in red. 107

6.23 Mass flow convergence Menter SST k-ω (*top left*), Menter SST k-ω on refined mesh (*top right*), SSG/LRR-ω (*middle left*), JH-ω^h (*middle right*) and Hellsten EARSM k-ω (*bottom left*), RANS residuals for all models (*bottom right*). 112

6.24 Unsteady mass flow convergence Menter SST k-ω (*top left*), SSG/LRR-ω (*top right*) and JH-ω^h (*bottom left*). 113

6.25 Radial traverses behind stator 1 (*left*), rotor 1 (*middle*) and stator 2 (*right*) obtained with the Menter SST k-ω model comparing steady and unsteady averaged results with steady results on the refined mesh. 114

6.26 Visualisation of the vortex system in stator 1 by a $\lambda_2 = -1.5$ isosurface coloured with streamwise vorticity ω_{sw}. 115

6.27 Streamwise vorticity ω_{sw} (*top*) and Mach number M (*bottom*) downstream of stator 1. 117

6.28 Visualisation of the vortex system in rotor 1 by a $\lambda_2 = -1.5$ isosurface coloured with streamwise vorticity ω_{sw}. 118

6.29 Streamwise vorticity ω_{sw} (*top*) and Mach number M (*bottom*) downstream of rotor 1. 119

6.30 Streamwise vorticity ω_{sw} (*top*) and Mach number M (*bottom*) downstream of stator 2. 121

6.31 Radial traverses of streamwise vorticity ω_{sw} (*top*) and Mach number M (*bottom*) behind stator 1 (*left*), rotor 1 (*middle*) and stator 2 (*right*) averaged from the unsteady simulations with Menter SST k-ω, SSG/LRR-ω and JH-ω^h models compared to experimental data. 122

6.32 Wall shear stress $\tau_{w,x}$ for stator 1, rotor 1, stator 2 (from left to right) from steady simulation. 123

List of Tables

3.1 Coefficients of Reynolds stress and dissipation rate equations for SSG/LRR-ω model (Cécora *et al.*, 2014). 24

3.2 Coefficients of Reynolds stress and dissipation rate equations for the JH-ω^h model (Morsbach *et al.*, 2015*a*). 25

3.3 Turbulence model coefficient functions simplified for homogeneous shear problem. 33

3.4 Steady-state solutions of homogeneous shear flow. 34

3.5 Initial conditions for phase space analysis of homogeneous shear flow. Non-realisable combinations of a_{ij} components are filtered. 36

4.1 Iterative convergence of turbulence models for duct segment testcase. . 55

5.1 Test case setup and DNS data sources for turbulent plane channel flow. . 57

5.2 Reattachment and secondary separation points in backward facing step flow at $Re_H = 36,000$ with expansion ratio 1.125 (Driver & Seegmiller, 1985). 80

6.1 Properties of Virginia Tech compressor cascade and inflow conditions. . 88

6.2 Boundary conditions for Ranque-Hilsch vortex tube. 99

6.3 Uncertainty due to the computational mesh for the Ranque-Hilsch vortex tube computed with the Menter SST k-ω model. 100

6.4 Properties of RWTH Aachen cold air turbine rig (Niewoehner *et al.*, 2015). 108

6.5 Blade properties of RWTH Aachen cold air turbine rig (Niewoehner *et al.*, 2015). 108

A.1 Coefficients of Menter SST k-ω model. 154

A.2 Coefficients of Hellsten EARSM k-ω model. 156

A.3 Coefficients of Reynolds stress and dissipation rate equations for SSG/LRR-ω model (Cécora *et al.*, 2014). 159

A.4 Coefficients of Reynolds stress and dissipation rate equations for the JH-ω^h model (Morsbach *et al.*, 2015*a*). 161

A.5 Formulation of gradient production $P_{\epsilon3}$ and cross-diffusion $CD_{k\omega}$ term for different versions of JH-ω^h model. 161

A Model specifications

A.1 Menter SST k-ω

The Menter SST k-ω model is implemented in its version of 2003 as documented by Menter *et al.* (2003) and verified by code-to-code comparison using the *Turbulence Modeling Resource* website (Rumsey *et al.*, 2010).

Turbulent kinetic energy and dissipation rate equations

$$\begin{aligned}\frac{D(\overline{\rho}k)}{Dt} &= \overline{\rho}P_k - \beta^*\overline{\rho}\omega k + \frac{\partial}{\partial x_i}\left[(\mu + \sigma_k\mu_T)\frac{\partial k}{\partial x_i}\right] &\text{(A.1)}\\ \frac{D(\overline{\rho}\omega)}{Dt} &= \gamma\frac{\overline{\rho}^2}{\mu_T}P_k - \beta\overline{\rho}\omega^2 + \frac{\partial}{\partial x_i}\left[(\mu + \sigma_\omega\mu_T)\frac{\partial \omega}{\partial x_i}\right] &\text{(A.2)}\\ &\quad +2(1-F_1)\frac{\sigma_{\omega 2}\overline{\rho}}{\omega}\frac{\partial k}{\partial x_i}\frac{\partial \omega}{\partial x_i}\end{aligned}$$

$$\beta^* = 0.09 \tag{A.3}$$

Production term

$$\overline{\rho}P_k = \min\left(2\mu_T S^*_{ij}S^*_{ij} - \frac{2}{3}\overline{\rho}kS_{ii}, 10\beta^*\overline{\rho}k\omega\right) \tag{A.4}$$

$$\begin{aligned}S_{ij} &= \frac{1}{2}\left(\frac{\partial U_i}{\partial x_j} + \frac{\partial U_j}{\partial x_i}\right) &\text{(A.5)}\\ S^*_{ij} &= S_{ij} - \frac{1}{3}S_{qq}\delta_{ij} &\text{(A.6)}\end{aligned}$$

Blending of coefficients

$$\phi = F_1\phi_1 + (1-F_1)\phi_2 \tag{A.7}$$

$$\begin{aligned}F_1 &= \tanh\left(\arg_1^4\right) &\text{(A.8)}\\ \arg_1 &= \min\left[\max\left(\frac{\sqrt{k}}{\beta^*\omega d}, \frac{500\mu}{\overline{\rho}d^2\omega}\right), \frac{4\overline{\rho}\sigma_{\omega 2}k}{CD_{k\omega}d^2}\right] &\text{(A.9)}\\ CD_{k\omega} &= \max\left(\frac{2\overline{\rho}\sigma_{\omega 2}}{\omega}\frac{\partial k}{\partial x_i}\frac{\partial \omega}{\partial x_i}, 10^{-10}\right) &\text{(A.10)}\end{aligned}$$

with the distance to the nearest wall d. Coefficients see Table A.1.

Table A.1: Coefficients of Menter SST k-ω model.

Constant	β	σ_k	σ_ω	γ
inner (1)	0.075	0.85	0.5	0.556
outer (2)	0.0828	1.0	0.856	0.44

Eddy viscosity

$$\mu_T = \frac{\rho a_1 k}{\max(a_1 k, S F_2)}, \quad a_1 = 0.31 \tag{A.11}$$

$$S = \sqrt{2 S_{ij} S_{ij}} \tag{A.12}$$

$$\begin{aligned} F_2 &= \tanh\left(\arg_2^2\right) && \text{(A.13)} \\ \arg_2 &= \max\left(\frac{2\sqrt{k}}{\beta^* \omega d}, \frac{500\mu}{\overline{\rho} d^2 \omega}\right) && \text{(A.14)} \end{aligned}$$

A.2 Hellsten EARSM k-ω

The Hellsten EARSM k-ω model is implemented and validated as documented by Franke (2010). The formulation of the eddy viscosity is mathematically equivalent.

Turbulent kinetic energy and dissipation rate equations

$$\begin{aligned} \frac{D(\overline{\rho}k)}{Dt} &= \overline{\rho}P_k - \beta^* \overline{\rho} \omega k + \frac{\partial}{\partial x_i}\left[\left(\mu + \sigma_k \mu_T\right)\frac{\partial k}{\partial x_i}\right] && \text{(A.15)} \\ \frac{D(\overline{\rho}\omega)}{Dt} &= \alpha \frac{\omega}{k} P_k - \beta \overline{\rho} \omega^2 + \frac{\partial}{\partial x_i}\left[\left(\mu + \sigma_\omega \mu_T\right)\frac{\partial \omega}{\partial x_i}\right] && \text{(A.16)} \\ &\quad + \sigma_d \frac{\overline{\rho}}{\omega} \max\left[\frac{\partial k}{\partial x_i}\frac{\partial \omega}{\partial x_i}, 0\right] \end{aligned}$$

$$\beta^* = 0.09 \tag{A.17}$$

Production term

$$\overline{\rho}P_k = -\overline{\rho u_i'' u_j''}\frac{\partial U_i}{\partial x_j} \tag{A.18}$$

Blending of coefficients

$$\phi = F_1\phi_1 + (1 - F_1)\phi_2 \tag{A.19}$$

$$\begin{aligned} F_1 &= \tanh\left(1.5\mathrm{arg}_1^4\right) && \text{(A.20)} \\ \mathrm{arg}_1 &= \min\left[\max\left(\frac{\sqrt{k}}{\beta^*\omega d}, \frac{500\mu}{\overline{\rho}\omega d^2}\right), \frac{20k}{\max\left(\frac{d^2}{\omega}\frac{\partial k}{\partial x_i}\frac{\partial \omega}{\partial x_i}, 200\cdot 10^{-12}\right)}\right] && \text{(A.21)} \end{aligned}$$

with the distance to the nearest wall d. Coefficients see Table A.2.

Constitutive relation

$$\overline{\rho u_i'' u_j''} = -2\mu_T S_{ij}^* + \frac{2}{3}\overline{\rho}k\delta_{ij} + \rho k a_{ij}^{\mathrm{ex}} \tag{A.22}$$

$$\begin{aligned} S_{ij}^* &= \frac{1}{2}\left(\frac{\partial U_i}{\partial x_j} + \frac{\partial U_j}{\partial x_i} - \frac{2}{3}\frac{\partial U_k}{\partial x_k}\delta_{ij}\right) && \text{(A.23)} \\ \Omega_{ij}^* &= \frac{1}{2}\left(\frac{\partial U_i}{\partial x_j} - \frac{\partial U_j}{\partial x_i}\right) && \text{(A.24)} \end{aligned}$$

Eddy viscosity

$$\mu_T = \frac{3}{5}\frac{N}{N^2 - 2II_\Omega}\overline{\rho}k\tau \tag{A.25}$$

This formulation is mathematically equivalent to the one stated by Franke (2010).

$$\tau = \max\left[\frac{k}{\epsilon}, C_\tau\sqrt{\frac{\mu}{\overline{\rho}\epsilon}}\right], \quad \epsilon = \beta^* k\omega, \quad C_\tau = 6.0 \tag{A.26}$$

$$\begin{aligned} S_{ij} &= \tau S_{ij}^* && \text{(A.27)} \\ \Omega_{ij} &= \tau\Omega_{ij}^* && \text{(A.28)} \end{aligned}$$

$$II_S = S_{ij}S_{ji}, \quad II_\Omega = \Omega_{ij}\Omega_{ji}, \quad IV = S_{ij}\Omega_{jk}\Omega_{ki} \tag{A.29}$$

Extra anisotropy

$$\begin{aligned} a_{ij}^{\mathrm{ex}} = &\beta_3\left(\Omega_{ik}\Omega_{kj} - \tfrac{1}{3}II_\Omega\delta_{ij}\right) + \\ &\beta_4\left(S_{ik}\Omega_{kj} - \Omega_{ik}S_{kj}\right) + \\ &\beta_6\left(S_{ik}\Omega_{kl}\Omega_{lj} + \Omega_{ik}\Omega_{kl}S_{lj} - II_\Omega S_{ij} - \tfrac{2}{3}IV\delta_{ij}\right) + \\ &\beta_9\left(\Omega_{ik}S_{kl}\Omega_{lm}\Omega_{mj} - \Omega_{ik}\Omega_{kl}S_{lm}\Omega_{mj}\right) \end{aligned} \tag{A.30}$$

Table A.2: Coefficients of Hellsten EARSM k-ω model.

Constant	α	β	σ_k	σ_ω	σ_d
inner (1)	0.518	0.0747	1.1	0.53	1.0
outer (2)	0.44	0.0828	1.1	1.0	0.4

β coefficients

$$\beta_1 = -\frac{N\left(2N^2 - 7II_\Omega\right)}{Q} \tag{A.31}$$

$$\beta_3 = -\frac{12N^{-1}IV}{Q} \tag{A.32}$$

$$\beta_4 = -\frac{2\left(N^2 - 2II_\Omega\right)}{Q} \tag{A.33}$$

$$\beta_6 = -\frac{6N}{Q} \tag{A.34}$$

$$\beta_9 = \frac{6}{Q} \tag{A.35}$$

$$Q = \frac{5}{6}\left(N^2 - 2II_\Omega\right)\left(2N^2 - II_\Omega\right) \tag{A.36}$$

$$N = \begin{cases} \frac{C_1'}{3} + \left(P_1 + \sqrt{P_2}\right)^{\frac{1}{3}} + \left(P_1 - \sqrt{P_2}\right)^{\frac{1}{3}}, & P_2 \geq 0 \\ \frac{C_1'}{3} + 2\left(P_1^2 - P_2\right)^{\frac{1}{6}} \cos\left(\frac{1}{3}\arccos\left(\frac{P_1}{\sqrt{P_1^2 - P_2}}\right)\right), & P_2 < 0 \end{cases} \tag{A.37}$$

$$P_1 = \left(\frac{C_1'^2}{27} + \frac{9}{20}II_S - \frac{2}{3}II_\Omega\right)C_1' \tag{A.38}$$

$$P_2 = P_1^2 - \left(\frac{C_1'^2}{9} + \frac{9}{10}II_S + \frac{2}{3}II_\Omega\right)^3 \tag{A.39}$$

$$C_1' = \frac{9}{5} + \frac{9}{4}C_{\text{diff}}\max\left(1 + \beta_1^{(\text{eq})}II_S, 0\right), \quad C_{\text{diff}} = 2.2 \tag{A.40}$$

$$\beta_1^{(\text{eq})} = -\frac{6}{5}\frac{N^{(\text{eq})}}{(N^{(\text{eq})})^2 - 2II_\Omega}, \quad N^{(\text{eq})} = \frac{81}{20} \tag{A.41}$$

A.3 DRSM: common terms

Reynolds stress transport equations

$$\frac{D\overline{\rho u_i'' u_j''}}{Dt} = \overline{\rho} P_{ij} + \frac{1}{2}\overline{\rho} R_{ij} - \overline{\rho}\epsilon_{ij} + \overline{\rho}\Pi_{ij} + \frac{\partial}{\partial x_k}\left[D^{\mu}_{ij,k} + D^{T}_{ij,k}\right] \tag{A.42}$$

Reynolds stress production

$$\overline{\rho} P_{ij} = -\left(\overline{\rho u_i'' u_k''}\frac{\partial U_j}{\partial x_k} + \overline{\rho u_j'' u_k''}\frac{\partial U_i}{\partial x_k}\right) \tag{A.43}$$

System rotation

$$\frac{1}{2}\overline{\rho} R_{ij} = -\left(\overline{\rho u_i'' u_q''}\Omega_{qj} + \overline{\rho u_j'' u_q''}\Omega_{qi}\right), \quad \Omega_{ij} = \Omega_p \epsilon_{ijp} \tag{A.44}$$

Pressure strain term

$$\Pi_{ij} = \Pi_{ij,1} + \Pi_{ij,2} + \Pi^{w}_{ij,1} + \Pi^{w}_{ij,2} \tag{A.45}$$

$$\Pi_{ij,1} = -\epsilon\left[C_1 a_{ij} + C_1'\left(a_{ik}a_{jk} - \frac{1}{3}\delta_{ij}A_2\right)\right] \tag{A.46}$$

$$\begin{aligned}
a_{ij} &= \frac{\widetilde{u_i'' u_j''}}{k} - \frac{2}{3}\delta_{ij} && \text{(A.47)}\\
A_2 &= a_{ij}a_{ji} && \text{(A.48)}\\
A_3 &= a_{ij}a_{jk}a_{ki} && \text{(A.49)}\\
A &= 1 - \frac{9}{8}\left(A_2 - A_3\right) && \text{(A.50)}
\end{aligned}$$

$$\begin{aligned}
\Pi_{ij,2} = \Big[& \left(C_3 - C_3'\sqrt{A_2}\right) k S^{*}_{ij} \\
& + C_4 k\left(a_{ip}S_{pj} + a_{jp}S_{pi} - \frac{2}{3}a_{pq}S_{pq}\delta_{ij}\right) \\
& + C_5 k\left(a_{ip}W_{pj} + a_{jp}W_{pi}\right) - \frac{1}{2}C_2' a_{ij}P_{qq}\Big]
\end{aligned} \tag{A.51}$$

$$\begin{aligned}
S_{ij} &= \frac{1}{2}\left(\frac{\partial U_i}{\partial x_j} + \frac{\partial U_j}{\partial x_i}\right) && \text{(A.52)}\\
W_{ij} &= \frac{1}{2}\left(\frac{\partial U_i}{\partial x_j} - \frac{\partial U_j}{\partial x_i}\right) && \text{(A.53)}
\end{aligned}$$

A.4 SSG/LRR-ω model

Dissipation term

$$\epsilon_{ij} = \frac{2}{3}\epsilon\delta_{ij} \tag{A.54}$$

Pressure strain wall correction

$$\Pi^w_{ij} = 0 \tag{A.55}$$

Diffusion term

$$D^{\mu}_{ij,k} + D^{T}_{ij,k} = \mu\frac{\partial\widetilde{u_i''u_j''}}{\partial x_k} + C_S\frac{\overline{\rho}k}{\epsilon}\widetilde{u_k''u_l''}\frac{\partial\widetilde{u_i''u_j''}}{\partial x_l} \tag{A.56}$$

Eddy viscosity

$$\mu_T = \frac{\overline{\rho}k}{\omega} \tag{A.57}$$

Dissipation equation

$$\epsilon = C_\mu k\omega, \quad C_\mu = 0.09 \tag{A.58}$$

$$\frac{D\overline{\rho}\omega}{Dt} = \alpha\frac{\overline{\rho}\omega}{k}P_k - \beta\overline{\rho}\omega^2 + \sigma_d\frac{\overline{\rho}}{\omega}\frac{\partial k}{\partial x_j}\frac{\partial\omega}{\partial x_j} + \frac{\partial}{\partial x_k}\left[(\mu + \sigma_\omega\mu_T)\frac{\partial\omega}{\partial x_k}\right] \tag{A.59}$$

Dissipation solid wall boundary condition

$$\omega|_{\text{wall}} = 10\frac{6\mu}{\beta_\omega\overline{\rho}y_1^2} \tag{A.60}$$

Blending of coefficients

$$\phi = F_1\phi^{\text{LRR},\omega} + (1 - F_1)\phi^{\text{SSG},\epsilon} \tag{A.61}$$

$$F_1 = \tanh\left(\text{arg}_1^4\right) \tag{A.62}$$

$$\text{arg}_1 = \min\left[\max\left(\frac{\sqrt{k}}{\beta^*\omega y_n}, \frac{500\mu}{\overline{\rho}y_n^2\omega}\right), \frac{4\overline{\rho}\sigma_{\omega 2}k}{CD_{k\omega}y_n^2}\right] \tag{A.63}$$

$$CD_{k\omega} = \max\left(\frac{2\overline{\rho}\sigma_{\omega 2}}{\omega}\frac{\partial k}{\partial x_i}\frac{\partial\omega}{\partial x_i}, 10^{-10}\right) \tag{A.64}$$

with the distance to the nearest wall y_n.

Table A.3: Coefficients of Reynolds stress and dissipation rate equations for SSG/LRR-ω model (Cécora *et al.*, 2014).

Coefficient	SSG,ϵ	LRR,ω
C_1	1.7	1.8
C_1'	-1.05	0
C_3	0.8	
C_3'	0.65	0
C_4	0.625	0.9709
C_5	-0.2	-0.5782
C_2'	0.9	0
C_S^{GGD}	0.22	0.75 C_μ
C_S^{SGD}	$2C_S^{\mathrm{GGD}}/3$	
α	0.44	0.5556
β	0.0828	0.075
σ_ω	0.856	0.5
σ_d	1.712	0

A.5 Jakirlić, Hanjalić and Maduta's $\overline{u_i u_j}$-ω^h model

Dissipation term

$$\epsilon_{ij} = \epsilon_{ij}^h + \frac{1}{2} D_{ij}^\nu \tag{A.65}$$

$$\epsilon_{ij}^h = \epsilon^h \left[\frac{2}{3}\delta_{ij} + f_s a_{ij} \right] \tag{A.66}$$

$$f_s = 1 - \sqrt{A} E^2 \tag{A.67}$$

$$\begin{aligned} e_{ij} &= \frac{\epsilon_{ij}^h}{\epsilon^h} - \frac{2}{3}\delta_{ij} && \text{(A.68)} \\ E_2 &= e_{ij} e_{ji} && \text{(A.69)} \\ E_3 &= e_{ij} e_{jk} e_{ki} && \text{(A.70)} \\ E &= 1 - \frac{9}{8}(E_2 - E_3) && \text{(A.71)} \end{aligned}$$

Pressure strain wall correction

$$\begin{aligned} \Pi_{ij}^w &= C_1^w f_w \frac{\epsilon^h}{k} \left(\widetilde{u_k'' u_m''} n_k n_m \delta_{ij} - \frac{3}{2} \widetilde{u_i'' u_k''} n_k n_j - \frac{3}{2} \widetilde{u_k'' u_j''} n_k n_i \right) \\ &\quad + C_2^w f_w \left(\Pi_{km,2} n_k n_m \delta_{ij} - \frac{3}{2} \Pi_{ik,2} n_k n_j - \frac{3}{2} \Pi_{kj,2} n_k n_i \right) \end{aligned} \tag{A.72}$$

$$f_w = \min\left[\frac{k^{\frac{3}{2}}}{2.5\epsilon^h y_n}, 1.4\right] \tag{A.73}$$

$$\mathbf{n} = \frac{\nabla y_n}{|\nabla y_n|} \tag{A.74}$$

Diffusion term

$$D^{\mu}_{ij,k} + D^{T}_{ij,k} = \frac{1}{2}\mu\frac{\partial \widetilde{u''_i u''_j}}{\partial x_k} + \sigma_\omega \mu_T \frac{\partial \widetilde{u''_i u''_j}}{\partial x_k} \tag{A.75}$$

Eddy viscosity

$$\mu_T = 0.144 A\overline{\rho}k^{\frac{1}{2}} \max\left[10\eta_K, L\right] \tag{A.76}$$

$$\eta_K = \left(\frac{\nu^3}{C_\mu k\omega^h}\right)^{\frac{1}{4}} \tag{A.77}$$

$$L = \frac{k^{\frac{1}{2}}}{C_\mu \omega^h} \tag{A.78}$$

Dissipation equation

$$\epsilon^h = C_\mu k\omega^h, \quad C_\mu = 0.09 \tag{A.79}$$

$$\begin{aligned} \frac{D\left(\overline{\rho}\omega^h\right)}{Dt} &= \frac{\partial}{\partial x_i}\left[\left(\frac{1}{2}\mu + \sigma_\omega\mu_T\right)\frac{\partial \omega^h}{\partial x_i}\right] + \alpha\frac{\overline{\rho}\omega^h}{k}P_k - \beta\overline{\rho}\left(\omega^h\right)^2 \\ &\quad + CD_{k\omega} + \frac{1}{C_\mu k}P_{\epsilon 3} \end{aligned} \tag{A.80}$$

$$\alpha = \left(C_{\epsilon 1} - 1\right) \tag{A.81}$$

$$\beta = C_\mu\left(C_{\epsilon 2} - 1\right) \tag{A.82}$$

Dissipation solid wall boundary condition

$$\omega^h\Big|_{\text{first cell}} = \frac{\mu}{C_\mu\overline{\rho}y_1^2}, \quad \left.\frac{\partial \omega^h}{\partial \mathbf{n}}\right|_{\text{wall}} = 0 \tag{A.83}$$

Table A.4: Coefficients of Reynolds stress and dissipation rate equations for the JH-ω^h model (Morsbach *et al.*, 2015*a*).

Model	Coefficient	Model	Coefficient
$\Pi_{ij,1}$	$C_1 = C + \sqrt{A}E^2$	Π^w_{ij}	$C^w_1 = \max\left[1.0 - 0.7C, 0.3\right]$
	$C = 2.5AF^{\frac{1}{4}}f$		$C^w_2 = \min\left[A, 0.3\right]$
	$F = \min\left[0.6, A_2\right]$	Diffusion	$C_S = \sigma_\omega C_\mu$
	$f = \min\left[\left(\frac{\mathrm{Re}_T}{150}\right)^{\frac{3}{2}}, 1\right]$	ω^h	$\alpha = 0.44$
	$Re_T = \frac{\overline{\rho}k^2}{\mu\epsilon^h}$		$\beta = 0.072$
	$C_1' = 0$		$\sigma_\omega = 0.9091$
$\Pi_{ij,2}$	$C_2 = 0.8\sqrt{A}$		$\sigma_d = 0.25$
	$C_2' = 0$		$C_{\mathrm{cr}} = 0.55$
	$C_3 = \frac{4}{3}C_2$		$C^1_{\epsilon 3} = 0.3$
	$C_3' = 0$		$C^2_{\epsilon 3} = 0.64$
	$C_4 = C_2$		$C^2_{\epsilon 3} = 2.0$
	$C_5 = -C_2$		

Table A.5: Formulation of gradient production $P_{\epsilon 3}$ and cross-diffusion $CD_{k\omega}$ term for different versions of JH-ω^h model.

Model	$P_{\epsilon 3}$	$CD_{k\omega}$
JH-ω^h	$\frac{0.3\mu k\widetilde{u_j''u_k''}}{\epsilon^h}\frac{\partial^2 U_i}{\partial x_j \partial x_l}\frac{\partial^2 U_i}{\partial x_k \partial x_l}$	$\frac{2\sigma_d\overline{\rho}}{\omega^h}\max\left[\frac{\partial\omega^h}{\partial x_i}\frac{\partial k}{\partial x_i}, 0\right]$
JH-ω^h (Maduta)	$\frac{2.0\mu\mu_T}{\overline{\rho}}\frac{\partial^2 U_i}{\partial x_p \partial x_q}\frac{\partial^2 U_i}{\partial x_p \partial x_q}$	$\frac{2}{k}\left(\frac{1}{2}C_{\mathrm{cr}}\mu + \sigma_d\mu_T\right)\frac{\partial\omega^h}{\partial x_i}\frac{\partial k}{\partial x_i}$
JH-ω^h (Maduta, $P^3_{\epsilon 3}$)	$\frac{0.64C_\mu\mu k^2}{\epsilon^h}\frac{\partial^2 U_i}{\partial x_p \partial x_q}\frac{\partial^2 U_i}{\partial x_p \partial x_q}$	$\frac{2}{k}\left(\frac{1}{2}C_{\mathrm{cr}}\mu + \sigma_d\mu_T\right)\frac{\partial\omega^h}{\partial x_i}\frac{\partial k}{\partial x_i}$

B Vortex detection methods

B.1 The λ_2-criterion

The λ_2 criterion detects vortices using the matrix

$$S_{ik}S_{kj} + W_{ik}W_{kj} \tag{B.1}$$

defined by the strain rate and vorticity tensors S_{ij} and W_{ij}. The second largest eigenvalue of this matrix is called λ_2. Negative values of λ_2 indicate a vortex (Jeong & Hussain, 1995).

B.2 Streamwise vorticity

The data available from the five hole probes does not provide the axial velocity gradient which is required to compute the streamwise vorticity

$$\omega_{\text{sw}} = \frac{U_i \epsilon_{ijk} \frac{\partial U_k}{\partial x_j}}{\sqrt{U_q U_q}}. \tag{B.2}$$

It is computed following the proposition by Reinmöller (2007) resulting in the following expressions:

$$\omega_x = \frac{1}{r}\left[\frac{\partial r c_\phi}{\partial r} - \frac{\partial c_r}{\partial \phi}\right] \tag{B.3}$$

$$\omega_r = \frac{1}{c_x}\left[\frac{1}{\rho r}\frac{\partial p}{\partial \phi} + \frac{1}{2r}\frac{\partial c^2}{\partial \phi} + c_r \omega_x\right] \tag{B.4}$$

$$\omega_\phi = -\frac{1}{c_x}\left[\frac{1}{\rho}\frac{\partial p}{\partial r} + \frac{1}{2}\frac{\partial c^2}{\partial \phi} - c_\phi \omega_x\right] \tag{B.5}$$

$$\omega_{\text{sw}} = \frac{c_x \omega_x + c_\phi \omega_\phi + c_r \omega_r}{\sqrt{c_x^2 + c_\phi^2 + c_r^2}} \tag{B.6}$$

Curriculum vitae

Personal data

Date of birth: 20.01.1983
Place of birth: Wuppertal

Employment

10/2009 – today	*Institute of Propulsion Technology, DLR e.V.* ▪ Research assistant, Department Numerical Methods	Cologne
09/2009 – 10/2009	*Fraunhofer Institute for Laser Technology* ▪ Research assistant, Department Surface Treatment	Aachen
09/2007 – 06/2009	*Fraunhofer Institute for Laser Technology* ▪ Student assistant, Department Surface Treatment	Aachen

Education

07/2008 – 08/2009	*Fraunhofer Institute for Laser Technology* ▪ Diploma thesis, Department Surface Treatment	Aachen
09/2006 – 06/2007	*Imperial College London* ▪ Erasmus scholarship	London, UK
10/2003 – 08/2009	*RWTH Aachen* ▪ Study of Physics, diploma	Aachen
08/1993 – 06/2002	*Private Sankt Anna Schule* ▪ Final examination: Abitur	Wuppertal

Civilian service

04/2003 – 06/2003	*Arbeiter Samariter Bund* ▪ Honorary work, mobile social service	Wuppertal
07/2002 – 04/2003	*Arbeiter Samariter Bund* ▪ Civilian service, mobile social service	Wuppertal